On the Breakdown of Helical Wake behind a Rotating Blade in Thermally Stratified Atmosphere

Nor Mazlin Binti Zahari

Department of Engineering

Durham University

This dissertation is submitted for the degree of
Doctor of Philosophy

April 16, 2020

Dedication

I would like to dedicate this thesis to my lovely family & friends;
especially to my parents who taught me to dream big and to work hard for achieving those dreams.

Thank you all for encouraging and believing in me.

On the of Breakdown of Helical Wake behind a Rotating Blade in Thermally Stratified Atmosphere

Nor Mazlin Binti Zahari

Submitted for the degree of Doctor of Philosophy
April 16, 2020

Abstract

In this thesis, a fundamental study on the breakdown mechanisms of a helical flow is conducted. The helical flow shares common traits with the wind turbine wake flow. The simulation data generated by a Direct Numerical Simulation (DNS) of flow around a rotating blade in a thermally stratified atmosphere were analysed in the physical space before two modal analysis techniques which are Dynamic Mode Decomposition (DMD) and Proper Orthogonal Decomposition (POD) were employed to the dataset. The DMD and POD analyses were able to determine the dynamics of the wake behind the rotating blade, i.e., the dominant mode of the helical flow structures and the corresponding frequency spectrum. As a result, the identification of the coherent structures and dynamics of the helical vortices behind the rotating blade in the stratified atmosphere is presented with the discussion on how the stratified temperature field influenced the deformation and breaking down of the helical wake structure. Various modes showed different characteristics of the flow fields. Focuses on the energy of flow; the POD technique could capture large-scale vortex structures and their organized behaviour, whereas the DMD method focuses on the frequency, and it represented the perturbation dynamics. Overall, the helical wake structure behind a rotating blade was proved to be remarkably influenced by the variation of the thermal stratification in terms of their characteristics, dynamics, and stability. Among all, the most affected is the one from the weakly stable stratified atmosphere.

Declaration

The work in this thesis is based on research carried out by Nor Mazlin Binti Zahari under the supervision of Dr. Lian Gan, and Dr. Peter Matthews within the Department of Engineering at the University of Durham in the United Kingdom. No part of this thesis has been submitted elsewhere for any other degree or qualification and it is all my own work unless referenced to the contrary in the text.

Nor Mazlin Binti Zahari

April 16, 2020

Acknowledgements

All praise to Allah for giving me the strength to be able to go through all the hard times of completing this Ph.D journey. This thesis would not have been completed if it was not for the assistance of many peoples, who have helped me throughout the four years since November, 2015. I would like to take this opportunity to thank them all. Specifically:

- My Ph.D supervisors, Dr. Lian Gan, and Dr. Peter Matthews, for their continuous support, guidance and positive words throughout the duration of this research.
- My former supervisor, Dr. Xuerui Mao, for providing valuable data and an opportunity to work on this research.
- Universiti Teknikal Malaysia Melaka, UTeM, and Government of Malaysia; for the opportunity and financial supports to pursue this Ph.D.
- The colleagues and friends (who means as much to me as my own family does) I met around the world throughout my travels and my time at Durham; for making the Ph.D tolerable.
- My family, especially my mom and dad; for always believing in me. Without their support and prayer, this would not have been possible and I would not be where I am today.

Contents

List of Figures

List of Tables

Chapter 1

Introduction

This first chapter starts with a general introduction of the research background and the problem statement in Section 1.1, followed by the motivation and objective of the study in Section 1.2 and Section 1.3, respectively. The chapter continues with Section 1.4 where the composition of the thesis is presented while in the last section (refer to Section 1.5), the whole chapter is to be summarized.

1.1 Background

In different kinds of flows, helical vortices are observed and found in nature and countless industrial applications. In rotating equipment such as propellers, wind turbines, and so forth they are often developed as tip vortices as depicted by some real-life events in Fig. 1.1. This kind of flow has been the topic of numerous theoretical, experimental and numerical studies, for instance, the study in the wake of helicopters [15], propellers [101] or wind turbines [105] in which a complex system of vortices is shed possessing the features of general three-dimensional flows. These flows are discovered to be somewhat easier: they fulfil a helical symmetry at least locally, i.e., by combining axial translation and rotation, these vortices are invariant.

The vortex sheet of the flow behind the rotor system was created by the lift distribution along with the blades. A roll-up process sets in immediately after the vortex sheet is developed due to the interaction between the vortex components, which in the instant near-wake behind the rotor forms powerful tips and root vor-

tices. The roll-up process is governed in essence by Biot–Savart's interaction law. The tip/root vortex system in most cases is unstable, eventually breaking down and forming small-scale turbulence further downstream owing to multiple instability mechanisms. What more complicated is the structure of the vortex sheet downstream a rotating wind turbine blade. The wake obtains a typical helical shape due to both rotational and axial velocity components. It is noted that the trailing vortex filaments follow a circular path.

Figure 1.1: Helical vortices created from different devices such as from a: (a) propeller [63]; (b) wing [176]; (c) rotor [27]; and (d) blade [38].

In the context of flow over a turbine blade, the occurrence of flow over a blunt body was discussed by Matin in her work [104], leading to vortex shedding. Fig. 1.2 shows the development of distinct vortices in near-wake regions to large-scale structures in the far wake that form through the process of vortex pairing and stretching [32].

As wakes can be damaging to wind turbine structures and detrimental to their power generation, it is essential to study the wake development to prevent the aforementioned undesirable wake impacts. For instance, smoke released from the end of a test blade in Fig. 1.1(d) demonstrates a horizontal-axis wind turbine helical pattern

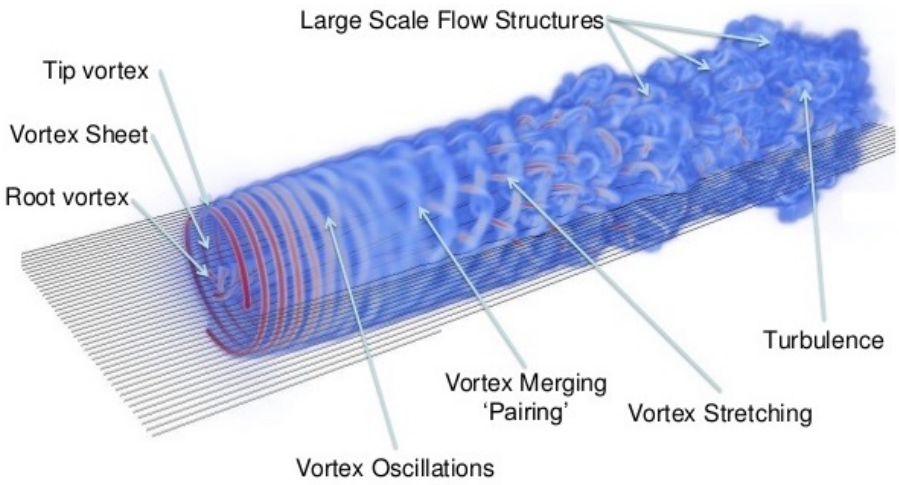

Figure 1.2: Evolution of a Wind Turbine Wake. Image is taken from [32].

of a tip vortex. Like air plane wings, wind turbine blades generate a vortex in their wake, and the vortices from each blade can interact downstream. These intricate wakes complicate wind turbine placement for wind farms. An example of an offshore wind farm provided in Fig. 1.3, where the reader can see how the wind turbines were positioned in the wind farm.

Figure 1.3: World's Largest Offshore Wind Farm, Walney Extension covering an impressive 145 sq km with 87 turbines from MHI Vestas and Siemens Gamesa. It is located in the Irish Sea that is situated near the Walney Island, Cumbria. Image from an article written by K. Vyas in [84].

A downstream turbine has higher fatigue loads than the upstream neighbour, and this explained its decreased power output. As illustrated in Fig. 1.2, a decrease in momentum happens once the flow moves through the turbine rotor, causing a region of momentum deficit in the wake. This results in a shear layer that mixes high-velocity components outside the wake region with the-low velocity components of the deficit region. As the wake axially progresses, it is expanding. The mixing process generates turbulent eddies resulting in the wake recovery or wake recharging [19]. Higher turbulence intensity improves the effectiveness of mixing, reducing the distance of wake recovery. Such level, however, leads to blade fatigue in the downstream turbine, thereby increasing maintenance costs. That is to say, the downstream turbine generates less energy and will wear out sooner. In response to this problem, many researchers visualize, measure, and simulate turbine wakes and their interactions to find the course of actions to maximize the wind power production.

Therefore, it is essential to have a thorough knowledge of wind turbine wakes and, in particular, a better understanding of the well-known but less well-understood wake-meandering phenomenon that causes the wake to move as a whole in both horizontal and vertical directions as it is conveyed downstream, see for instance Fig. 1.4. This wake oscillatory movement is crucial for downstream turbine loading as it increases fatigue loads and especially yaw loads on turbines as the wake drifts in and out of the rotor planes of downstream turbines [104, 112]. Meandering can also reduce the wake's overall deficit to eventually ease power losses [19]. Early wake meandering study has shown that meandering has an important effect on reducing the magnitude of wake deficits [56].

Over the past century, much of fluid dynamics studies have shifted away from the growth of statistical models, focusing on identifying and describing the dynamics of so-called coherent structures. While a number of authors have suggested their own definitions, there is no fixed definition. Hussain first defined a coherent structure as "a connected, large-scale turbulent fluid mass with phase-correlated vorticity over its spatial extent" in [5]. More recently, Adrian & Marusic in their works described the coherent structures as coherent motions of individual entities, that contribute

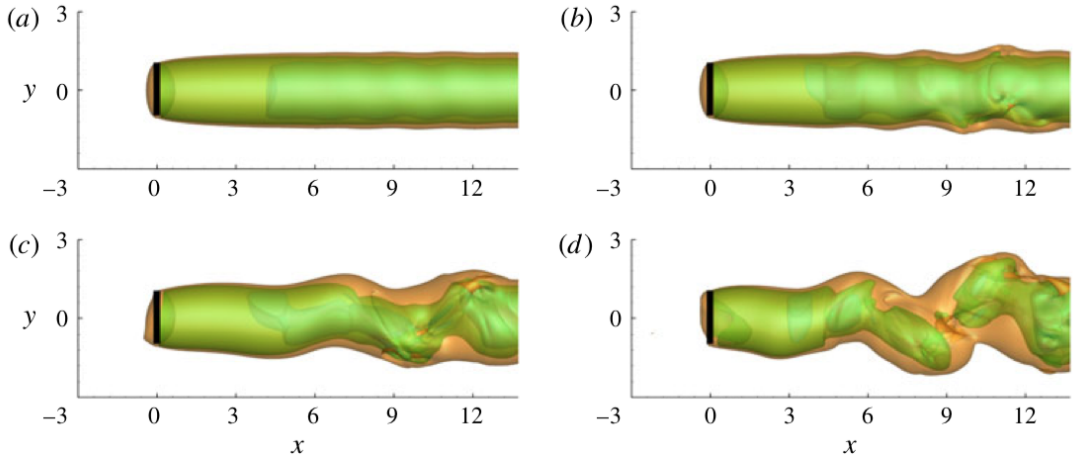

Figure 1.4: Far-Wake Meandering, according to [178].

significantly, but are not solely spatially consistent, to mean flow and momentum fluxes. While a universal definition may not yet exist, it is agreed that coherent structures are spatially and temporally coherent and are the construction blocks of turbulent flows [142, 143].

There are several methods in fluid mechanics to identify these coherent structures. Some of them are based on the identification of invariants of the velocity gradient tensor [5,53,121], which is defined in terms of the velocity field spatial derivatives. In this context, the swirling strength [76], Q-criterion, and λ_2-criterion [61] are some of the most common methods for identifying the vortical structure. Section 4.2 of Chapter 4 gives detailed elaboration on the mathematical expressions of these criteria. Other alternative that can be found is Direct Lyapunov Exponents (DLE), which can be used to identify the Lagrangian coherent structures [45, 95]. At every point in space, in the DLE method, this scalar is a function of the separation rate of adjacent particle trajectories initialized near that point. More specifically, if $\boldsymbol{x}(t, \boldsymbol{x}_0, t_0)$ denotes the position of a particle at time t, which started at $\boldsymbol{x}_0$ at the time of t_0, the expansion coefficient σ_T at any finite integration time T, is defined as the square of the largest singular value of the deformation gradient $\partial \boldsymbol{x}(t_0 + T, \boldsymbol{x}_0, t_0)/\partial \boldsymbol{x}_0$:

$$\sigma_T(\boldsymbol{x}_0, t_0) = \lambda_{max} \left(\left[\frac{\partial \boldsymbol{x}(t_0 + T, \boldsymbol{x}_0, t, 0)}{\partial \boldsymbol{x}_0} \right]^T \left[\frac{\partial \boldsymbol{x}(t_0 + T, \boldsymbol{x}_0, t, 0)}{\partial \boldsymbol{x}_0} \right] \right) \tag{1.1.1}$$

where $\lambda_{\max}$ signifies the maximum eigenvalue. The DLE field is then defined as

$$\mathrm{DLE}_T(\boldsymbol{x}_0, t_0) = \frac{1}{2T} \log \sigma_T(\boldsymbol{x}_0, t_0) \tag{1.1.2}$$

Since in the definition of σ_T, the maximum eigenvalue is used, direction information in $\mathrm{DLE}_T(\boldsymbol{x}_0, t_0)$ does not retain. If there is a large amount of expansion in one direction, even if there is compression in all other directions, a point $\boldsymbol{x}_0$ will have a high DLE value.

Most of these techniques enable instantaneous vortical structures to be identified, allowing the monitoring and extraction of significant trajectories and lifetime features. These methods, however, are based only on instantaneous spatial statistics and do not take the temporal evolution of the coherent structures into consideration.

An alternative to these methods is based on identifying the structures that enumerate the most statistically to the signal variance under evaluation; these methods are referred to as modal decomposition techniques. In simple words, modal decomposition technique is a method in which the flow system can be developed as an expansion of modes of the structure and subsequently extract its coherent structure. The Proper Orthogonal Decomposition, POD, is a classical approach to fluid mechanics [64]. In the case of a velocity signal, the POD technique can identify those flow structures that most contributed to the turbulent kinetic energy, revealing their spatial structure (POD modes) and temporal dynamics (POD coefficients). Even so, as Schmid et al. noted in [129]; one restriction of the POD method is that it assumes that the turbulent processes are linear, this is usually met by the dynamics of large-scale constructions, but is usually not true in the global analysis of lower turbulent field scales. The Dynamic Mode Decomposition, DMD [25, 129], is a recent alternative that assumes temporal orthogonality, distinct from the POD, which assumes a spatial one. DMD makes it possible to identify coherent structures in a highly non-linear turbulent mechanism better, but one limitation is that it can not rank the resulting modes in terms of their contribution to a certain magnitude, as the POD does with the variance. Although DMD may give the key to describe coherent structures of temporal significance, it has only been effectively implemented to highly theoretical works [60].

1.2 Motivation

The motivation of this research is to understand the basic physics of helical wake in the thermally stratified field, taking the wind turbine as an application. Remark that the Reynolds number of the present study is much lower compared to the real-life wind turbine cases. This is due to the drawbacks of Direct Numerical Simulation (DNS - a method used in this study to model turbulent flows), which causes it to suffer from the overall computational cost, thus limiting practical applications of turbulent flows to small Reynolds numbers. The computing resources required by a DNS will surpass the capability of the most powerful computers currently available for the Reynolds numbers encountered in most industrial applications. Nonetheless, DNS is a useful tool in fundamental turbulence research. Through DNS, "numerical experiments" can be conducted and extract from them the information that is difficult or impossible to obtain in the laboratory, thereby enabling a better understanding of turbulence physics. Therefore, this fundamental study is essential before one can enhance the positioning of offshore wind farms by avoiding the hazards imposed by wake impacts on energy production. It is, therefore a fundamental case that shares common traits with the wind turbine flows was studied. Most of the past research was carried out with designs of wind turbines positioned in flows with uniform incoming flow velocity and comparatively low turbulence intensity. Anyhow, in reality, wind turbines always operate along the elevation direction in atmospheric boundary layer winds with significant wind shear and turbulence intensity. However, (owing to some restrictions) the present study considers only the atmospheric boundary layer winds with uniform incoming flow velocity and low turbulence.

In this present study, a fundamental study on the evolution of helical wake stability behind a rotating blade in the thermally stratified atmosphere was carried out in order to see the influence of temperature effects on the wake flow. Afterwards, two modal analysis techniques, which are DMD and POD, were employed to that three-dimensional unsteady fluid flow to identify the coherent structure of the flow from different atmospheric stability conditions. While the real-life wind turbine has three blades, this study considered just a single blade due to the high computational cost. Even so, this is good enough for the fundamental study of the real wind

turbine. Acknowledging the differences, strengths, and weakness of both methods as mentioned in [20] and will be as well discussed in further details in Section 3.4 of this thesis, this work is not about comparing these two methods like what some researchers did [44, 135, 169], but rather about collecting all the important information from both methods. At the end of this study, the identification of the coherent structures and the dynamics of the helical vortices behind a rotating blade in the thermally stratified atmosphere are expected to be able to be presented with the discussion on how the stratified temperature field can effects the evolution of the helical vortices wake structure.

1.3 Objectives

The main question of this research is how much the helical wake flow behind wind turbine can be affected in a different thermally stratified atmosphere. This subsequently motivate the researcher to analyse the characteristics of helical flow in different stability of the atmospheric stratification conditions and hence determine the dynamics of the wake behind a rotating blade as a fundamental case which shares a common traits with the wind turbine flows, e.g. the energetic/dominant mode of the helical flow structures and the corresponding frequency spectrum from the data generated by a Direct Numerical Simulation with different temperature gradient fields at various Reynolds number.

In order to accomplish the ultimate goal, the analyses on DNS datasets are carried out, and these are listed as the objectives of the present study. The objectives to be performed are:

- to carry out a fundamental study on the evolution of helical wake stability behind a rotating blade in a thermally stratified atmosphere.
- to investigate the helical wake structure behind a rotating blade under the influence of temperature effects.
- to look into a fundamental study of the helical wake structure behind a rotating blade under the impact of Reynolds number effects.

1.4 Structure of the Thesis

This thesis provides the analysis of the helical wake vortices measured behind a rotating blade in the stratified atmosphere, including the effect of the temperature gradients and Reynolds numbers on the helical structures.

The thesis will be organized as follows:

In Chapter 1, the problem statement was introduced before the motivation of working on this research, the objectives and the scope of the thesis were stated.

In Chapter 2, the literature review on few subjects relating to the aims of the thesis was described and overviewed.

In Chapter 3, the numerical and computational in which how the data was constructed was firstly introduced. Next, the theory of both modal analysis techniques used in this work (DMD and POD) will be described in detail. Furthermore, the algorithms of both techniques will be presented, as well as their strengths and weaknesses.

In Chapter 4, the analyses of all cases where the helical wake flow behind the rotating blade from different atmosphere stratification conditions; weakly, neutral, and strongly stable were performed at Re = 1000, and Re = 2000 were presented.

In Chapter 5, the POD method will be employed to all cases of different atmospheric conditions at Re = 1000 and Re = 2000. The correlation between the result from POD (POD modes from velocity POD) and PODT (POD modes from temperature POD) modes will also be put into the discussion.

In Chapter 6, the DMD method will be applied to the same datasets as in Chapter 5, provided together with the analysis and discussion of the results. The reciprocity between DMD (DMD modes from velocity DMD) and DMDT (DMD modes from temperature DMD) modes was to be compared to the POD and PODT modes from the previous chapter.

Finally in Chapter 7, the conclusion made from the whole work will be given, and some recommendation on the future study that has the potential to be explored will be listed.

1.5 Chapter Summary

The very first chapter of this thesis was about a general introduction of the research in which the background and the problem statement of this study were provided. The background talked about the helical wake, what meandering, the importance of understanding helical wake instability behind a wind turbine, and the motivation of the study. The objectives were listed before the structure of this thesis was finally presented. The continuation chapter is all about the review of previous research discussed on related questions to this study.

Chapter 2

Literature Review

This report continues with a chapter that provides a number of comprehensive summary of previous research on topics related to this study. A review of prominent work for simulating wind farm wakes and a review of several studies done on the helical wake flow is included in Section 2.1 and Section 2.2, respectively. Another component of the research is to investigate the effect of temperature stratification on general flow instability. Section 2.3 provides the prior study regarding the wake in a thermally stratified atmosphere. Also, previous works in two considered modal analysis techniques are included in Section 2.4. The last section of this chapter, Section 2.5) presents a summary of the whole chapter.

2.1 Experimental Study on the Helical Wake

The fact that for a downstream wind turbine, the lower energy output, the enhanced unsteady loads, and the noise produced can be immediately connected with the turbine blades passing through the streamwise vortices generated by the upstream wind turbine. Therefore, as reviewed in [1, 19, 50, 92], wind turbine wakes were the topic of comprehensive research using both experimental and numerical methods.

Helical vortex wake flow was experimentally studied by few researchers such as Felli et al. [101] studied the spatial development of marine propeller wakes for two to four blades: disturbance growth resulted in vortex groupings and eventually dissipation of the coherent structures. This study disclosed the existence of the

hub vortex at the axis that plays a part in the process of instability. Bolnot et al. [47] and Quaranta et al. [49], on the other hand, used a water channel where helical wakes were closely controlled by one- and two-bladed rotors. Modification of the rotor angular velocity or a tiny asymmetry between the two blades compelled instability modes. The temporal growth rates measured as a function of the imposed wavelength were discovered to agree with the concept of the filament.

In recent decades, a number of wind-tunnel experiments have been performed to investigate the freestream (uniform and nearly laminar) airflow around wind turbines. Vermeer et al. [92] offer a comprehensive review of this literature. Wind tunnel studies have also been conducted over the past few years to study the interaction of turbulent boundary layer flows with wind turbines or farms. Cal et al. [136] performed an observational wind tunnel analysis considering the horizontally distributed boundary layer structure over an array of wind turbine models. The research focuses on the large-scale structure in conjunction with the boundary layer. At this point, the variables of interest are the horizontally averaged velocities and, Reynolds stresses. It is claimed that dispersive stresses (stresses associated with mean velocity spatial variations), in theory, can also be responsible for the transfers of momentum and kinetic energy [99]. Noted that the dispersive stress arises due to correlations among the spatially non-homogeneous horizontal and vertical mean velocities. The results of the measurement in the wind tunnel show that the dispersive stresses are fairly small relative to the stresses of Reynolds, although it may lead to a wake-up recovery in the near-wake region this is cancelled mostly by an opposite behaviour in the front region of the flow. The horizontally average structure of the flow can be understood using momentum theory, in the sense that consistency exists between the friction velocities prevalent above and below the wind turbine region with the turbine thrust coefficient.

A detailed wind tunnel experiment was proposed by Bastankhah and Porté [96] to research the interaction of a turbulent boundary layer with a wind turbine working under various tip-speed ratios and yaw angles. In the recirculating wind tunnel, a three-bladed horizontal-axis wind turbine was mounted in a neutrally stratified boundary layer. In addition, a high-resolution particle object velocimetry (PIV)

test to quantify the flow in the upwind, near-wake, and far-wake regions was carried out. Using both instantaneous and phase-averaged vorticity fields, the evolution of tip and root vortices was studied for the near-wake region. The results suggest that it is impossible to determine the vortex breakdown location on the basis of phase-averaged statistics, particularly for tip vortices under turbulent conditions of inflow. Moreover, the near-wake region measurements indicate a complex velocity distribution with a wake centre speed-up the region, especially for higher tip-speed ratios. Particular emphasis was placed on studying the characteristics of large turbulent structures in the boundary layer and their interaction with wind turbines to elucidate the meandering tendency of far wakes. Although these structures are elongated in the direction of the stream, their cross-sections are found to have a size similar to the area of the rotor, so that the presence of the turbine can impact them. Furthermore, the study of spatial coherence in turbine wakes reveals that due to the effect of wake meandering, any statistics based on streamwise velocity fluctuations can not provide reliable information on the size of large turbulent structures in turbine wakes. The findings also suggest that wake meandering magnitude is not contingent on the conditions of turbine-operating.

Hyvárinen et al. [3] performed an experimental analysis of the wake propagation behind one or two aligned wind turbines on flat and hilly terrains with homogeneous and sheared turbulent inflow conditions. The wind turbine design scale was about 1000 times smaller than full-size turbines, indicating that the findings should be extrapolated to real-field scenarios only qualitatively. Wind tunnel measurements are made using stereoscopic particle velocimetry to describe the velocity of flow in planes perpendicular to the direction of flow. As the wakes dispersed downstream of the turbines, they broke down their tip-vortex regions and became less distinct. At the same time, the wakes seemed to become more prone to the perturbations of the vertical flow generated by the hills, leading to greater deflections of the wake. Such studies also provided valuable information about the flow structure of the turbine wakes in boundary-layer flows, showing significant variations in freestream flows.

Most of the experimental results on the near-wake vortices exposed in the literature are obtained from small-scale experimental studies conducted in controlled

environments. There are many explanations for this. On one side, field experiments with full-scale wind turbines give invaluable data, but difficult tasks are due to the highly chaotic nature of the inflow conditions, clear exposure of the physical phenomena, and analysis of the underlying mechanisms. On the other side, wind tunnel experiments on large-scale rotors would lead to the most appropriate outcomes, but there are only a few documented sources in the literature owing to the economic costs engaged in such projects [51, 160]; refer [7, 92] for comprehensive reviews as reported by Vermeer et al. and Nemes, respectively. The laboratory experiments, while confined to a lower range of Reynolds numbers, provide a streamlined but beneficial approach that can assist elucidate the rather complex wake dynamics.

However, covering large ranges of helical pitches, core sizes, and Reynolds numbers is hard in experiments. This can be done more readily using a numerical approach. Hence, simulation models are increasingly needed to include the unsteady aerodynamic loads and the aeroelastic response of the wind-turbine structures [105]. A number of distinct models are used today, ranging from fast and simple blade element momentum techniques to computational fluid dynamics [70, 72].

2.2 The Study of Helical Wake through Numerical Computations

Numerical simulations are an efficient and complementary tool for understanding rotor wake aerodynamics. They are split primarily into two categories. The numerical studies can be carried out in the computational domain with or without the presence of the rotor. The former is mainly focused on engineering problems such as aerodynamic rotor crafting, aero-mechanical efficiency, or noise reduction. An instance of this kind of simulation is presented in Fig. 2.1, where the purple helical vortices are embedded in a small-scale green-coloured turbulent flow. While giving insight into realistic flow dynamics as much as possible, it continues hard to separate the distinct physical phenomena clearly. The computational cost is also improved with the rotor model in the computational domain owing to the requirement that the boundary layer is resolved, e.g., Fig. 2.1 was produced using 1,536 cores with a

supercomputer.

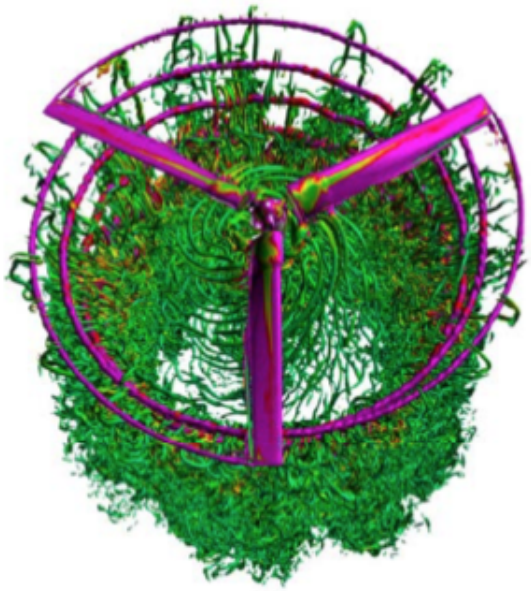

Figure 2.1: Snapshot of a Rotor Model and its Near Wake as plotted by Selçuk [149].

Several techniques, such as the actuator disk method (ADM) [71] or the actuator line method (ALM) [153], were used to solve the latter difficulty. These techniques depict rotors distributed on a permeable disk or on lines in a flow domain by equal forces. Such methods have been applied to predict a single wind turbine wake but also to predict a whole wind farm's power extraction [81]. Martínez et al. [85] compared the performance of actuator disk and actuator line models in predicting wind turbine power production and wake velocity deficits. The schematic of the ALM and ADM with an example of the wake and vortex system created by both models were nicely depicted by [85] and shown in Fig. 2.2.

The turbulence produced by wind turbine wakes due mainly to the presence of the distinct tip and root vortices. The structured tip/root vortex system is unstable in most cases and eventually breaks down and forms chaotic small-scale turbulent structures. Remember that if a wind turbine is in the wake, consisting of the stable tip and root vortices, the loading of fatigue is more extreme than if the tip vortices were already broken down by instability mechanisms [70]. It is,

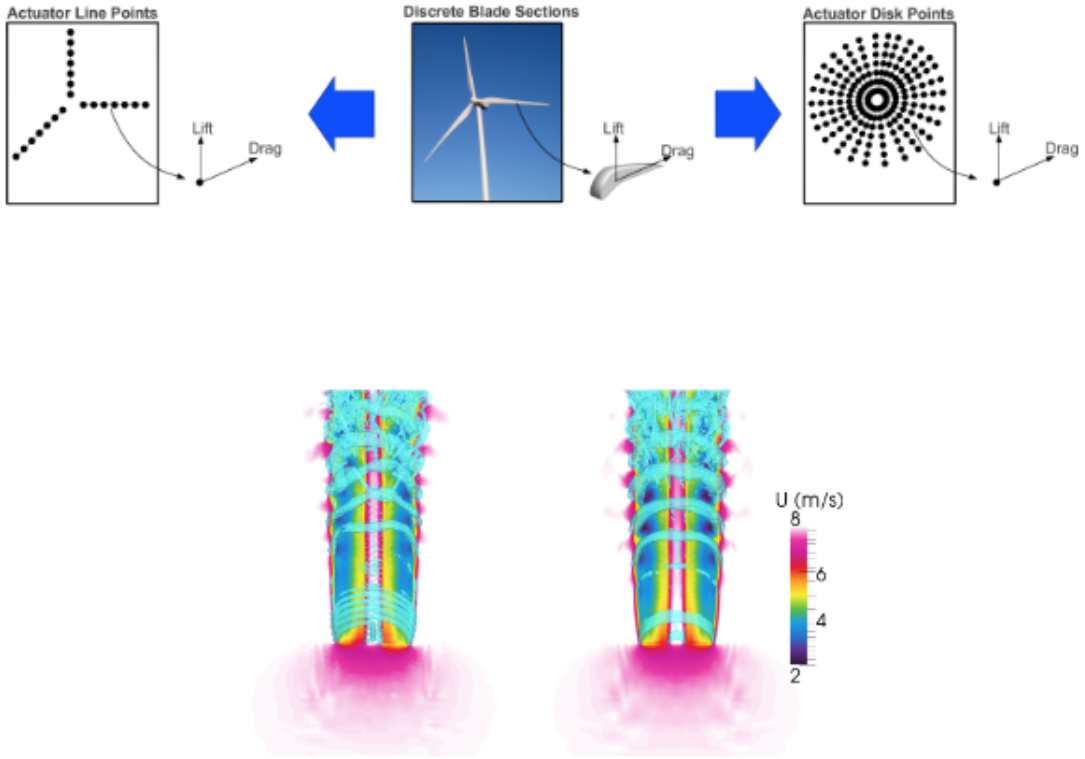

Figure 2.2: (Above) Schematic of an: ALM (left) and ADM (right) turbine model as developed by Martínez et al. [85]. (Below) Simulation of ALM on the left and ADM on the right where the blue isosurface is of the second invariant of the velocity-gradient tensor. Note that the contours are of streamwise velocity.

therefore, important to understand the physical nature of the vortices and their dynamics in the wake of a turbine for the optimum design of a wind farm. One of the first to suggest a design capable of representing the dominant features of a propeller in 1912 was Joukowski [113]. The proposed model consisted essentially of two revolving horseshoe vortices representing the tip vortices and straight root vortices. The study by Okulov & Sørensen [172] in 2007 showed that the far wake of the model is completely unstable.

Depending on the number of blades, the wake behind rotors such as propellers, wind turbines, and helicopter rotors can be treated as single or multiple helical vortices. The early study of a twisted helix dates back to work by Widnall [151] in which the theoretical framework was given to study the linear stability of a single helical vortex for inviscid flows. Widnall was among the pioneers proving the exis-

tence of at least three different mechanisms of instability and showed that helical vortices of finite core size are unstable to small sinusoidal displacements, particularly as the pitch of the helix becomes small. The pitch of the helix is defined as the displacement of one complete helix turn, measured parallel to the helix axis. A short-wave instability mechanism can occur in the presence of disturbances with a large number of waves for a relatively large helix pitch, and it may most likely be found in all curved filaments. In addition, if the (normalized) wave-number of the perturbations drops to less than unity, long-wave instability can occur. The adjacent filament begins to interact strongly when the pitch of the helix decreases beyond a certain threshold, which constitutes the underlying mechanism for mutual inductance instability. Felli et al. [101] performed extensive research on propeller wakes and noticed the traces in the experiments of all three forms of instability mechanisms.

Gupta & Loewy [16] and Bhagwat & Leishman [102] studied the stability of small perturbations in helical vortex filaments. In static thrust or axial flight mode, the vortices mimic a helicopter rotor or propeller. A free vortex wake calculation was used to classify the unstable modes in the wake structure. Results are reported as there are neutrally stable (zero growth rate) and unstable (positive growth rate) conditions for all perturbation wave-numbers. A maximum growth rate has been recorded for wave-number disturbance equal to half-integer multiples of the number of blades, e.g., $K = N_b(i + 1/2)$ for all integer i where K is the wave-number disturbance and N_b is the blade number. Remember that the above experiments were carried out using quantitative methods where the viscosity effect was ignored.

A study about the stability of the tip vortices of a wind turbine was carried out by Ivanell et al. [154] using computational fluid dynamics (CFD) in combination with the ALM. The presence of the blades is implemented as a body force in the ALM developed by Sørensen & Shen [72], and the flow field around the blades is calculated by solving the Navier–Stokes equations using large-eddy simulations (LES). Subsequently, the resulting wake was perturbed by imposing a harmonic excitation near the tip of the blade. Analysis of the flow field that the instability is dispersive and that spatial growth occurs for specific frequencies and spatial structures with

wave-numbers equal to half-integer multiples of the number of blades, as previously discovered in inviscid investigations similar to [16, 72] and discussed above.

A few distinct analytical mean flow models were created using various fundamental approximations [56, 117, 152] to describe the mean wake field. Jensen [117] made a simple model for the wake behind a wind generator. Before being used in an example where the output from a circular cluster of ten wind generators was measured, the model was compared to some full-scale experimental results. The simple wake model was then expanded to deal with a number of aligned generators, and an example was finally given where it was possible to calculate the output from a linear cluster of ten generators. Meanwhile, Ainslie [56] presented a single wake model that can be used to measure the wake velocity field behind a wind turbine, taking into account all possible meteorological influences. The model is relatively simple, and on a desktop machine, the equations can be solved speedily. Consequently, it is proposed that the model can be used to provide accurate estimates of wake deficits for use in wind farms planning and design. It is, therefore, proposed that the model can be used to provide reliable estimates of wake deficits for use in wind farms planning and design.

Frandsen et al. [152] proposed an empirical model for the wind speed deficit in wind farms, including both small wind farms and large-scale wind farms. The model handles a regular array of geometry with straight rows of wind turbines and equidistant spacing between units in each row and the equidistant spacing between rows, as is often the need for offshore wind farms. The model accurately and reliably incorporates the flow characteristics of very large wind farms (with sufficient experimental calibration). Nevertheless, these models do not include the dynamic wake elements normally expected to be necessary for the loads and power generation of a wake-flow turbine.

When the turbulence length scales are larger than the wake width based on the basic wake meandering model, wake meandering, which is defined as random oscillation, is generated and powered [35, 41, 43]. It can be used to assess power generation and the loading of wind turbines. The importance of wake meandering study lies in its potential for application in optimizing the topology and operation of

wind farms as well as in optimizing wind turbines for wind farms applications [41]. Considering the meandering of the velocity deficit is an original move to include dynamical behaviour. This is normally performed by assuming that the meandering is primarily triggered by the large-scale dynamics of the atmospheric boundary layer (ABL) [40, 41, 62]. The wake meandering model is said to be based on a fundamental assumption that it is possible to model the transportation of wakes in the atmospheric boundary layer by considering wakes to serve as passive tracers powered by large-scale turbulence structures. Consequently, the simulation of the meandering process involves considerations of an appropriate description of the stochastic transport media "carrier" and an appropriate interpretation of the cut-off frequency defining large-scale turbulence structures in this context [40].

These procedures, however, do not consider the deficit structure temporal dynamics that can lead to very elevated loads. Besides, it is not entirely clear whether the meandering can simply be dealt with as a passive tracer driven by the dynamics of the large scale. By using LES with actuator disk or actuator line models, it should be feasible to portray the turbines in more detail [4, 20, 99]. Regardless of their simplifications, these simulations continue to experience the ill effects of rather long computational times that severely restrict their efficiency for practical purposes such as optimizing the wind farm. Developing computationally effective wake models, including dynamic behaviour, is crucial in this manner.

It is possible to divide the wake behind a wind turbine into the near wake region and the far wake region [92]. But, according to the description of the wake behaviour by Crespo et al. [1], the wake of a wind turbine can be separated into three regions: a near wake region, a far wake region, and a transition region in-between. Fig. 2.3 shows the development of the vertical velocity profile downstream a wind turbine. The area is divided into four regions in the direction of flow: the (uninterrupted) free stream region upstream of the rotor and the three wake regions. The picture shows a velocity profile for each region. The near wake region ends at about two rotor diameters downstream of the rotor, and the far wake begins downstream at about 4-5 rotor diameters.

The near wake region begins at the rotor surface where means of a pressure drop

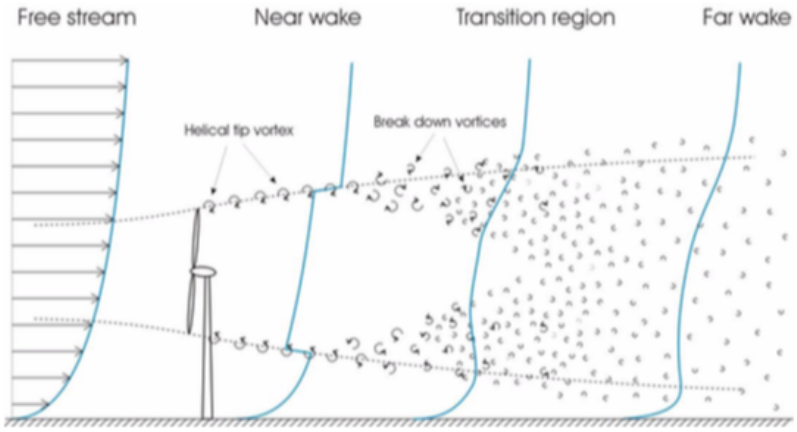

Figure 2.3: Development of the vertical velocity profile downstream a wind turbine as depicted by [34].

over the rotor plane extracted wind energy. The cylindrical shear layer separates the slow-moving air inside the wake from the air outside the wake. A helical direction is accompanied by vortices inside the shear layer that are expelled from the turbine blades. Inside the wake, the velocity deficit increases as a result of the increasing pressure inside the wake until this pressure reaches the external flow pressure. As a result of the increasing velocity deficit, the wake expands. Inside the shear layer, the stable structure of helical vortices creates only a small amount of turbulence. The thickness of the shear layer grows slowly due to limited turbulent diffusion within the shear layer. In [36], PIV measurements showed that the influence of individual blades on axial velocity disappears beyond a distance of one rotor diameter while the tip vortices remain for a much longer time.

The tip vortices begin to break down at the end of the near wake region and produce high turbulence rates. Due to the increased turbulent diffusion, the thickness of the shear layer increases more rapidly. The near wake stops when the shear layer hits the wake axis, and the transition region begins. The transition region ends where the wake is fully developed with self-similar distribution profiles of the velocity deficit and turbulence intensity.

The wake has fully developed in the far wake area, and there is no longer the shear layer between the wake and the outer flow (see Fig. 2.3). Also, the aerodynamic properties of the rotors are no longer apparent, which makes it somewhat

easier to model the far wake than the near wake. There is often a clear distinction between near and far wake models in engineering models used for wind farm energy predictions, whereas in reality, the regions are obviously related. Furthermore, kinematic far-wake models isolate the effects of wind speed deficit and wake turbulence strength while these phenomena are connected in reality.

The rotor shape, amount of blades, blade aerodynamics (attached or stalled flows), and 3D effects have a strong effect on the near wake [48]. The helical structure of tip vortices, which are shed from the blades, is another strong feature of the near wake. These vortices have been discovered to have a significant impact on the turbulent flow structures in the wake [48] and also have a powerful effect on the wind turbine rotor behaviour as a whole [92]. The vortices were also discovered to be a cause of noise generation and blade vibrations [36]. The far wake is the wake component where the real shape of the rotor is less essential. Turbulence is the primary contributor to the flow regime in the far wake region where in large-scale and small-scale motions, called eddies, has developed [181]. Eddies are rotating flow swells that are present in the far wake.

2.3 Wakes in Thermally Stratified Atmosphere Flows

Whether wind turbines, propellers, or helicopter rotors, the blades of rotor systems shed vortices into the wake that advect downstream and are characterized by helical paths. In wind energy [172], aviation [37, 102], and marine industries [101], the evolution and breakdown dynamics of these vortical wakes are not fully grasped and remain an important question. In the field of vortex dynamics, it is also of basic concern [8, 16, 151, 171, 172].

Widnall in [151] first predicted the stability features of helical vortices. The author performed the linear stability analysis of a helical vortex filament with respect to sinusoidal perturbations and found that the system was subject to three types of unstable mode: a long-wavelength mode, a mutual-inductance mode, and a short-wavelength mode. The work then was extended by Gupta and Loewy [16] to several helical vortices forming a regular array. The modes analogous to those obtained for

one single vortex and additional ones arising from the mutual interaction between distinct vortices were found from the study. It is noteworthy that in the limit of infinite wavelengths, these latter modes are compatible with the helical symmetry constraint. Okulov [171] focused specifically on these helically symmetrical modes in arrays of N vortices with circular cores and constant vorticity. The author showed that such systems are unstable when the helical pitch is smaller than a threshold value. Later, in order to study the more realistic case of rotor wakes, Okulov and Sørensen [172] investigated the effect of a central hub vortex and found that the stability of such flows strongly depends on the vorticity profile in the core and that the central hub has a destabilizing effect.

These helical vortices play a significant part in the growth of the wake directly downstream of the rotor (the near-wake) in the case of wind turbines, and their evolution and breakdown dynamics impact the features of the resulting far-wake downstream rotor diameter. This has immediate consequences in wind farms where wake interaction with downstream turbines can lead to dynamic blade loading and a drop in the efficiency of wind farms. Such industrial difficulties provide the motivation to study these structures [108].

While worthwhile information has been discovered by these past research, it should be observed that most of these experimental research has been performed with models of wind turbines installed in air or water flows with homogeneous, uniform incoming flow rate and comparatively low turbulence intensity. In fact, however, most wind turbines work along vertical paths in atmospheric boundary layer winds with important differences in mean wind speed as well as turbulence intensity concentrations. The impacts on the dynamic wind loads of the important differences in the mean wind speed and turbulence intensity levels of the atmospheric boundary layer winds; and the evolution of the unsteady vortex and turbulent flow structures in the wake of wind turbines were not fully studied.

Turbulence is produced primarily by vertical shear during the neutrally stratified periods, while thermally driven buoyancy plays a significant part in turbulence generation during the unstable stratified periods [139] (see Fig. 2.4). As the ground surface heats up, the near-surface flow warms with it, and buoyancy makes a ben-

eficial contribution to the energy budget, thereby improving vertical mixing and turbulence kinetic energy (TKE) output. In contrast, turbulence is primarily dissipated by buoyancy during stable stratification periods, resulting in a sharp reduction in a mixing [73, 88, 94]. As a result, the wind farm's performance relies heavily on atmospheric stratification, see [21, 42, 82, 93, 167]. Thus, understanding the interaction of wind farms with the time-changing atmospheric thermal stratification is critical to the effective growth of wind energy resources.

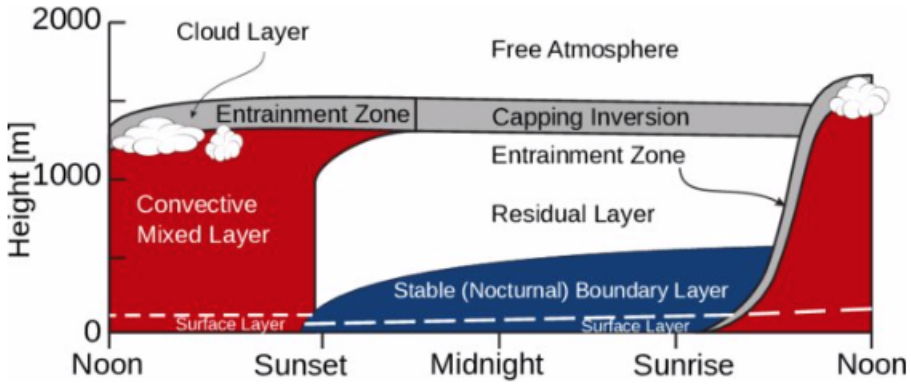

Figure 2.4: Boundary-layer Structure during a Diurnal Cycle in a High-Pressure Region over Land as illustrated by [139].

The boundary layer is not frozen in time but instead changes dramatically during the course of the day. It consists of a mixed layer stirred by solar heating of the surface and convection of warm moist air, which sporadically emerges from place-to-place, and time-to-time, mixing the air within the boundary layer as a consequence. It takes about 10 to 20 minutes for this convective stirring to go from bottom to top. As the air bubbles up, it mixes with the surrounding air and the top air from the free troposphere, producing an entrainment zone where the clouds are located.

As the sun sets, the surface solar heating, and the convection and associated turbulent eddies cease. Air from the surface no longer mixes with air throughout the convective boundary layer, and the air mixed during the day remains in a layer called the residual layer above the much lower stable boundary layer at night. Within this nocturnal boundary layer, any gaseous or particle emissions from the surface are mixed. Because convection stops at night, the friction caused by convection no

longer affects the winds in the residual layer, and they accelerate in the presence of a gradient of horizontal pressure. The residual layer winds are thus accelerating, blowing harder across the top of the more stagnant nocturnal boundary layer, and shear is forming. This shearing is volatile and produces turbulence that mixes the boundary layer air and the remaining layer air close to the interface so that the nocturnal boundary layer grows slightly during the night.

The sun returns to heat the surface in the morning and begin convection driving and mixing again. This convection bubbles up in the residual layer, bumping in and bringing in air. The convection has more energy as solar heating increases and can grow higher and induce more air from the residual layer. Ultimately, the convection-driven air reaches its highest energy level, and this peak energy limits how high the boundary layer will develop into the above stable free troposphere. Fig. 2.5 is referred to for this whole explanation.

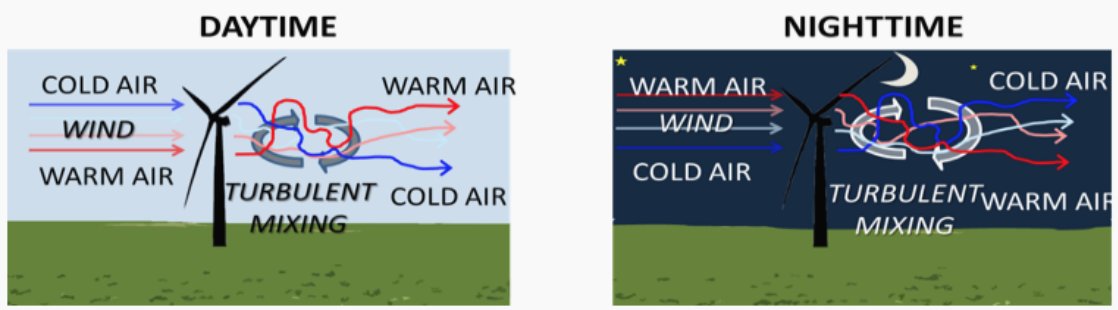

Figure 2.5: Conceptualization of wind farm turbulent mixing during: daytime (left) and night time (right). Image is taken from [100].

Hu et al. in [48] conducted an experimental study to characterize the dynamic wind loads and evolution of the unsteady vortex structures in the near wake of a horizontal axis wind turbine (HAWT) model installed in an atmospheric boundary layer wind. The wandering of the tip vortices was concluded to be strongly linked to the elevated turbulence levels of the atmospheric boundary layer winds as well as the wake meandering phenomena reported by Bingöl et al. [35] and Larsen et al. [41].

Besides, a large bluff body in a stable layer was then regarded by Haywood & Sescu [74], and findings were recorded and debated composed of vertical profiles

of turbulent momentum, thermal flux, and turbulence intensity. The variation in thermal stratification was discovered to have only a slight impact on all statistical quantities, but in comparison to the smaller wind velocity, the bigger wind velocity substantially influenced all vertical profiles. Contrary to the slight impact seen in statistical quantities, differences in heat stratification considerably influenced the distribution of helical modes obtained from POD analysis at the highest levels. The profiles in the wake of the turbulence intensity and the vertical turbulent momentum flux were only slightly affected by the thermal stratification variance (refer to Fig. 2.6(a) & Fig. 2.6(b), respectively). This can be interpreted as the rise in thermal stratification, which concentrates the turbulent energy in the higher energy levels, manifesting as more helical modes at higher energy levels, thus leaving the overall statistics largely unaffected. Through looking at Fig. 2.6(c), on the other hand, maintaining constant wind velocity to increase thermal stratification and hence, increased the relative energy levels of the POD modes.

Abkar & Porté-Agel [93] investigated the impact of thermal stability on a wind turbine wake. The spatial distribution of the mean velocity and wake meandering downstream of the turbine are highly correlated with the stability of the atmosphere. Under the unstable situation, the wake's development rate is about 2.4 times that of the stable one. Here, in the context of power extraction, the different conditions that conform to the turbulence kinetic energy budget are regarded.

2.4 Modal Analysis Techniques

Complex flows such as separation, shear layer, and turbulence always show dynamic behaviour in both space and time across a wide range of scales. Due to the diversity of these scales and their interactions, describing the fundamental fluid dynamics is a difficult task. Looking for and extracting physically important features or modes as a first step in the analysis has become common practice in the analysis of flows. In practice, decomposition of the entire flow field into modes can be performed to capture and recognize the dominant features as interpreters of dominant flow structures. The mathematical derivation of the two model decomposition techniques

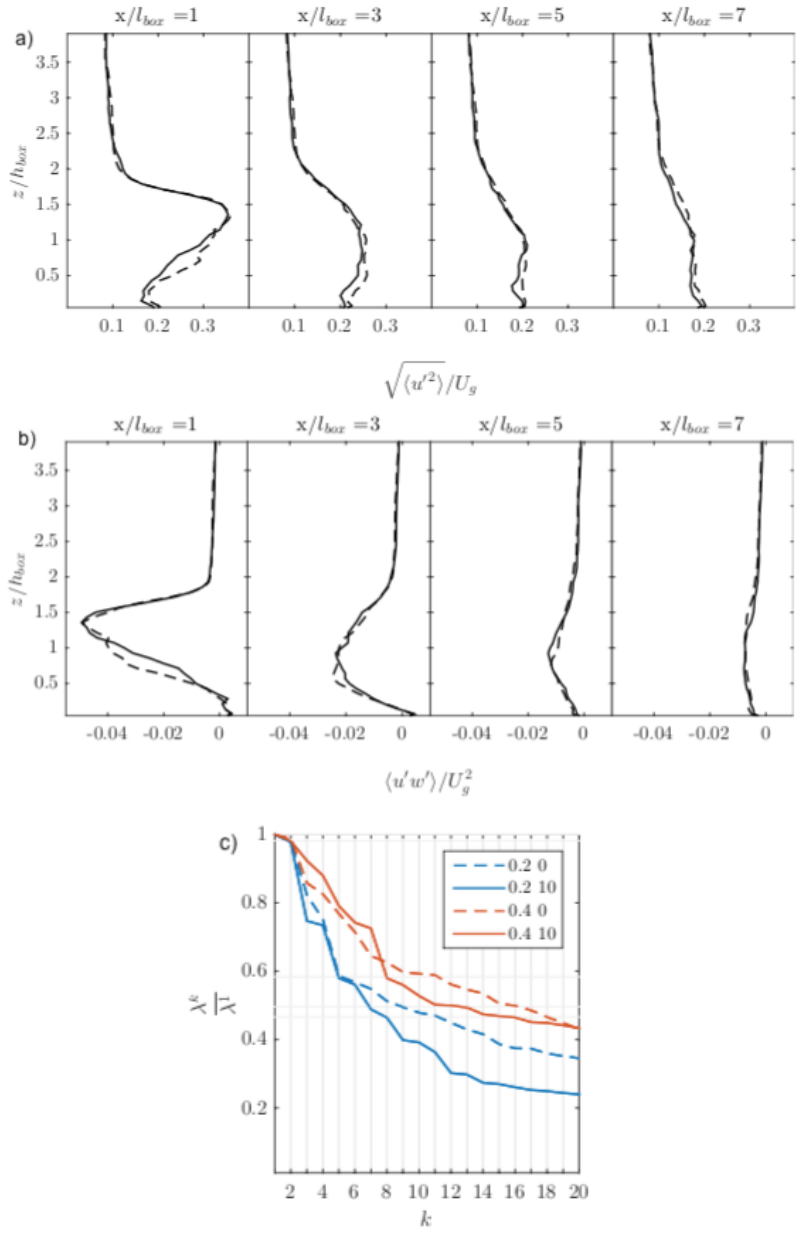

Figure 2.6: Vertical Distribution, z/h_{box} of (a) turbulence intensity, $\sqrt{\langle u'^2 \rangle}/U_g$, (b) vertical turbulent momentum flux, $\langle u', w' \rangle / U_g^2$; measured every two box lengths from the rear of the body with wind velocity, $U_g = 18m/s$. $\Delta T = 0.2$K represented by - - - while — represents $\Delta T = 0.4$K. (c) The first twenty POD mode energies normalized with the first mode energy. The blue and red solid lines are representative of $\Delta T = 0.2$K and $\Delta T = 0.4$K for $U_g = 18m/s$. Remark that the two dashed lines were for $U_g = 8m/s$ and will not be described in this discussion. Figure courtesy by [74].

that will be used widely in this analysis will be presented in Section 3.4 of the subsequent chapter.

Many mathematical methods have been suggested over the past two centuries for the purpose of coherent structures identification. Taira K. et al. [83] provided a short summary of several well-established methods, outlined some of their works and analyses that have emerged in recent decades [26, 67, 68, 123, 127, 174]. Table 2.1 is a table constructed by Taira K. et al. in [83], where all the reviewed modal decomposition techniques were listed together with their general description. Above all, POD and DMD have enjoyed widespread used among all of the techniques. Beyond the bounds, both POD and DMD methods can be employed to numerical simulation flow field data and experimental measurements [83].

There are some DMD applications in various flow configurations. For instance, DMD has been applied in the study of the wake behind a flexible membrane [125], detonation waves [89], cavity flows [10, 125], and various jets [25, 125, 126, 130]. Schmid [125] used DMD on a number of examples ranging from plane Poiseuille flow (for validation purposes) to the cavity flow, from wake flow behind a flexible membrane determined by time-resolved PIV to jet flow between two cylinders. DMD has proved itself from all the tests as a powerful and effective algorithm for spatio-temporal coherence structures extraction.

DMD was employed to study the self-excited fluctuations aided by transversely unstable detonations in the study conducted by Massa et al. [89]. The study focuses on the stability of the limit cycle solutions and their response to forcing. Floquet analysis of the unforced conditions reveals that the least stable disturbances are nearly sub-harmonic with the ratio between global mode frequency and fundamental frequency $\lambda_i/\omega_f = 0.47$. This indicates the emergence of period-doubling modes as the route to chaos observed in larger systems.

Seena & Sung [10] established large-scale vortical structures responsible for self-sustained oscillations through the use of a DMD of turbulent flow pressure fluctuations over an open cavity. DMD was applied to incompressible turbulent flows over an open cavity at Re_D =3000 and 12000, with upstream turbulence of Re_θ =670 and 300, respectively, respectively, given at the inlet. The dynamic modes extracted

	Techniques	Inputs	General Descriptions
data-based	POD	data (L or NL flow; C&E)	Determines the optimal set of modes to represent data based on L2 norm (energy).
	Balanced POD	data (L forward & L adjoint flow; C)	Gives balancing and adjoint modes based on input-output relation (balanced truncation).
	DMD	data (L or NL flow; C&E)	Captures dynamic modes with associated growth rates and frequencies; linear approximation to non-linear dynamics.
operator-based	Koopman analysis	theoretical (also see DMD)	Transforms non-linear dynamics into linear representation but with an infinite-dimensional operator; Koopman modes are approximated by DMD modes.
	Global linear stability analysis	L NS operators & mean flow (C)	Finds linear stability modes about base flow (i.e., steady state); assumes small perturbations about base flow.
	Resolvent analysis	L NS operators & mean flow (C)	Provides forcing and response modes based on input-output analysis with respect to mean flow; can be applied to turbulent flow.

Table 2.1: Summary Table of selected Modal Analysis reviewed by [83]. The considered modal decomposition/analysis techniques for fluid flows where linear denotes as L, nonlinear (NL), computational (C), experimental (E), and Navier–Stokes (NS).

from the thick boundary layer suggested that the upcoming boundary layer structures and the shear layer structures along the cavity lip line coexisted with coincident frequency space but with different wave-number space, while structures with a thin boundary layer displayed complete consistency between modes to generate self-sustained oscillations. This finding indicates that the hydrodynamic resonances that gave rise to self-sustained oscillations occurred when the upcoming boundary layer structures and shear layer structures interacted, not only in frequencies but also in wave-numbers.

Schmid, in 2011, applied the DMD technique to two different jets. In the case of visualizations by a passive scalar field, the results from Schlieren pictures of a low-density helium jet have shown typical modal structures on the jet's shear layer showing the commonly known scaling of temporal frequencies and spatial wave-numbers of the associated modal structure. The DMD can clearly distinguish between the flow fields of a forced and unforced axisymmetric jet when using time-resolved PIV-data. This difference was reflected in both the temporal spectrum and the spatial structure of the associated least damped dynamic modes [130]. Later, Schmid [126] employed the DMD to a series of slow jet flow images entering a quiescent liquid, showing the identification of dynamically specific coherent structures that play an important role in characterizing the fluid activity over the time interval analysed. It was concluded that the DMD has clear advantages over the POD as the former attempts to reflect the prevailing flow characteristics within a temporarily orthogonal system (i.e., pure frequencies), while the latter is based on a spatially orthogonal model. For fluid phenomena characterized by distinct frequency bands, it should be particularly suitable. In conclusion, both studies have been conducted to prove that DMD is capable of providing experimentalists with a helpful tool for detecting and quantifying important mechanisms in time-resolved measurements of complex fluid flow and helping to understand fundamental fluid processes further.

While for POD, it has been applied in the works involving the turbulent jet in flow [77,148], wake flows [39,55,97,155], turbulent separated flow over an air foil [133] and open cavity flow [116]. Also, some applications of POD have included stratified turbulent patches [124], free shear flows [165, 166], and boundary layer flows [141].

Bernero & Fiedler [148] conducted experiments on a round jet in a uniform counterflow with a PIV. POD analysis was then applied to time series of PIV data at high-velocity ratios to distinguish a few common trends from a jet's chaotic fluctuation in a counter-flow. Later in 2007, a comprehensive instantaneous velocity field of a cross flow jet was calculated using stereoscopic PIV [77]. The jet emerged from a turbulent pipe flow that was fully developed and entered a cross flow with a turbulent boundary layer. The POD analyses of the experimental data found that the shear-layer vortices are not coupled with the wake vortices dynamics.

Subsonic flow over an open cavity was studied by Murray et al. [116] for five free-stream Mach numbers ranging from 0.19 to 0.73 by analysing both the surface pressure and the field of velocity. The implementation of the POD was carried out separately from each of the different free stream cases on the velocity fields, resulting in a spatially dependent basis set. The spatial distribution of the first several modes demonstrated some correlations over the spectrum of free-stream Mach numbers had been analysed. The similarity in the modes was quantitatively verified using a similarity parameter, which relies on the orthogonality of the modes. The similarity in the modes was verified quantitatively using a similarity parameter dependent on the orthogonality of the modes. The fact that there are so many similar POD modes from the different free-stream conditions implies that the underlying turbulence structure is quite similar regardless of the variations in the mean flow recirculation.

Diamessis et al. [124] applied the POD method to two-dimensional vorticity transects obtained from numerical simulations of the stratified turbulent wake of a towed sphere at a Reynolds number $\mathrm{Re} = 5 \times 10^3$ and Froude number $Fr = 4$. In terms of the relative effect of buoyancy on flow dynamics, POD tends to provide a normal decomposition of the vorticity field within the wake core. The geometry of the eigenmodes reveals a vorticity structure that is dominated by buoyancy at the lowest modes and is increasingly turbulent as the mode index increases.

Gordeyev & Thomas introduced the study of free shear flows in the continuity papers [165,166], where in the priors of the planar turbulent jet [165], the possibility of large-scale organized motions in the similarity region was suggested. The large-scale term has been used to denote a spatial scales of the order of the local jet half-

width. The application of POD experimentally examined the coherent structure in the similarity region of the turbulent planar plane. The POD results suggest that the flow supports a planar structure aligned in the spanwise direction as well as an essentially three-dimensional structure with asymmetric shape in the direction of the cross-stream and pseudo-periodically distributed in the spanwise direction. There is, however, some uncertainty about the presence of large-scale organized motions in the similarity region of the planar turbulent jet, questions regarding the origin, topology, and dynamics remain. Therefore, the later study [165] was performed to provide the answer. The primary aim of the later study is to provide a more detailed description of the structural topology in the planar turbulent jet that is responsible for large-scale motions. The topology of the large-scale structure was tested experimentally in the similarity area of a turbulent planar plane. The large-scale structure was reconstructed in physical space by projection on instantaneous flow-field realizations of measured POD eigenmodes. Results indicate that in the planar jet, the self-similar large-scale structure consists of a dominant planar component consisting of two lines of large-scale spanwise vortices arranged approximately asymmetrically in relation to the jet centreline. This planar part of the structure is similar to the classic Kármán vortex street. On opposite sides of the plane, there is a strong interaction between structures in the form of almost two-dimensional lateral streaming motions that extend well across the flow.

In turbulent flows, Gurka et al. [141] proposed a framework for defining and characterizing large-scale coherent structures. The method is based on the linear combination of vorticity POD modes. The POD approach explicitly complies with the proposed guidelines for any objective and statistically significant identification procedure which is; first, the study uses an entire data set rather than a single flow field; second, it provides the spatial characteristics of a turbulent flow as opposed to single-point statistics; third, it does not depend on the choice of the basic functions (i.e., sinusoidal functions in Fourier transform or wavelet-based functions), and last but not least; is dependent on a rigorous mathematically defined POD method.

Table 2.2 lists a number of examples of the successful application of these two methods to various flows.

Table 2.2: List of the Application of POD and DMD to various analysis

Literature	Applications, findings, and variants	
	POD	DMD
Meyer et al., 2007a [77]	Turbulent jet in crossflow (PIV)	-
Meyer et al., 2007b [78]	Turbulent jet in crossflow (PIV & LES)	-
Rowley et al., 2009 [25]	-	Jet in crossflow (DNS)
Schmid et al., 2009 [129]	Flow in a lid-driven cylindrical cavity (PIV)	
Diamessis et al., 2010 [124]	Stratified turbulent wake of a towed sphere (LES)	-
Schmid, 2010 [125]	-	Plane Poiseuille flow; linearized two-dimensional flow over a square cavity; wake of a flexible membrane (PIV); jet between two cylinders (PIV)
Feng et al., 2011 [86]	Flow around circular cylinder under synthetic jet control (experiment), flow field measurement (PIV)	-

Continue on the next page

Table 2.2: List of the Application of POD and DMD to various analysis(cont.)

Literature	Applications, findings, and variants	
	POD	DMD
Pan et al., 2011 [22]	-	Wake of a NACA 0015 airfoil with Gurney flap (PIV)
Schmid et al., 2011 [126]	-	Passive tracer in flame simulation and axisymmetric water jet (experiment)
Schmid et al., 2011 [130]	-	Schlieren snapshots of a helium jet; PIV snapshots of an acoustically forced jet
Seena & Sung, 2011 [10]	-	Turbulent cavity flow (DNS)
Chen et al., 2012 [80]	-	Transitional cylinder flow (DNS)
Duke et al., 2012 [30]	-	Annular liquid sheet instabilities (experiment)
Muld et al., 2012 [169]	Wake of high-speed train model (Detached Eddy Simulation, DES)	
Schmid et al., 2012 [131]	-	Transitional water jet with tomographic (PIV)
Tirunagari et al., 2012 [163]	Subsonic jets flow (LES)	

Continue on the next page

Table 2.2: List of the Application of POD and DMD to various analysis(cont.)

Literature	Applications, findings, and variants	
	POD	DMD
Andersen et al., 2013 [155]	Flow in an infinitely long row of turbines (LES)	-
Munday & Taira, 2014 [133]	Turbulent separated flow over an air foil (CharLES)	-
Nemes et al., 2014 [8]	Three-bladed Glauert wake flow in water channel (experiment)	-
Sarmast et al., 2014 [159]	Wind turbine wakes (LES)	
Shah & Bou-Zeid, 2014 [161]	Thermally stratified ABL flows (LES)	
Tu et al., 2014a [58]	-	Wake of a cylinder (DNS); finite-thickness flat plate (PIV)
Tu et al., 2014b [59]	-	Flow past a cylinder (PIV); temporally sparse data
Zhang et al., 2014 [135]	Flow past a single cylinder & two cylinders of different size (Time Resolved PIV, TR-PIV)	

Continue on the next page

Table 2.2: List of the Application of POD and DMD to various analysis(cont.)

Literature	Applications, findings, and variants	
	POD	DMD
Bastine et al., 2015 [28, 29]	Wind turbine wakes (LES)	-
Liu & Zhang, 2015 [182]	-	Separated flow over a finite blunt plate (TR-PIV)
Tang et al., 2015 [157]	Two-dimensional flow over circular cylinder (experiment)	-
Ali et al., 2017 [110]	Wake flow in thermally stratified wind turbine array(LES)	-
Towne et al., 2018 [11]	Complex Ginzburg-Landau equation; turbulent jet	
Haywood & Sescu, 2019 [74]	Wake flow in thermally stratified large bluff body (LES)	-

Using the POD to develop reduced-order models for particular flow problems is one of the simplification methods that occasionally used in fluid dynamics [39,55,97]. Berkooz et al. described the POD technique and demonstrated its use in the analysis and modelling of turbulent flows in their study [39]. This gave the coherent structure a brief theory of POD as well as other techniques.

The large-scale structures in a turbulent mixing layer were analysed in the works of Delville et al. [55] through the use of correlation and POD. In a turbulent plane mixing layer, extensive experimental measurements were obtained using the means of two cross-wire rakes aligned normally with the direction of the mean shear and perpendicular to the mean flow direction. The correlation tensor was determined using data collected with two cross-wire rakes lying perpendicular to the splitter plate. In order to acquire the necessary data, two separate experiments were conducted, and the missing information was filled in using the continuity relationship. The POD was applied twice: first, only to the $u-$ and $v-$components of the correlation tensor and, secondly, to the full correlation tensor, i.e. u, v and w. In the mean square sense, this decomposition yields an optimal basis. The energy in the POD modes converges rapidly with the dominant first mode (49% of the TKE). Examination of these modes reveals that the first mode provides evidence in the mixing layer of both recognized flow organizations, i.e., quasi-two-dimensional spanwise structures and streamwise aligned vortices.

Bergmann et al. [97] investigated the optimum control approach for active control and drag optimization of incompressible viscous flow through circular cylinders. The technique was introduced in the laminar regime (Re=200) for unstable rotary control of the cylinder wake. The optimal control problem was solved with a POD reduced-order model (ROM) of the controlled flow as the state equation, specifying a cost-functional representation of the wake instability. The optimization method solution was then used with the Navier-Stokes equations as a flow model to control the wake flow numerically. Eventually, the amplitude of the drag coefficient was found to be significantly reduced (25%). Even so, since the earlier numerical studies on mean drag reduction were confirmed: it is shown, in general, that the proposed solution was energetically inefficient without a proper penalization of the control

output.

In 2013, Andersen et al. [155] used data from LES simulations with actuator line models to apply the POD to the flow in an infinitely long row of turbines. The simulated data gave insight into the performance of the wind turbines operating in the wake of others as well as details on key turbulent quantities. One of the key features of wakes behind wind turbines is the dynamic wake meandering that is shown to be connected to the spacing of the wind turbine and the turbine vortex shedding as a bluff body. Through applying POD, the flow was analysed and reconstructed. The spatial POD modes show symmetries as well as the pairing of configuration. The first 10 POD modes comprise 51% of the TKE, while 403 modes comprise 90%. Reconstruction of the flow field reveals that 74% of total TKE production is accounted for by the first 10 POD modes.

Meanwhile, Bastine et al. [28] applied the POD to LES data of a single wake of a wind turbine modelled by an actuator disk. Unlike [155], they analysed a single wake situation and included a more realistic inflow by modelling a turbulent ABL in the case of a neutrally stable atmosphere. The POD was applied to a plane perpendicular to the main flow in the far wake of the turbine. In order to isolate the wake from the ABL structures, it is possible to extract well-defined POD modes with sufficient preprocessing. It turned out that these modes are similar to the modes obtained by Andersen et al. [155] for an infinitely long row of turbines without ABL suggesting that wake dynamics can generally be represented by similar kinds of modes. Depending on the number of POD modes used, field reconstructions are investigated. Although it took a large number of modes to recover a large part of the turbulent kinetic energy, the results indicate that only a few modes can recover relevant aspects of a wake flow. Particularly, it is possible to partly capture the dynamics of the average velocity over a potential disk in the wake using only three modes.

DMD was developed by Schmid [125] on the basis of Koopman analysis of dynamic systems [25, 52]. This technique uses snapshots of the flow field only and is capable of describing the flow components that characterize the dominant dynamic behaviour without any recurrence to the underlying governing equations [125]. In

contrast to POD, it has advantages in providing temporarily orthogonal dynamic information of the flow field, such as the temporal dynamics and the related spatial shapes, thus offering a more compact and instructive way of understanding the fluid system. In 2011, Pan et al. proved that the DMD is a powerful tool for decomposing quasi-periodic flow fields and studying the underlying temporal dynamics [22]. Nevertheless, it can be difficult to determine which modes are the most physically important since there is no single right way to rank eigenvalue importance like what POD can do [83].

One of the extra benefits of the DMD is the capability to process limited or spatially restricted data [125]. The multiple flow domains and the instability mechanism were presented in a lot of realistic applications such as in [147], Kelvin–Helmholtz-like instabilities of the counter-rotating vortex sheet that exists together with wake-vortices and the breakdown of horse-shoe vortices for a jet in cross flow. Within a global stability analysis, it is hard to extract and separate these local instabilities because they act on distinct time scales. Nevertheless, the DMD algorithm is able to determine the system matrix for every sub-domain by extracting the measurements from the corresponding localizes regions. Consequently, it can efficiently and competently depict the dominant dynamical features of a multi-scale process.

It is also feasible even for the analysis of spatially evolving disturbance dynamics [125, 128]. Other DMD applications in a time or space environment include countless aspects of regular data processing requirements for experimental measurements. These include the low-dimensional representation of a dynamic process, the filtering of raw information based on structural and dynamic coherence, and the recovery of information from gappy measurements or signals [126].

As the data sequence becomes adequately long, owing to the fact that only neutrally stable fluid elements will remain and be recognized, [126] expected a naturally stable eigenvalue for a temporally ordered data sequence from a non-linear process. It is either inadequate sequences of data or the decomposition of temporally transient phenomena that may have led the eigenvalues to grow or decay. There are regions in the flow domain where a linear process within a spatial setting can properly describe the flow. In this situation, eigenvalues and dynamic modes can grow

or decay spatially.

In contrast to the POD, where the enforcement of spatial orthogonality of the identified structures was applied in each individual POD mode at the expense of a mixture of frequencies, the DMD aims at timely orthogonality (by identifying pure frequencies). The resulting dynamic modes are usually non-orthogonal [126].

Coherent structures with distinct spatial and temporal scales characterize fluid flows in large part. The temporal analysis deals with the evolution of spatially wave-like solutions, while the spatial approach deals with the growth or decay of time-harmonic perturbations upstream and downstream from their origin. Despite the fact that more research has yet to be done on complex two and three-dimensional flows, the theoretical refinement between a temporal and spatial analysis persists in a global analysis of stability.

In [125], they reorganized the flow fields by presenting a snapshot sequence in space and caused the quantities to be sliced differently through a spatio-temporal data set. The low-dimensional full-rank matrix, extracted in the same way from a spatially ordered data sequence, then represents the mapping from a stream field at one spatial area to a flow field at the following spatial area. Consequently, the eigenvalues give information about the spatial dynamics of the underlying flow. An example of spatial DMD was demonstrated on the flow in the wake of the flexible membrane.

Three-dimensional flow fields of a transitional water jet were extracted from experiments by using the time-resolved tomographic PIV in [131]. In addition to the existence of obviously identifiable frequencies and wave-numbers, the flow fields were characterized by a wide spectrum of spatial and temporal scales. A DMD technique was applied to a sequence of forty time-snapshots, where each captured with a spatial resolution and three velocity components. In both temporal and spatial cases, the DMD method isolated the coherent structures and their spectral properties and thus proved that it is effective in providing coherent dynamics with a low-dimensional representation.

These two famous modal analyses were implemented efficiently over a wide spectrum of turbulent flows, including the atmospheric flows and the wake of wind

turbine. For example, Shah & Bou-Zeid (2014) [161] applied the POD method to thermally stratified ABL flows to study the existence of large-scale turbulent features, demonstrating that the effect of buoyancy flux in the dominant POD modes is significant to the energy balance. In the first POD modes of the unstable case, streamwise rolls were noted, which were invisible in the stable case. The first modes also demonstrated sheet-like motions under unstable stratification, i.e., motions situated in low-rotation regions that do not contribute to vortical structures. Refer to Fig. 2.7 for the illustration.

Concerning turbulent flow in wind farms, VerHulst & Meneveau [24] used POD to study the turbulence structure in the canonical, neutral wind turbine array boundary layer (WTABL). As a function of the wind farm layout, the results illustrated the contribution of individual POD modes to the energy input. Consisting of streamwise counter-rotating vortex pairs that are much larger than the individual wind turbine scale, the most energetic structures have been discovered. Less than ten of these roller modes captured 20% –30% of the domain TKE and more than 14% of the turbine rate kinetic energy output. In the lower region of the boundary layer where the wind turbines reside, the influence of the wind farm on POD modes is most noticeable. The energy content of the POD modes also varies from case to case. In cases with wind farms, greater TKE was presented, and some energy from the large-scale structures of the ABL was distributed between small-scale modes of lower-energy. Also, Andersen et al. [155] employed POD to analyse the LES data of a large wind farm, demonstrating that the wake meandering dynamics are strongly dependent on the spacing of the turbines. It was shown that the first 10 modes were sufficient to capture more than 51% of the total TKE and that the following 400 modes captured less than 40%.

Bastine et al. [29] developed a POD analysis of LES data of a characteristic wind turbine wake. The spatial modes characteristic of the isolated wind turbine wake could be identified from the findings. In that research, a few modes were adequate to capture the flow dynamics, with the first mode being exclusively linked to the large-scale turbulence horizontal movement.

More recently, POD was used by Hamilton, Tutkun & Cal [114] to identify

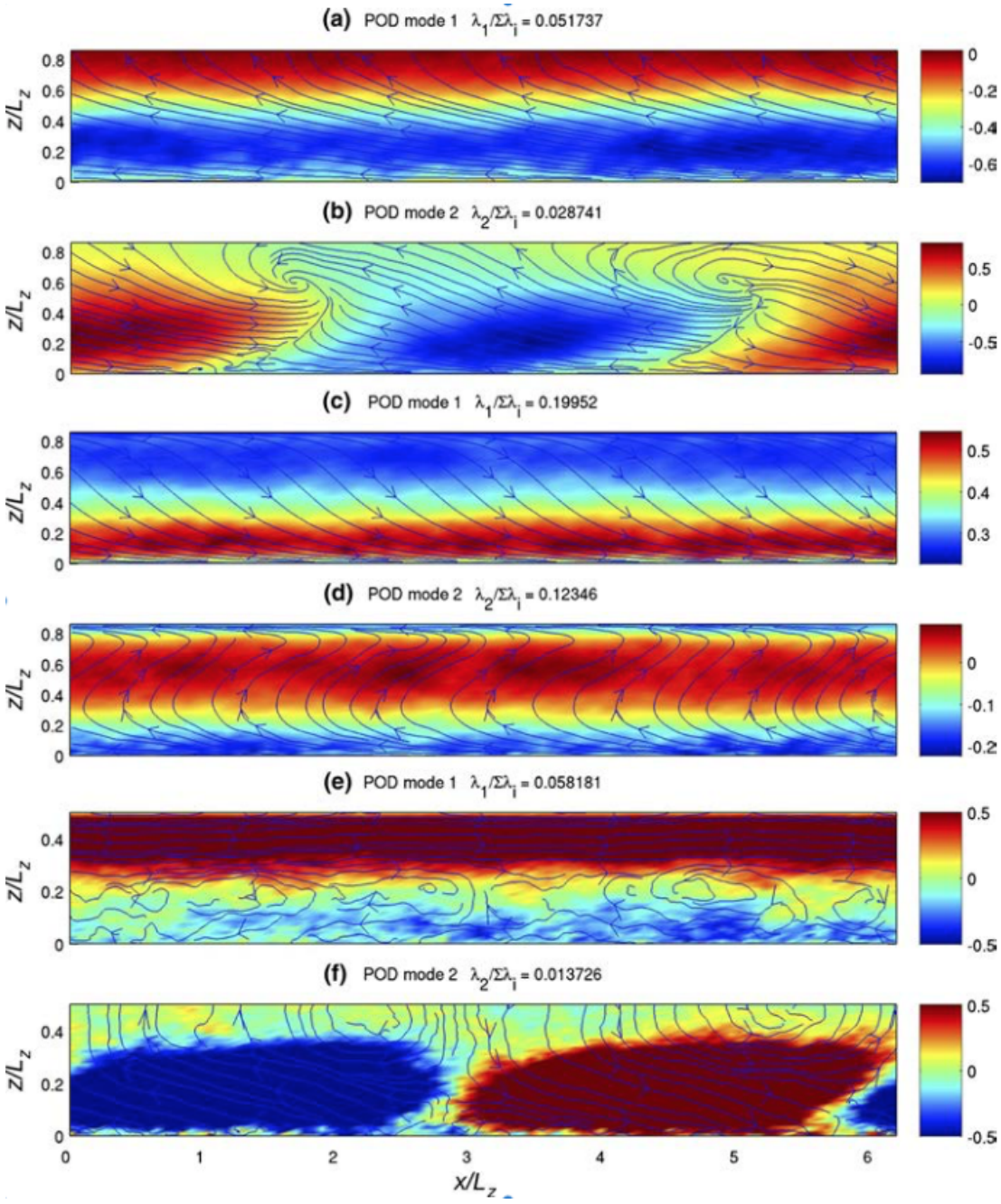

Figure 2.7: The first two POD modes in the xz-plane for the neutral (a,b), unstable case (c,d), and stable case (e,f). The colour bar indicates the normalized u component of the POD mode, which is in the x-direction. The blue contours show u- and w- components in the plane. The numbers above each sub-figure indicate the value of TKE as a fraction of the total TKE presented by [161].

the coherent structures of aligned and staggered wind farm settings in the wind turbine wake, demonstrating that the turbulent flux and output are rebuilt with

only 1% of the total orthogonal POD modes. In subsequent experimental work, Hamilton, Tutkun & Cal [115] developed the double POD in the wind turbine wakes to determine the sub-model organization of the largest projection and correction modes coefficients. Only 0.015% of the total degrees of freedom of the original flow field needed to represent the turbine wakes with this approach.

Under the thermal stratification regimes, Ali et al. [110] used POD to extract coherent structures of the turbulent flow. In order to reproduce the distinctive flow conditions found in realistic atmospheric boundary layer flows, three different regimes of thermal stratification, stable, unstable, and neutral, were regarded. The research offers a fresh view on how wind turbines under different thermal stratification conditions interfere with the atmospheric flow. Under various thermal stratification conditions, the findings discovered in their study were claimed to benefit the optimization and control of new generation wind farms.

DMD was applied by Xiang et al. [179] to an experimental data of wakes produced in a stably stratified background by a towed grid and effectively-recognized the dynamically significant flow patterns and revealed the impact of stratification on their initiation and evolution. The distribution of energy overs various length scales ranges, as defined by DMD, shows a simple Froude number, Fr dependence in the near wake. Not only do the properties of the lee wave depend on Fr, but they also affects the evolution of shear modes. While at Re = 2700, a smaller Fr reduces the energy contained in all vortical modes, at Re = 11000, it mainly limits the growth of Kelvin–Helmholtz billows and their pairing and retains more energy for longer distance in smaller scales.

In the numerical field, a rather complex flow can now be analysed as to their global stability, receptivity, and controllability with the ever-increasing computer resources [138, 173, 175]. The modern techniques which adapted to linear algebra problems from fast iterative algorithms are becoming widespread in many large-scale problems and multi-physics calculation.

2.5 Chapter Summary

This overview chapter gave a detailed literature review of the helical wake study in experiments and numerical computations; and thermally stratified atmosphere flow and modal decomposition methods of extracting the coherent flow structure. The computational model which simulates the wake flow behind a rotating blade will then be presented in the next chapter together with the mathematical background of the two model decomposition techniques, POD and DMD that will be deeply discussed in Chapter 5 & 6, respectively.

Chapter 3

Simulation and Modal Analysis Techniques

This chapter consists of two sections in which the governing equations were derived in Section 3.1, followed by the description of the computational modelling of wake flow behind the rotating blade in Section 3.2. Section 3.3 presents the information on the actuator model, and Section 3.4 explains the mathematical background, the algorithm, and the strengths and weaknesses of both model decomposition techniques in Subsection 3.4.2.1 and Subsection 3.4.2.2. Finally, the last section concludes this whole chapter.

3.1 The Governing Equations

The wind turbine wake features helical vortices, which are shed from the tips of blades and inflict undesirable fatigue loading on downstream turbines. Earlier studies of helical vortices concentrated on their hydrodynamic instabilities, and the following breakup in the neutrally stable, isothermal atmospheres where gravity balances the buoyancy force. Be that as it may, the atmosphere is usually unstable during the day and mostly stable at night, but is rarely neutral. Mao & Hussain in [177] presented numerical work by addressing the helical vortices growth in a thermally stratified atmosphere and also focuses on the stable condition, which is typical for offshore applications. This work is a continuation of the work previously

performed by [177] by giving detail analyses on the helical wake simulated by Mao.

There is a critical Reynolds number for all flows where the flow is laminar below this critical point, and there is a transition to turbulence above this point. Turbulence is the usual state of motion of fluids except at low Reynolds numbers. Understanding the physics of the turbulence is essential, and thus, turbulence models that allow steady state simulation is important and desirable to be performed for turbulent flow. Direct Numerical Simulation (DNS), Large Eddy Simulation (LES - which is similar to DNS, but the small scale motions are modelled, and used at a lower level of approximation) and Reynolds Averaged Navier–Stokes (RANS) are three methods that can be used to model turbulent flows.

LES is a mathematical model for turbulence used in computational fluid dynamics (CFD). It was originally proposed for simulating atmospheric air currents by Joseph Smagorinsky in 1963 [75] and first explored by Deardorff in 1970 [54]. In LES, large-scale turbulent flow motions (large eddies) are computed directly, and only small-scale motions (sub-grid scale (SGS)) are modelled. That is why the space grid and time steps may be much longer than DNS, leading to a significant reduction in computational cost compared to DNS. Nevertheless, its unsteady simulation with small time steps generates long run times and large volumes of data.

A wide range of RANS approach then was introduced around 1972 (see, e.g., Launder and Spalding [13] and Launder et al. [14]). In the approach of RANS, the starting point is the Reynolds decomposition of the flow variables (velocity and pressure in the case of an incompressible fluid) into mean and fluctuating parts. The introduction of the Reynolds decomposition in the non-linear Navier-Stokes equations followed by an ensemble averaging of the equations themselves gives rise to an unknown term – the Reynolds-stress tensor – that has to be modelled in order for the RANS equations to be solved. This operation essentially consists of the problem of the closure of the system of the Navier-Stokes equations. In short, RANS approach is based on ensemble-averaged governing equations; hence, it can not predict the local unsteadiness in the flow.

It has been shown at the end of the last century that DNS projections are in line with experimental outcomes acquired with Laser Doppler Anemometry (LDA)

and PIV (see [57] & [120], for example) of weakly turbulent flows, i.e., low Reynolds numbers, are considered. The first DNS was proposed by Orszag and Patterson [145] in 1972. In spite of its widely accepted merit for basic flow research, DNS has not yet been able to shake off the prejudice that it is of little use to solve industrial flow problems. The reason might be that the computing resources needed to be increased by approximately the third power of the Reynolds number, and most of the industrially relevant flows, and especially aircraft or vehicle aerodynamics, are characterized by very high Reynolds numbers.

Although being expensive, it does not mean that DNS can not be used at all. In fluid mechanics, turbulent flow can theoretically be simulated using DNS, for instance, the direct numerical solution of the Navier-Stokes equations. However, the computational resources required to calculate even the smallest of domains is very high, resulting in very limited use of DNS for practical applications. If DNS is not practical, the Navier-Stokes equations can be filtered and only the largest scales solved (for example, in LES), but when analysing the data, the effects, and assumptions related to this filtering need to be taken into account.

Statistical and deterministic are the most crucial currents in turbulence analytical research. However, there are some disadvantages with these approaches, such as closure problems and limited criteria in studying and analysing only transition and pre-turbulence. A significant advantage of DNS is to be able to solve the Navier-Stoke equation numerically, without turbulence modelling. As well as having a higher order of accuracy, the computation can be done on complex geometries with non-conformal meshes in local refinements. However, increasing the Reynolds number make this method challenging and costly (according to the reciprocal ratio of the lowest turbulent eddies to $Re^{\frac{3}{4}}$), especially in the inhomogeneous turbulence flow. Simple geometries and low Reynolds numbers are therefore restricted to the cases.

While DNS is the most accurate simulation method for turbulent flows, it is impossible to apply to many industrial flows because of the data storage and computational resource limitations. For example, for the wind turbines in the atmospheric boundary layer, the largest scales of motion are of the order of a several hundred meters while the boundary layer formed around the blades is of the order

of millimetres. DNS is, therefore, mostly used for validation purposes and for flows at low Reynolds numbers. Since this work provides a fundamental case that shares common traits with the wind turbine flows, this proves that DNS is one of the best available methods.

In this study, DNS of helical wake flow behind a rotating blade in neutral (N), weakly stable (WS), and strongly stable (SS) stratification were performed at $Re = 1000$, and $Re = 2000$ defined as $Re = \dfrac{U_\infty D}{\nu}$ where U_∞ is the free-stream velocity, D is the radius of the rotating blade, and ν is the kinematic viscosity. The thermal stratification of the atmosphere will be described in detail at the end of this subsection.

The following dimensional equations are the continuity and momentum equation that has been derived from the incompressible Navier-Stokes equations:

$$\nabla^* \cdot \boldsymbol{u}^* = 0 \tag{3.1.1}$$

$$\rho_o \left(\frac{\partial \boldsymbol{u}^*}{\partial t^*} + \boldsymbol{u}^* \cdot \nabla^* \boldsymbol{u}^* \right) = -\nabla^* p^* + \mu \nabla^{*2} \boldsymbol{u}^* + \rho g^* \tag{3.1.2}$$

where $\boldsymbol{u}^*$ and p^* are velocity and pressure fields; g^* is the gravity; t^* is time; ρ is density; ρ_o is a constant density; μ is the fluid dynamic viscosity; ∇^* is the gradient operator; ∇^{*2} is the Laplacian operator, and $\nabla^* \cdot$ is the divergence operator. The asterisks (*) represent the dimensional quantity as the non-asterisks form is reserved for the dimensionless quantity that will be used most in this thesis.

The buoyancy term can be rewritten as $(\rho_o + \Delta p) g^*$, where $\Delta\rho = \rho - \rho_o$ represents the density variation with respect to the reference density, ρ_o. This yields:

$$\rho_o \left(\frac{\partial \boldsymbol{u}^*}{\partial t^*} + \boldsymbol{u}^* \cdot \nabla^* \boldsymbol{u}^* \right) = -\nabla^* p^* + \mu \nabla^{*2} \boldsymbol{u}^* + (\rho_o + \Delta\rho) g^* \tag{3.1.3}$$

The Boussinesq approximation states that in the buoyancy term, only the density variation is essential and can be ignored in the rest of the equation. The foundation of this approximation is that there are flows in which the temperature differs slightly, and thus the density varies slightly, yet in which the motion is driven by the buoyancy. Hence, the density variation is overlooked everywhere except in the term of buoyancy. This is a very commonly used assumption, a more detailed discussion of the Boussinesq approximation and its validity can be found in [46] and [150].

The reason for using the approximation is the resulting simplifications to the governing equations. In order to avoid having to evaluate the fluid density based on the local temperature, the buoyancy term $\Delta\rho g^* = (\rho - \rho_o)g^*$ can further be rewritten as $(\rho - \rho_o)g^* = -\rho_o\beta(T^* - T_{\text{ref}})g^*$, where β is the coefficient of thermal expansion. For ideal gases, $\beta = \dfrac{1}{T_{\text{ref}}}$ and becomes $-\rho_o\dfrac{(T^* - T_{\text{ref}})}{T_{\text{ref}}}g^*$. Applying the Boussinesq approximation to the momentum equation, Eq. 3.1.3 gives

$$\rho_o\left(\frac{\partial \boldsymbol{u^*}}{\partial t^*} + \boldsymbol{u^*}\cdot\nabla^*\boldsymbol{u^*}\right) = -\nabla^* p^* + \mu\nabla^{*2}\boldsymbol{u^*} + \rho_o g^* - \rho_o\beta(T^* - T_{\text{ref}})g^* \tag{3.1.4}$$

or alternatively

$$\frac{\partial \boldsymbol{u^*}}{\partial t^*} + \boldsymbol{u^*}\cdot\nabla^*\boldsymbol{u^*} = -\frac{1}{\rho_o}\nabla^* p^* + \nu\nabla^{*2}\boldsymbol{u^*} + (1 - \beta(T^* - T_{\text{ref}}))g^* \tag{3.1.5}$$

where $\nu = \dfrac{\mu}{\rho_o}$ is the kinematic viscosity.

In thermal convection problems, the flow is created by the density gradients related to the temperature gradients. As a result, Eq. 3.1.5 needs to be coupled with an equation for the temperature, T^* and they have to be solved together. This equation can be obtained from the energy equation. There are many different ways to write an energy equation, such as the one given below:

$$\rho\left[\frac{\partial h^*}{\partial t^*} + \nabla^*\cdot(h^*\boldsymbol{u^*})\right] = -\frac{Dp^*}{Dt^*} + \nabla^*\cdot(k\nabla^* T^*) + \Phi^* \tag{3.1.6}$$

where h is specific enthalpy which is related to specific internal energy, e^* as $h^* = e^* + \dfrac{p^*}{\rho}$. T^* is the absolute temperature, and Φ^* is the viscous-dissipation function representing the work done against viscous forces, which is irreversibly converted into internal energy. This last term is generally negligible but, in general, it is given by following equation:

$$\begin{aligned}\Phi^* = \mu\Bigg\{2\left[\left(\frac{\partial u^*}{\partial x^*}\right)^2 + \left(\frac{\partial v^*}{\partial y^*}\right)^2 + \left(\frac{\partial w^*}{\partial z^*}\right)^2\right] + \left(\frac{\partial u^*}{\partial y^*} + \frac{\partial v^*}{\partial x^*}\right)^2 + \\ \left(\frac{\partial u^*}{\partial z^*} + \frac{\partial w^*}{\partial x^*}\right)^2 + \left(\frac{\partial v^*}{\partial z^*} + \frac{\partial w^*}{\partial y^*}\right)^2\Bigg\}\end{aligned} \tag{3.1.7}$$

where u^*, v^*, w^* are the velocity components in the of x^*, y^*, z^* directions, respectively. Since all terms in Eq. 3.1.7 are quadratic; the viscous-dissipation terms are always positive such that the flow always tends to lose its available energy due to dissipation.

Pressure term on the right-hand side of Eq. 3.1.6 is usually neglected. To derive this energy equation, the conduction heat transfer governed by Fourier's law was being considered with k is the thermal conductivity of the fluid.

As it has been known, the relationship between density, pressure, and temperature is given by the perfect gas relations, $p = \rho R T^*$ where the gas constant, $R = (c_p - c_v)$ with c_p is the specific heat for constant pressure and c_v is the specific heat for constant volume. The following relations can also be used to relate enthalpy and internal energy to temperature for an ideal gas so that the energy equation can be written as the temperature is the only unknown.

$$dh^* = c_p dT^*, \qquad de^* = c_v dT^* \tag{3.1.8}$$

Conservation of energy given in Eq. 3.1.6 then can be simplified and written as:

$$\rho c_p \left[\frac{\partial T^*}{\partial t^*} + (\boldsymbol{u^*} \cdot \nabla^*) T^* \right] = k \nabla^{*2} T^* \tag{3.1.9}$$

Note that $c_p \approx c_v$ for incompressible flows.

Thus the final form of the energy equation is

$$\frac{\partial T^*}{\partial t^*} + \boldsymbol{u^*} \cdot \nabla^* T^* = \kappa \nabla^{*2} T^* \tag{3.1.10}$$

where $\kappa = k/\rho_o c_p$ is the thermal diffusivity since the fluid was assumed to have a constant heat capacity per unit volume given by $\rho_o c_p$ under the Boussinesq approximation.

The continuity equation (Eq. 3.1.1,) the momentum equation (Eq. 3.1.5) and, the energy equation (Eq. 3.1.10) are called Boussinesq equations and describe the motion of a Boussinesq fluid. Hence, complete the governing equations scheme.

By using the free-stream velocity, U_∞, a characteristic length scale (which in this study is the diameter of the blade, D), characteristic pressure, p_∞, and characteristic temperature, T_∞, the terms of the governing equations can be non-dimensionalized.

$$\nabla = \nabla^* D,\ \boldsymbol{u} = \frac{\boldsymbol{u^*}}{U_\infty},\ t = \frac{t^*}{D/U_\infty},\ g = \frac{g^* D}{U_\infty^2},\ T = \frac{T^* - T_\infty}{T_{\text{ref}}},\ p = \frac{p^* - p_\infty}{\rho_o U_\infty^2}$$

When the above terms are substituted, this set of the equation becomes:

$$\nabla \cdot \boldsymbol{u} = 0 \tag{3.1.11}$$

$$\partial_t \boldsymbol{u} + \boldsymbol{u} \cdot \nabla \boldsymbol{u} + \nabla p - Re^{-1} \nabla^2 \boldsymbol{u} + T_s g = 0 \tag{3.1.12}$$

$$\partial_t T + \boldsymbol{u} \cdot \nabla T - Re^{-1} Pr^{-1} \nabla^2 T = 0 \tag{3.1.13}$$

where u, t, p, g, T_s, and Re represent the dimensionless velocity flow, time, pressure, gravity term, thermal term, and Reynolds number, respectively. Meanwhile, Pr is Prandtl number given by $Pr = \dfrac{\nu}{\alpha} = 0.72$ where α is thermal diffusion and $T_s = 1 - \beta(T - T_{\text{ref}})$ with the reference temperature, $T_{\text{ref}} = 298K$.

Dirichlet boundary condition specifies the value of a variable at a boundary. It may also be referred to as a fixed boundary condition. Therefore, it is used when a value needs to be imposed at a boundary. Typically, this study is dealt with a Dirichlet condition where the velocity is fixed at the inlet and the pressure is fixed at the outlet. Noted also, the rotational speed is constant for all the computations, $\Omega = 5rad/s$.

3.2 Computational Model of Helical Flow behind a Rotating Blade

Three-dimensional numerical simulations have been performed in cylindrical coordinate system with z, r and θ representing the streamwise, radial, and azimuthal coordinates, respectively, is adopted to study the flow behind the rotating blade. The computational domain, as shown in Fig. 3.1 is a cylinder with dimensions $L_z = 63$, $L_r = 35$, where $-3 < z < 60$, $0 < r < 35$, respectively, and a rotating blade is located at $(z, r) = (0, 0)$. The computational domain then was normalized by D.

A higher-order accuracy method, the Spectral Element Method (SEM), is a popular technique for applying to fluid flow DNS with moderate Reynolds number. The method offers both the effectiveness of global spectra method and flexibility in geometry of the finite element method, provided by non-conforming deformed

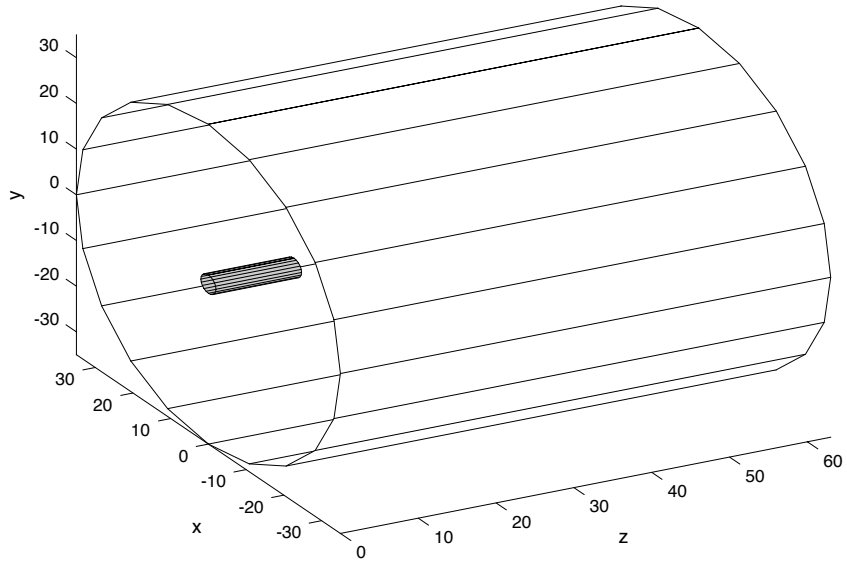

Figure 3.1: Schematic of the computational domain along the streamwise direction. Note that the inner cylinder is the sub-domain that will be used most in this study to perform the analysis.

hexahedral elements [158]. For every case in this study, the $z-r$ plane is decomposed into 5109 spectral elements, each of which is further discretised with nodal based Gauss-Labatto-Legendre basis functions with a different order of the polynomial, O (refer to Table 3.1). In the azimuthal direction, a Fourier decomposition is applied, and a number of Fourier modes, F_m are calculated. The simulations were performed in Fourier because it is more time consuming to carry out the computation in physical space [23]. The simulations in Fourier space are used to extend the total time interval simulated, and to apply the scheme to finer meshes. The corresponding parameters for each case are listed in Table 3.1 below:

The raw data parameters from each case, including the number of time steps, t, time separation, Δt and sample frequency, $f_s = 1/\Delta t$ were listed in the separated table of Table 3.2:

The atmospheric boundary layer can be classified into three types according to the thermal stratification and the dominant mechanisms of turbulence generation, which are neutral, convective (unstable), and stable. There is little heating or cooling on the surface in the neutral case. Consequently, the mean potential temperature is approximately constant with height, and turbulence is generated primarily by shear

Atmospheric Conditions	Re	Notation	Parameters	
			O	No. of F_m
Neutral, N	1000	N, Re1k	8	100
	2000	N, Re2k	9	100
Weakly Stable, WS	1000	WS, Re1k	8	100
Strongly Stable, SS case 1, SS1	1000	SS1, Re1k	9	100
	2000	SS1, Re2k	9	100
Strongly Stable, SS case 2, SS2	1000	SS2, Re1k	8	100

Table 3.1: Parameters of the Computational Model per Cases

Atmospheric Conditions	t	Δt	f_s
N, Re1k	200	0.08	12.5
N, Re2k	93	0.04	25
WS, Re1k	90	0.40	2.5
SS1, Re1k	155	0.16	6.25
SS1, Re2k	220	0.08	12.5
SS2, Re1k	91	0.40	2.5

Table 3.2: The number of time steps, t; time separation, Δt; and sample frequency, f_s of all cases.

near to the surface. During comparatively brief transition periods after sunset or in windy conditions with a complete cloud cover, the neutrally stratified is noted. Whilst, in the daytime, when the surface is warmer than the air, the unstable is typically observed. Under convective conditions, heat transfer between the surface and air yields positive buoyancy, enhancing TKE and the vertical transport of momentum, heat, and moisture. Lastly, in reaction to surface cooling by long-wave radiation to outer space, the stably stratified generally happens at night. Turbu-

lence is produced by shear and demolished by adverse buoyancy and viscosity, under this atmospheric condition [93]. Fig. 2.5 in the previous chapter depicted the effects of atmospheric conditions.

The atmospheric lapse rate, ζ refers to the change of an atmospheric variable with altitude transition. Lapse rates are typically expressed as the amount of temperature change associated with a specified amount of altitude change, such as 9.8°Kelvin (K) per kilometre or the equivalent 0.0098°K per meter. The lapse rate can be expressed as a negative number if the ambient air cools with increasing altitude. If the air heats at higher altitudes, the lapse rate then can be expressed as a positive number [98].

Atmospheric stability is atmospheric resistance to vertical air movement. A very stable atmosphere is one which has very little, if any, vertical air movement while a stable atmosphere is one which discourages vertical motion but has some air movement. On the other hand, an unstable atmosphere is one that promotes constant upward or downward vertical motion of the air. A neutral environment is one that neither discourages nor facilitates vertical air movement, and is also called conditionally stable. The stability depends on how the temperature of the air varies with altitude (the lapse rate of temperature).

In this study, all four atmospheric stability conditions were defined by setting their temperature field as given by Eq. 3.2.1 below and illustrated in Fig. 3.2.

$$T = \frac{y}{C} \tag{3.2.1}$$

with $-3 < y < 3$ and $C = 0, 200, 500, 1000$ for N, SS1, SS2 and WS, respectively.

When the temperature increases with altitude, a temperature inversion. Air is negatively buoyant at ground level and does not grow. If air is forced to rise, it will sink back towards the ground again. This is when the atmospheric condition is said to be in a strongly stable. In the present study, the lapse rates for both SS1 and SS2 as can be calculated from Fig. 3.2(a) & Fig. 3.2(d) is $\zeta_{SS1} = \dfrac{0.006}{6} = 0.001$, and $\zeta_{SS2} = 0.002$, respectively. In Fig. 3.2(b), it shows that the temperature is the same as the dry adiabatic lapse rate with $\zeta_N = 0$. i.e., if air is forced to rise, it will cool at the same rate as the temperature around it drops. In this case, it will be neutrally buoyant and categorized as neutral. Last but not least, Fig. 3.2(c) shows how the atmospheric stability was classified as weakly stable. It is when the

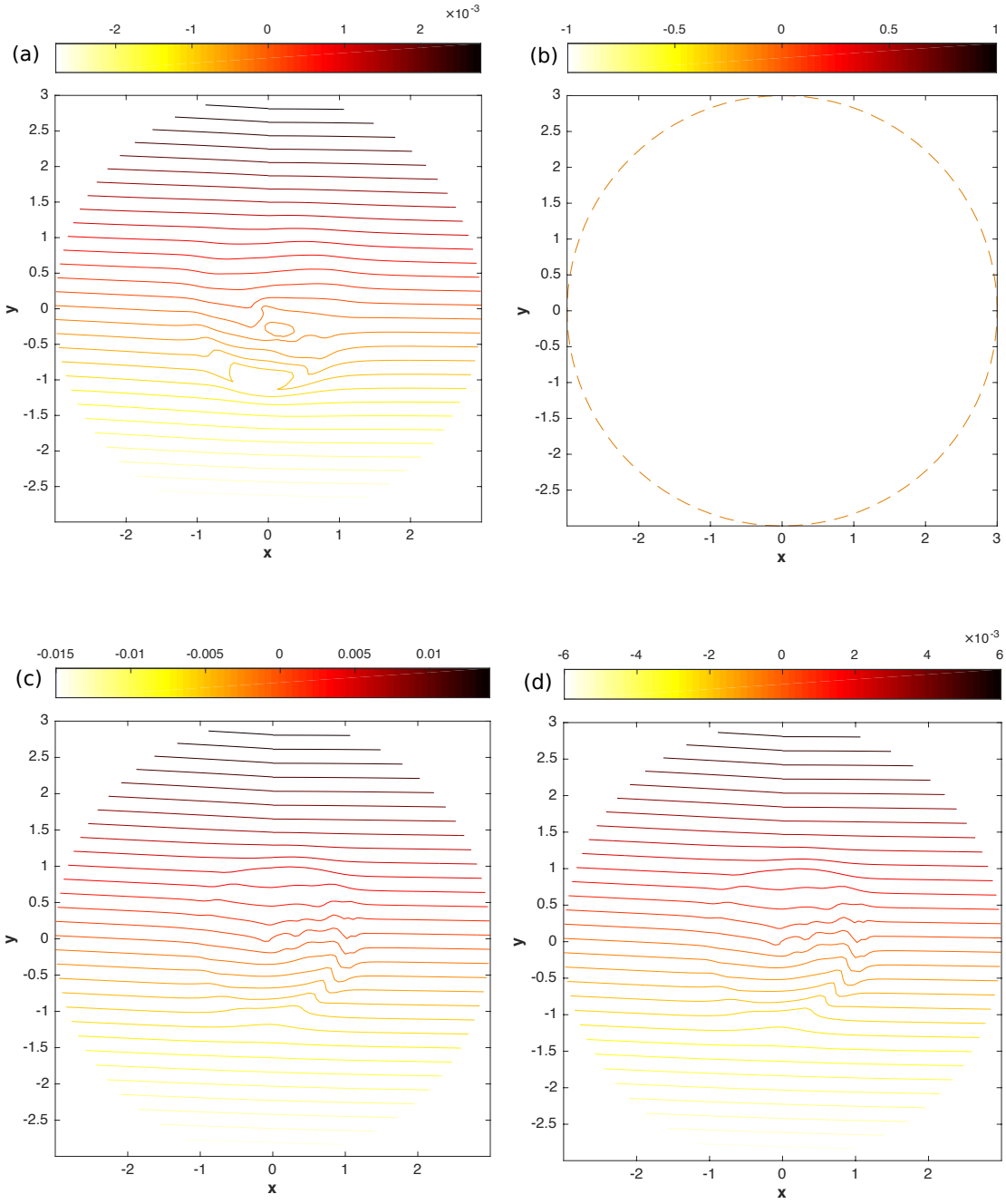

Figure 3.2: Temperature contours of: (a) SS1, (b) N, (c) WS, and (d) SS2 in the xy-plane at $z = 5.5$.

temperature lapse rate is less than the dry adiabatic lapse rate (i.e. it falls less than by 0.0098°K), but temperature does decrease with altitude. In this study, $\zeta_{WS} = 0.005$.

3.3 Actuator Models

In the past few years, actuator models have been proposed, including the Actuator Disk Model (ADM) and the Actuator Line Model (ALM), in order to avoid the computational cost associated with resolving the blade boundary layer as well as the atmospheric boundary layer. Using the ADM and ALM techniques avoids the need for resolving the development of the boundary layer over the blades, allowing the use of a higher resolution to capture the details of the wake. In these actuator models, the body forces are distributed in the flow field. In the ALM model, body forces representing the aerodynamic loads on the rotor are distributed along with points on rotating lines representing the individual blades, which allows information about the force on the blades to be directly provided as a function of the blade azimuth angle. Meanwhile, in the ADM model, the body forces are distributed on points over a rotating disc represented on a local polar mesh, which can provide information about the local forces on the disc as a function of the azimuth angle. The body forces in both techniques are smeared into their imposition points with a three-dimensional Gaussian function [140].

ADM was initially used in the far wake simulation of the wind turbines. However, it could not replicate the tip vortex system accurately [118]. Then, Sørense & Shen [72] launched ALM to resolve this difficulty where the body forces were distributed radially along with the blades and added as the source item to the three dimensional Navier-Stokes equation. In addition, ALM is also an efficient technique for anticipating the loading on the blades with only simple structured grids, which has been demonstrated by Troldborg [118]. As shown in [119], the conventional uniform actuator disk is not a great choice for a cross-flow turbine wake generator, regardless of the fact that performance predictions are not typically computed.

Moreover, the ALM is capable of capturing flow structures near the blades, such as root and tip vortices, which the ADM does not capture [85]. It was also being said that if the simulations are more concerned with the far wake, the ADM will offer the right solution without compromising the time-step of simulation. For all these reasons and as the ALM allows for a more realistic representation of the wind turbine rotor, the numerical simulations presented in this work were all conducted

using the ALM, where a single rotating blade was replaced by a line of forcing. As ALM is well known for its expensive computational cost, this work was carried out with the study of just a single rotating blade instead of three blades, which normally being considered as it gives a better approximation to the real-life wind turbine.

For the comparison to the ALM method, the ADM (with $\Delta T = 0$) was computed by decomposed the $z - r$ plane into 4522 spectral elements before it was further discretized with polynomial order 7 and 96 Fourier modes were employed in the azimuthal direction. Fig. 3.3 is an example of the wake and vortex system created by the ALM and ADM for Neutral case at Re = 1000.

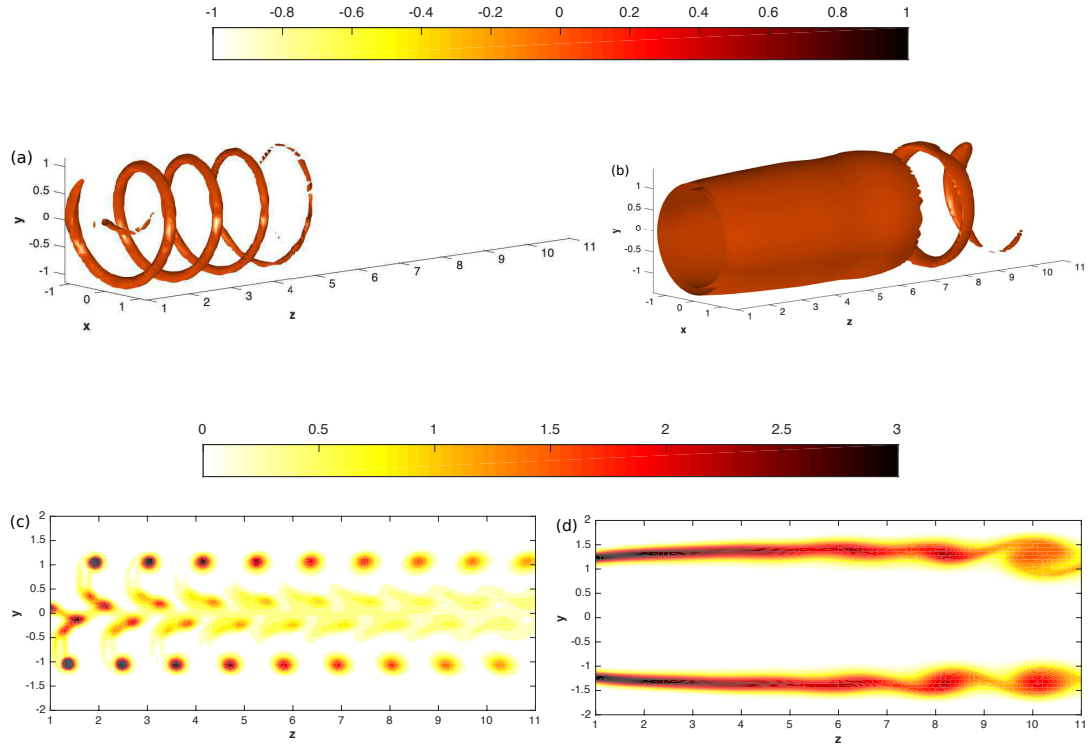

Figure 3.3: Isosurface of Vorticity Magnitude, $|\omega| = ({\omega_x}^2 + {\omega_y}^2 + {\omega_z}^2)^{\frac{1}{2}}$ resulting from the use of the ALM (a) and ADM (b) and their contours (c, d), respectively for Neutral case at Re = 1000. Note that (a, b) is the 3D $|\omega|$ and (c, d) is their 2D's, respectively.

As can be seen in Fig. 3.3, when using the ALM, there is a formation of tip and root vortices, but not in the ADM. The circulation around the individual blade forms these structures. A continuous disk covering the blade's swept area leaves no room for circulation to occur in ADM. The structure of the ALM wake is not symmetric

concerning the centre of the wake because the vortical structures produced by the individual blade are helical and asymmetric across the wake. Whilst, the ADM wake is symmetric about the centre of the wake. This is because the rotor is being modelled as a continuous disk instead of the individual blade.

3.4 Modal Analysis Techniques

The simulation of the flow does not provide the knowledge of fundamental dynamics in it as it can not really reveal the physics of the flow; the simulation outcome needs to be analysed. On the other hand, coherent structures approach to turbulence provides a distinct picture, based on this idea that some turbulent ones are not so complicated that they look at first sight. In other words, it is presumed that such flows consist of the set of structured motions with simple spatial structures. Complexity of such turbulent flows produced by the superposition in space and time of these organized, so-called coherent structures [33]. Applying modal decomposition to identify coherent structures and dynamics of the evolving flow field is a solution to overcome the difficulties of the study of turbulent flows. The set of the modes acquired by modal decomposition can be represented as the base of reduced-order, which is an approximation of the initial flow. There are various former derived decomposition techniques, but two of them will be considered in the current study, which is POD and DMD.

3.4.1 Proper Orthogonal Decomposition

Lumley [64] first launched the POD technique in the context of fluid mechanics. It is also recognized in various areas under a multitude of names: POD, principal component analysis (PCA), Hotelling analysis, empirical component analysis, quasi-harmonic modes, empirical eigenfunction decomposition, and others. This technique is used to find a set of spatially orthogonal modes which are ordered by their contribution to the total variance, i.e., turbulent kinetic energy in the case of velocity time series, or enstrophy in the case of vorticity fields.

3.4.1.1 Mathematical Theory

The main idea of POD is to classify structures in the velocity field with the largest mean square energy, the most energetic fluctuations in a random field. Different approaches to the POD system were used, depending on how the data were collected and the nature of the available data. The classical and snapshot POD methods are the two main approaches to perform POD of the flow field data. The classical approach, as proposed by Lumley [64], is a method where a temporal average is used in statically stationary flows. Meanwhile, the snapshot method initiated by Sirovich [91] using a uniformly sampled discrete time spatial average of N.

The classical POD method is the original formulation in which the ensemble average is temporal. The POD determined the set of essential functions that can represent the flow field data optimally. First, given the flow field $\boldsymbol{q}(\boldsymbol{\xi}, t)$, snapshots of the flow field stacked in terms of a collection of column vectors $\boldsymbol{x}(t)$ were then prepared. Consider, therefore, a set of finite-dimensional data vectors representing the flow field

$$\boldsymbol{x}(t) = \boldsymbol{q}(\boldsymbol{\xi}, t) - \bar{\boldsymbol{q}} \in \mathbb{R}^n, \quad t = t_1, t_2, ..., t_m. \tag{3.4.1}$$

$\boldsymbol{x}(t)$ is taken to be the fluctuating component of the data vector with the time-averaged value $\bar{\boldsymbol{q}}(\boldsymbol{\xi})$ being omitted. While it is possible to write the data vector as $\boldsymbol{x}(\boldsymbol{\xi}, t)$, it is simply written as $\boldsymbol{x}(t)$ to show that it is being considered as a snapshot at time t.

Reynolds decomposition in fluid dynamics is a statistical method used to distinguish the expectation value of a quantity from its fluctuations. This decomposition was applied to the input dataset in the Cartesian coordinate. The reason for using the fluctuating velocity components in the Cartesian system for both modal decomposition techniques and how the process was carried out will be further explained in Section 5.1.1 of Chapter 5.

The objective of the POD analysis is to find the optimal basis vectors that can best represent the given data. In classical POD, it is vital to look for the vectors of orthogonal modes, $\boldsymbol{\phi}_j(\boldsymbol{\xi})$ which can represent $\boldsymbol{q}(\boldsymbol{\xi})$ in an optimal way and with a minimum number of modes. The problem can be solved by finding the eigenvectors, $\boldsymbol{\phi}_j$, and the eigenvalues, λ_j from

$$\boldsymbol{R}\boldsymbol{\phi}_j = \lambda_j \boldsymbol{\phi}_j, \quad \boldsymbol{\phi}_j \in \mathbb{R}^n, \quad \lambda_1 > ... > \lambda_n > 0 \tag{3.4.2}$$

where $\boldsymbol{R}$ is the covariance matrix of vector $\boldsymbol{x}(t)$.

$$\boldsymbol{x}(t_i)\boldsymbol{R} = \sum_{i=1}^{m} \boldsymbol{x}(t_i)\boldsymbol{x}^{\boldsymbol{T}}(t_i) = \boldsymbol{X}\boldsymbol{X}^{\boldsymbol{T}} \in \mathbb{R}^{n\times m} \tag{3.4.3}$$

where the matrix $\boldsymbol{X}$ represents the m snapshot data being stacked into a matrix form of

$$\boldsymbol{X} = [\boldsymbol{x}(t_1) \;\; \boldsymbol{x}(t_2) \;\; \ldots \;\; \boldsymbol{x}(t_1 m)] \in \mathbb{R}^{n\times m}. \tag{3.4.4}$$

The size of the n covariance matrix is dependent on the spatial degrees of freedom of the data. As shown in Eq. 3.4.9, n is usually large for fluid flow data and is equal to the number of grid points times the number of variables to be included in the data.

The eigenvectors found from Eq. 3.4.2 are called the POD modes. It should be noted that the POD modes are orthonormal, which implies that the inner product between the modes is orthonormal:

$$\langle \boldsymbol{\phi_j}, \boldsymbol{\phi_k} \rangle \equiv \int_V \boldsymbol{\phi_j} \cdot \boldsymbol{\phi_k} \, dV = \delta_{jk}, \quad j,k = 1,\ldots,n. \tag{3.4.5}$$

As a result, the eigenvalues λ_k express how well each eigenvector ϕ_k captures the original data in the sense of $L2$(scaled by m). The eigenvalues correspond to the kinetic energy were captured by the respective POD modes when the velocity vector is used for $\boldsymbol{x}(t)$. It is possible to arrange the POD modes in the order of importance in terms of capturing the kinetic energy of the flow field if the eigenvalues are arranged in decreasing order from the largest to the smallest.

The eigenvalues can be used to determine the number of modes necessary to represent the fluctuations in the flow field data. Notably, the number of modes, r was retained to express the flow such that

$$\sum_{j=1}^{r} \lambda_j / \sum_{j=1}^{n} \lambda_j \approx 1. \tag{3.4.6}$$

The flow field can be represented only in terms of finite or truncated series with the determination of essential POD modes

$$\boldsymbol{q}(\boldsymbol{\xi}, t) \approx \sum_{j=1}^{r} a_j(t)\boldsymbol{\phi_j}(\boldsymbol{\xi}) \tag{3.4.7}$$

in an optimal way, effectively reducing the high-dimensional (n) flow field to be represented only with r modes. The temporal coefficients are determined by

$$a_j(t) = \langle \boldsymbol{q}(\boldsymbol{\xi}, t) - \bar{\boldsymbol{q}}(\boldsymbol{\xi}), \boldsymbol{\phi_j}(\boldsymbol{\xi}) \rangle = \langle \boldsymbol{x}(t), \boldsymbol{\phi_j} \rangle \tag{3.4.8}$$

where $\bar{\boldsymbol{q}}$ is the mean flow variable.

The size of the correlation matrix $\boldsymbol{R} = \boldsymbol{X}\boldsymbol{X}^{\boldsymbol{T}}$ becomes very large ($n \times n$) when the size of the data n is enormous. This makes it virtually impossible to use the classical POD method to find eigenfunctions. Sirovich [91] pointed out that the matrix of temporal correlation would produce the same dominant spatial modes while generating a much smaller and more computationally tractable eigenvalue problem. Another alternative approach called the snapshots method takes a series of $\boldsymbol{x}(t_i)$ snapshots at a discrete time level of $t_i, i = 1, 2, ..., m$ with $m \ll n$ and solves an eigenvalue problem of a smaller size of ($m \times m$) to find the POD modes.

Nonetheless, due to the advantages of its computational efficiency, it is more customary to use the snapshot POD. Hence, the present work uses the so-called snapshot POD method by Sirovich [91].

In this study, the fluctuating velocity components, (u_j^n, v_j^n, w_j^n) where u, v, w denote the fluctuating part of each of the three velocity components were being investigated. Index n runs through the N snapshots, and j runs through the M positions of velocity vector in a given snapshot, i.e. $u_j = u(x_j, y_j, z_j)$. All the time-dependent fluctuating velocity components from N snapshots are arranged in a matrix $\boldsymbol{V}$ as

$$\boldsymbol{V} = [\boldsymbol{v}^1 \boldsymbol{v}^2 \dots \boldsymbol{v}^N] = \begin{bmatrix} u_1^1 & u_1^2 & \dots & u_1^N \\ \vdots & \vdots & \vdots & \vdots \\ u_M^1 & u_M^2 & \dots & u_M^N \\ v_1^1 & v_1^2 & \dots & v_1^N \\ \vdots & \vdots & \vdots & \vdots \\ v_M^1 & v_M^2 & \dots & v_M^N \\ w_1^1 & w_1^2 & \dots & w_1^N \\ \vdots & \vdots & \vdots & \vdots \\ w_M^1 & w_M^2 & \dots & w_M^N \end{bmatrix} \tag{3.4.9}$$

Also, let T be the scalar temperature component:

$$T = [t^1 t^2 \dots t^N] = \begin{bmatrix} t_1^1 & t_1^2 & \dots & t_1^N \\ t_2^1 & t_2^2 & \dots & t_2^N \\ \vdots & \vdots & \ddots & \vdots \\ t_M^1 & t_M^2 & \dots & t_M^N \end{bmatrix} \tag{3.4.10}$$

The autocovariance matrix, $\widetilde{C}$ is created as

$$\widetilde{\boldsymbol{C}} = \boldsymbol{V}^T \boldsymbol{V} \tag{3.4.11}$$

where and the superscript, ^{T} here denotes the transpose operator. Thus, the corresponding eigenvalue problem can be resolved by

$$\widetilde{\boldsymbol{C}} \boldsymbol{A}^i = \lambda^i \boldsymbol{A}^i \tag{3.4.12}$$

where A^i is the eigenvector, and λ^i is the eigenvalue. The solutions are ordered by the size of the eigenvalues

$$\lambda^1 > \lambda^2 > \dots > \lambda^N = 0 \tag{3.4.13}$$

which is from large to small to guarantee the first few modes are the most significant energy modes. The eigenvectors of Eq. 3.4.12 make up a basis for constructing the POD modes $\boldsymbol{\phi}^i$,

$$\boldsymbol{\phi^i} = \frac{\sum_{n=1}^{N} A_n^i \boldsymbol{v}^n}{||\sum_{n=1}^{N} A_n^i \boldsymbol{v}^n||}, \qquad i = 1, 2, \dots, N \tag{3.4.14}$$

where A^i is the n^{th} component of the eigenvector corresponding to λ^i from Eq. 3.4.12 and the discrete 2-norm is defined as

$$||\boldsymbol{y}|| = \sqrt{y_1^2 + y_2^2 + \dots + y_M^2} \tag{3.4.15}$$

Each snapshot can be expanded in a series of the POD modes with expansion coefficients for each POD mode i. The POD coefficients are determined by projecting the fluctuating part of the velocity field onto the POD modes

$$\boldsymbol{a}^n = \boldsymbol{\psi}^T \boldsymbol{v}^n \tag{3.4.16}$$

where $\boldsymbol{\psi}^T = \left[\boldsymbol{\phi}^1 \boldsymbol{\phi}^2 \dots \boldsymbol{\phi}^N\right]$ has been introduced. The expansion of the fluctuating part of a snapshot n is

$$\boldsymbol{v}^n = \sum_{t=1}^{N} a_i^n \boldsymbol{\phi}^n = \boldsymbol{\psi} \boldsymbol{a}^n \tag{3.4.17}$$

It has been shown in [79] that the amount of the total kinetic energy from velocity fluctuations in the snapshots that are associated with a given POD mode is proportional to the corresponding eigenvalue. The ordering of the eigenvalues and eigenvectors in Eq. 3.4.13, therefore, ensures that the most important modes in terms of energy are the first modes. This generally implies that large-scale flow structures are associated with the first few modes. Therefore, if a flow has dominant flow structures, these are reflected in the first POD modes, and thus, a given snapshot can often be satisfactorily reconstructed using only the first few modes. See [66] and [123] for more information on the POD.

3.4.1.2 The Algorithms

The complete algorithm is given below:

Inputs : Snapshots of spatial field (1D, 2D or 3D) of any scalar (e.g., pressure, temperature) or vector (e.g., velocity, vorticity) field, $\boldsymbol{q}(\boldsymbol{\xi}, t)$, over discrete spatial points at $\boldsymbol{\xi}$ discrete time t_i.

i. Arrange the data as Eq. 3.4.9.

ii. Calculate the matrix Eq. 3.4.11.

iii. Solve the eigenvalues problem in Eq. 3.4.12.

iv. Arrange solutions by eigenvalues as Eq. 3.4.13.

v. The POD modes are found by Eq. 3.4.14.

Outputs: Set of orthogonal modes, $\boldsymbol{\phi}_j(\boldsymbol{\xi})$, with the respective temporal coefficients, $a_j(t)$, and energy levels, λ_j, arranged in the order of their relative amount of energy. The initial field is described as a linear combination of the modes and their corresponding temporal coefficients, $\boldsymbol{q}(\boldsymbol{\xi}, t) = \sum_j a_j(t) \boldsymbol{\phi}_j(\boldsymbol{\xi})$.

3.4.1.3 POD Virtues and its Limitations

Virtues:

- POD provides such a valuable property in the construction of a flow field reduced-order model gained from its orthogonal set of basis vector with minimal dimension.
- POD modes can simply be computed using both classical or snapshot methods. However, the snapshots technique is particularly appealing to high-dimensional spatial datasets.
- POD is able to remove high order modes from the expansion simply, and this made it able to be used to remove the incoherent noise from the dataset.
- POD (PCA) analysis is commonly used in a wide range of research. It is used to recognize patterns, process images, and to store/compress large databases optimally.

Limitations:

- Since POD is based on the correlation of second-order (Eq. 3.4.11), correlations of higher order are ignored.
- POD modes usually correspond to a mix of frequencies.
- POD arranges modes, not in the order of the dynamical significance but in terms of energy level. Balanced POD and DMD analyses are addressing this point.
- The number of POD modes that should be kept is not always precise, and there are various criteria for truncation.
- POD modes are not suitable for describing travelling wave structures as the technique assumes that the flow field can be separated into temporal and spatial functions.

POD is one of the powerful tools used to decompose the flow field [17, 39, 87]. Diagonalizing the correlation matrix of the temporal-spatial velocity field ensemble has extracted the orthogonal structures and provides an order of coherent structures ranked by their energy. In spite of that, there is a loss of phase information caused by the averaging process associated with the production of the correlation tensor [122] for example, the spatial POD modes might be temporally dependent on one another, which is critical for the dynamic identification.

3.4.2 Dynamic Mode Decomposition

Schmid [125] firstly proposed and studied DMD and introduced the method that is able for the extraction of dynamic information from flow fields that are either generated by the numerical or experimental data. The mathematical background and algorithm of the method are summarized below, and more details can be found in [125, 126, 130]. DMD is known to be equivalent to a global stability analysis for data sequences from a linearised flow simulation. Meanwhile, for data sequences from a non-linear flow, it generates modes of the tangential linear approximation of the full-system matrix and describes dominant dynamic behaviour in the data sequence. DMD is supposed to be analogous to Fourier transform (FFT) for a periodic signal. The DMD-based predictions were superior for a small number of snapshots [168]. The most important reason DMD is more beneficial than FFT is that FFT suffers from spectral leakage when a wave with less than a full period is considered, as visible by the peaks. DMD does not exhibit the same pattern, and due to the robustness of the DMD method, this decomposition technique will be used to analyse the helical wake flow behind a rotating blade.

3.4.2.1 Mathematical Theory

The aim of DMD is to extract the dynamic characteristics of the dynamic process defined by $\boldsymbol{A}$ based on the sequence $\boldsymbol{V}1^N$, such as eigenvalues, eigenvectors, pseudoeigenvalues, energy amplification, resonance behaviour, and so forth. There are two methods to obtain these eigenvalues and modes of identification. The first is Arnoldi-like, in which, due to its connection with Krylov methods, it is useful for the-

oretical analysis. The second is an approach based on singular value decomposition (SVD) that is more robust to noise in the data and numerical errors.

The general flow field data first will be assumed and denote each such field by a vector $\boldsymbol{v}_j$. An N snapshot sequence is then written as Eq. 3.4.9, where two subsequent snapshots $\boldsymbol{v}_j$ and $\boldsymbol{v}_{j+1}$ are presumed to have an equal time interval Δt. For experimental data, a non-linear process produces the snapshots $\boldsymbol{v}_j$. An assumption that a linear mapping $\boldsymbol{A}$ connects the flow field from one snapshot to the next is then should be made and can thus write

$$\boldsymbol{v}_{j+1} = \boldsymbol{A}\boldsymbol{v}_j \tag{3.4.1}$$

This mapping is also taken over the data sequence as roughly the same. As in Arnoldi method which by following the idea underlying Krylov techniques [2,90], the linear map was expressed and approximated using an $(N-1)$ dimensional snapshot basis $\boldsymbol{V}_1^{N-1}$ as written below

$$\{\boldsymbol{v}_2, \boldsymbol{v}_3, \ldots, \boldsymbol{v}_N\} = \boldsymbol{A}\{\boldsymbol{v}_1, \boldsymbol{v}_2, \ldots, \boldsymbol{v}_{N-1}\} \approx \{\boldsymbol{v}_1, \boldsymbol{v}_2, \ldots, \boldsymbol{v}N-1\}\boldsymbol{S} \tag{3.4.2}$$

or

$$\boldsymbol{V}_2^N = \boldsymbol{A}\boldsymbol{V}_1^N \approx \boldsymbol{V}_1^N\boldsymbol{S} \tag{3.4.3}$$

where $\boldsymbol{S}$ is a companion matrix with sub-diagonal entries that can simply shift the snapshots 1 through $N-1$, and the last snapshot can be approximated by a linear combination of the previous N snapshots [9].

In this form, the eigenvalues of $\boldsymbol{S}$ approximate some of the eigenvalues, λ_i of the full system matrix $\boldsymbol{A}$, called empirical Ritz values [25]. The eigendecomposition is performed on $\boldsymbol{S}$ rather than $\boldsymbol{A}$ because $\boldsymbol{S}$ is much smaller than $\boldsymbol{A}$, so the computational cost of DMD is determined by the number of snapshots rather than the size of a snapshot.

Furthermore, the eigenvalues can be mapped logarithmically as

$$\upsilon_j = \frac{\log \lambda_j}{\Delta t} \tag{3.4.4}$$

where $\Delta t = f^{-1}$ is the separation time between successive snapshots. The discrete frequencies of the decomposed data, o_j, are determined from the imaginary part of

the logarithmically mapped eigenvalues as

$$o_j = 2\pi \text{Imag}(\upsilon_j) = \frac{\arg(\lambda_j)}{2\pi\Delta t} \tag{3.4.5}$$

Typically, the eigenvalues emerge as complex conjugate pairs, resulting in complex conjugate eigenvectors (modes). It is the result of using a matrix of real-valued data. These conjugate modes have the same stability characteristics and frequencies but a different sign. Note that since the negative frequencies are ignored, only the mode with the positive-valued frequency defines each mode pair.

Besides, the logarithmic mapping of these eigenvalues also provides the growth rate determined from the real part:

$$\sigma_j = 2\pi \text{Real}(\upsilon_j) \tag{3.4.6}$$

The empirical Ritz values lying on the unit circle represent the modes with zero growth rates, whereas the eigenvalues lying inside and outside the unit circle represent the damped and undamped modes, respectively.

The associated eigenvectors provide the coefficients of the linear combination that is necessary to express the modal structure within the snapshot basis. Then the following equation obtained

$$\min_s ||\boldsymbol{v}_N \approx \boldsymbol{V}_1^N \boldsymbol{S}|| \tag{3.4.7}$$

where s denotes the last column of the companion matrix $\boldsymbol{S}$. The vector s can be computed by a straightforward least-squares procedure which minimizes the overall residue. In particular, if the QR – decomposition of $\boldsymbol{V}_1^{N-1} = \boldsymbol{QR}$ was taken, the solution to the above equation will be obtained as

$$\boldsymbol{s} = \boldsymbol{R}^{-1}\boldsymbol{Q}^H \boldsymbol{v}_N \tag{3.4.8}$$

where $\boldsymbol{Q}^H$ is the complex conjugate transpose of $\boldsymbol{Q}$ from the QR – decomposition of $\boldsymbol{V}_1^{N-1}$.

As noted in [122], despite the fact that the above decomposition based on a companion matrix is mathematically correct [9], computing accurately more than the first couple modes and eigenvalues on experimental data sets can be hard.

Thus, a more robust implementation that results in a 'full' matrix instead of computing the companion matrix $\boldsymbol{S}$ was chosen for the present study. The SVD – based approach yields the matrix $\widetilde{\boldsymbol{S}}$ that is related to $\boldsymbol{A}$ via a similarity transform. The advantage of this approach over the Arnoldi – like approach is that noise in the data and numerical truncation issues can be compensated for by truncating the SVD of $\boldsymbol{V}_1^{N-1}$.

In order to achieve the robustness, the preprocessing step was done using an SVD of the data sequence in the form

$$\boldsymbol{V}_1^{N-1} = \boldsymbol{U}\boldsymbol{E}\boldsymbol{W}^H \tag{3.4.9}$$

where $\boldsymbol{U}^T\boldsymbol{U} = \boldsymbol{V}^T\boldsymbol{V} = 1$ with $\boldsymbol{U}$ (an $m \times m$ matrix) is an orthonormal eigenvector of $\boldsymbol{V}_1^{N-1}(\boldsymbol{V}_1^{N-1})^T$, matrix $\boldsymbol{W}$ (an $n \times n$ matrix) is an orthonormal eigenvector of $(\boldsymbol{V}_1^{N-1})^T\boldsymbol{V}_1^{N-1}$ and $\boldsymbol{E}$ is a diagonal $m \times n$ matrix with non-negative real numbers on the diagonal.

Then, by substituting Eq. 3.4.9 into Eq. 3.4.3, and upon some rearrangement, we obtain

$$\boldsymbol{U}^H\boldsymbol{V}_2^N\boldsymbol{W}E^{-1} = \boldsymbol{U}^H\boldsymbol{A}\boldsymbol{U} \equiv \widetilde{\boldsymbol{S}} \tag{3.4.10}$$

Then, the modal structures were extracted from the matrix $\widetilde{S}$ in a manner analogous so that the global modes can be recovering from the eigenvectors of the Hessenberg matrix $\boldsymbol{H}$ of the standard Arnoldi method. In this research, the following expression was defined as the dynamic modes, $\boldsymbol{\varphi_i}$:

$$\boldsymbol{\varphi_i} = \boldsymbol{U}\boldsymbol{y}_i \tag{3.4.11}$$

where $\boldsymbol{y}_i$ is the i^{th} eigenvector of $\widetilde{\boldsymbol{S}}$ such that $\widetilde{\boldsymbol{S}}\boldsymbol{y}_i = \lambda_i\boldsymbol{y}_i$, and $\boldsymbol{U}$ is the right singular vectors of the snapshot sequence $\boldsymbol{V}_1^{N-1}$.

3.4.2.2 The Algorithms

The complete algorithm is given below:

Inputs : A set of snapshot pairs from fluid experiments or simulations, where there is a constant interval of time between two snapshots in each pair. This will

often come from a time-series of data. Let a sequence of N snapshots $\{\boldsymbol{v}_1, \boldsymbol{v}_2, ..., \boldsymbol{v}_N\}$ sampled equispaced in time with Δt.

i. Arrange the data $\{\boldsymbol{v}_1, \boldsymbol{v}_2, ..., \boldsymbol{v}_N\}$ into matrices
$\boldsymbol{V}_1^{N-1} = \{\boldsymbol{v}_1, \boldsymbol{v}_2, ..., \boldsymbol{v}_{N-1}\}$, $\boldsymbol{V}_2^{N} = \{\boldsymbol{v}_2, \boldsymbol{v}_3, ..., \boldsymbol{v}_N\}$

ii. Compute the (reduced) SVD of $\boldsymbol{V}_1$, writing as Eq. 3.4.9.

iii. Define the matrix as Eq. 3.4.10.

iv. Compute the eigenvalues, λ_i, and eigenvectors, $\boldsymbol{y}_i$ of $\widetilde{\boldsymbol{S}}$.

v. The DMD mode, $\boldsymbol{\varphi_i}$ corresponding to the DMD eigenvalues, λ_i is then given by Eq. 3.4.11.

The separation Δt between the snapshots and the number N of processed snapshots are the main parameters of the algorithm, while the last one can be determined by the observation of the residual obtained from the least-squares step. The separation between samples has to consider the characteristic time-scale of the fluid phenomenon under investigation for the case involves a restricted amount of snapshots. An excessively low or too high sampling frequency leads to the dissatisfying results.

Outputs: The eigenvalues and modes of DMD. The modes are spatial structures oscillating and/or growing/decaying at rates provided by the respective eigenvalues. These come from the eigendecomposition of a best-fit linear operator, which approximates the dynamics presents in the data.

3.4.2.3 DMD Virtues and its Limitations

Virtues:

- DMD requires neither prior deductions nor any understanding of the fundamental dynamics as it is entirely data-driven.
- DMD can be employed to a variety of data types or even concatenation of disparate data sources.

- DMD provides the Koopman operator, an infinite-dimensional linear operator that can be used to describe non-linear dynamics, under certain conditions.
- DMD modes can isolate specific dynamic structures in which associated with a particular frequency.
- DMD has evinced to be quite tailor-able in the sense that the limitations listed below are addressed by a number of suggested modifications.

Limitations:

- It is too subjective and can be hard in the determination of the most physically important modes because unlike other methods such as POD; there is no single right way to rank the eigenvalue importance.
- Even though there is an existence of extensions, DMD typically needs time-resolved data to identify the dynamics [58, 59].
- The resulting model will be linear if DMD is used to identify the system without any modifications.
- For a non-linear system, DMD can be unreliable. Specifically, an adequately rich set of measurements in each snapshot must be carefully selected for a non-linear system. The connection with the Koopman operator and the fundamental dynamical system may be lost if it was handled without care. In addition, there are additional complications that could restrict the applicability of DMD and associated algorithms for non-linear systems with complex and chaotic dynamics.
- DMD output can be susceptible to noisy data that has been displayed empirically [30] and analytically [164]. Also explored was the impact of process noise, which is a disturbance that influenced the system's dynamics [146]. Sensor noise, however, has more robust algorithms [107, 164].
- DMD should generally be used only for autonomous systems. Unless these are explicitly accounted for, the governing equations should have no time reliance or external inputs [65]).

- There are no orthogonal DMD modes. This has a number of drawbacks: for example, if the modes are used for a reduced-order model as a basis/coordinate system, the model will have additional terms due to the non-zero spatial inner product between different modes. Note that the orthogonalized DMD modes are considered by a recent variant, recursive DMD [18].

- DMD is basically depended on the separation of variables, as does POD, and therefore does not easily extend to the problems of travelling waves.

- Typically, DMD does not operate well for extremely intermittent dynamic systems. Multi-resolution variants [69] and time-delay variants [156], however, are promising to overcome this weakness.

3.5 Chapter Summary

This chapter presented how the wake flow behind a rotating blade was simulated using a computational model. Three methods widely used in turbulent flows modelling were briefly described, but DNS is the one used in this study. The dimensionless incompressible Navier-Stokes equations used in this study were derived, and the difference between two actuator models which are ALM and ADM were provided before the definition of four stratified atmospheric stability conditions were given in the first section. The second section of this chapter provided a detailed mathematical background of the two model decomposition techniques, which will be used in this study. For the databased method, POD analysis captures the most energetic modes, while DMD extracts the dynamic modes along with their growth rates and frequencies from the flow field data. Apparently, both POD and DMD methods can use the flow field data from numerical simulation and experimental measurement. The following chapter will provide an interesting analysis of the physics of the helical vortex core from four different atmospheric stratification conditions. Few characteristics and behaviours of the helical flow will be investigated, and the difference between every case will be discussed.

Chapter 4

Helical Vortex Breakdown – Analysis in the Physical Space

In this chapter, the helical wake flow behind a rotating blade was studied in four different stratification atmospheres which are in weakly stable, neutral and two different temperature gradients from the strongly stable stratification as discussed in Section 4.2. In the strongly stable, case 1 and neutral stratification, the analysis were carried out at two Reynolds numbers, Re = 1000, and Re = 2000. The other two cases, which are weakly stable and strongly stable case 2 were studied at Re = 1000. The analysis on the vortex identification, deformation, vorticity dynamics, breaking mechanism, and the core centroids analysis of the vorticity magnitude for all six cases will be presented in Subsection 4.2.1, 4.2.2, 4.2.3, 4.2.4, and 4.2.5, respectively. Section 4.3 is about the physical interpretation of the flow on the analysis of power spectra before this chapter ends with the conclusion in Section 4.4. The computational domain of the simulation of the wake flow behind the rotating blade will be described in Section 4.1.

4.1 Helical Flow behind a Rotating Blade

The sub-domain of the complete computational domain was being considered to perform the analysis in order to decrease the size of the computations and concentrate on the interesting part appropriate to the physics in the flow. In the sub-domain

$1 < z < 11$, the perturbation growth is linear and the magnitude of the velocity of the perturbations remain low compared to the base flow. The non-linear effects in the wake breakdown and the turbulent wake are out the sub-domain. Thus, the analysis has been performed to the three components of the instantaneous velocity, $\boldsymbol{u} = (u, v, w)$ in a smaller region of the computational domain as shown in Fig. 3.1 of Section 3.2.

The wake behind a wind turbine is typically divided into two sections; near wake and far wake, where it is difficult to determine exactly the boundary between the two sections. Nevertheless, it is known that the end of the near wake is where the shear layer hits the wake axis [19]. Crespo et al. [1] concluded that this normally takes place at around $2 - 5D$. The velocity deficit declines slowly downstream of the turbine in the far wake, and the wake is fully developed. Consequently, axis-symmetry and thus a self-similar wake structure can be assumed [19].

Fig. 4.1 was referred for the view of Fig. 3.1 in $z - y$ plane. This is to focus on the smaller domain which were studied in this work.

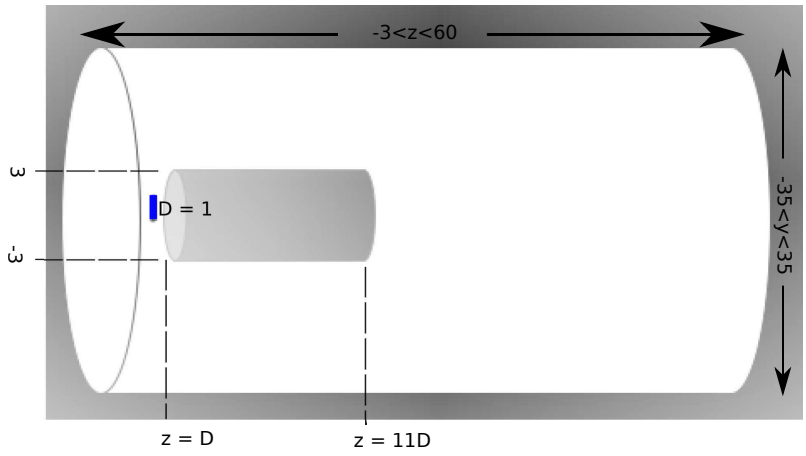

Figure 4.1: The side view of Fig. 3.1 with the blue rectangle represents the radius of the rotating blade, $D = 1$, located at $(z, y) = (0, 0)$.

4.2 Analysis of Instantaneous Helical Flow behind a Rotating Blade

Wakes originate from the shed trailing vortices of the spinning blades that form the concentrated helical tip and root vortex structures. In considering the effect of upstream turbines on downstream turbines, the growth and lifetime of tip vortices are being the subjects of interest. Due to self-induced instability and ambient atmospheric turbulence, the tip vortices break up. Therefore, when considering the aerodynamic loads and fatigue on impacted turbines, the lifetime of tip vortices and the process of the break up is valuable knowledge. For this reason, [159] conducted a study focusing on the stability properties of tip vortices and the mechanisms leading to vortex pairing.

4.2.1 Vortex Identification

Fluid mechanics is a discipline in applied mechanics concerned with the behaviour of liquids and gasses at rest or in motion. The fluid dynamics is the component of the fluid movement. Fluid mechanical problems are often dominated by vortical structures, and in flow fields, vortices are usually considered to be the most important structures. The vortices are commonly associated with turbulence, but occur in laminar flow as well. Thus, the identification of vortices is important as it can be seen as a tool for a better understanding of complex flow phenomena.

In the literature over the past three decades, numerous vortex identification methods, vortex definitions and vortex core visualization techniques have been proposed [53,61,76,106,121]. Various vortex identification schemes that distinguish the region-type definitions of a vortex from the line-type definitions of a vortex core. In practice, these approaches may be effectively combined [162]. Although there is no final agreement on what is a vortex, fluid vortices were mostly related to a quite rigorous and physically well-established quantity representing an average fluid component angular velocity, the so-called vorticity.

The widely used local criteria such as Q-criterion, Δ-criterion and λ_2-criterion sharing a basis in $\nabla \boldsymbol{u}$ which are local in character. There are two distinct Galilean-

invariant definitions of a vortex proposed using invariants of the velocity gradient tensor [53, 106, 109] which can be expressed as the following three-dimensional matrix:

$$\nabla \boldsymbol{u} = \frac{\partial u_i}{\partial x_j} = \begin{bmatrix} \frac{\partial u_x}{\partial x} & \frac{\partial u_x}{\partial y} & \frac{\partial u_x}{\partial z} \\ \frac{\partial u_y}{\partial x} & \frac{\partial u_y}{\partial y} & \frac{\partial u_y}{\partial z} \\ \frac{\partial u_z}{\partial x} & \frac{\partial u_z}{\partial y} & \frac{\partial u_z}{\partial z} \end{bmatrix} \tag{4.2.1}$$

As this is a second order tensor in Cartesian coordinates it can be decomposed into a symmetric and a skew-symmetric part

$$\nabla \boldsymbol{u} = \boldsymbol{S}_{ij} + \boldsymbol{\Omega}_{ij} \tag{4.2.2}$$

where $\boldsymbol{S}_{ij} = \frac{1}{2}(\nabla \boldsymbol{u} + \nabla^T \boldsymbol{u}) = \frac{1}{2}\left(\frac{\partial u_i}{\partial x_j} + \frac{\partial u_j}{\partial x_i}\right)$ and $\boldsymbol{\Omega}_{ij} = \frac{1}{2}(\nabla \boldsymbol{u} - \nabla^T \boldsymbol{u}) = \frac{1}{2}\left(\frac{\partial u_i}{\partial x_j} - \frac{\partial u_j}{\partial x_i}\right)$. $\boldsymbol{S}_{ij}$ is known as the rate-of-strain tensor, and $\boldsymbol{\Omega}_{ij}$ is the vorticity/rotation tensor.

The velocity gradient tensor, $\nabla \boldsymbol{u}$ has the following characteristic equation:

$$\lambda^3 + P\lambda^2 + Q\lambda + R = 0 \tag{4.2.3}$$

where λ is the eigenvalues of $\nabla \boldsymbol{u}$ and P, Q and R are the three invariants of the velocity gradient tensor. Using the decomposition into symmetric and anti-symmetric parts these invariants can be expressed as follows:

$$P = -\nabla \cdot \boldsymbol{u} = \left(\frac{\partial}{\partial x}, \frac{\partial}{\partial y}, \frac{\partial}{\partial z}\right) \cdot (u_x, u_y, u_z) = -\left(\frac{\partial u_x}{\partial x} + \frac{\partial u_y}{\partial y} + \frac{\partial u_z}{\partial z}\right) \tag{4.2.4}$$

$$Q = -\frac{1}{2}\left(\frac{\partial u_i}{\partial x_j}\frac{\partial u_j}{\partial x_i}\right) = \frac{1}{2}(\|\boldsymbol{\Omega}^2\| - \|\boldsymbol{S}^2\|) \tag{4.2.5}$$

$$R = -\det\left(\frac{\partial u_i}{\partial x_j}\right) \tag{4.2.6}$$

The Q-criterion defines a vortex as "a connected fluid region with a positive second invariant of $\nabla \boldsymbol{u}$" [170], i.e $Q > 0$. This criterion also provides a secondary pressure condition, requiring reduced pressure than ambient pressure in the vortex. Looking at the definition of the second invariant, it is clearly shown that Q represents the local equilibrium between the rate of shear strain and the magnitude of vorticity, $|\omega|$ defining vortices as areas where $|\omega|$ is greater than the magnitude of rate-of-strain [53, 170].

The Δ-criterion defines vortices as "regions in which the eigenvalues of $\nabla \boldsymbol{u}$ are complex and the streamline pattern is spiralling or closed" [170]. In order to determine if the eigenvalues are complex, the discriminant of the characteristic equation was examined.

$$\Delta = \left(\frac{Q}{3}\right)^3 + \left(\frac{R}{2}\right)^2 > 0 \tag{4.2.7}$$

For incompressible flows where $P = 0$ is valid this definition. If two of the eigenvalues form a complex conjugate pair, the streamlines are said to be closed or spiralling. From Eq. 4.2.7, it is shown that $Q > 0$ and this implifies that Q-criterion more restrictive than Δ-criterion [121].

The λ_2-criterion seeks for a minimum pressure, but by discarding these terms, it removes the impacts from unsteady straining and viscosity. Taking the gradient of the Navier-Stokes equations results in

$$a_{i,j} = -\frac{1}{\rho} p_{ij} + \nu u_{i,jkk} \tag{4.2.8}$$

where a_{ij} is the gradient of acceleration and p_{ij} is symmetric. The decomposition of the acceleration gradient into symmetric and antisymmetric parts provides the transport equation of vorticity as the antisymmetric part, and the symmetric part

$$-\frac{DS_{ij}}{Dt} - \nu S_{ij,kk} + \Omega_{ik}\Omega_{kj} + S_{ik}S_{kj} = -\frac{1}{\rho} p_{ij} \tag{4.2.9}$$

The first two terms on the left hand side, respectively, represent unsteady irrotational strain and viscous effects. Therefore, it is regarded only $\boldsymbol{S}^2 + \boldsymbol{\Omega}^2$ to determine if there is a minimum local pressure that involves a vortex. A vortex is defined as "a region connected with two negative eigenvalues of $\boldsymbol{S}^2 + \boldsymbol{\Omega}^2$" [61]. Since $\boldsymbol{S}^2 + \boldsymbol{\Omega}^2$ is symmetric, it has only real eigenvalues and by ordering the eigenvalues $\lambda_1 \leq \lambda_2 \leq \lambda_3$ the definition becomes equivalent to requiring that $\lambda_2 < 0$. Generally visualized as isosurfaces for different values of $-\lambda_2$ [61]. The three conditions described above are equal in planar flows.

On the other hands, vorticity is defined as the curl of the velocity by the following equation:

$$\boldsymbol{\omega} = \nabla \times \boldsymbol{u} \tag{4.2.10}$$

where ∇ is the del operator and $\boldsymbol{u}$ is the flow velocity. Since it is equal to the rotation of the fluid at (x, t), it can be used directly to identify vortices.

Mathematically, the vorticity of a three-dimensional flow is a pseudo-vector (a quantity that transforms like a vector under a proper rotation) field that describes the local spinning motion of a fluid near some point (the tendency of something to rotate), as would be seen by an observer located at that point and travelling along with the flow. It is usually denoted by $\boldsymbol{\omega}$, defined as the curl or rotational of the instantaneous velocity field $\boldsymbol{u}$ describing the continuum motion. In Cartesian coordinates, Eq. 4.2.10 is written as

$$\boldsymbol{\omega} = \left(\frac{\partial}{\partial x}, \frac{\partial}{\partial y}, \frac{\partial}{\partial z}\right) \times (u_x, u_y, u_z) = \left(\frac{\partial u_z}{\partial y} - \frac{\partial u_y}{\partial z}, \frac{\partial u_x}{\partial z} - \frac{\partial u_z}{\partial x}, \frac{\partial u_y}{\partial x} - \frac{\partial u_x}{\partial y}\right) \tag{4.2.11}$$

In words, the vorticity tells how the velocity vector changes when one moves in a direction perpendicular to it, through an infinitesimal distance. It can be readily visualized by plotting the isosurfaces of vorticity magnitude, $|\omega|$ given by the following equation, in which was commonly used for representing vortex cores [6, 31, 144].

$$|\omega| = ({\omega_x}^2 + {\omega_y}^2 + {\omega_z}^2)^{\frac{1}{2}} \tag{4.2.12}$$

where $\omega_x, \omega_y, \omega_z$ is the vorticity of its three components.

Fig. 4.2 shows the isosurface of all three vortex identification techniques, Q-criterion, Δ-criterion and λ_2-criterion including $|\omega|$ in the streamwise direction for the Strongly Stable at Re = 1000 case (SS1, Re1k). The readers are reminded that all these quantities are dimensionless since the calculations are based on dimensionless velocities. It is the same for x, y, z as it was dimensionalized by the radius of the rotating blade, D.

As it can be seen in Fig. 4.2, there is no difference between all the vortex identification methods in visualizing the vortex. Thus, $|\omega|$ will be used in the following analysis to further understand the characteristics and behaviours of the vortices since the other three criterion mentioned before can not be used to calculate the circulation. The significance of the circulation is that it helps at quantifying the actual strength of a vortex and tells the force that will exert on surrounding the helical flows.

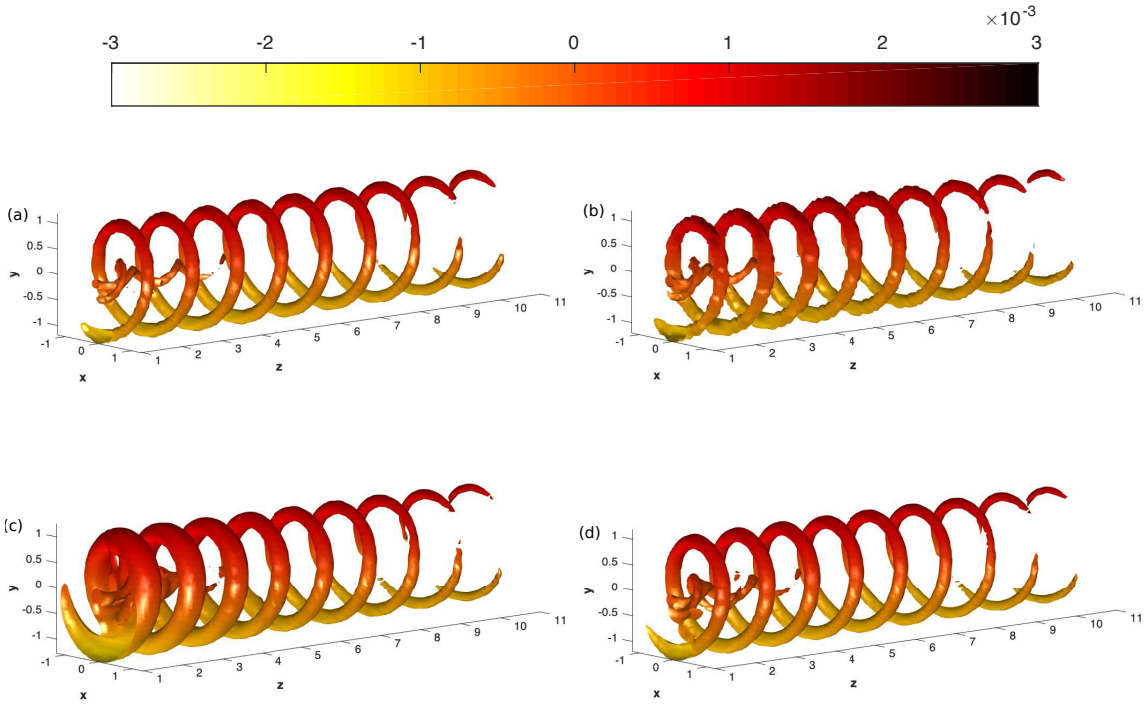

Figure 4.2: Isosurface of: (a) $Q = 0.0025$, (b) $\Delta = 1e^{-8}$, (c) $\lambda_2 = 0.006$, and (d) $|\omega| = 1.25$ with contours indicate the temperature field of SS1, Re1k.

The isosurface of $|\omega|$ for SS1, Re1k and all the other cases which are SS1 at Re = 2000 (SS1, Re2k), Strongly Stable case 2 at Re = 1000 (SS2, Re1k), Weakly Stable at Re = 1000 (WS, Re1k), and Neutral at Re = 1000 and Re = 2000 (N, Re1k, and N, Re2k, respectively) can be seen in the Fig. 4.3 below:

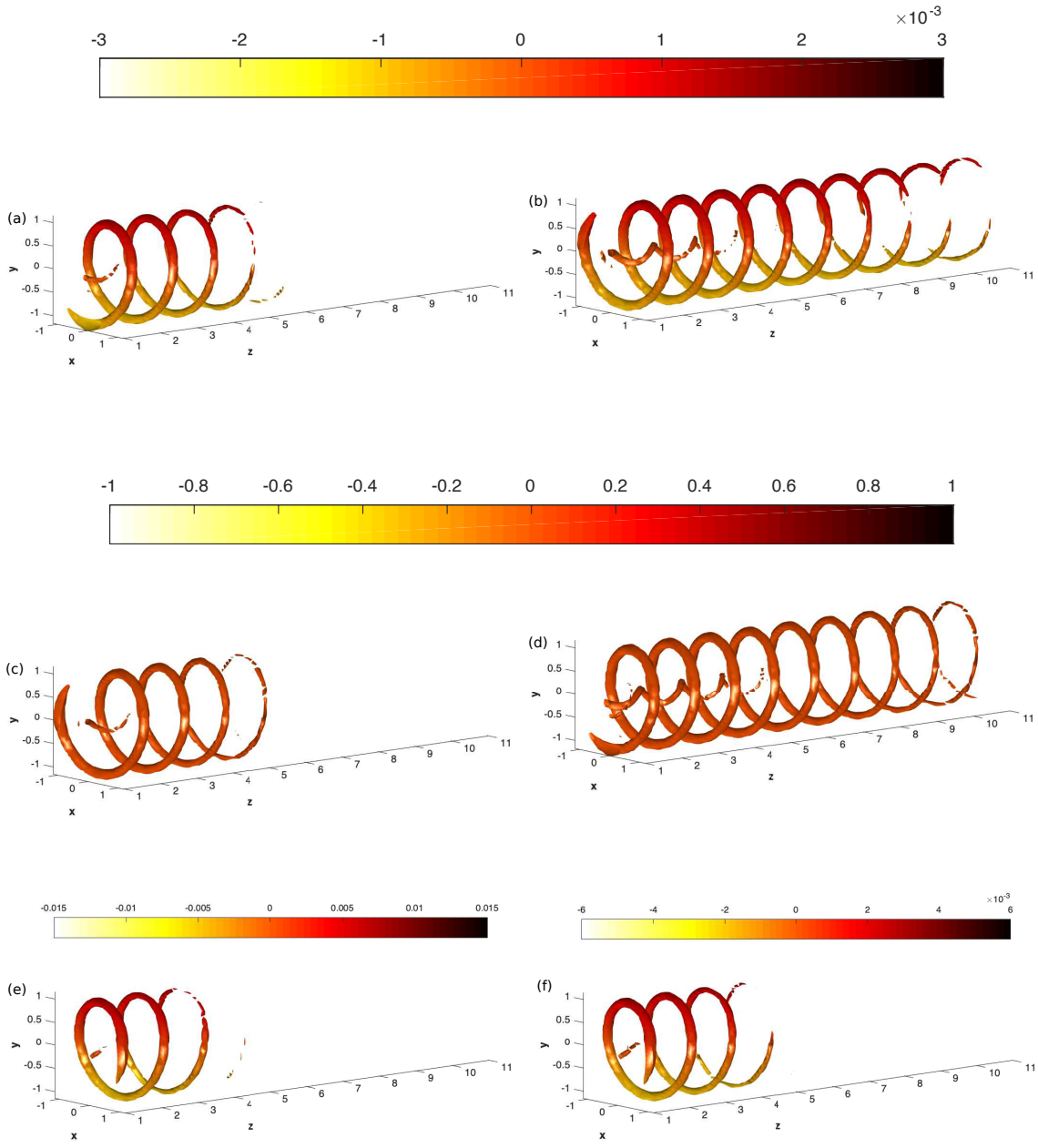

Figure 4.3: Isosurface of $|\omega| = 2.5$ for: (a) SS1, Re1k, (b) SS1, Re2k, (c) N, Re1k, (d) N, Re2k, (e) WS, Re1k, and (f) SS2, Re1k cases with contours indicate their temperature field.

In particular, the tip and root vortices may interact depending on the tip speed ratio. However, the root vortices break down faster than the tip vortices as it can be seen in Fig. 4.4, due to their weak proximity. The root vortices are therefore not included in this analysis as there is a very weak interaction between root and tip vortices.

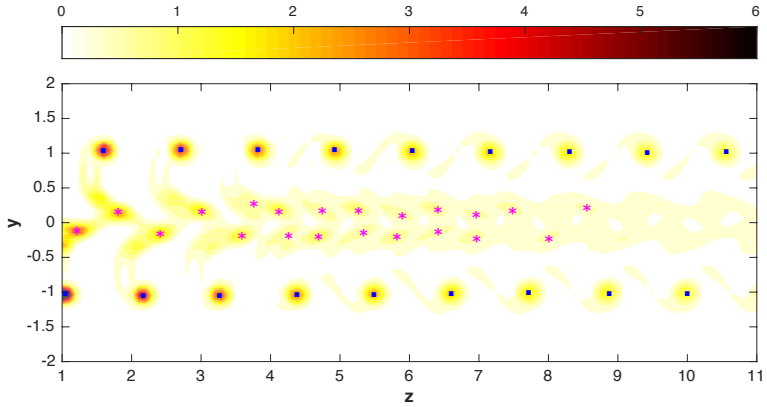

Figure 4.4: Contour of $|\omega|$ in yz-plane cut (SS1, Re1k). The blue squares represent the tip vortices while the pink stars are the root vortices.

4.2.2 Deformation of the Helical Wake Flow

In this study, the deformation of the flow structure was defined to be the degree of eccentricity (non-circularity) the helical wake is. In order to quantify it, we average through slices of $|\omega|$ in the streamwise direction over a range where the helical core makes a complete revolution (from now it will be called as 'cycle') as shown in Fig. 4.5.

The available streamwise distance $1 < z < 11$ typically accommodates nine complete cycles, as shown in Fig. 4.6. In each sub-figure, the black circle was plotted from the mean distance, $\bar{d}$ (which will be described later in the next paragraph) and the red circle with $r = 1.5$ were plotted for indicative purposes, to show qualitatively how non-circular the wake is.

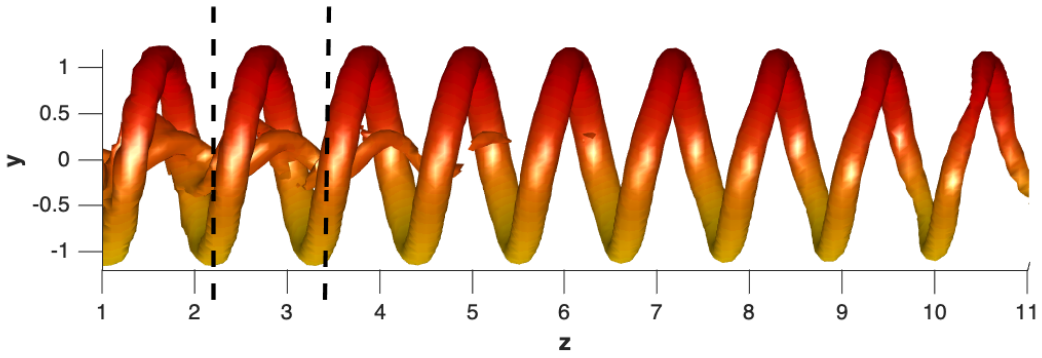

Figure 4.5: Isosurface of $|\omega|$ from SS1, Re1k case for nine complete cycles with the dashed lines indicate the second complete cycle at $2.1 \leq z \leq 3.2$

The root-mean-square (RMS) error is a measure of the variations between the expected values and the actual observed values that are often used. It represents the sample standard deviation of the differences between the values of prediction and observation. The RMS of the distance between the core points to the origin, d (shows in Fig. 4.7) for observations of the mean distance, $\bar{d}$ was computes for $N = 9$ complete cycles (as shown in Fig. 4.6 (a) – (i)) as the square root of the mean of the square of the deviations:

$$\text{RMS} = \sqrt{\frac{\sum_{i=1}^{N}(d_i - \bar{d}_i)^2}{N}} \tag{4.2.13}$$

A total of 100 core points as represented by the blue stars in Fig. 4.7 were referred to the points with the highest values of $|\omega|$ (after this will be called as the "core points") that formed the helical core structure of $|\omega|$.

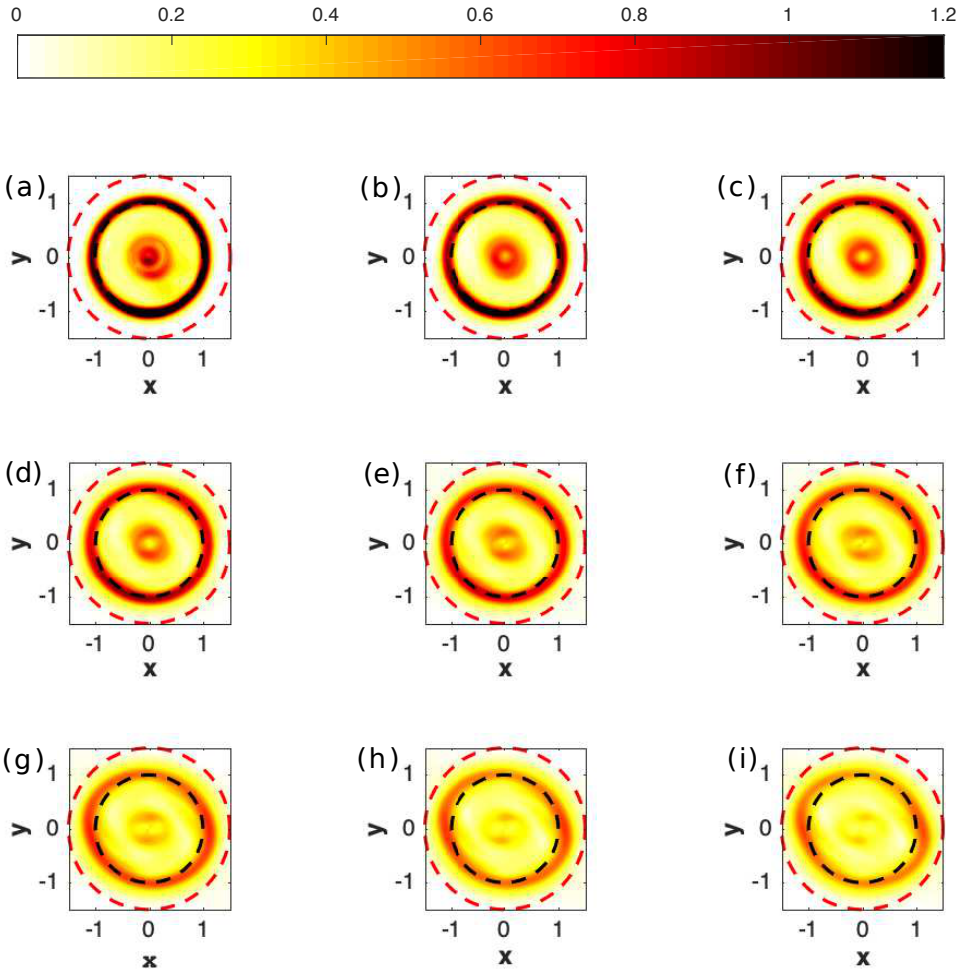

Figure 4.6: Contour of $|\omega|$ (SS1, Re1k) at: (a) $1 \leq z \leq 2.1$, (b) $2.1 \leq z \leq 3.2$, (c) $3.2 \leq z \leq 4.3$, (d) $4.3 \leq z \leq 5.4$, (e) $5.4 \leq z \leq 6.5$, (f) $6.5 \leq z \leq 7.6$, (g) $7.6 \leq z \leq 8.7$, (h) $8.7 \leq z \leq 9.8$, and (i) $9.8 \leq z \leq 10.9$.

Fig. 4.8 shows the RMS values of the tip vortices. The deformation of the helical flow structure increased as the flow moves downstream except for both N cases. It shows how non-circular the helical flow is for every cycle and indirectly tells that the circular helical flow deformed to the ellipse at the end.

Fig. 4.6, Fig. 4.9, Fig. 4.10, and Fig. 4.11 were referred for a better visualization of how the helical flow shape distorts from its initial circular to an ellipse one in the process.

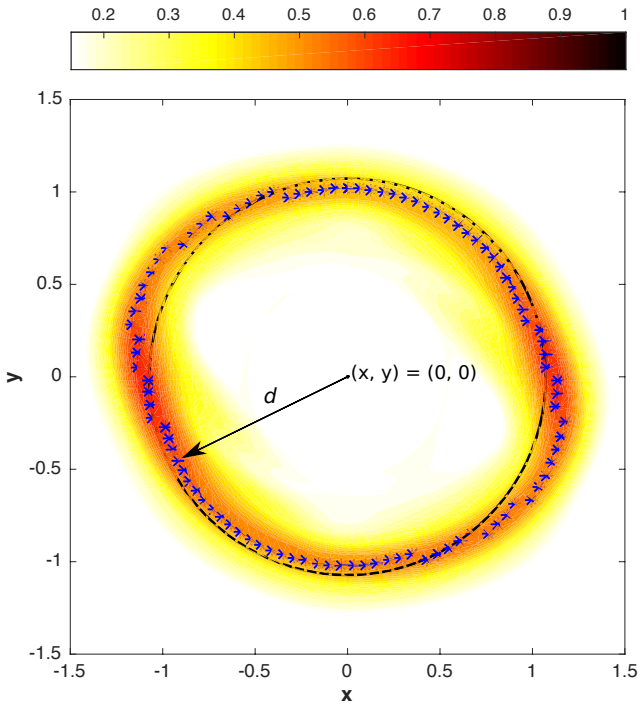

Figure 4.7: Contour of $|\omega|$ at $8.7 \leq z \leq 9.8$ with black arrow indicates the distance, d, the black dashed line is the mean distance, $\bar{d}$ of the cores from the origin, (0,0) and the blue stars are the core points from 100 angles of the cycle.

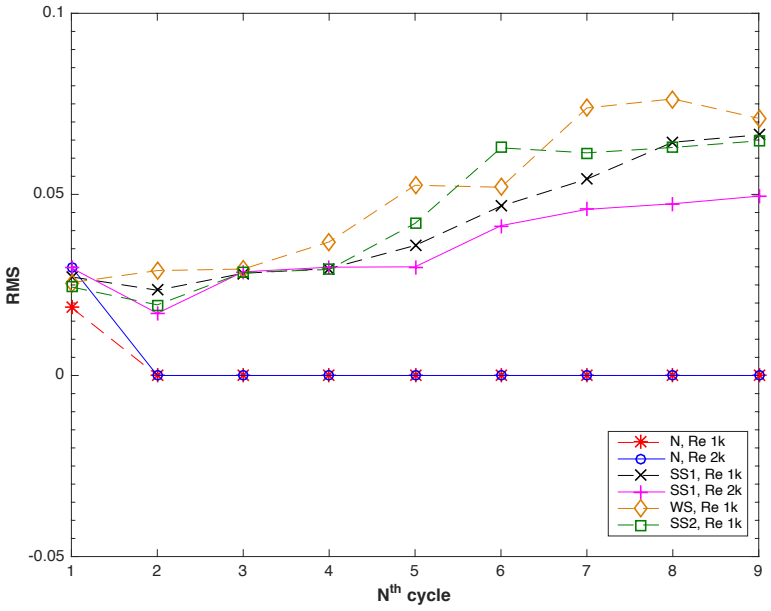

Figure 4.8: RMS Error of $|\omega|$ cores for all cases.

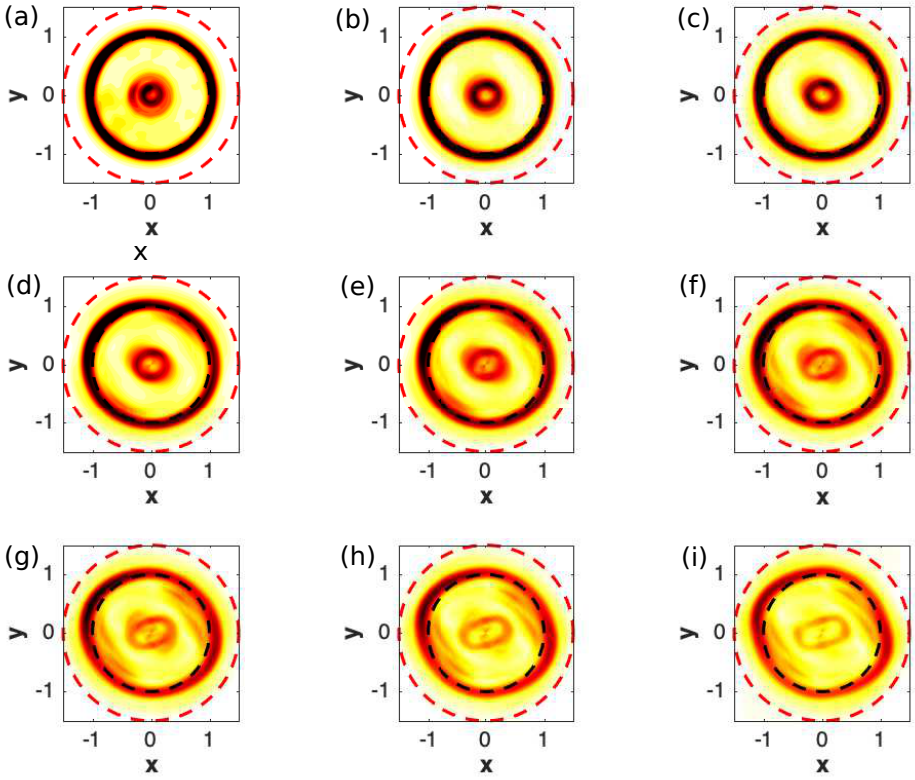

Figure 4.9: Caption and colormap as Fig. 4.6, but for SS1, Re2k.

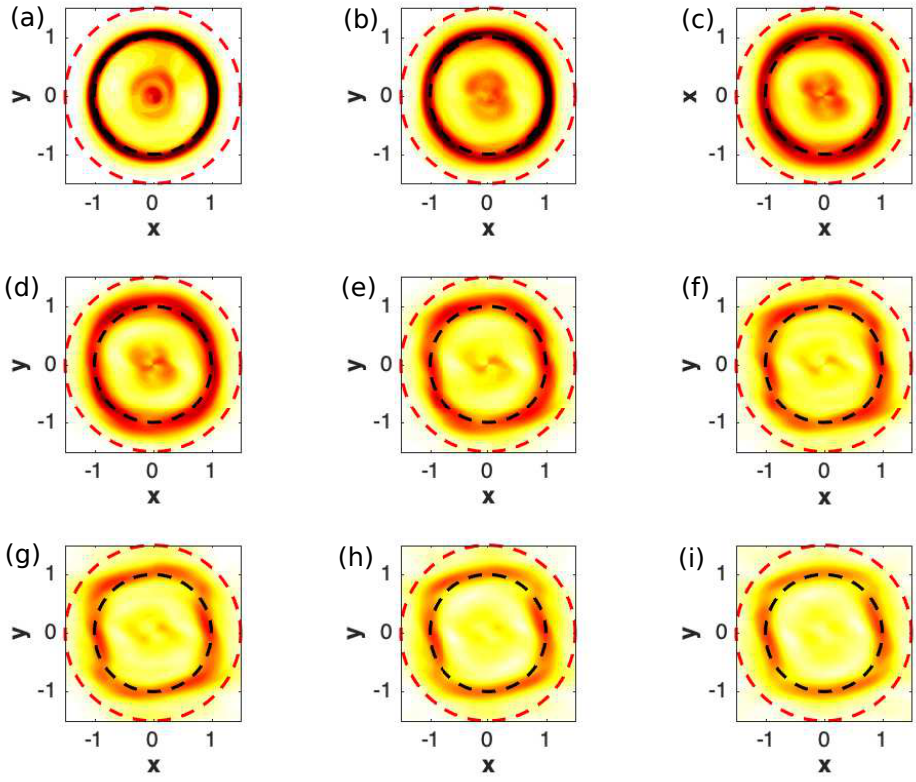

Figure 4.10: Caption and colormap as Fig. 4.6, but for WS, Re1k.

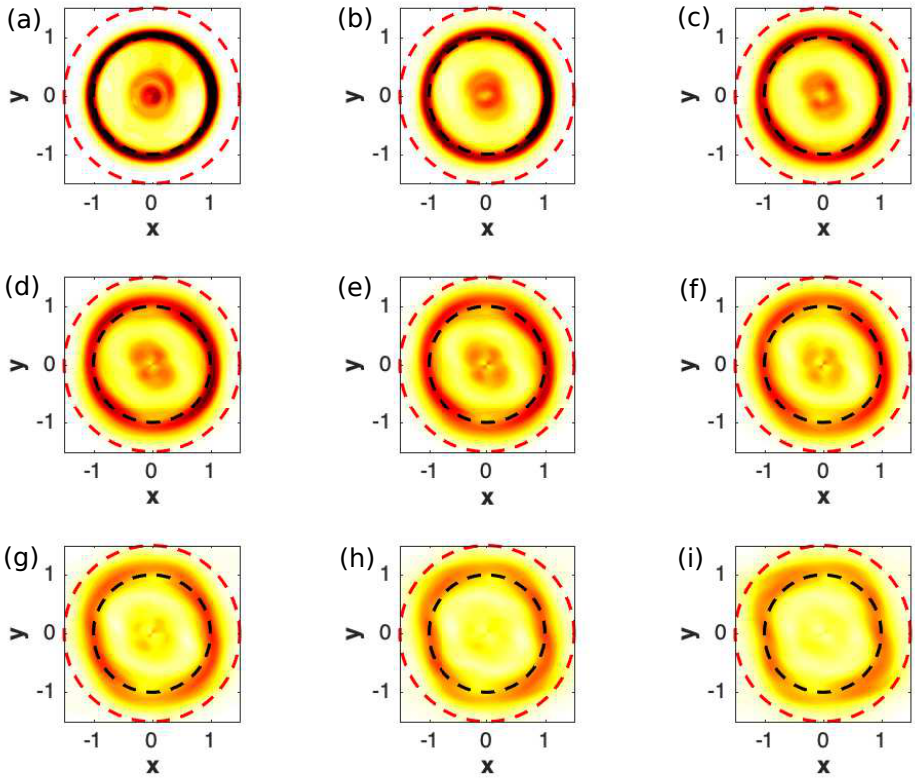

Figure 4.11: Caption and colormap as Fig. 4.6, but for SS2, Re1k.

However, for the neutral cases (refer to the Fig. 4.12), the helical flow started as non-circular as other cases before it went through the deformation into the perfect circle with zero RMS value. The blue and red line from Fig. 4.8 support this observation when they both drop to zero in the second cycle and remain till the last.

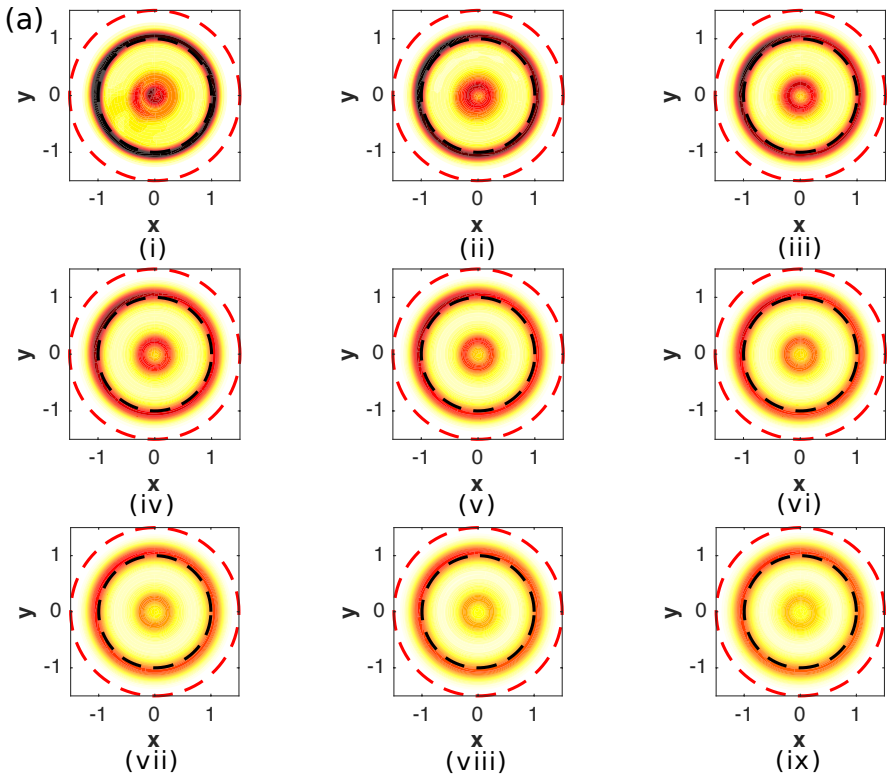

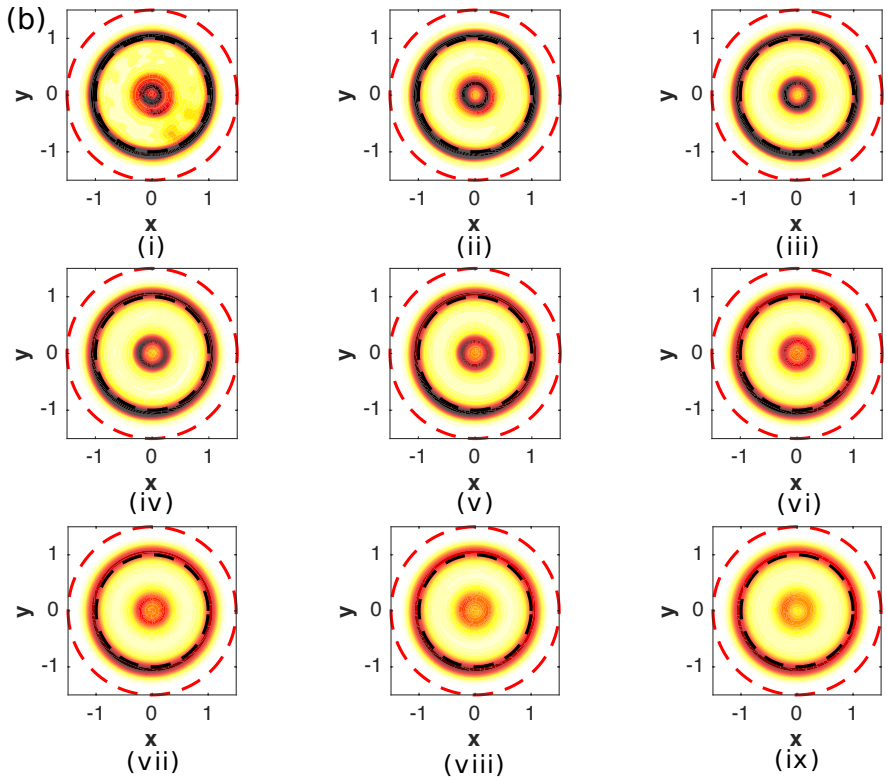

Figure 4.12: Caption and colormap as Fig. 4.6, but for (a) N, Re1k, and (b) N, Re2k cases.

4.2.3 Vorticity Dynamics

In order to further comprehend the evolution of the vortex structure in terms of vorticity dynamics, the spatial derivative terms of the vorticity transport equation given by the following equation were evaluated.

$$\frac{D\boldsymbol{\omega}}{Dt} = (\boldsymbol{\omega} \cdot \nabla)\boldsymbol{u} + \nu\nabla^2\boldsymbol{\omega} \tag{4.2.14}$$

where $\boldsymbol{u} = (u_z, u_r, u_\tau)$ with z, r and τ representing the streamwise, radial and tangential components, respectively. The tangential velocity, u_τ is related to the angular velocity, u_θ and the radius, r as $u_\tau = ru_\theta$. As justified in [12], owing to the rotating nature of flow motion, it is better to represent the vector fields in a series of rotating Cartesian frames rather than a single fixed Cartesian frame. The velocity field in rotating Cartesian frame, $\boldsymbol{u}(z, r, \tau) = (u_z, u_r, u_\tau)$ is related to that in the fixed Cartesian frame, $\boldsymbol{u}(z, x, y) = (u_z, u_x, u_y)$ by the relationship:

$$\boldsymbol{u}(z, r, \tau) = J(\theta)\boldsymbol{u}(z, x, y) \tag{4.2.15}$$

where J is the Jacobi rotation matrix which is a function of θ, the azimuthal angle. The same relation applies to all the other vector fields. The details of the derivation of Eq. 4.2.14 are provided in [12] & [132].

The individual components of Eq. 4.2.14 then can be written as

$$\dot{\omega}_i = -(\boldsymbol{u} \cdot \nabla)\omega_i + (\boldsymbol{\omega} \cdot \nabla)u_i + \nu\nabla^2\omega_i \tag{4.2.16}$$

where $i = z, r, \tau$ and $\dot{\omega}_i = \partial\omega_i/\partial t$. It can be seen that the temporal change of local vorticity is equal to the sum of the convection $-(\boldsymbol{u} \cdot \nabla)\omega_i$, tilt/stretch $(\boldsymbol{\omega} \cdot \nabla)u_i$, and dissipation terms $\nu\nabla^2\omega_i$, which are essentially derived from the spatial distribution.

The tilt/stretch term then can be expanded as

$$(\omega \cdot \nabla)u_i = \frac{\partial u_i}{\partial z}\omega_z + \frac{\partial u_i}{\partial r}\omega_r + \frac{\partial u_i}{\partial \tau}\omega_\tau \tag{4.2.17}$$

The terms on the right-hand side can be separated into tilting and stretching components as follows.

As for the streamwise component $i = z$, $(\partial u_z/\partial z)\omega_z$ represents the vortex stretching, while the other two terms $(\partial u_z/\partial r)/\omega_r$ and $(\partial u_z/\partial \tau)\omega_\tau$ represent the vortex

tilting from the vertical and tangential components, respectively. In this study, the focus is on the two tilting terms (which then were normalized by $||\omega||^2_{\max}$) as it helps in further understanding the deformation of the helical structure discussed in the previous Subsection 4.2.2.

Vortex tilting is the mechanism that normally tilts a vortex to give the vortex a small component of the vorticity in a perpendicular direction to its core. Note that the direction of streamwise vorticity was chosen in this analysis because it provides a significant illustration for vortex tilting (as Fig. 4.6 shows the helical flow mostly tilted in the two directions perpendicular to streamwise direction), which appear to be the dominant components.

The vorticity tilting of ω_z in x- and y-direction in the fixed Cartesian frame are shown in the isosurface plot of $|\omega|$ as the isocolor of Fig. 4.13(a) and Fig. 4.13(b), respectively. However, it is hardly to see the vortex tilting clearly from it. This poor result somehow shows a good agreement to what [12] said about the advantage of using the rotating Cartesian frame instead. Hence, this study on the vortex dynamics will then be carried out and discussed in rotating Cartesian frame.

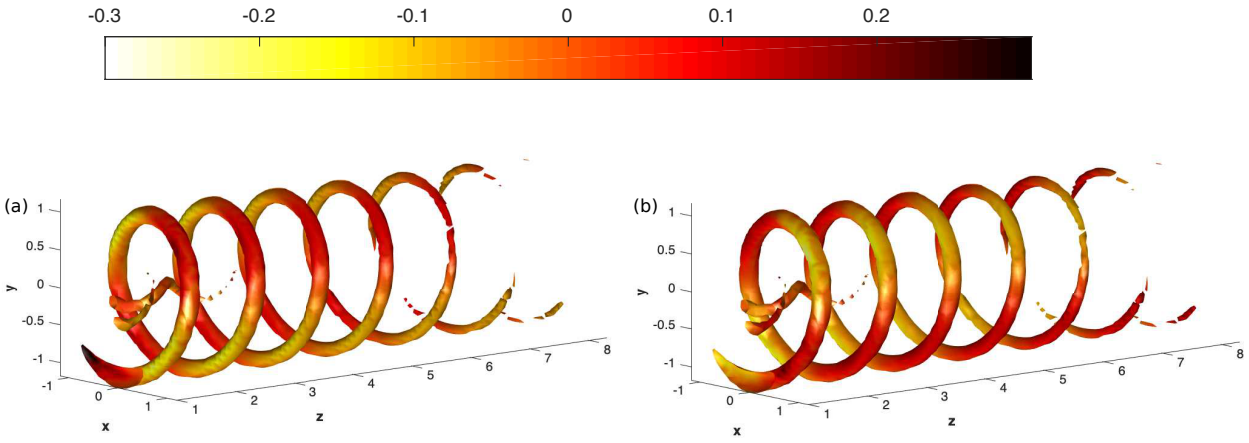

Figure 4.13: Isosurface of $|\omega|$ coloured by streamwise vorticity tilting, into: (a) x-direction, and (b) y-direction in the fixed Cartesian frame for SS1, Re1k.

The vorticity tilting of ω_z along radial, r- and tangential, τ- direction in the rotating Cartesian frame as the flow goes downstream were shown in Fig. 4.14(a) – Fig. 4.19(a) and Fig. 4.14(b) – Fig. 4.19(a), respectively.

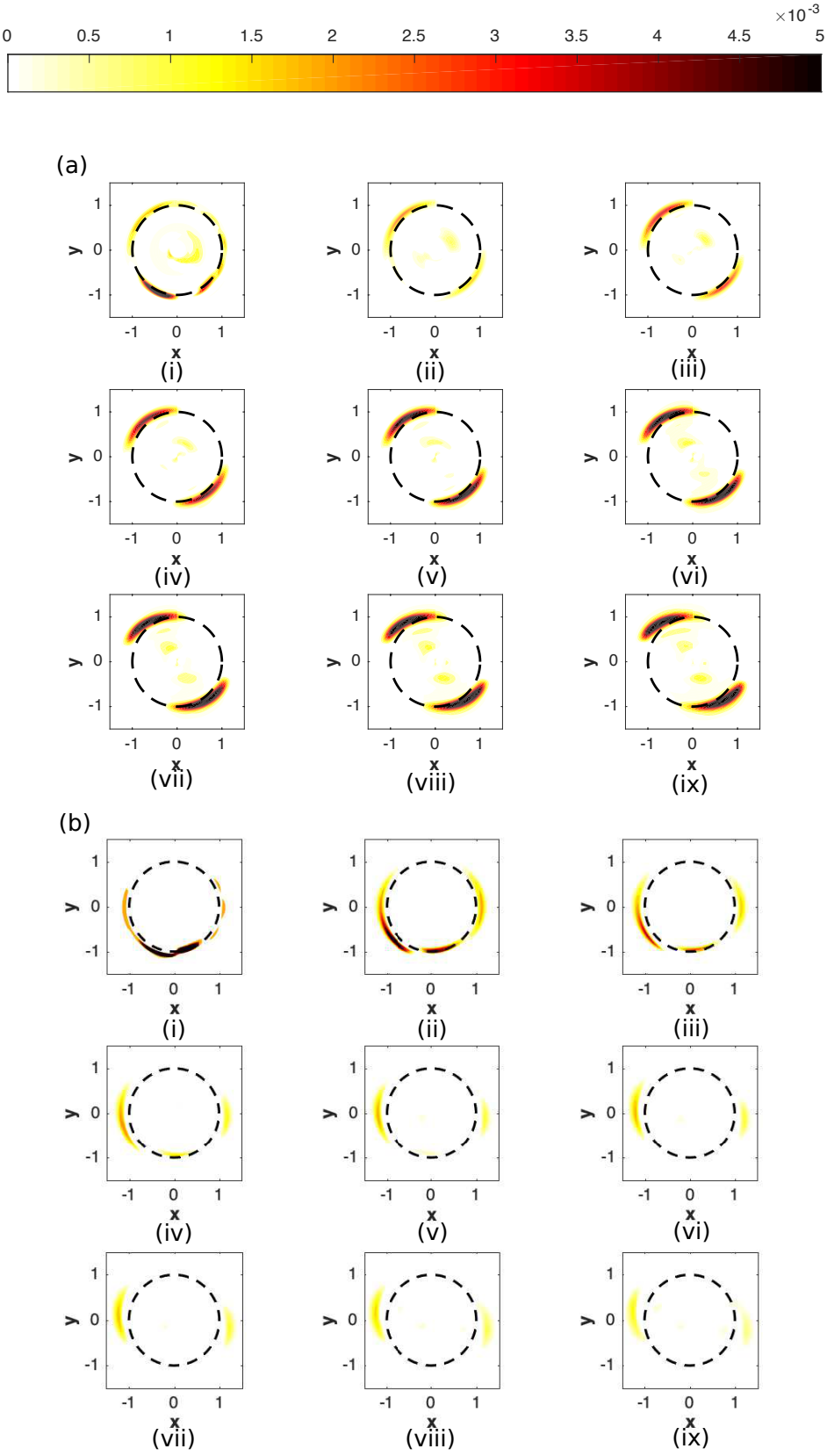

Figure 4.14: Tilting of streamwise vorticity, ω_z into r-direction (a), and τ-direction (b), respectively in the rotating Cartesian frame for SS1, Re1k at: (i) $1 \leq z \leq 2.1$, (ii) $2.1 \leq z \leq 3.2$, (iii) $3.2 \leq z \leq 4.3$, (iv) $4.3 \leq z \leq 5.4$, (v) $5.4 \leq z \leq 6.5$, (vi) $6.5 \leq z \leq 7.6$, (vii) $7.6 \leq z \leq 8.7$, (viii) $8.7 \leq z \leq 9.8$, and (ix) $9.8 \leq z \leq 10.9$. Remark that the black dashed line is the mean distance, $\bar{d}$ of the cores from the origin, (0,0).

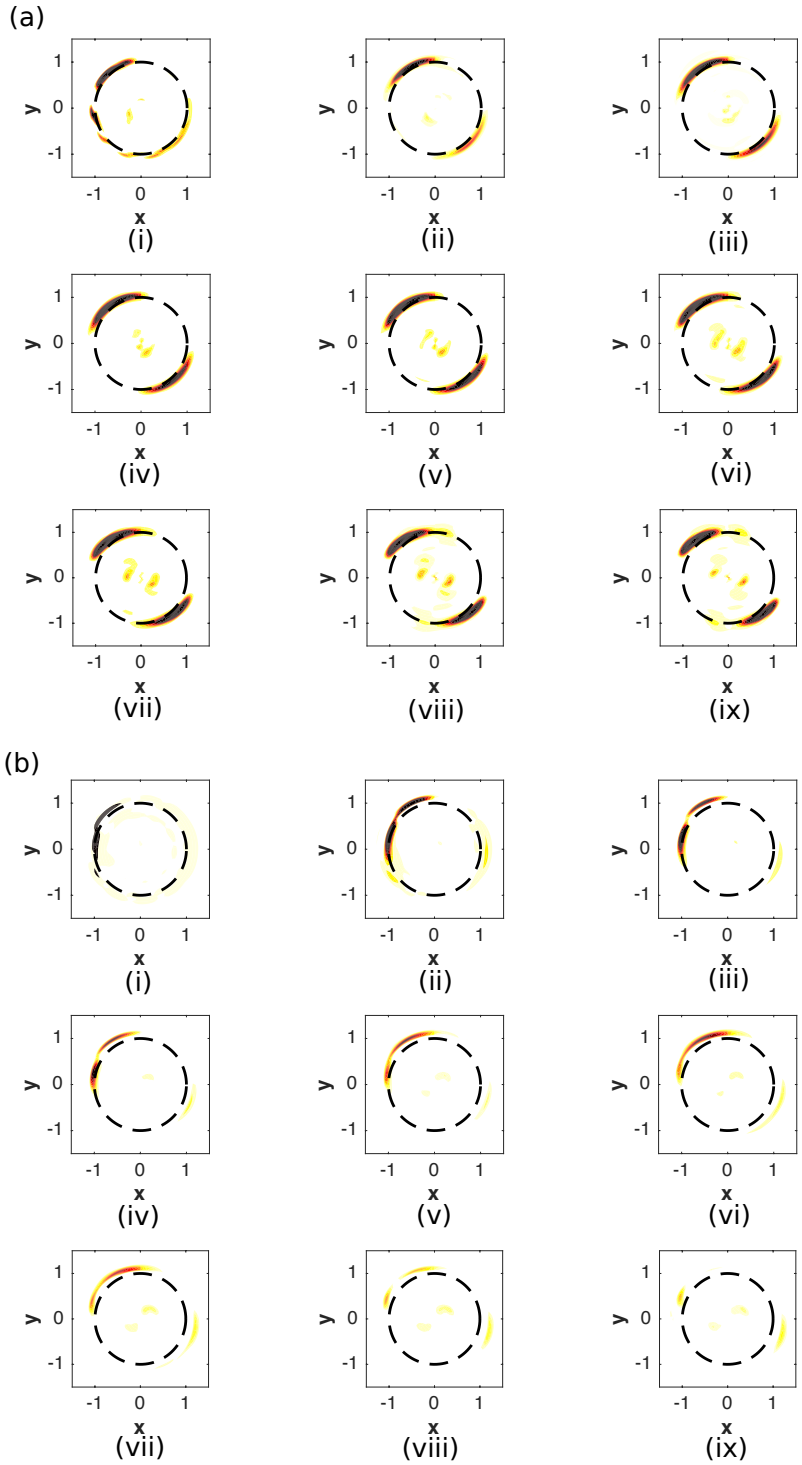

Figure 4.15: Caption and colormap as Fig. 4.14, but for SS1, Re2k.

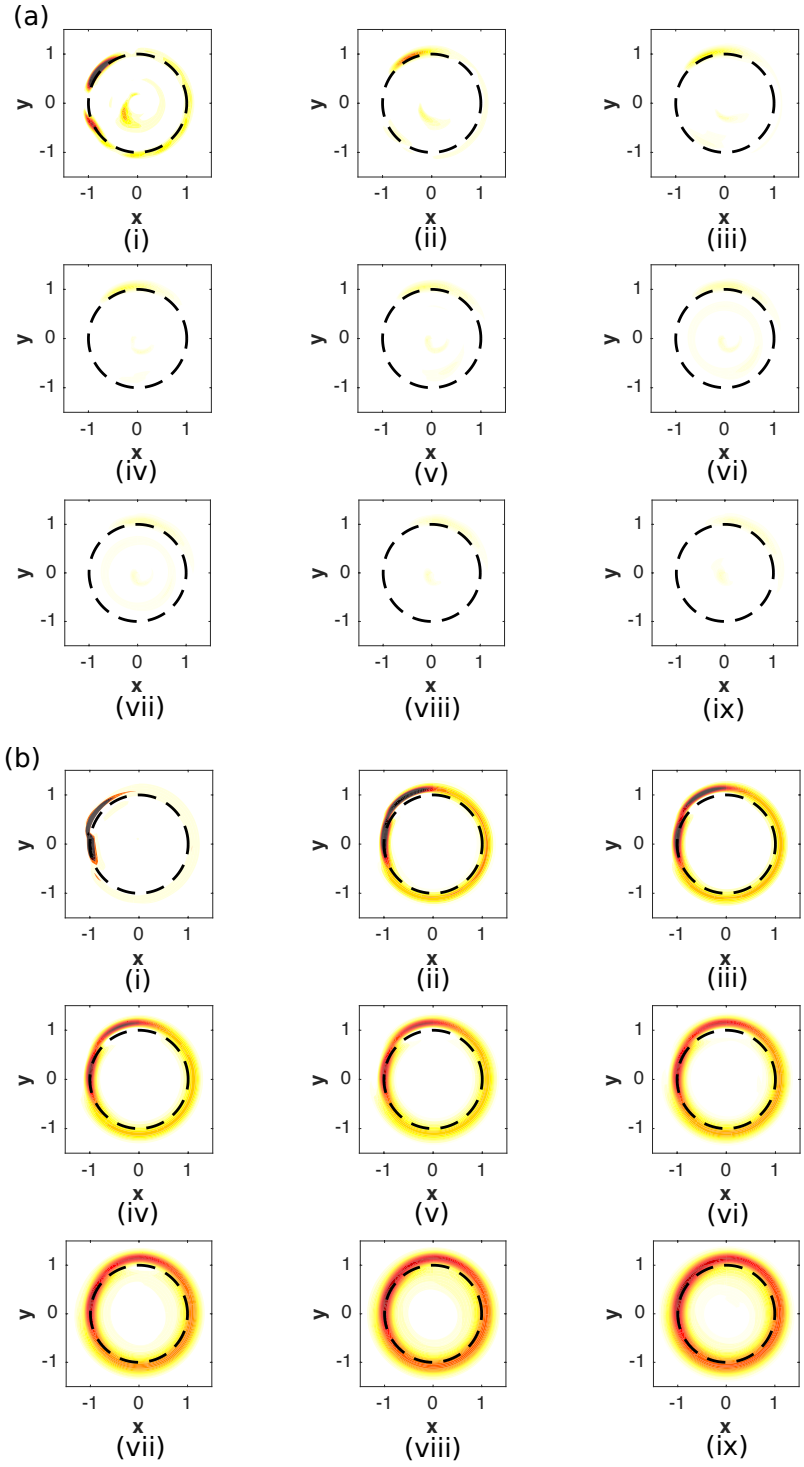

Figure 4.16: Caption and colormap as Fig. 4.14, but for N, Re1k.

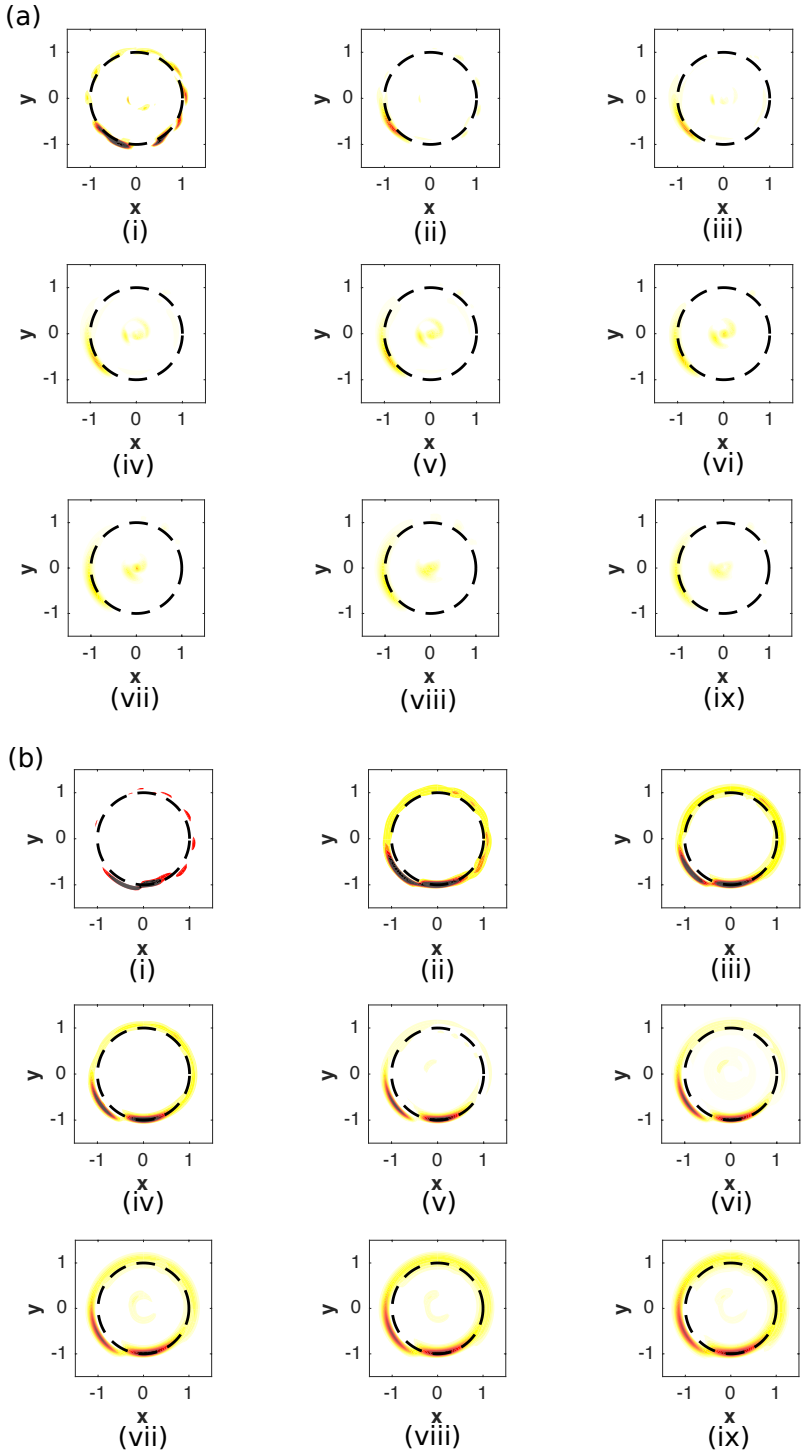

Figure 4.17: Caption and colormap as Fig. 4.14, but for N, Re2k.

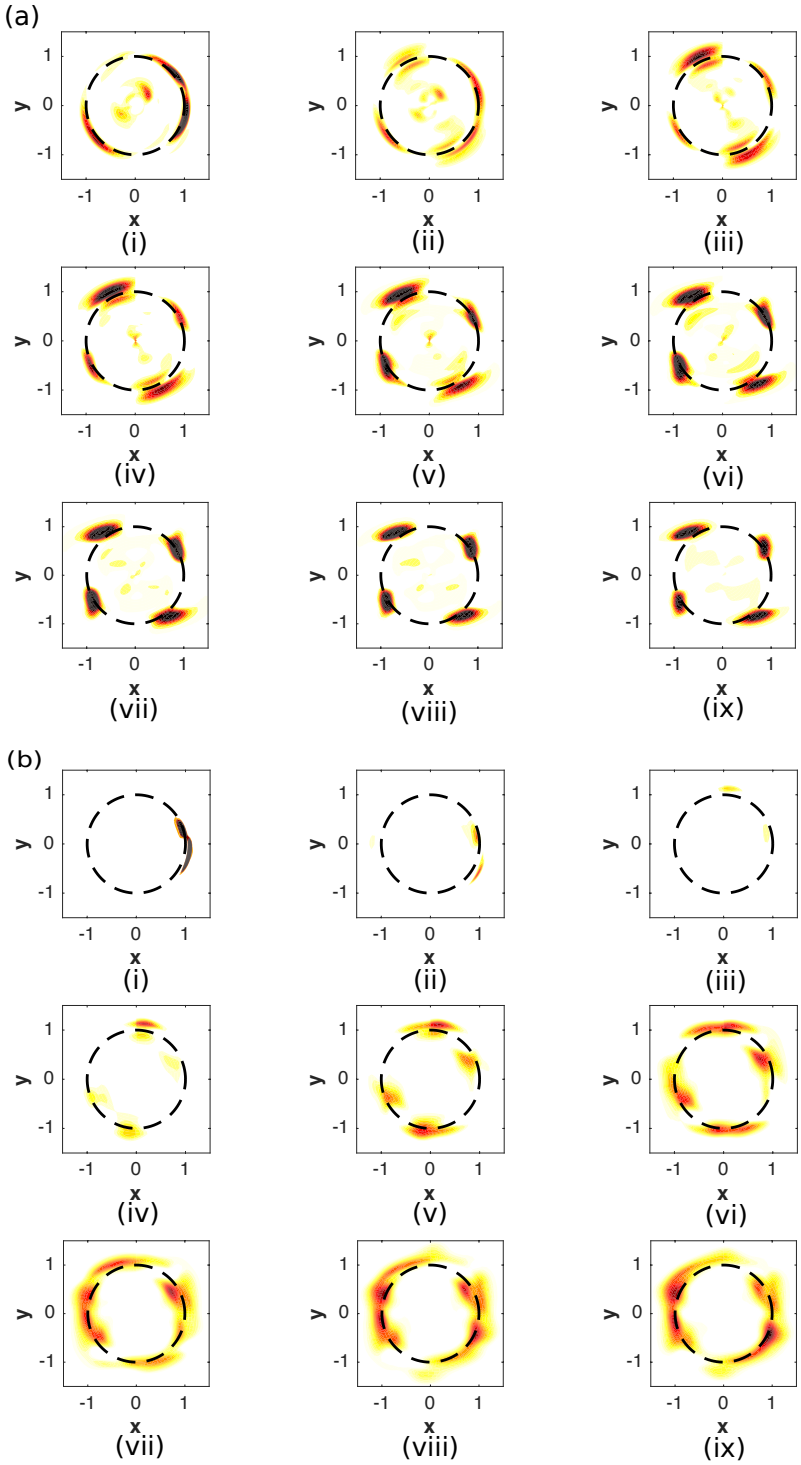

Figure 4.18: Caption and colormap as Fig. 4.14, but for WS, Re1k.

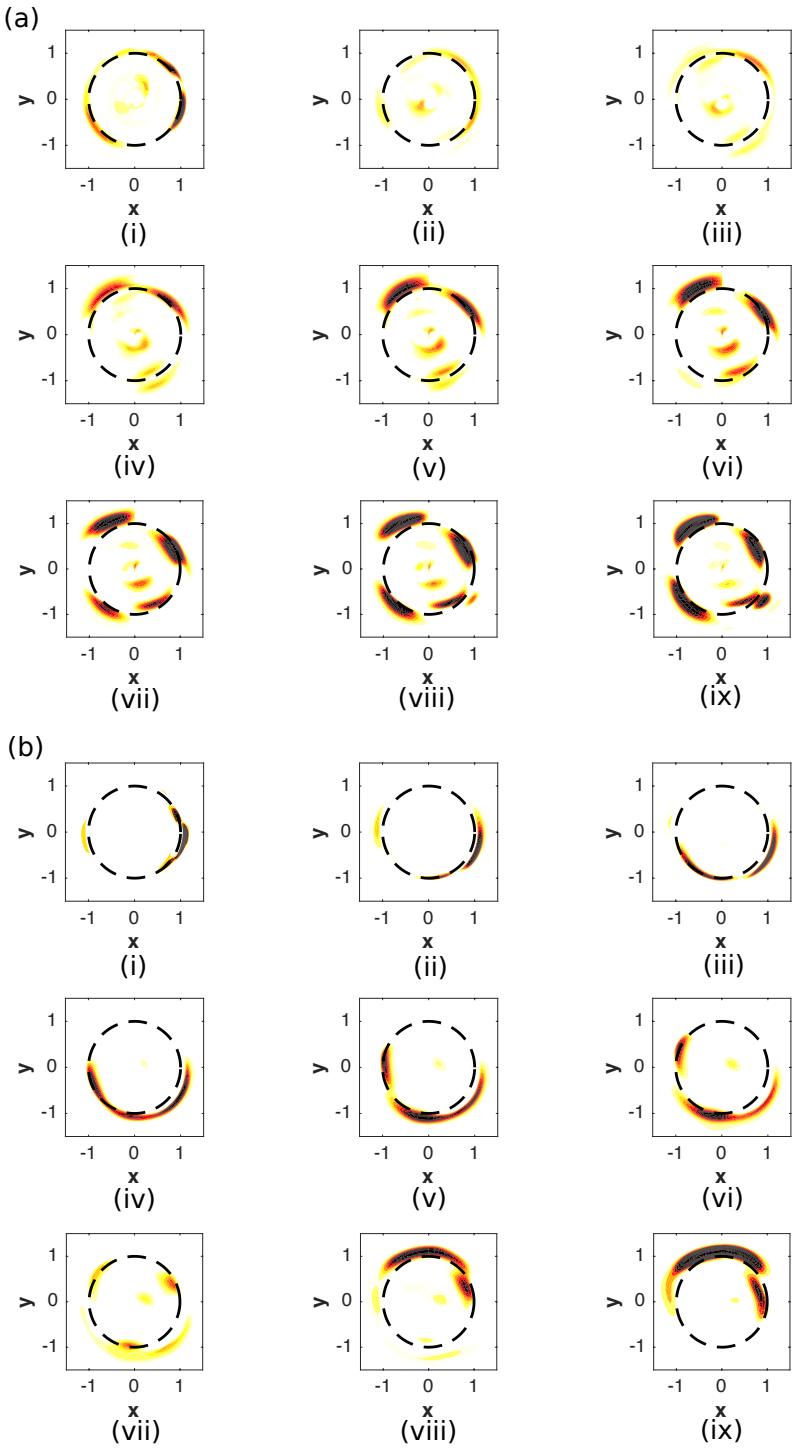

Figure 4.19: Caption and colormap as Fig. 4.14, but for SS2, Re1k.

It was found that the contribution of the tilting along radial direction for both weakly stable cases is significant compared to the tangential direction. In comparison, the contribution due to tilting by radial flow in both neutral case is quiet low and may be neglected as it is even smaller than the tangential. Meanwhile, the vorticity tilting in both directions give significant contributions to both WS, Re1k and SS2, Re1k although the radial flow contributes more than tangential.

For SS1, Re1k & SS2, Re2k cases, the tilting term in the significant direction, r as shown by Fig. 4.14(a) & Fig. 4.15(a) is clearly dominant in the left diagonal portion of the vorticity distribution. The tilting term increased from the first cycle to the end and this observation suggest that the deformation of the circular helical flow to the ellipse (as discussed before in Subsection 4.2.2) was caused by the tilting term of the streamwise vorticity, ω_z along the radial direction.

This is totally opposite to the neutral case for both Re since the tilting term is dominant all over the portion of the vorticity distribution along tangential direction as in Fig. 4.16(b)(ii - ix) & Fig. 4.17(b)(ii - ix). On the other hand, the decrease of tilting value as the flow moves downstream and since the tilting term in the first cycle occurred in just one part of the circle (refer to Fig. 4.16(b)(i) & Fig. 4.17(b)(i)) support the result of the deformation in previous discussion where the helical flow of the first cycle is not completely circle compared to others.

As for the weakly stable case, Fig. 4.18(a) shows the tilting along r-direction where it dominant in all four corners and the intensity keeps increasing towards the end. This makes the circular helical flow distorts to (almost) perfect square. The same observation was observed for the last case in Fig. 4.19(a) where the tilting term becomes more intense as the flow went downstream and it dominant in the four corners. This finally turned the circular helical to (almost) a square helical at the end. Again, the tilting term in r- direction for both strongly stable cases is mainly a distorting effect just like both in weakly stable cases.

4.2.4 Breaking Mechanism

The instabilities and breakdown of the helical vortices are crucial to the development of the wake flow and consequently impose significant impacts on downstream wind turbines in terms of fatigue loading, lifetime and acoustic noise. Better understanding of the helical vortices breaking mechanism would lead to more advanced wind turbine design and wind farm layout techniques, more reliable lifetime predictions of wind turbines and wind farms generating energy, and potentially lower wind energy prices.

From the isosurface of $|\omega|$ plotted in Fig. 4.5, the helical structure starts to break at a certain angle as the flow move downstream at a fixed threshold. In order to see where it started to break, the broken angle of the structure was determined for each cycle. The values for all core points in every cycles of all cases which less than $\frac{1}{3}|\omega|_{max}$ were set to be zero so that, it can be clearly seen where the breaking structure happened in every cycles as illustrates in Fig. 4.20 – Fig. 4.25 below. This threshold value was chosen because it gives the ideal contour plot of all cases by explicitly highlighting the breaking/non-breaking part of all cycles. Note that the contour detection is closely linked to the optimum threshold.

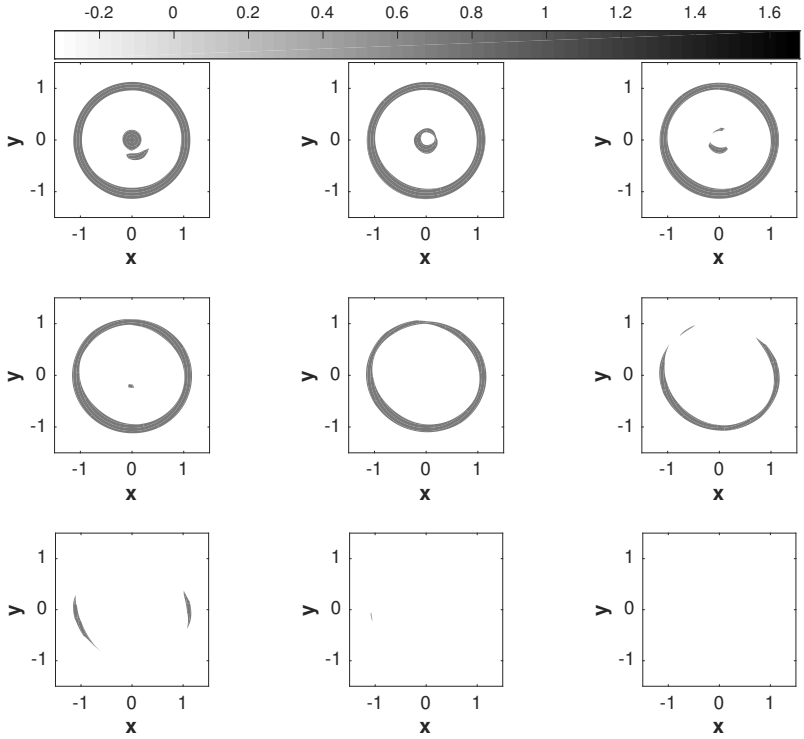

Figure 4.20: Contour of all nine cycles with the threshold more than $\frac{1}{3}|\omega|_{max}$ in SS1, Re1k.

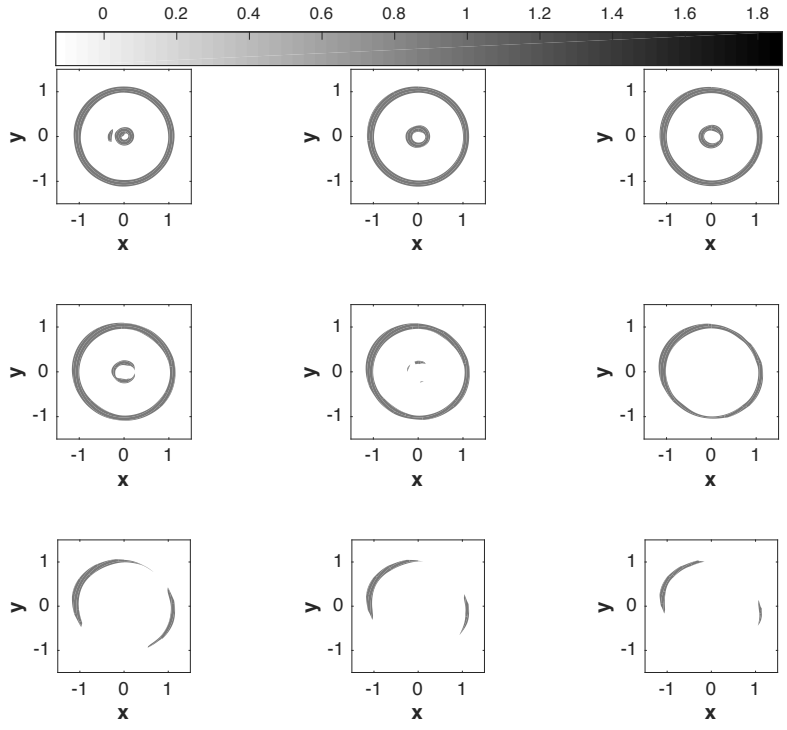

Figure 4.21: Caption as Fig. 4.20, but for SS1, Re2k.

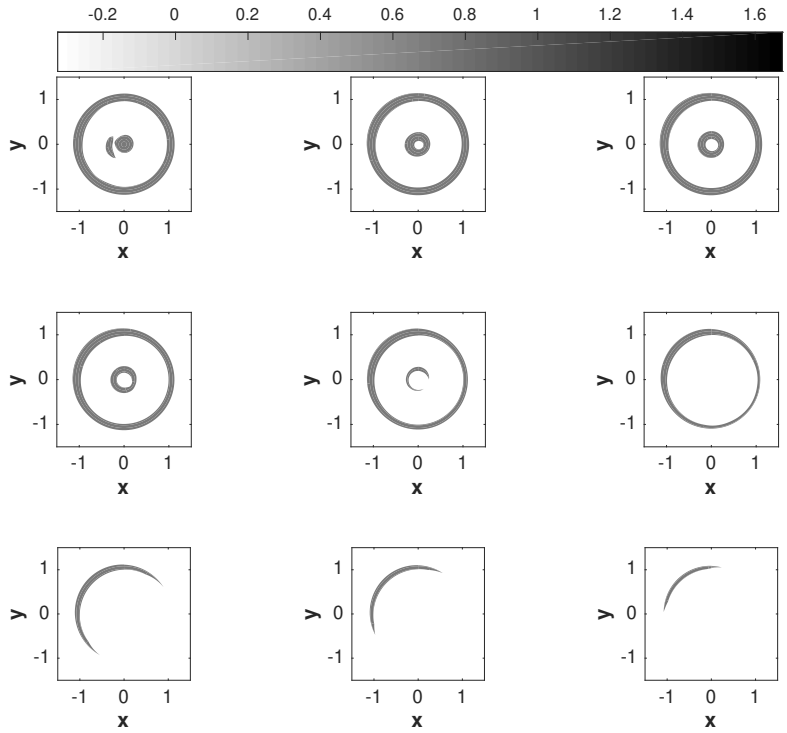

Figure 4.22: Caption as Fig. 4.20, but for N, Re1k.

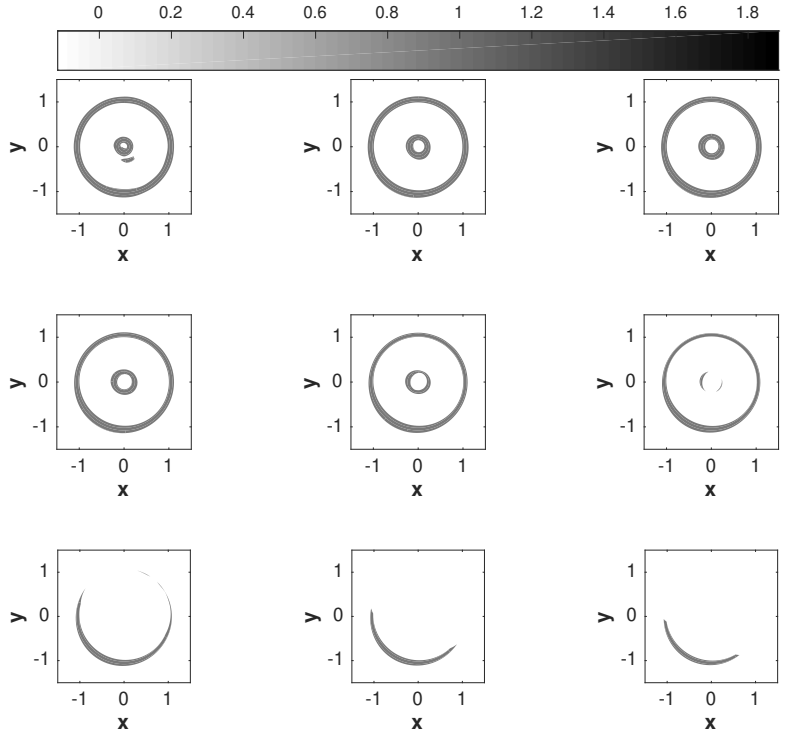

Figure 4.23: Caption as Fig. 4.20, but for N, Re2k.

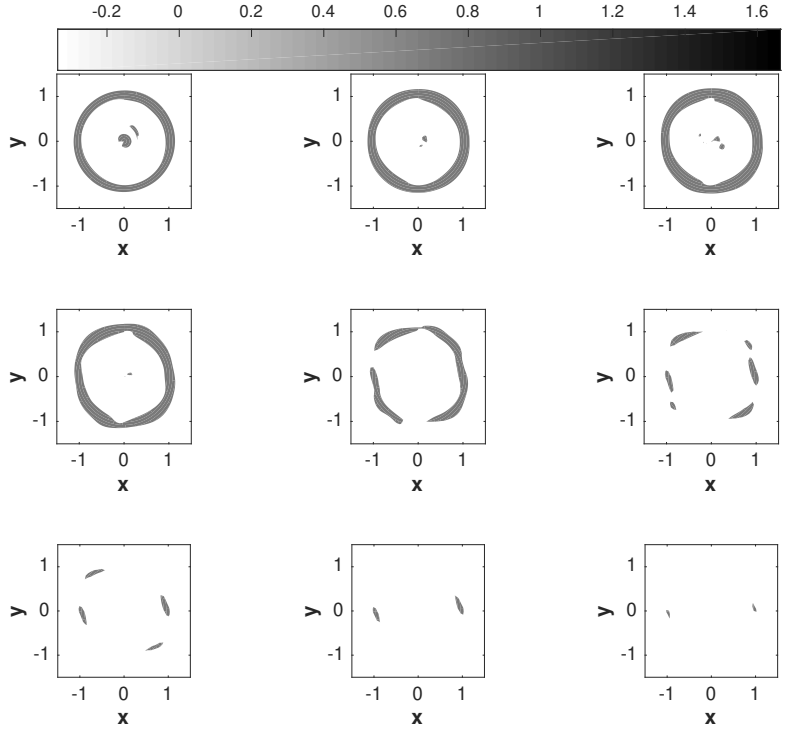

Figure 4.24: Caption as Fig. 4.20, but for WS, Re1k.

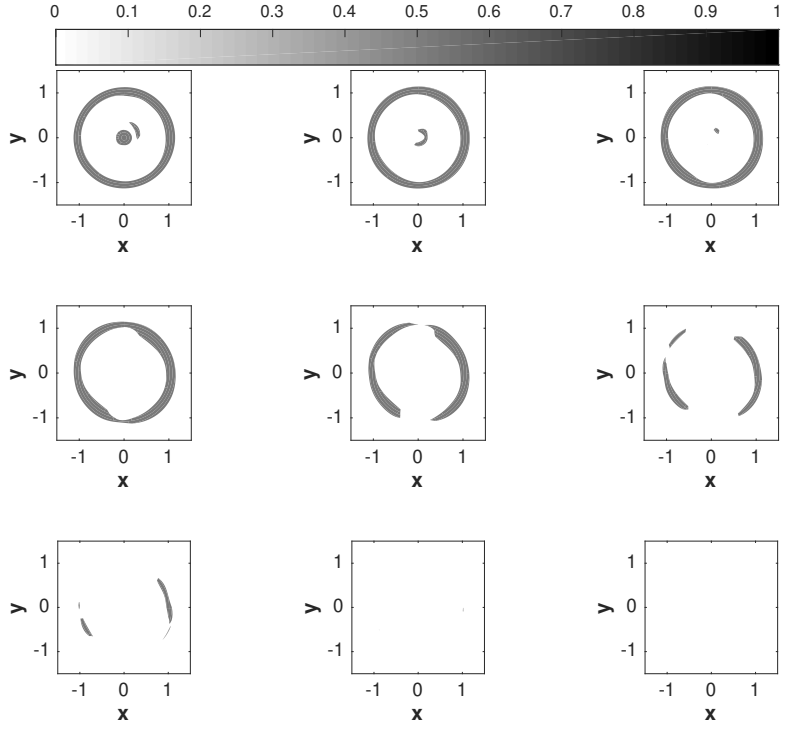

Figure 4.25: Caption as Fig. 4.20, but for SS2, Re1k.

As for the selected threshold value, the flow seems to start break up at the sixth cycles. By taking that particular cycle (refer to Fig. 4.20(f)) as example, it clearly can be seen that the helical structure breaks at θ for $\Delta\theta$ broken angle. Referring to Fig. 4.26, the two lines, P_1 and P_2 were determined by connecting the tip point of each remaining contour, (px_1, py_1) & (px_2, py_2), respectively, to the origin while the red dashed line is the horizontal line at $y = 0$. The angle of the broken structure, $\Delta\theta$ then can be calculated by

$$\Delta\theta = \tan^{-1}\left[\frac{m_2 - m_1}{1 + m_2 \cdot m_1}\right] \tag{4.2.18}$$

where m_1 and m_2 are the slops of line P_1 and P_2, respectively given by and $m_1 = \dfrac{py_1}{px_1}$ and $m_2 = \dfrac{py_2}{px_2}$.

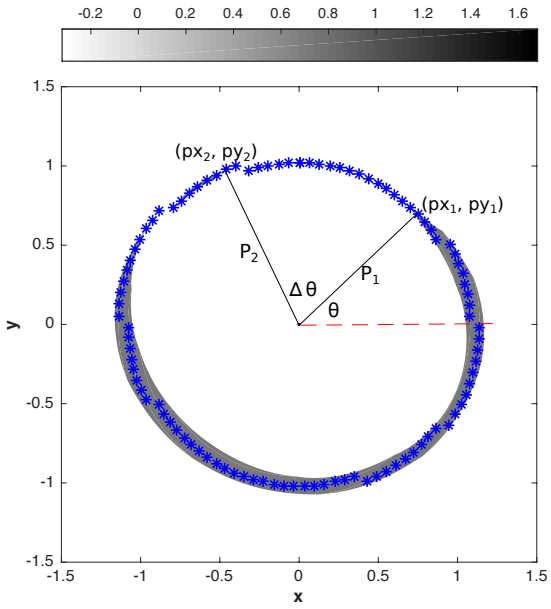

Figure 4.26: Contour of $|\omega|$ at $6.5 \leq z \leq 7.6$ (SS1, Re1k) for contour level [1.5 6] with two solid black lines P_1 and P_2 which represent the radius from point (px_1, py_1) & (px_2, py_2), respectively; and a red dashed line, $y = 0$. The blue stars are the core points from 100 angles of the cycle.

As for θ, the angle measured anticlockwise from the red dashed line with $m = 0$ which gives $\theta = \tan^{-1}(m_1) = \tan^{-1}(\dfrac{py_1}{px_1})$. Thus, Table 4.1 concludes where and how much (in π) the flow structure breaks for the last few cycles.

Atmospheric Conditions	Angles (in π)									
	$5.4 \leq z \leq 6.5$		$6.5 \leq z \leq 7.6$		$7.6 \leq z \leq 8.7$		$8.7 \leq z \leq 9.8$		$9.8 \leq z \leq 10.9$	
	θ	$\Delta\theta$	θ	$\Delta\theta$	θ	$\Delta\theta$	θ	$\Delta\theta$	θ	$\Delta\theta$
N, Re1k	-	-	-	-	1.3278π	0.8833π	1.1222π	1.2111π	0.9722π	1.3939π
N, Re2k	-	-	-	-	0.2389π 0.3833π	0.0944π 0.4389π	1.7833π	1.1833π	1.7056π	1.3389π
WS, Re1k	0.8167π 1.3889π	0.1278π 0.1944π	0.1611π 0.2667π 0.7833π 1.1111π 1.2333π 1.8167π	0.0333π 0.3167π 0.1611π 0.0556π 0.3944π 0.1222π	0.1167π 0.7778π 1.1056π 1.6944π	0.5389π 0.1833π 0.5889π 0.1944π	0.1167π 1.0722π	0.8444π 0.9056π	0.0611π 1.0556π	0.9056π 0.9444π
SS1, Re1k	-	-	0.2722π 0.7444π	0.3889π 0.1055π	0.1167π 1.2722π	0.7944π 0.6056π	1.0556π	1.9556π	0π	2π
SS1, Re2k	-	-	-	-	0.1167π 1.1222π	0.1667π 0.5278π	0.0944π 1.0722π	0.4055π 0.7167π	0.0444π 1.0556π	0.5278π 0.8277π
SS2, Re1k	0.4388π 1.3611π	0.0944π 0.2111π	0.3222π 0.8222π 1.2889π	0.3833π 0.1055π 0.3667π	0.2278π 0.9944π 1.2167π	0.7556π 0.1111π 0.6556π	0π	2π	0π	2π

Table 4.1: The breaking helical flow at θ for $\Delta\theta$ broken angle of all cases.

Overall, the flows with the atmospheric stratification condition (all cases except neutral) break at the upper and lower part of the helical structure and the remaining structure usually located at the right and left helical flow. If this result to be related to the previous analysis, the breaking part is actually the one with higher tilting vorticity values. As for a comparison, both neutral cases have a flow which only breaks at one part of the helical structure.

Considering the breaking helical flow from SS1, Re1k as an example, it shows clearly that the helical structure breaks at the sixth cycle where $6.5 \leq z \leq 7.6$, the next question raised is "At what exact location of z does the helical flow actually started to break?". An analysis of the core points at all twelve slices which made the sixth cycle were done. All the core points of the twelve considered slices together with their θ location were displayed in Fig. 4.27. Note that the same threshold, $\frac{1}{3}|\omega|_{max}$ was used for this analysis. Subsequently, all the θ values of Fig. 4.27 were plotted in Fig. 4.28(a) in order to observe the weakest $|\omega|$ which caused the breaking of the helical flow. The same things were done to the rest of the cases and shows in Fig. 4.28(b) – Fig. 4.28(f).

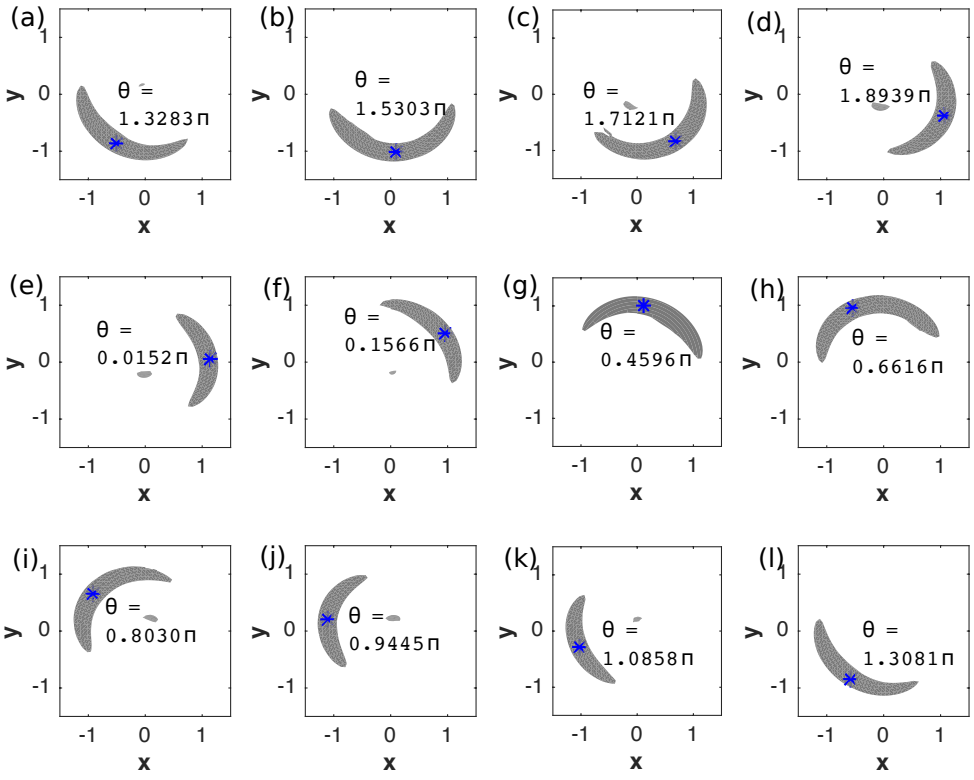

Figure 4.27: Contour of $|\omega|$ of SS1, Re1k case at:(a) $z = 6.5$, (b) $z = 6.6$, (c) $z = 6.7$, (d) $z = 6.8$, (e) $z = 6.9$, (f) $z = 7.0$, (g) $z = 7.1$, (h) $z = 7.2$, (i) $z = 7.3$, (j) $z = 7.4$, (k) $z = 7.5$, and (l) $z = 7.6$. The grey coloured region is the area where the same contour level of $|\omega|$ as Fig. 4.20 was applied while the blue star is the core point of every slices located at the stated θ in every picture, respectively.

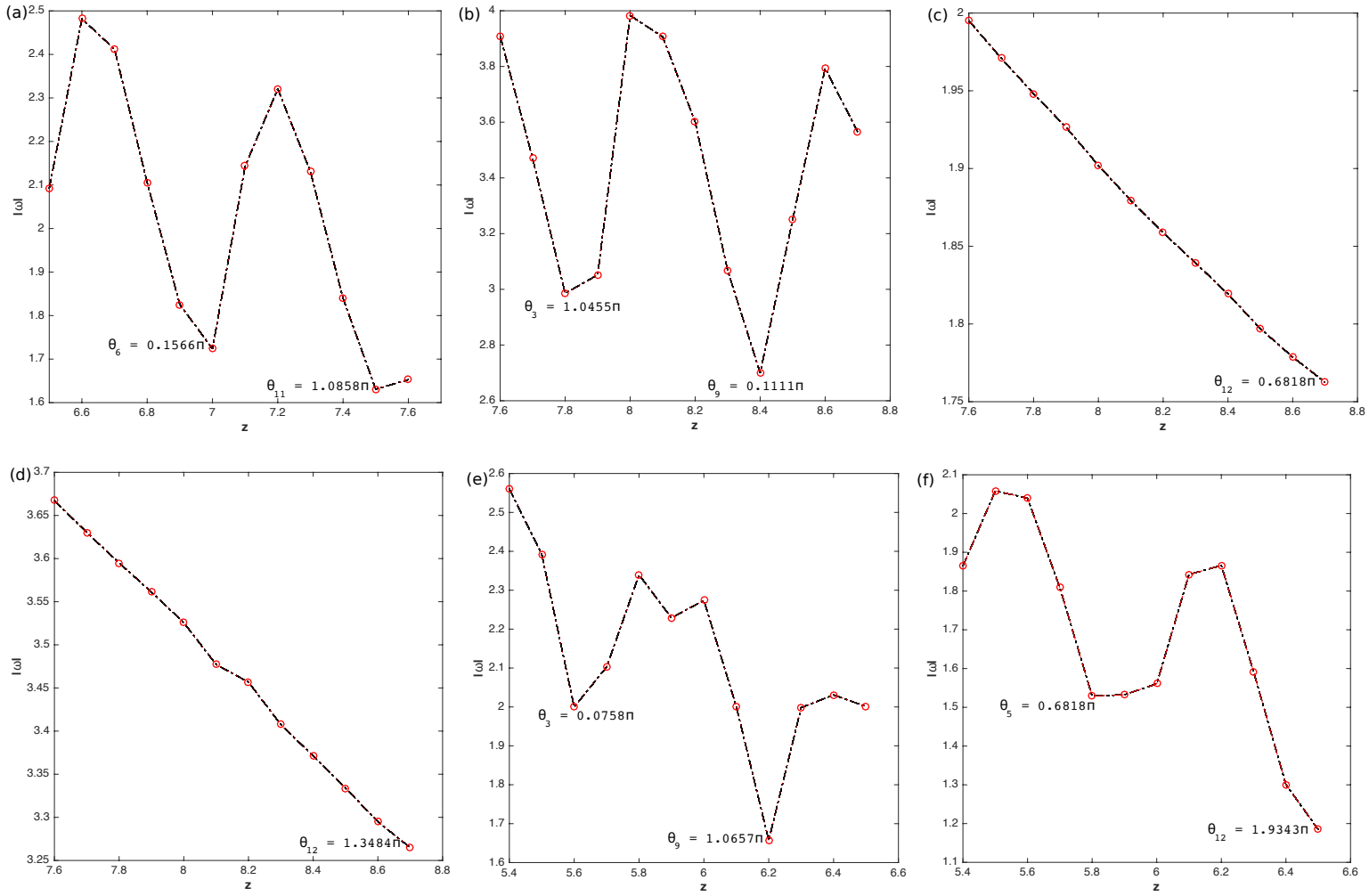

Figure 4.28: $|\omega|_{\min}$ of broken angle at: (a) $6.5 \leq z \leq 7.6$, (b) $7.6 \leq z \leq 8.7$, (c) $7.6 \leq z \leq 8.7$, (d) $7.6 \leq z \leq 8.7$, (e) $5.4 \leq z \leq 6.5$, and (f) $5.4 \leq z \leq 6.5$ of SS1, Re1k; SS1, Re2k; N, Re1k; N, Re2k; WS, Re1k; and SS2, Re1k, respectively.

As the result, Fig. 4.28(a) shows the first core point to hit a low value is at $z = 7.0$ which reveals the location of the first breaking flow started in streamwise direction. Noted that θ values provided in Fig. 4.28 represent the location of the breaking point in azimuthal direction. As for SS1, Re1k, the flow breaks at the upper hand side of helical structure where $\theta = 0.1566\pi$ at $z = 7.0$.

For the next strongly stable case 1 at Re = 2000 (Fig. 4.28(b)), the helical flow started to break later at $z = 7.8$ at $\theta = 1.0455\pi$. The earliest to break is the flow from weakly stable case WS, Re1k (Fig. 4.28(e)), where the breaking mechanism started as early as at $z = 5.6$ at $\theta = 0.0758\pi$ followed by SS2, Re1k (Fig. 4.28(f)), later at $z = 5.8$ at $\theta = 0.6818\pi$. On the other hand, the latest to break are the helical flows from both neutral case (Fig. 4.28(c & d)), to which happen at the same streamwise location, at $z = 8.7$. This might be due to the kinetic energy recovery in the streamwise direction. Basically, the kinetic energy is enhanced at lower Reynolds numbers and lessen at higher Reynolds numbers.

4.2.5 Analysis on Centroid of the Cores

The fact that the broken angle of the helical structure getting more prominent as it moves downstream concluded that the flow consequently experiences the decay of the structure. In order to explain the decay of helical flow, the Gaussian function was fitted to each centroid of the core points and precisely determined the height of the curve's peak, the position of the centre of the peak, and the width of the "bell". The centroid method takes advantage of a Gaussian function's symmetry, enabling an efficient determination of the Gaussian peak position [137, 180].

Centroid, by definition in mathematics and physics, is the centre of mass of a geometric object. The position of the core centroids (row and column) for each plane (in azimuthal direction) are calculated in pixels through a weighted average: each pixel is assigned a weight equal to its intensity (in this case, $|\omega|$). In the present study, this centroid of the system of point vortices is also often called the centre of vorticity. The following equations give the row and column of the centroid.

$$z_c = \frac{\int\int z|\omega|dzdy}{\int\int |\omega|dzdy} \quad ; \quad y_c = \frac{\int\int y|\omega|dzdy}{\int\int |\omega|dzdy} \tag{4.2.19}$$

where z_c and y_c represent the row and column coordinate of the centroid, respectively. For all cases, the threshold was set to be $\frac{1}{2}|\omega|_{max}$.

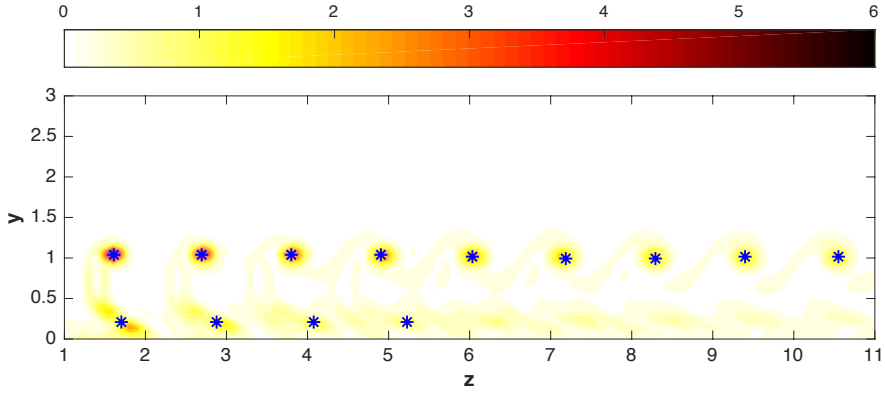

Figure 4.29: Contour of the $|\omega|$ cores from the first plane, $\theta = 1$ with the blue asterisks, indicates the centroid of each core.

Binary image of $|\omega|$ from the first azimuthal plane, $\theta = 1$ was read, and the centroids for connected components in the image were calculated using the build-in function, "regionprops" in Matlab. Then, for each of the core centroids (shown in Fig. 4.29 for SS1, Re1k), the Gaussian function was fitted to the row and column coordinate separately, as displayed in Fig. 4.30:

Mathematically, a Gaussian function (in this case, called Gaussian vortex core) is of the form:

$$f = ae^{-\frac{(x-b)^2}{2c^2}} \tag{4.2.20}$$

for arbitrary real constants a, b, and non zero c. This function can be graphed with a symmetrical bell-shaped curve centred at $x = b$, with a is the peak's height and c is the width-controller. The tails (low-amplitude portions) of the curve on both sides of the peak fall off rapidly and approach the x-axis.

As shown in Fig. 4.30, the highest peak in Fig. 4.30(b) corresponding to the one at the farthest left of the curves in Fig. 4.30(a) and the rest of the peaks follow the same sequence. The decreasing of the peaks in both figures proves the fact that the helical flow structure decays as it moves downstream. The following Fig. 4.31

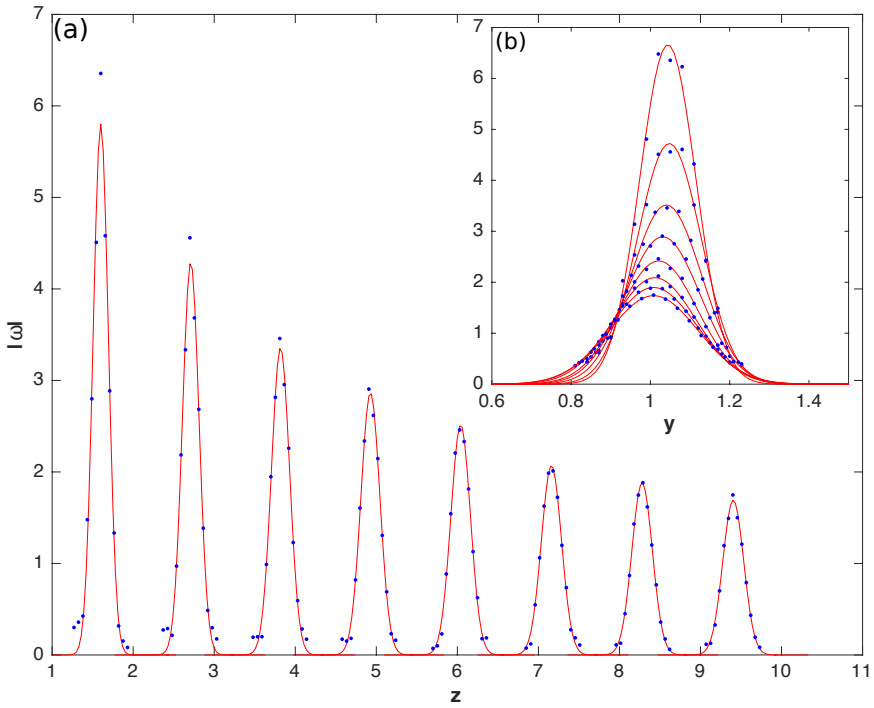

Figure 4.30: Gaussian Fit of all eight core centroids for the first plane, $\theta = 1$ in: (a) z-, and (b) y-direction of SS1, Re1k case. Red lines are the Gaussian curve, while the blue dots are the actual data.

concludes the pattern of Gaussian peaks of all cases. Several lines, such as the line of WS, Re1k, and SS2, Re1k stop earlier owing to the number of their core centroids. Due to instability of the flow, there are just two, and three core centroid found, respectively. This is one of the arguments to show that the two cases decay earlier compared to the others.

As clearly shown below in Fig. 4.31, the fastest helical flow to decay is from WS, Re1k, since it has the lowest Gaussian peak's value. Recall from the previous discussion; it is the same case in which the helical flow breaks the earliest.

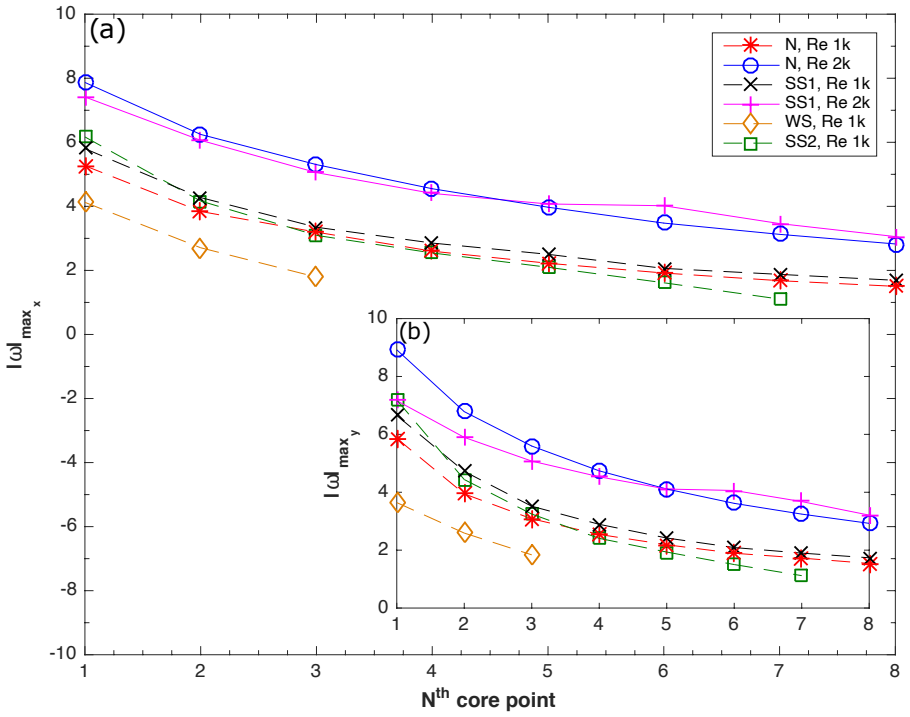

Figure 4.31: Gaussian Peaks of the first plane, $\theta = 1$ in: (a) z-, and (b) y-direction for all cases plotted from the red Gaussian fit curve in Fig. 4.30 (SS1, Re1k).

Next, the size of the core can then be determined from the same Gaussian function by calculating the full width of the Gaussian curve at half the maximum, FWHM. This is somewhat larger than σ (in this case, standard variation, $\sigma = c$) and can easily be shown to be:

$$\text{FWHM} = 2\sigma\sqrt{2\ln 2} \approx 2.355\sigma \tag{4.2.21}$$

This is illustrated in Fig. 4.32, where the first Gaussian curve in Fig. 4.30(b) is being considered as an example.

The graph of FWHM in both z- and y- direction in Fig. 4.33 describes how the size of the core continues to increase up to the last core. The difference in FWHM values in both direction indirectly tells that the shape of the core must be some sort of ellipse. The oval shape of all core from all cases remains the same as the flow goes downstream.

From the two figures, Fig. 4.31, and Fig. 4.33, the conclusion can be made that as the flow develops, the core size keeps increasing, and this leads to the next question about the force that will exert on surrounding the helical flows.

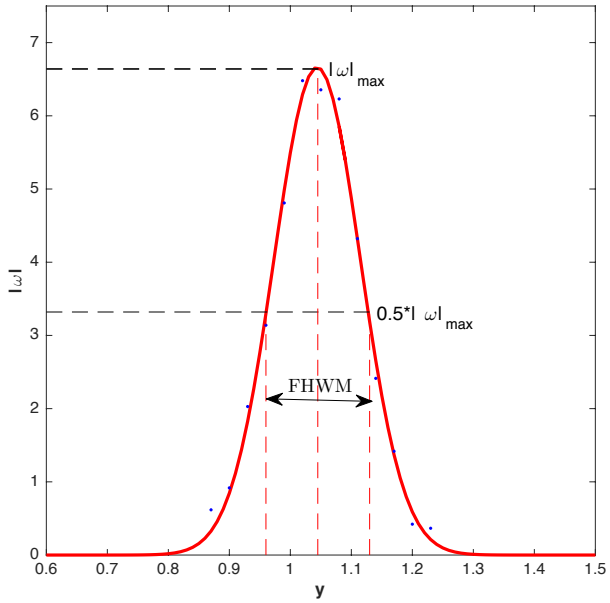

Figure 4.32: Halfwidth of a Gaussian Distribution.

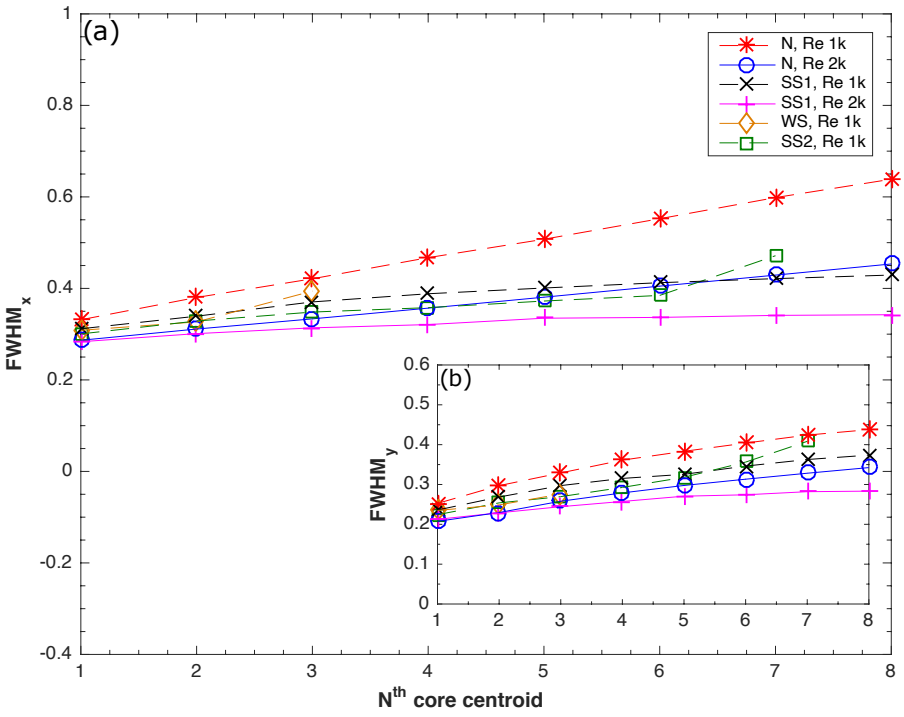

Figure 4.33: Full width at half the maximum, FWHM of the first plane, $\theta = 1$.

Another vortex property that can be analysed is the vortex core circulation strength, Γ. This analysis will answer the question mentioned before about the energy of the flow. It is widely known that the vorticity and circulation are the two primary measures of rotation in a fluid. If $|\omega|$ is a microscopic measure of rotation

from a vector field at any point in the fluid, Γ which is a scalar integral quantity, is a macroscopic measure of the rotation for a finite area of the fluid. The circulation around a closed core centroid region, C is defined as the line integral evaluated along the contour of the azimuthal component, θ of the velocity vector since it is locally tangent to the contour:

$$\Gamma = \oint_C \vec{u} \cdot d\vec{l} = \int_S (\nabla \times \vec{u}) \cdot d\vec{S} = \int \int \omega_\theta \cdot dz \cdot dy \tag{4.2.22}$$

where S is an arbitrary surface bounded by C.

Physically, circulation can be considered as the amount of force that pushes along a closed boundary [103]. Fig. 4.34 shows the decrease of the circulation strength of the vortex core, Γ from the first core towards the last. The Γ values in Fig. 4.34 were interpolated so that the circulation can be seen clearly for every z location. The same pattern happened to all the cases. There is a good agreement between the circulation and the core size (refer Fig. 4.33) as the relationship between those two quantities is inversely proportional. Again, the fastest to decay with the lowest Γ value is the helical flow from WS, Re1k followed by the second strongly stable case, SS2, before SS1, Re 1k and, SS1, Re 2k. The slowest to decay as before are from both neutral cases. Hence, this result strongly supports the previous study in Subsection 4.2.4.

Since the core trajectory of each plane was successfully derived earlier in this subsection, it is possible to build a 3D helical structure from it. Fig. 4.35 shows the construction of the helical structure from the core centroid of all planes. Note that the figure was illustrated from the strongly stable case 1 at Re = 1000.

A helix is a curve for which the tangent makes a constant angle with a fixed-line. As a space curve, it is generally given by the following parametric equations:

$$(x, y, z = r\cos\theta, r\sin\theta, h\theta) \tag{4.2.23}$$

where $r > 0$ is the radius of the helix, $\theta \in [0, 2\pi])$ is the angle of the point (x, y, z) makes with the x-axis (projected to the xy-plane) and h is a constant where $2\pi h$ gives the separation of the helix loops.

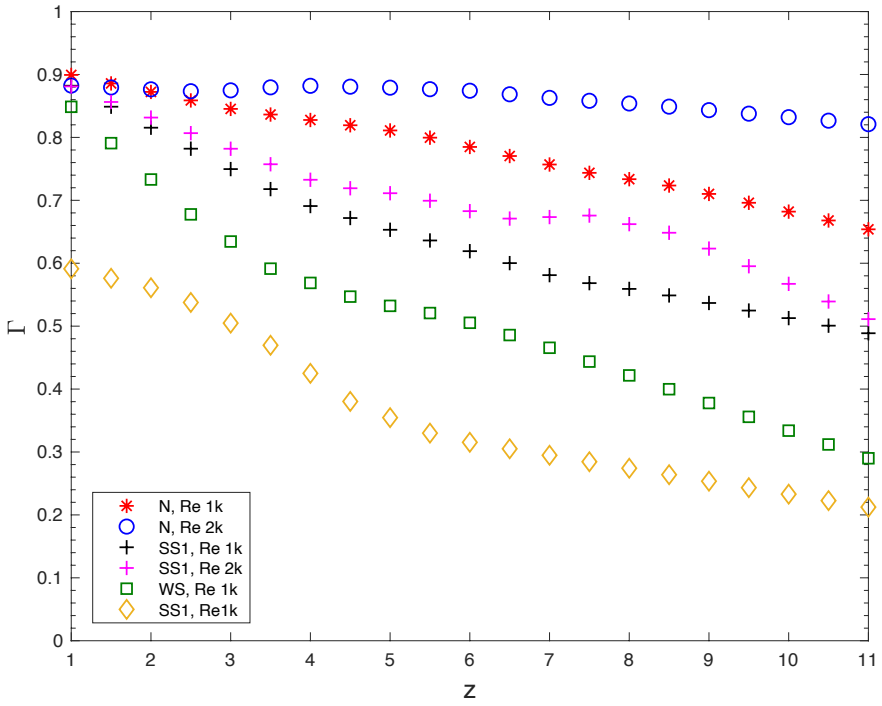

Figure 4.34: The decay of the vortex core circulation, Γ of the first plane, $\theta = 1$ for all cases.

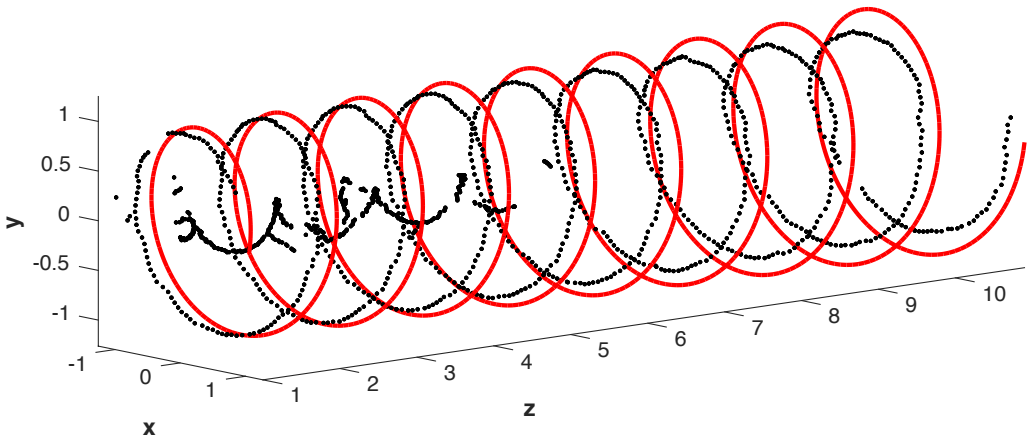

Figure 4.35: Helical structure of $|\omega|$ from all core centroids in SS1, Re1k indicated by the black dots, and the red line is the one constructed from the best fit.

Earlier in Subsection 4.2.2, a discussion on how the flow went through a deformation from a circular helix to an ellipse has been carried out, and this gives the idea that the changes of the radius depend on its angle as it moves downstream. Thus, a simple linear regression such that the best fit line (in a least-squares sense)

of

$$r = a\theta + b \tag{4.2.24}$$

with constants, a, b was performed to the y_c of all planes with the helix axis in the z-direction. The parameter r for each case are listed in Table 4.2, together with the norm of residual, Norm$_r$. In order to signify the "goodness" of fit, Norm$_r$ was used. This term was calculated as the square-root of the sum of squares of residuals:

$$\text{Norm}_r = \sqrt{\sum_i (R_i - r_i)^2} = \sqrt{\sum_i (e_i)^2} = \|e\| \tag{4.2.25}$$

where R_i is the radius from the input dataset, r_i is a fitted R value and $e_i = R_i - r_i$ is the residuals.

The Norm$_r$ ranges between 0 and infinity, with smaller numbers indicating better fits and zero indicating a perfect fit. Hence, it can be concluded that the best fitted helical flow is the one from N, Re2k while, the worse one is from SS1, Re1k. Note that this analysis does not aim for the discussion on the distortion of the helical flow. In the near field, the radius of helical wave is nearly constant, so it is not a bad approximation to fit the core trajectory with a constant r. Thus, the presented results were obtained by fitting the flows with a non-uniform radius to the circular helix (with fixed-radius).

Atmospheric Conditions	Radius, $r(\theta)$	Norm of residual, Norm$_r$
N, Re1k	$-0.0001\theta + 1.0577$	0.2247
N, Re2k	$0.0001\theta + 1.0510$	0.1200
WS, Re1k	$0.0021\theta + 1.0511$	0.6174
SS1, Re1k	$0.0068\theta + 1.0593$	1.1581
SS1, Re2k	$0.0024\theta + 1.0568$	0.8535
SS2, Re1k	$0.0046\theta + 1.0516$	1.1327

Table 4.2: Parameter, r, and norm of residual, Norm$_r$ of the helical for all cases.

A 3D helix formed from Eq. 4.2.23 was then plotted on the same figure (Fig. 4.35) as the core centroids helical structure to illustrate how they match each other.

4.3 Power Spectra Analysis

Before the modal analysis of the flow was employed in the next chapter (Chapter 5), a general understanding of the flow, such as the signal distribution, is needed. The impact of fluctuating velocity flow on the Fast Fourier Transform (FFT) of the signals in the frequency domain was studied. Power Spectral Density (PSD) was used to provide information about how the energy of the flow signal is distributed concerning the frequency. The goal of spectral estimation is to describe the distribution (over frequency) of the power contained in the flow signal, based on a finite set of data. The input from each case is based on the number of time steps, t and time separation, Δt as listed in Table 3.2 in Section 3.2.

A time series model generally reflects the fact that observations close together in time will be more closely related than observations further apart. One of the uses of a time series model is to describe and explain the general characteristics of the series. Time series analysis in the spectral analysis was used to examine the cyclic behaviour since the time series, x_t can be expressed as a combination of cosine (or sine) waves with differing periods, T (how long it takes to complete a full cycle) and amplitudes, A (maximum/minimum value during the cycle), i.e. $x_t = A\cos(2\pi\omega t + \phi)$ with $\omega = \dfrac{1}{T}$ is the frequency which controls how rapidly the cosine (or sine) curve oscillates, and ϕ represents the phase as it determines the starting point, in angle degrees, for the cosine wave.

The power spectrum of a time series defines the energy distribution into frequency components composing the flow signal [134]. Any physical signal can be decomposed down into a several discrete frequencies, or a spectrum of frequencies over a constant range, according to Fourier analysis. The statistical average of a given signal (or any kind of signal), including noise, is called its spectrum, as analysed in terms of its frequency content. More commonly used is the PSD or simply referred to as power spectrum, which applies to all-time existing signals, or over a sufficiently long period of time, especially concerning the duration of a measurement, that it could also have exceeded an infinite time interval.

In practice, one can only get an estimation of the PSD of the process, and hence, in the present study, the spectral estimator called periodogram was applied. It is

used for the identification of the dominant periods or frequencies of a time series. It is comparable to the Fourier transform but is optimized for various shapes in periodic signals and for uneven time-sampled data. The periodogram for real-valued, h_j, of evenly spaced data, Δt is defined by

$$\hat{P}(f) = \frac{2\Delta t}{N} \left| \sum_{j=0}^{N-1} h_j e^{-i2\pi j \Delta t f} \right|^2 \tag{4.3.1}$$

i is the imaginary unit.

However, it should never be calculated explicitly from Eq. 4.3.1 since it is much faster and mathematically equivalent to use the FFT, which is an intelligent, fast, and efficient ($\sim N \log N$) algorithm used to compute the Discrete Fourier Transform (DFT).

$$X_k = \sum_{j=0}^{M-1} e^{-i2\pi kj}, \qquad k = 0, 1, \ldots, M-1 \tag{4.3.2}$$

for any array of M (in general complex) values of $x_0, x_1, \ldots, x_{M-1}$

The results X_k are in general complex (even if x_j are real). Putting $M = N$ and $x_j = h_j$, gives

$$\hat{P}(f_k) = \frac{2\Delta t}{N} |X_k|^2, \qquad k = 0, 1, \ldots, N-1 \tag{4.3.3}$$

where $f_k = \dfrac{k}{\Delta t}$ is the discrete frequencies

For a better understanding of the flow behaviour, the time series data from the fluctuating streamwise velocity, $u'(t)$ at the spatial location $(x, y) = (-1.04, -1.04)$ of three different z locations which are z= 6, 8.5 & 11 where the core of helical flow located was examined. The time series of u' at the monitored point, as can be observed in Fig. 4.36(above) shows a periodic state of asymptotic finite-amplitude. Such oscillations period is measured from the data by using the PSD as shown in Fig. 4.36(below).

The signal power spectrum is useful when analysing the power distribution contained in a signal. Note that Fig. 4.36(below) are the power of signals in the range of 0-3.125 Hz for all cases except 0-1.25 Hz for both strongly stable cases. The PSD units depend on the units of the signal and the sample rate. For this study, the PSD units would be dB/Hz. Decibels, dB is always a comparison between two power levels as it is a unit measurement used to express the ratio of one value of a

power to another on a logarithmic scale, the logarithmic quantity being called the power level. A better definition of decibels is $10\log_{10}(P/P_0)$, where P and P_0 is the measured power and reference power, respectively. This explains the presence of negative values and is perfectly normal.

A steady time variation of all cases in Fig. 4.36(a, b, c, d, & f) show that the flow is well sustained before it slowly reduced in magnitude at the end of the domain. This is, however different for the weakly stable case. In the time series figure of WS, Re1k (refer to Fig. 4.36(e)), it shows a fluctuating time variation where the flow started with the lowest magnitude at $z = 6$ then increased to the highest magnitude before it dropped at $z = 11$. This is probably due to the instability of the flow.

It can also be seen from the power spectra density figure, portrayed by Fig. 4.36(a) & Fig. 4.36(b) that the amount of energy for both the neutral case without the atmospheric stratification (N, Re1k & N, Re2k) are less than those with it (Fig. 4.36(c) – Fig. 4.36(f)). This means that the fluctuations of the streamwise component of velocity for the wake flow where the atmosphere is stratified gave a fluid flow with a higher turbulence level.

The fundamental properties of FFT are the inability to compute the growth rates, as well as the predetermination of frequency regardless of data content. In addition, if the dataset covers less than one corresponding period, FFT failed to capture a specific frequency. Moreover, if the data are non-periodic, the decay of temporal FFT energies is slow [80]. Hence for these reasons, there is the need for the two modal analysis techniques to be carried out in the next Chapter 5 & Chapter 6 since their global solutions may provide more valuable information and better result.

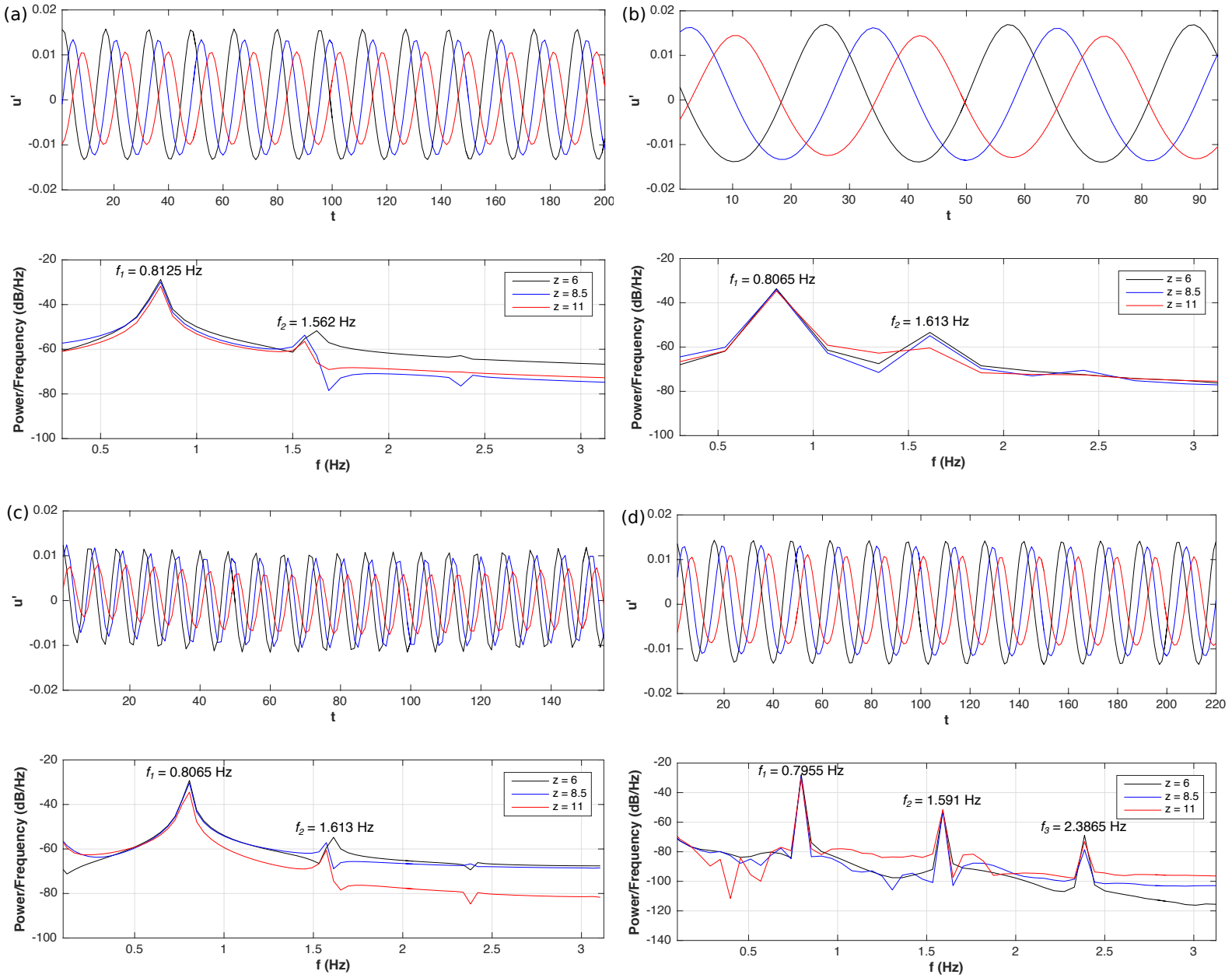
(a)
u'
t
Power/Frequency (dB/Hz)
f_1 = 0.8125 Hz
f_2 = 1.562 Hz
z = 6
z = 8.5
z = 11
f (Hz)
(b)
u'
t
Power/Frequency (dB/Hz)
f_1 = 0.8065 Hz
f_2 = 1.613 Hz
z = 6
z = 8.5
z = 11
f (Hz)
(c)
u'
t
Power/Frequency (dB/Hz)
f_1 = 0.8065 Hz
f_2 = 1.613 Hz
z = 6
z = 8.5
z = 11
f (Hz)
(d)
u'
t
Power/Frequency (dB/Hz)
f_1 = 0.7955 Hz
f_2 = 1.591 Hz
f_3 = 2.3865 Hz
z = 6
z = 8.5
z = 11
f (Hz)

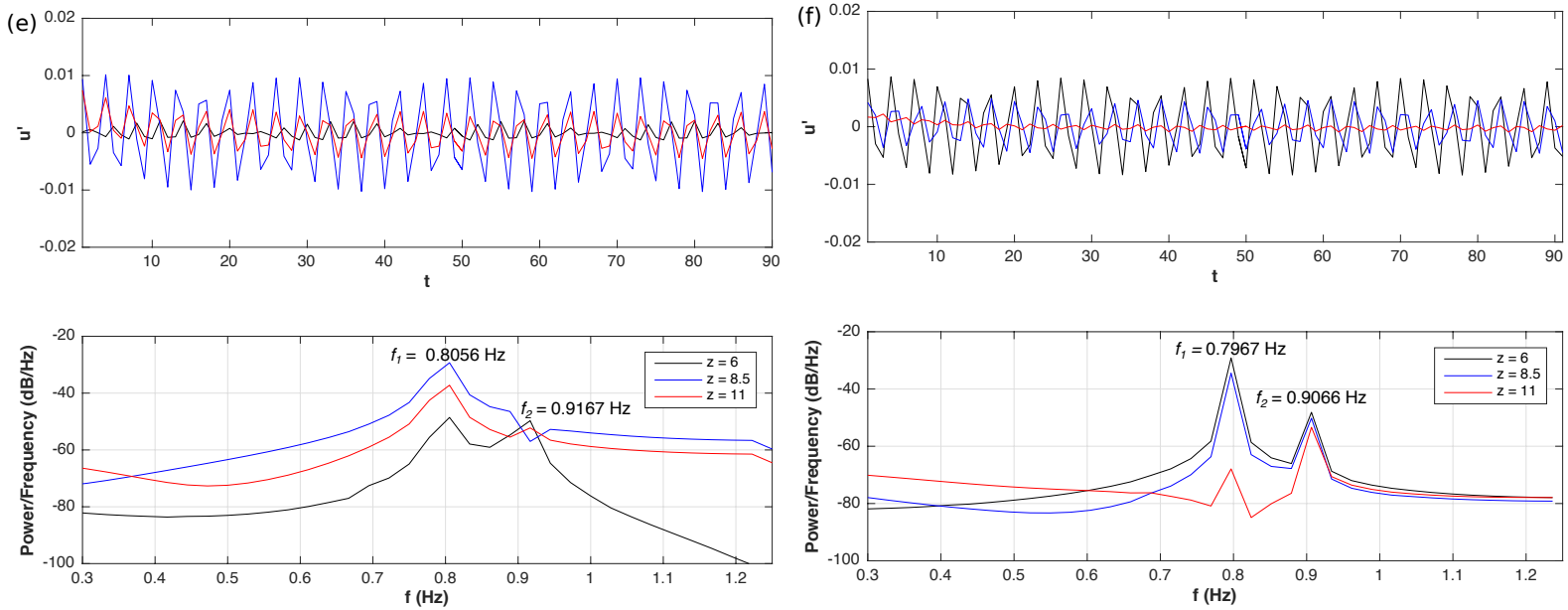

Figure 4.36: Time Series (above) and Power Spectra Density (below) of u' for (a) N, Re1k, (b) N, Re2k, (c) SS1, Re1k, (d) SS1, Re2k, (e) WS, Re1k, and (f) SS2, Re1k.

4.4 Chapter Summary

In this chapter, the instantaneous helical wake behind a rotating blade of the six cases from three different atmospheric stratification conditions has been investigated. A few of vortex identification techniques were presented, and the decision to carry out the following study using the vorticity magnitude, $|\omega|$ was made. There is some interesting characteristics of the wake flow identified, such as its deformation/distortion, vorticity dynamics, vortex breakdown, and the centroid of the cores. All these analyses were focused only on the tip vortices. In the study of the deformation, the RMS values of the tip vortices were calculated to see how non-circular the helical flows are. Next, as for the vorticity dynamics, the vorticity transportation equation was being considered, but only the tilting term was highlighted and being discussed in detail. This is because the deformation of the circular helical seems to happen due to the tilting of the flow. Instead of study the velocity field in the fixed Cartesian frame, this work study the vorticity tilting in the rotating Cartesian frame as it gives a better representation of the vector field as justified in [12]. As the wake flow will eventually go through the breaking of its structure, the location of the breaking was determined at both streamwise and angular directions. The analysis of the core centroids started with Gaussian fit to find the FWHM and the circulation, Γ of the core in both z and y directions. The FWHM values gave the size of the cores while Γ granted the energy of the core. Later, 3D helical structure was built up using the position of core centroid and made it is possible to fit all different helix curves from all the cases into one single general equation that varies in radius. It was concluded from the final section of this chapter that the results from power spectra analysis of the instantaneous flow conclude that in the stable case, turbulence is stronger than in the neutral case. Hence in the next chapter, the first modal decomposition method called POD will be employed to the DNS data of a rotating blade before the analysis with some discussion will be presented. This will validate the current findings.

Chapter 5

Proper Orthogonal Decomposition of the Helical Wake

This chapter begins with Section 5.1 where a brief explanation of the preparation of the input datasets before it can be used in both techniques was presented. Next, the result from both POD methods will be reported in three sections, which the comparison between POD modes gained from the individual velocity POD and all velocity components POD in Section 5.2. the analysis of POD in the near field presents in Section 5.3, followed by the study of temperature POD, PODT mode in Section 5.4. The next POD analysis will be on the far wake for Neutral Re1k case provided in Section 5.5. This chapter ends with a brief conclusion in Section 5.6.

In each case for both modal decomposition analyses, a set of $t-1$ snapshots, N (refer to Table 3.2 in Section 3.2) of the full three-dimensional temperature and velocity field, $\mathbf{u}(z,x,y)$ equispaced in space, $\Delta z = \Delta x = \Delta y = 0.1$ where z,x,y are the streamwise, spanwise and vertical components, respectively was used in this work. The datasets are also equispaced in time with an interval of Δt (Table 3.2 in Chapter 3). Note that the present study excluded the analysis of pressure field, p as to the author's knowledge, there are not many interesting findings extracted from it since the pressure field coupled very well with the velocity field. By the same token, Towne et al. exclusively visualized all the modes in [11] using the pressure field, instead.

5.1 Preprocessing of the Datasets

Before any modal analysis techniques were employed to the input dataset, the velocity field was preprocessed. Since the incompressible Navier-Stokes solvers were adapted to a non-uniform mesh and the modal analysis methods should be done to the equispaced datasets [125, 126, 130], an interpolation was first adopted to the raw dataset. Before that, the raw dataset in the cylindrical system was converted to the Cartesian. It is also important for both techniques to apply the algorithms on the fluctuating data where the mean should be removed so that the frequency base will be uniformed, similar to the one obtained by the Fourier transform [80]. Otherwise, the decomposition on the raw data without subtracting the mean will be resulting to a non-uniform frequency content.

5.1.1 Interpolation of the Raw Datasets

For the first step of data preprocessing, the raw datasets, which are in a cylindrical coordinate system, was transformed into Cartesian before the interpolation was done. A built-in function in MATLAB called "griddata" function interpolates scattered data values on a plane or a sphere to a regular grid, an irregular grid, a specified set of interpolates, or scattered data points. It was used to fit the velocity field, $\mathbf{u}(z_0, x_0, y_0)$ where z_0, x_0, y_0 are the streamwise, spanwise, and vertical components, respectively; to the data in the non-uniformly spaced vectors, (z_0, x_0, y_0). It interpolates the velocity field at the points specified by a uniform grid of $-2 < x < 2$ and $-2 < y < 2$, which was produced by "meshgrid" in order to create $\mathbf{u}(z, x, y)$. The analysis of both modal analysis methods was applied to sub-domains of $6 < z < 11$.

5.1.2 Mean Subtraction

The time-mean velocity, $\bar{\mathbf{u}}(x)$ described here, is the average of the flow passing a point over a duration of time. It is simply known as the time-average flow fields given by

$$\bar{\mathbf{u}}(x) = \lim_{T\to\infty} \left(\frac{1}{T} \int_0^T \mathbf{u}(x,t)dt \right) \tag{5.1.1}$$

where $\mathbf{u}(x, t)$ is the velocity flow field.

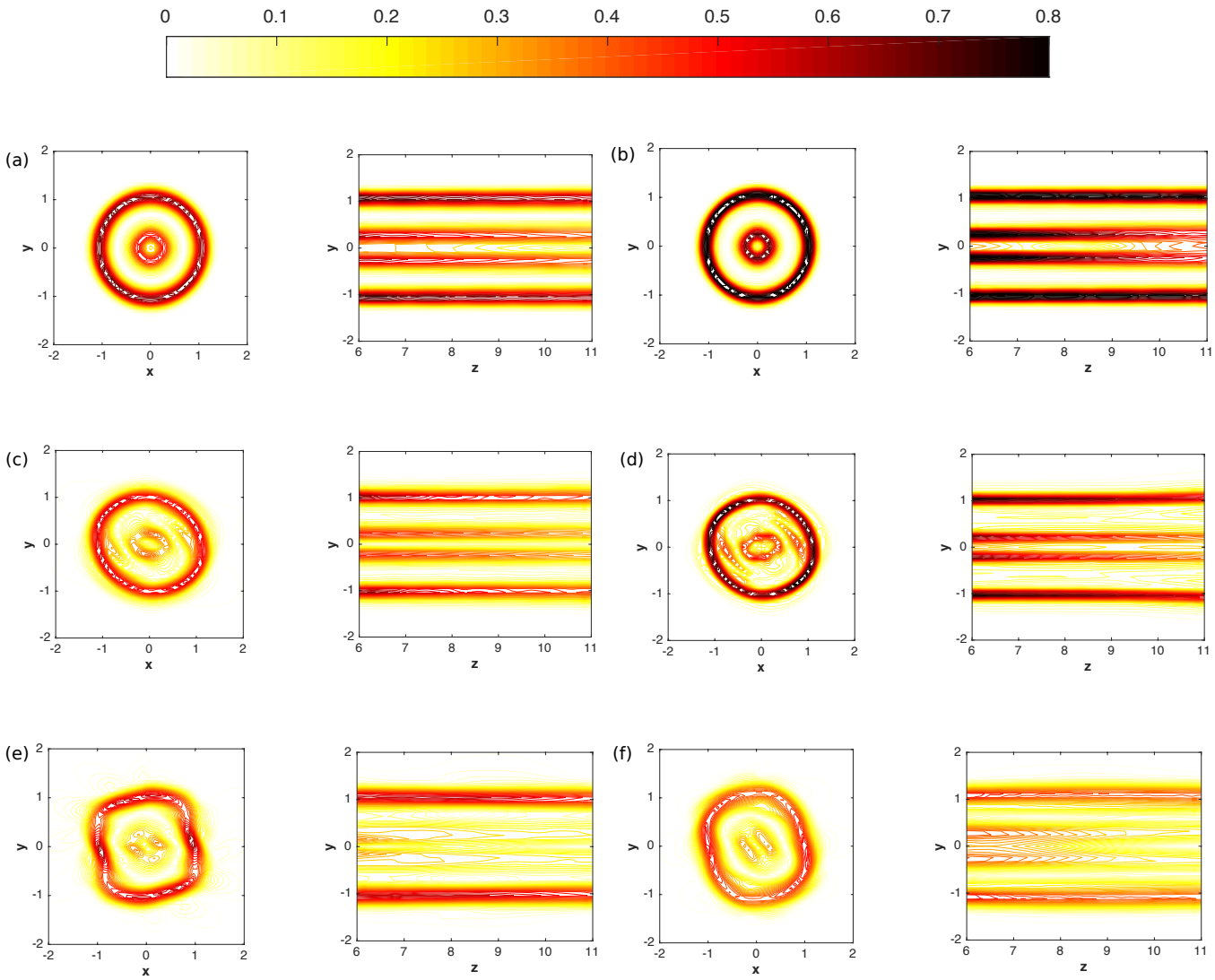

Figure 5.1: Contour plot of $|\omega|$ from time mean velocity field for (a) N, Re1k, (b) N, Re2k, (c) SS1, Re1k, (d) SS1, Re2k, (e) WS, Re1k, and (f) SS2, Re1k in xy-cut at $z = 8.5$ (left) and zy-cut at $x = 0$ (right).

Fig. 5.1 provides the contour plot of $|\omega|$ from Eq. 4.2.12 constructed from $\bar{\mathbf{u}}(x)$ of each case. If this mean flow is not being removed before the modal decomposition techniques were employed, it then will come out as the first mode with the highest energy level at frequency $f = 0$ Hz. This so-called mean mode does not relevant to the total flow, or it decays very fast, not being of much importance in the long term.

Afterwards, the mean-subtracted data which also known as the fluctuating data, $\mathbf{u}^{'}(x,t)$ was defined as

$$\mathbf{u}^{'}(x,t) = \mathbf{u}(x,t) - \bar{\mathbf{u}}(x) \in \Re^n, \quad t = t_1, t_2, \cdots, t_m. \tag{5.1.2}$$

The snapshots of the flow field then were stacked in terms of a collection of column vectors $\mathbf{u}^{'}(x,t)$ as in Eq. 3.4.9. That is, a collection of finite-dimensional data vectors that represent the flow field was considered. For a more detailed discussion on the subtraction of the data mean including its implications toward the modal decomposition methods, [80] can be referred.

5.2 Separated versus Combined Velocity-based POD

A velocity-based POD analysis can be performed either combining all the velocity components or separately [86, 157]. Hereafter, the velocity-based POD means that all velocity components (u, v, w) are used as input (see Eq. 3.4.9) to do the POD analysis, whereas the u-, v- or w-based POD means that either u, v or w is used as the input.

In order to create a hierarchy of coherent structures based on the time-averaged spatial correlation tensor, the eigenvalues decomposition was carried out by the POD algorithm. The total turbulence kinetic energy in the vector space is equivalent to the summation of the eigenvalues and can be presented in either cumulative or normalized form. The energy content in each individual POD mode, Er_n, relative to the total resolved energy is then given by

$$Er_n = \frac{\lambda_n}{\sum_{j=1}^{N} \lambda_j} \tag{5.2.1}$$

While the cumulative energy provides a direct measure of the rate of energy convergence of the POD modes with n and is given by

$$Ec_n = \frac{\sum_{j=1}^{n} \lambda_j}{\sum_{j=1}^{N} \lambda_j} \tag{5.2.2}$$

For this particular section, the entire domain $-3 < z < 60$ was separated into two sub-domains which are $6 < z_n < 11$ and $21 < z_f < 26$ for near and far wake region, respectively, while $-2 < x < 2$ and $-2 < y < 2$ is the same for both regions. The purpose of having separated sub-domains is to observe the flow difference in two different regions besides to maximize the accuracy of mode shape while minimizing the computational time. Fig. 5.2 presents both the relative energy content Er and the cumulative energy Ec of the POD modes for u-, v-, w- and velocity-based POD in near and far wake.

It clearly shows that combining all velocity components in the near wake leads to the same results as obtained with the individual velocity component. However, this does not really apply to the far wake case. This is consistent with [86, 157], which suggested that the POD analysis using only one velocity component is appropriate for investigating the near wake.

Even so, the u-, v-, w-based POD are not suitable to be used in this work because the study of $|\omega|$ needs all the velocity components to go through the decomposition method together. For this reason, note that from now on all the POD analysis will be carried out using the velocity-based POD.

5.3 POD Analysis of the Results in the Near-field Region

The wakes can be divided into near and far wake regions. The near wake is the area just downstream of the blade, where the flow field is determined by the impact of the blade properties, including the blade aerodynamics and geometry. Near wake study in the real-life application focuses typically on the efficiency of the wind turbine and the physics of energy extraction. The far wake, on the other hand, is the region beyond the near wake, where the blade details are less important. In this section, the

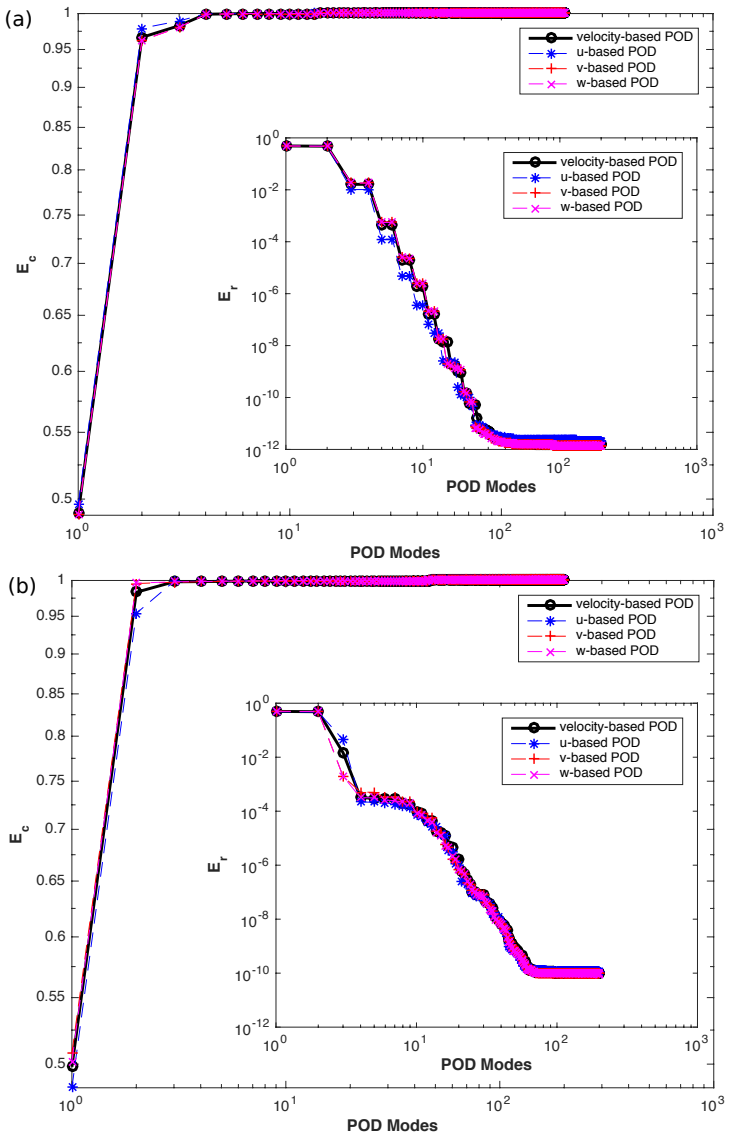

Figure 5.2: Relative (inside) and Cumulative (outside) Energy Content of the POD Modes in the (a) Near Wake and (b) Far Wake from N, Re1k.

POD analysis of all cases was performed and focused on the near wake flow where $6 < z < 11$. Even though $z = 6D$ is not the immediate downstream, the end of the near wake is said to be where the shear layer reaches the wake axis [19]. Moreover, from the observation, the wake flow before it reaches $z = 6D$ does not show much exciting features to be explored. Due to the matrix size limitation in MATLAB, the study of the wake flow was in $6 < z < 11$ rather than considering a more extended domain. The discussion covered the energy contribution, the eigenvalues & eigenvectors, and the coefficients of the first few energetic POD modes.

Before further discussion, it is better to have a good understanding of the contribution of both root and tip vortices of the flow. Turbulence kinetic energy (TKE) in fluid dynamics is the mean kinetic energy per unit mass associated with eddies in a turbulent flow. Physically, measured root-mean-square (RMS) velocity fluctuations characterizes the TKE. TKE, in general, is defined as half the sum of the variances (square of standard deviations) of the velocity components given by TKE $= \frac{1}{2}\left(\overline{(u')^2} + \overline{(v')^2} + \overline{(w')^2}\right)$.

The percentage of TKE for both inner (root) and outer (tip) cores where the considered x, y domain is $D_{\text{in}} = \{(x_{\text{in}}, y_{\text{in}}) : -0.4 \leq x_{\text{in}} \leq 0.4, -0.4 \leq y_{\text{in}} \leq 0.4\}$ and $D_{\text{out}} = \{(x_{\text{out}}, y_{\text{out}}) : (-1.2 \leq x_{\text{out}} \leq -0.8) \cup (0.8 \leq x_{\text{out}} \leq 1.2), (-1.2 \leq y_{\text{out}} \leq -0.8) \cup (0.8 \leq y_{\text{out}} \leq 1.2)\}$, respectively, were calculated as the flows went downstream and plotted in the following Fig. 5.3.

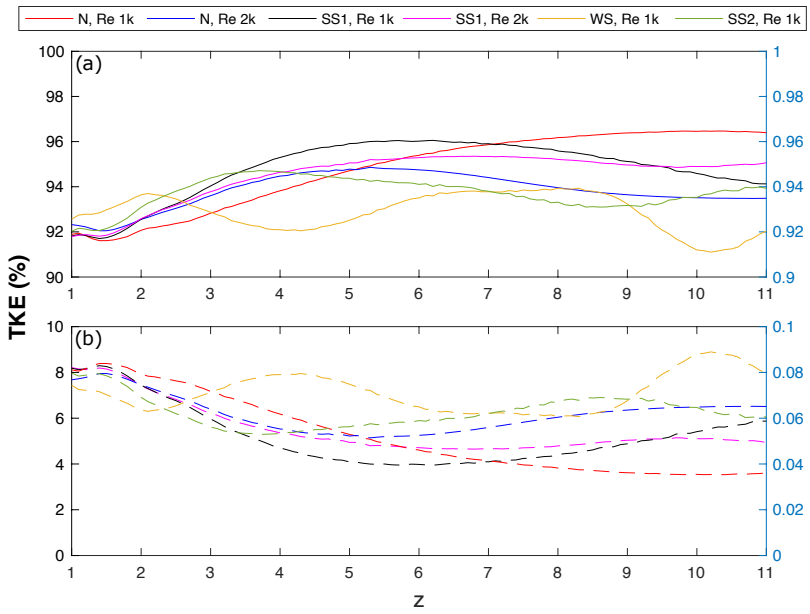

Figure 5.3: Percentage TKE (%) of the (a) tip vortices represent by the solid lines and (b) root vortices designate by dashed-lines for all cases.

All in all, the TKE of root vortices decay for all cases, while the tip vortices increase in the percentage TKE. However, the fact that the tip vortices containing over 90% of the kinetic energy made the root vortices' contribution to both modal analysis less important and can be neglected. Therefore, the following discussion will only focus on the tip vortices.

5.3.1 Energy Distribution

Energy distribution of the first seven POD modes was plotted relatively and cumulatively in Fig. 5.4. Note that the contribution of modes beyond the seventh mode is practically negligible. It shows that the first few POD modes contain the highest amount of relative energy. The fact that the energy of the following modes continues to reduce as the mode number increase ensures that the most important modes in terms of energy are the first modes. The most energetic modes can be viewed as 'dominant' flow structures. The less dominant modes may correspond to measurement noise and smaller eddies.

The energy distribution in the neutral atmospheric condition as portrayed in Fig. 5.4(a) & Fig. 5.4(b) show that the first two POD modes contain more energy, and these modes correspond to the dominant flow features buried within the flow solution.

Fig. 5.4(c) & Fig. 5.4(d) show that the percentage of the cumulative POD modes energy to the total one for both Re of strongly stable case 1. It is indicated that the first few modes occupy most energy, while the energy percentage for higher mode decreases to zero gradually. This is because the first few modes represent the large-scale coherent structures that dominate the global flow field, while higher modes represent the small-scale turbulent structures.

For both weakly stable and strongly stable case 2 (see Fig. 5.4(e) & Fig. 5.4(f)), the first two modes contain about 0.8994 – 0.9183 of the energy while the remaining energy was shared mostly between the third and fourth modes; the contribution of modes beyond the fourth modes is practically negligible.

Based on the energy distribution for the POD modes, the main features of these wake vortices are mostly described by the first two modes. Precisely, the first four modes of all cases are all needed to capture approximately 99% of the turbulent kinetic energy of the flow field for all cases. For this reason, the POD reconstructions of the fluctuation can be carried out from only these four modes. Thus, the rest of the analysis will be focused only on these first four captivating modes (POD_1, POD_2, POD_3, and POD_4) and will be analysed with further discussion.

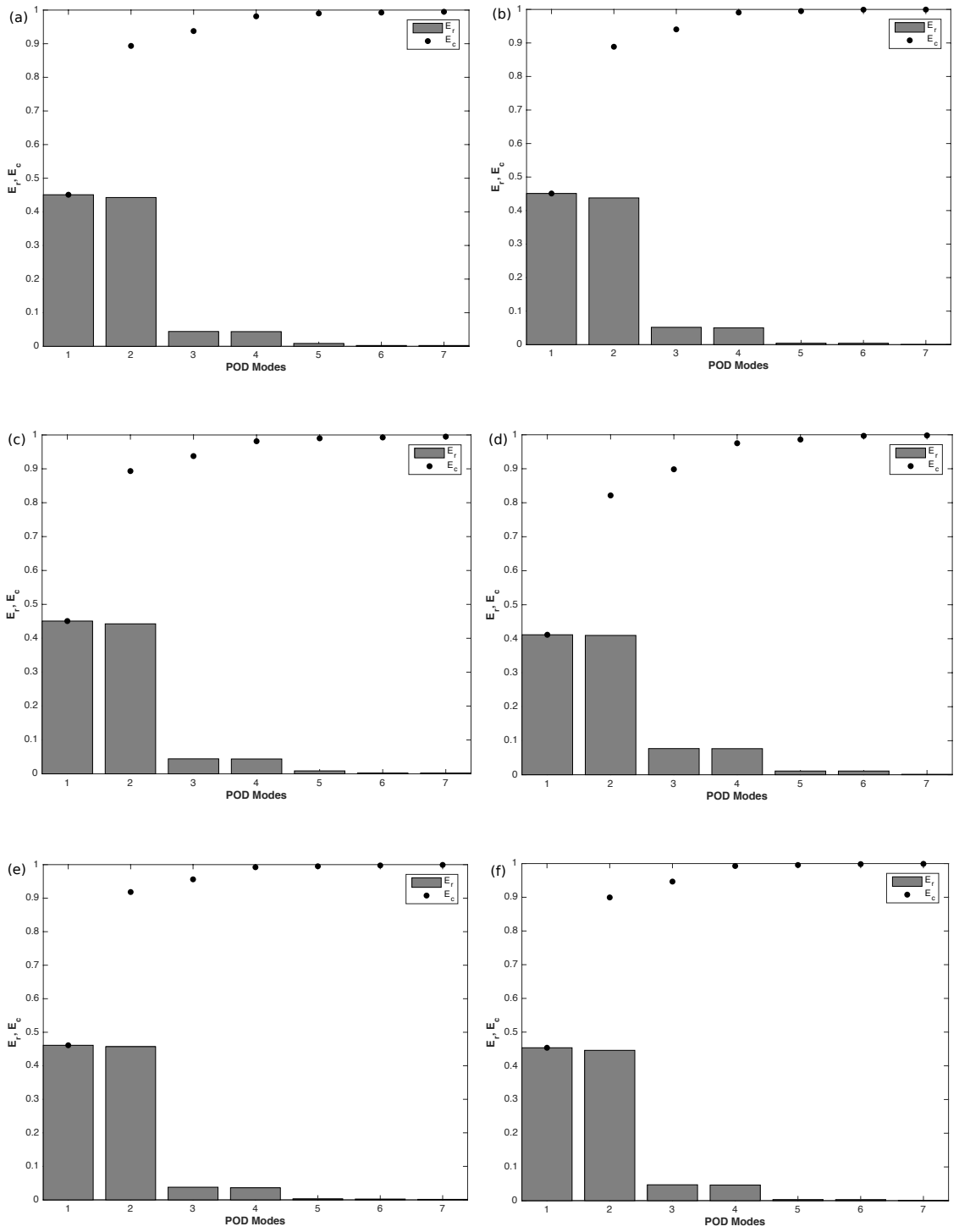

Figure 5.4: Energy Distribution of POD Modes in Near Wake for: (a) N, Re1k, (b) N, Re2k, (c) SS1, Re1k, (d) SS1, Re2k, (e) WS, Re1k, and (f) SS2, Re1k. E_r and E_c referred to relative and cumulative energy, respectively.

5.3.2 POD Modes

The obtained eigenvectors from Eq. 3.4.14, which also known as the POD modes, were shown in Fig. 5.5 – Fig. 5.10. $|\omega|$ POD modes of those four modes were

plotted in the streamwise direction. In particular, with growing mode number, the modes demonstrate clear structures with a trend from larger to smaller scales. This trend is readily clarified by the fact that the modes are sorted with respect to energy, and the kinetic energy in a turbulent flow typically decreases with scale. Furthermore, it is essential to note that the first two modes, POD_1 & POD_2, contain distinct dipole structures, implying that these modes are accountable for periodic lateral motions [96]. The wavelength of the periodic motion induced by each of these modes is twice the streamwise distance between consecutive negative and positive poles. The amplitude of this periodic motion is equal to the lateral distance between positive and negative poles [96].

Meanwhile, the second pair of most energetic modes, POD_3 & POD_4 shows a quadrupole structure and the next pair of modes. POD_5 & POD_6 of N, Re1k and N, Re2k cases give a hexapole structure, as one may expect since they have similar energy contribution (as shown in Fig. 5.11). These well-defined multi-pole modes are remarkably similar to the ones discovered by [28, 29, 155] and indicate vague statistical isotropy [39] in which the wake dynamics seem to partially retain some of its symmetric behaviour even though the atmospheric boundary layer (ABL) breaks this rotational symmetry.

Similar trends are observed from all other cases, except for weakly stable and strongly stable case 2. This might be due to their chaotic flows with random noise. It is hard to see a clear helical flow from POD_1 & POD_2 of WS, Re1k in Fig. 5.9 as the contour plots look a bit messy. On the other hand, POD_3 & POD_4 from the same case decay quite early at $z = 8$, and this situation happen just for these two POD modes only. Last but not least, POD_1 & POD_2 from the SS2, Re1k case show two helical flows with different radius moving together close to each other, as illustrated in Fig. 5.10, while their second pair of mode displays a vaguely quadrupole-like structure.

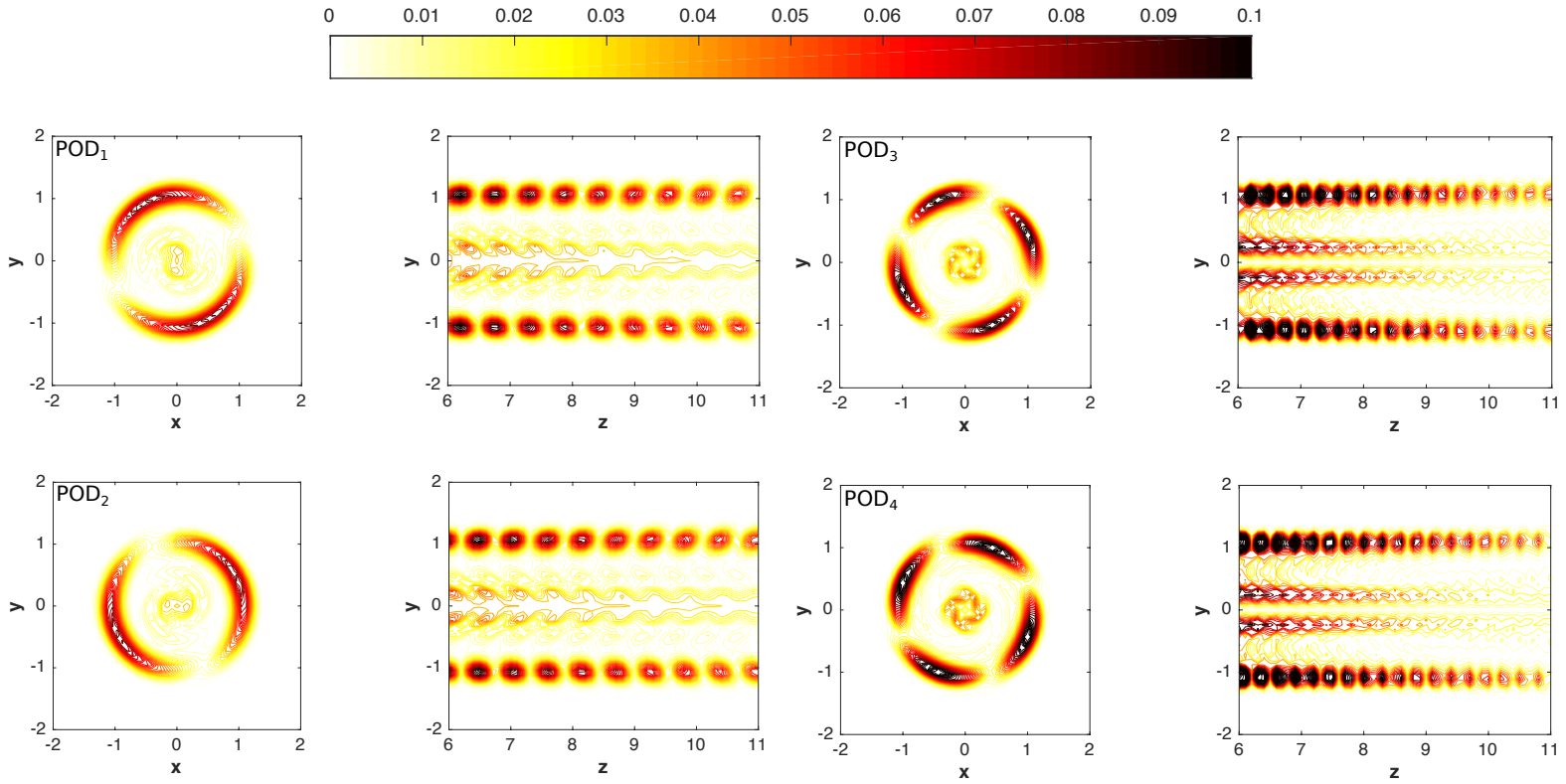

Figure 5.5: POD Modes illustrated using contours of $|\omega|$ for the corresponding first four dominant modes, i.e POD_1 (top left) followed by POD_2, POD_3, and POD_4 respectively in xy-cut at $z = 8.5$ (left) and zy-cut at $x = 0$ (right) for N, Re1k.

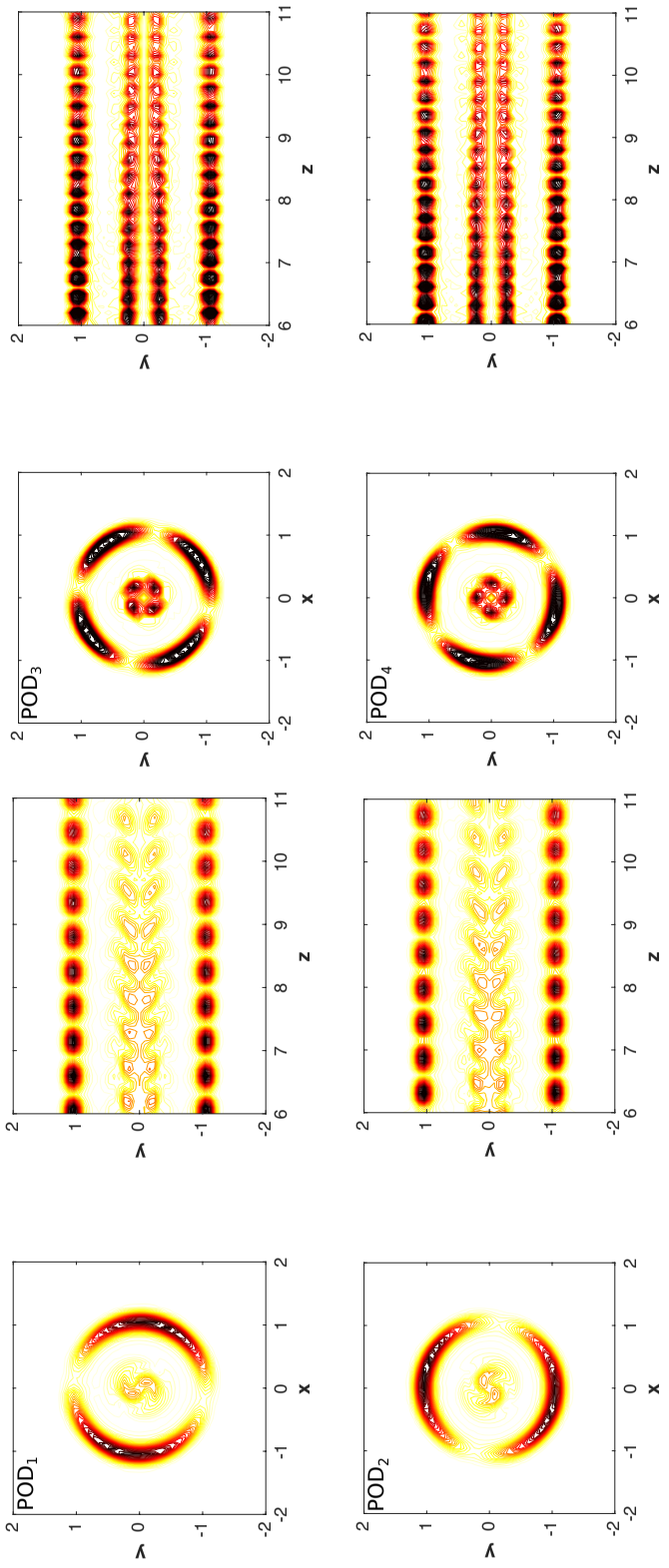

Figure 5.6: Caption and colormap as Fig. 5.5, but for N, Re2k.

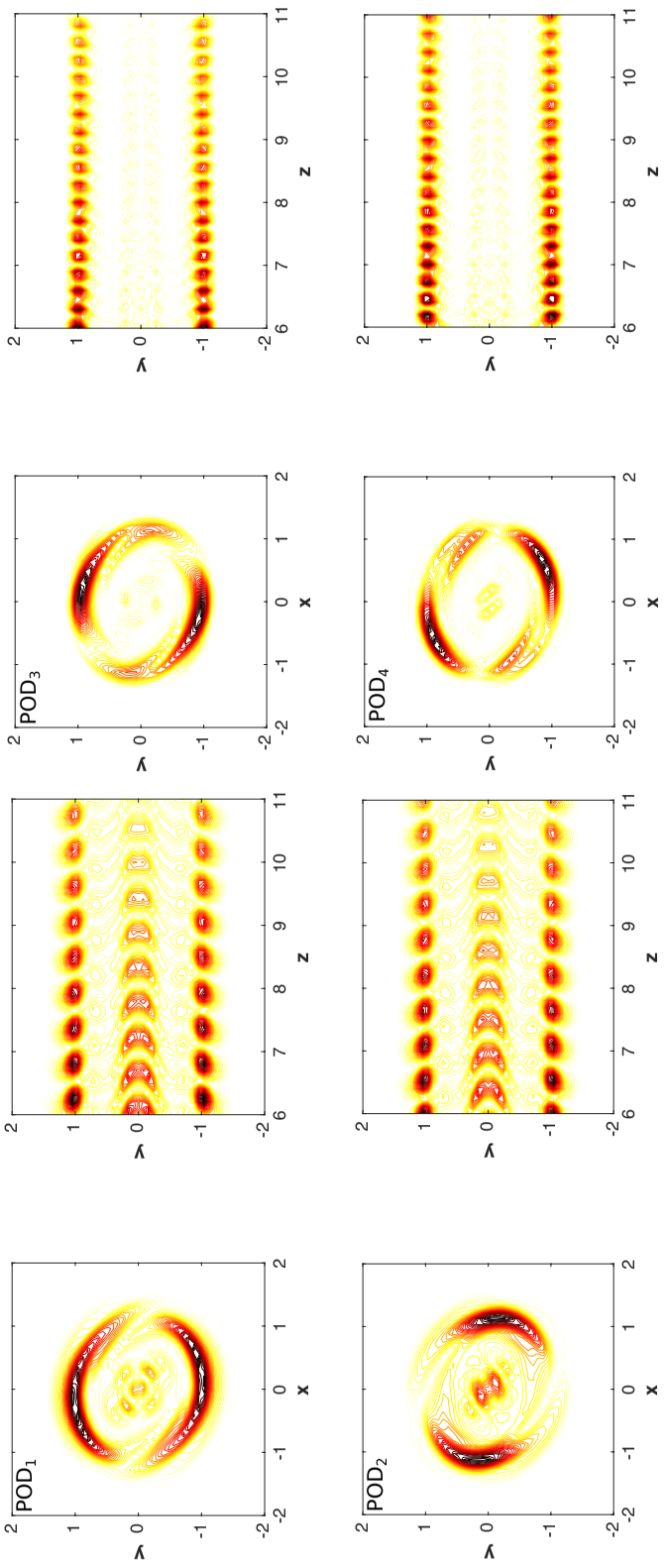

Figure 5.7: Caption and colormap as Fig. 5.5, but for SS1, Re1k.

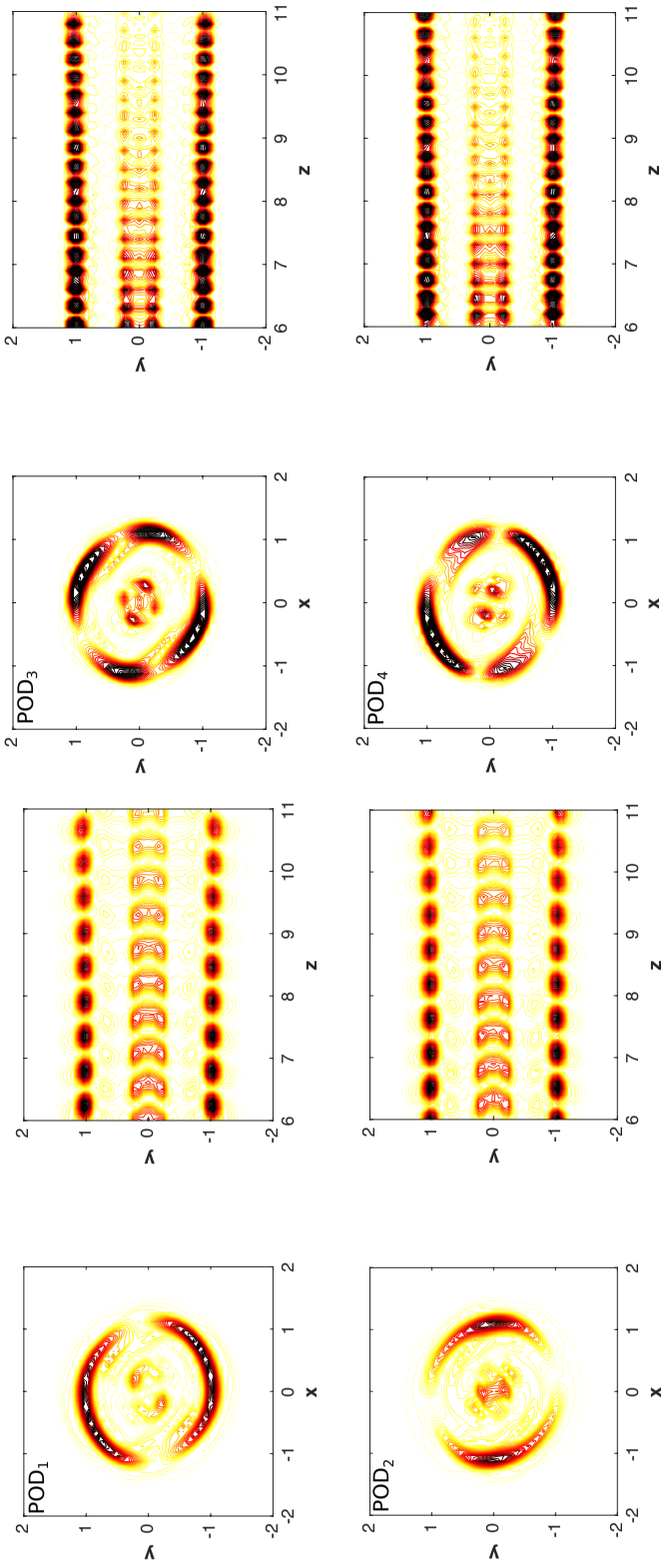

Figure 5.8: Caption and colormap as Fig. 5.5, but for SS1, Re2k.

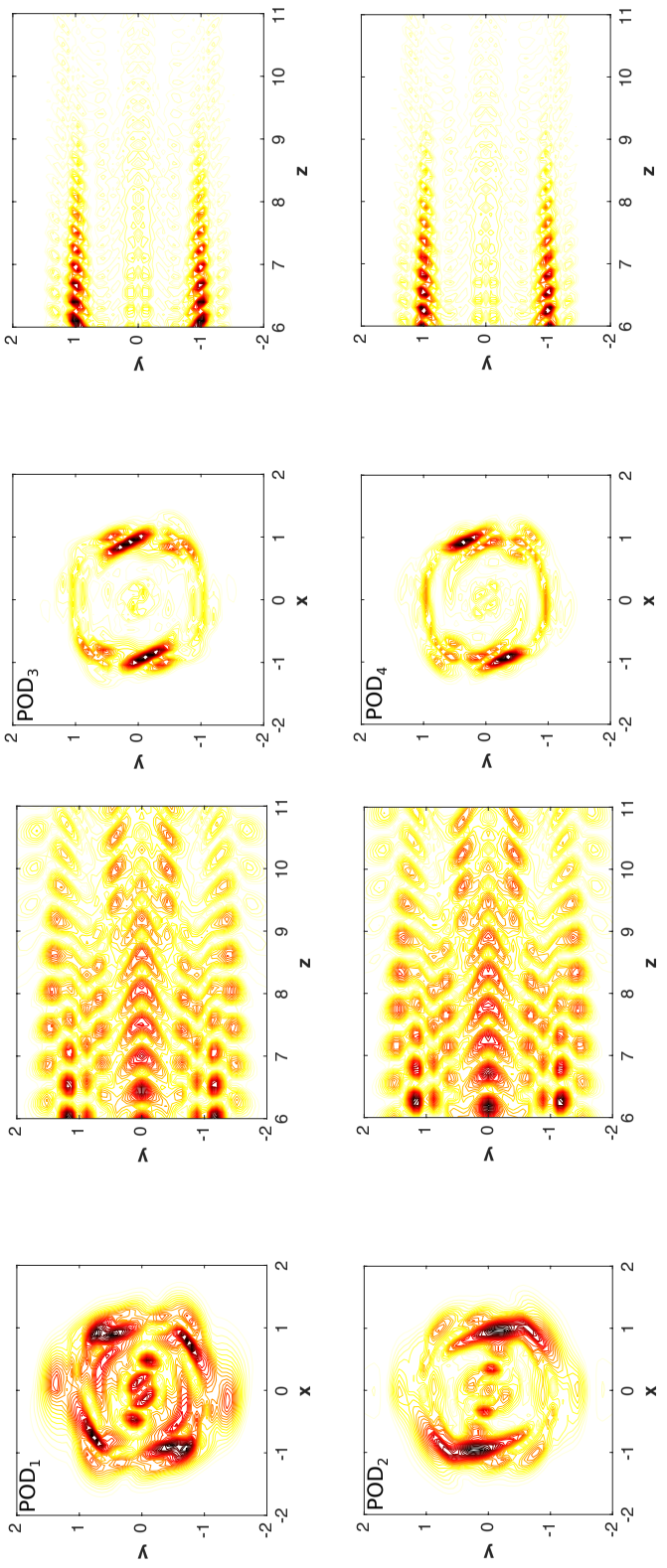

Figure 5.9: Caption and colormap as Fig. 5.5, but for WS, Re1k.

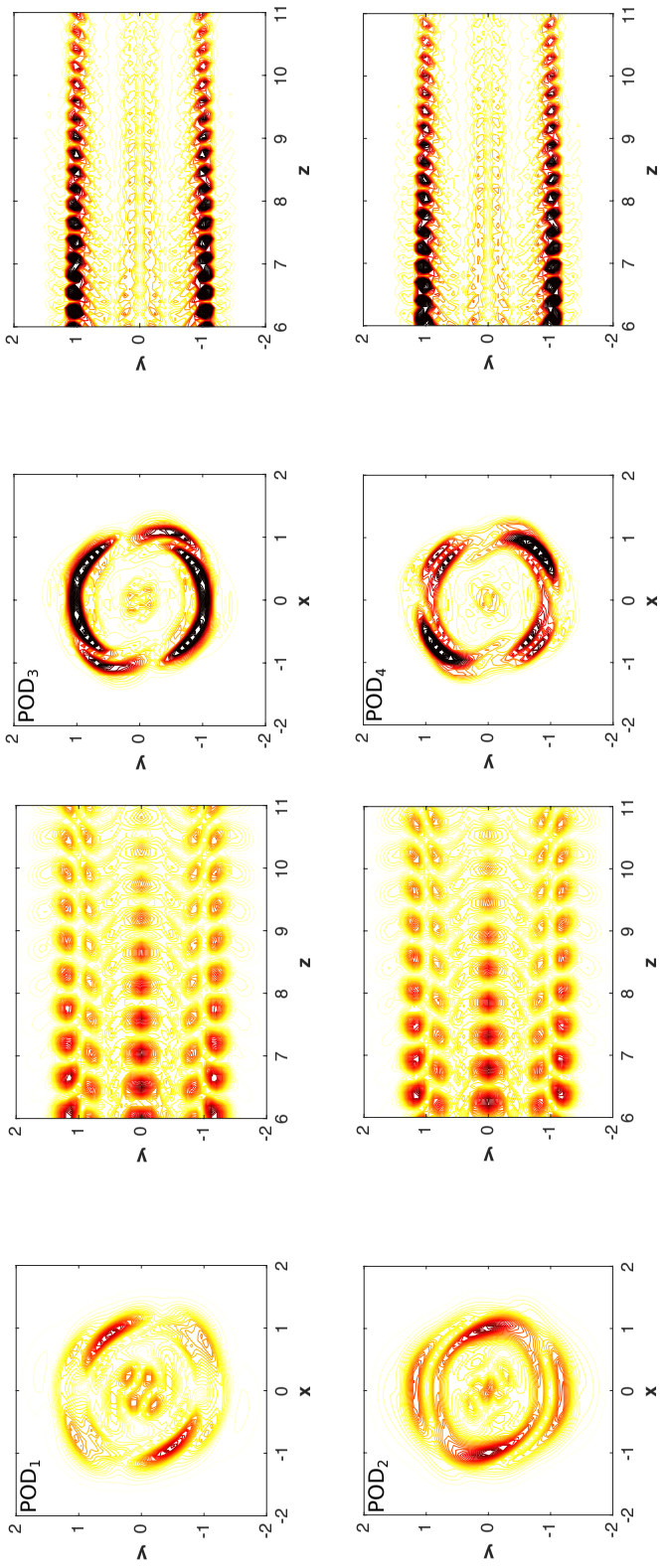

Figure 5.10: Caption and colormap as Fig. 5.5, but for SS2, Re1k.

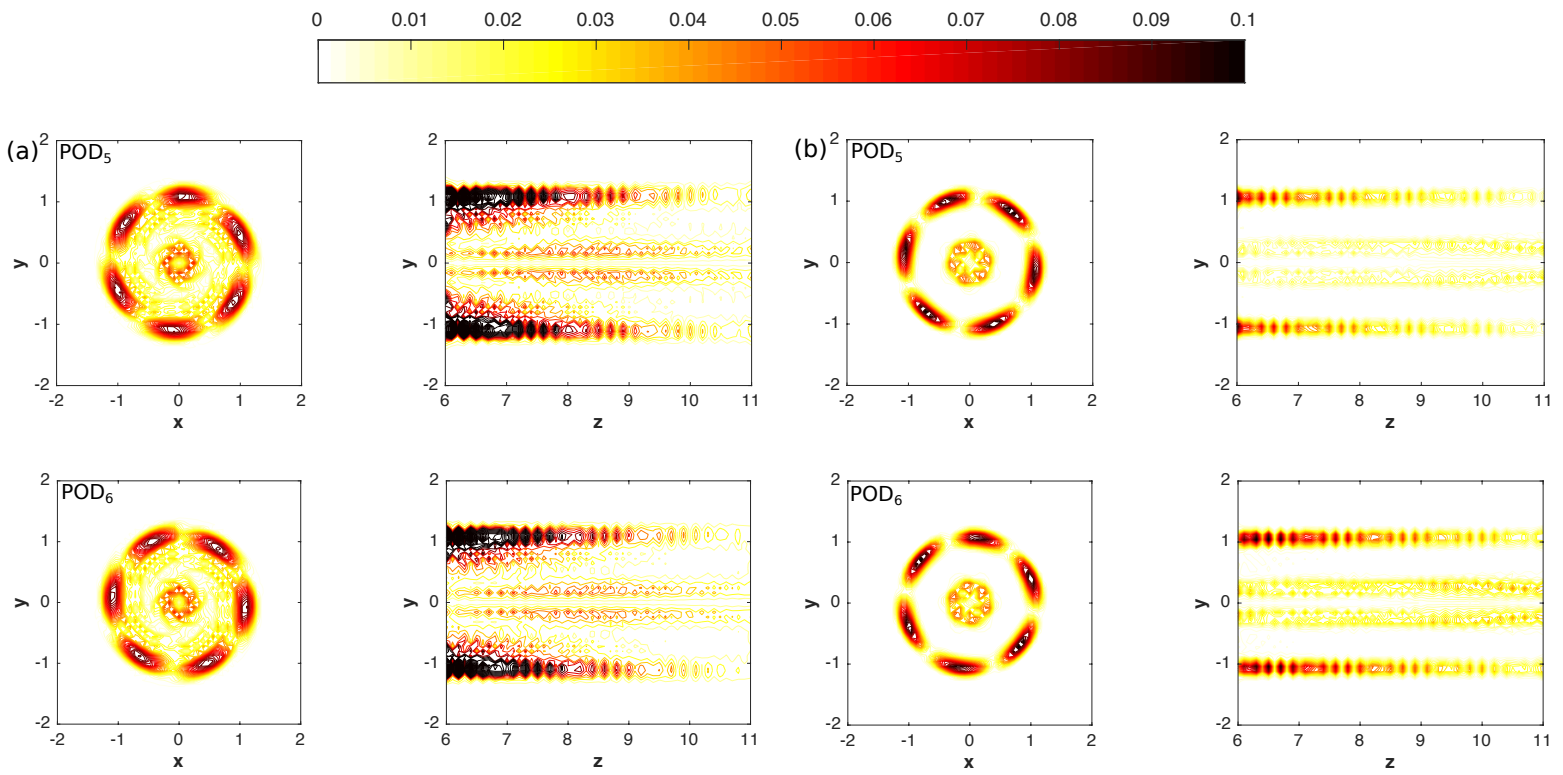

Figure 5.11: POD Modes illustrated using contours of $|\omega|$ for POD_5 (above), and POD_6, respectively in xy-cut at $z = 8.5$ (left) and zy-cut at $x = 0$ (right) for (a) N, Re1k, and (b) N, Re2k.

For better visualization of the most energetic mode, POD_1, the isosurface of its $|\omega|$ in streamwise direction for all cases were plotted in Fig. 5.12 below:

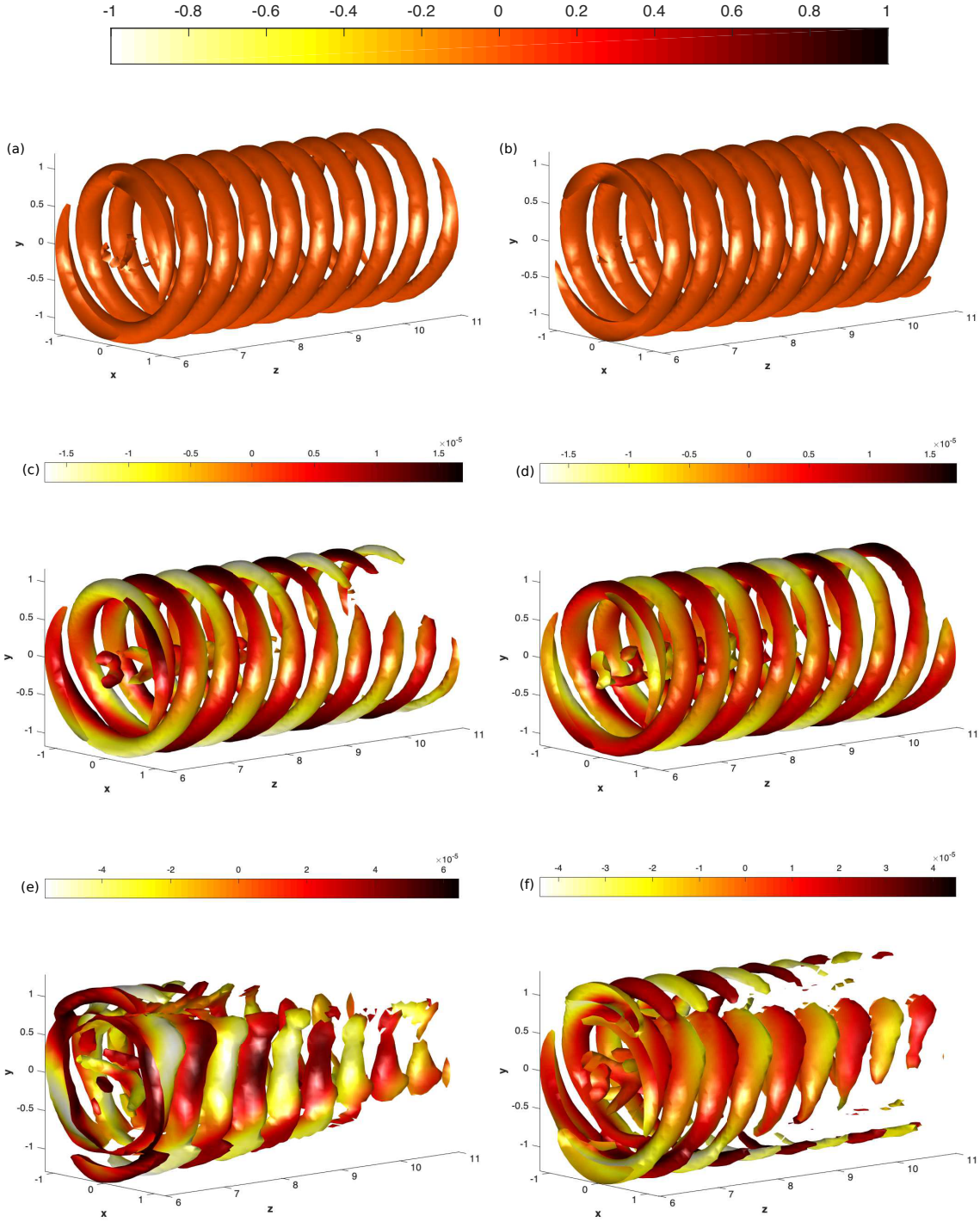

Figure 5.12: Isosurface of $|\omega| = 0.05$ POD_1 for: (a) N, Re1k, (b) N, Re2k, (c) SS1, Re1k, (d) SS1, Re2k, (e) WS, Re1k, and (f) SS2, Re1k cases coloured by their respective POD_1 of temperature field.

5.3.3 The POD Mode Coefficients

Eq. 3.4.16 tells that each snapshot can be reconstructed. The importance of the distinct modes for a given snapshot can be expressed by the POD coefficients discovered by projecting the snapshot onto the POD modes, as illustrated by Eq. 3.4.16 [25]. For all snapshots, it is possible to show the relation between two consecutive modes as a scatter plot of the two coefficients. Fig. 5.13(a) – Fig. 5.18(a) shows a circular pattern of scatter plots for the coefficients of the first two modes, a_1 and a_2 followed by Fig. 5.13(i) – Fig. 5.18(i) for a circular pattern of a_3 and a_4. All the points are located near a circle with a radius in the range from $\approx 1.7D$ up to $\approx 10D$. The circular distribution of the (a_1, a_2) and (a_3, a_4) coefficients indicate a cyclic variation of the first two pairs of POD modes, which is precisely what is anticipated when two POD modes describe distinct phases of a smooth process that creates and convects vortices [77].

Next, the POD coefficients variation in time was plotted as in Fig. 5.13(b)&5.13(ii) – Fig. 5.18(b) & 5.18(ii). As expected, the two pairs of POD coefficients change similarly to cosine and sine functions in a time-resolved study of the flow. The amplitude of each modal coefficient series is proportional to the kinetic energy fluctuation embedded in the corresponding mode. As the mode index increases, the amplitude of the modal coefficients decreases, as expected. For example, the amplitude of the second pair modal series is always lower than the first one.

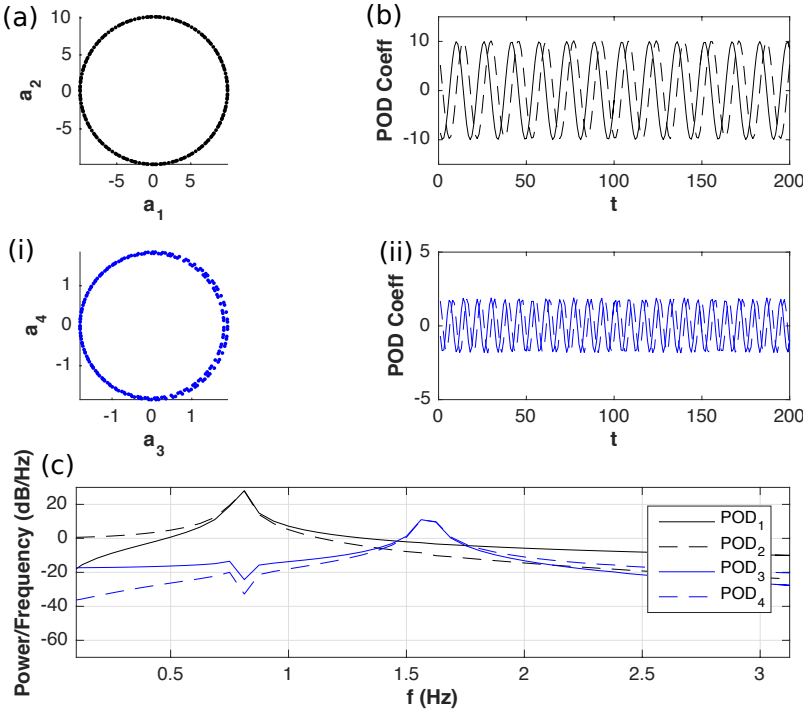

Figure 5.13: Distribution (a, i), and Time Variation (b, ii) of the first four POD modes coefficients, a_1 & a_2 (a, b), and a_3 & a_4 (i, ii) for N, Re1k in the near wake region. (c) PSD of the first four POD coefficients.

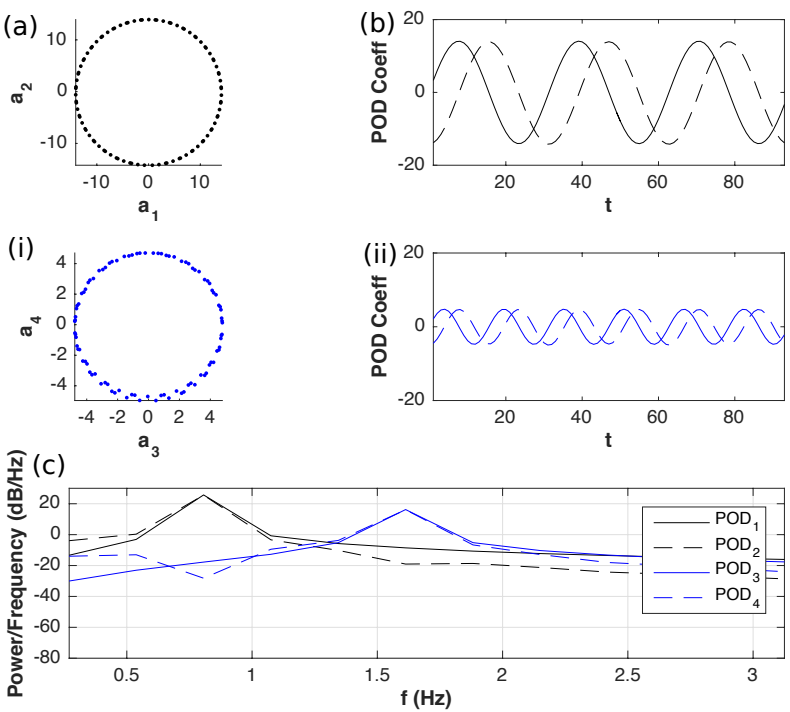

Figure 5.14: Caption as Fig. 5.13, but for N, Re2k.

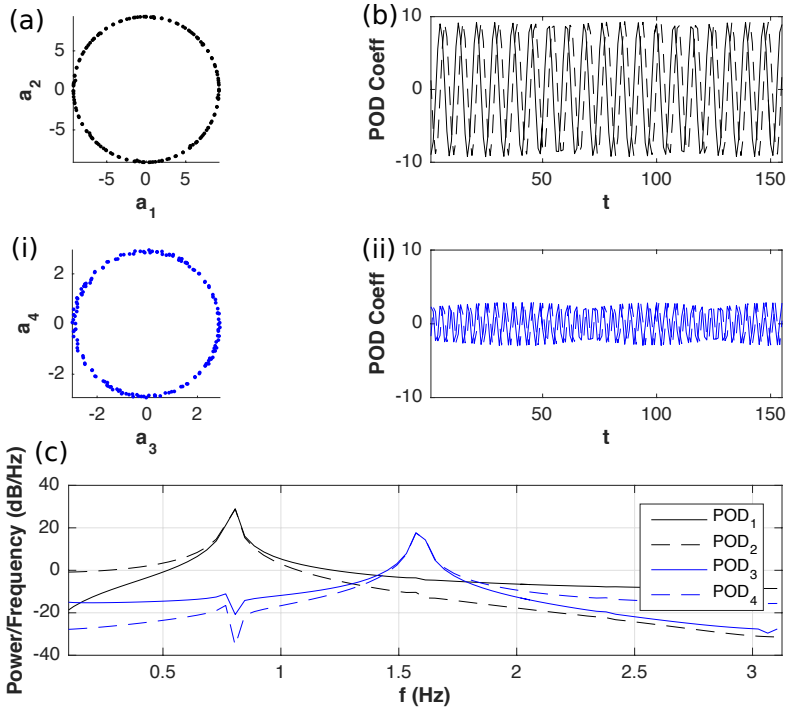

Figure 5.15: Caption as Fig. 5.13, but for SS1, Re1k.

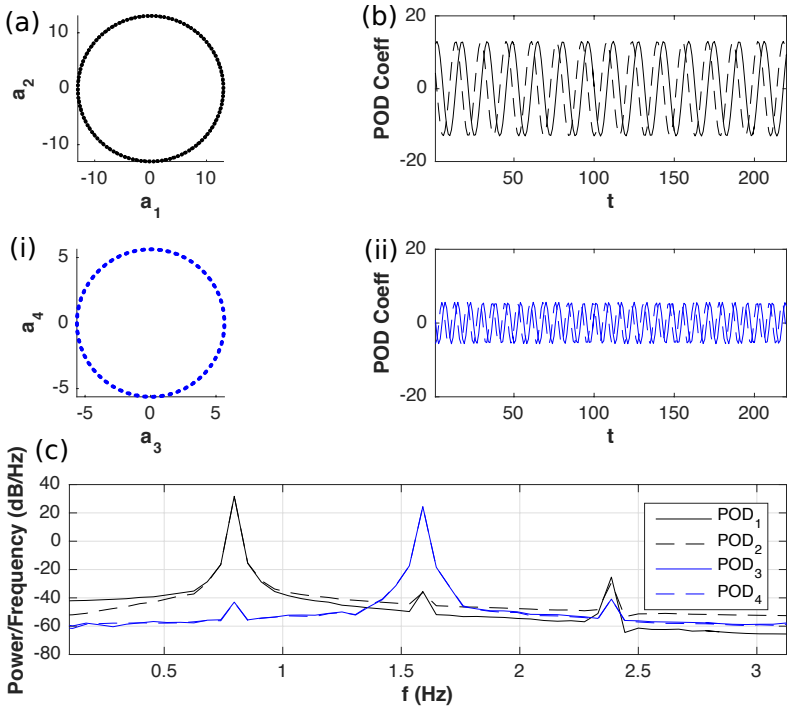

Figure 5.16: Caption as Fig. 5.13, but for SS1, Re2k.

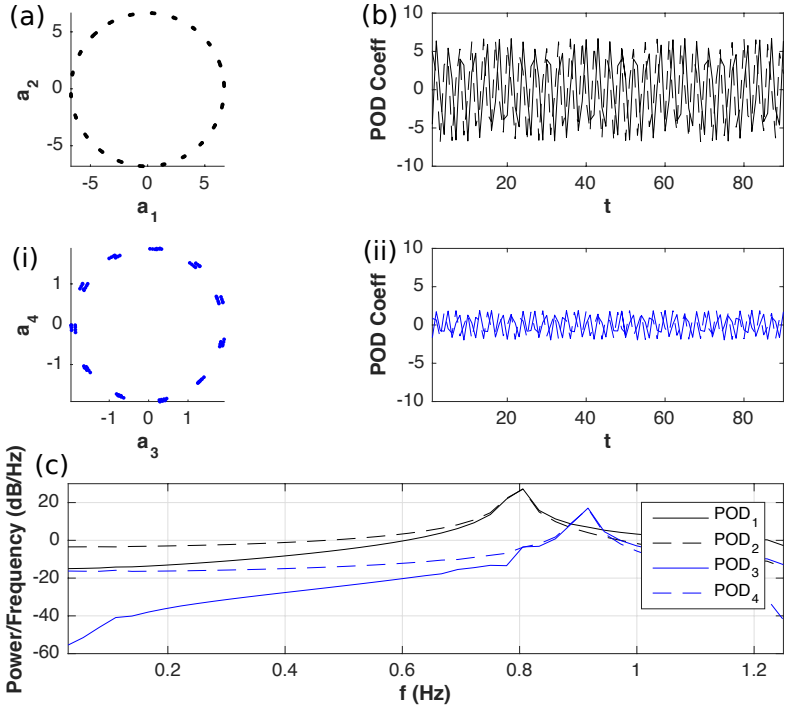

Figure 5.17: Caption as Fig. 5.13, but for WS, Re1k.

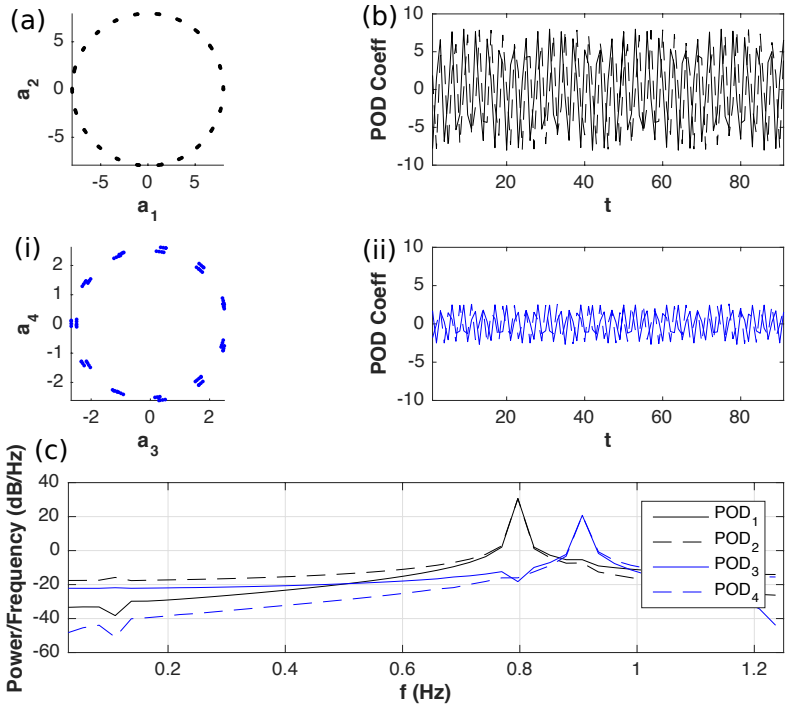

Figure 5.18: Caption as Fig. 5.13, but for SS2, Re1k.

By plotting the power spectra of the POD coefficients in Fig. 5.13(c) – Fig. 5.18(c) above, generally, for all cases, two distinct amplitude peaks are readily picked up from the first and second pairs of POD modes, respectively. The frequency of every peak shown in those figures was listed in the following Table 5.1:

Atmospheric Conditions	f (Hz)	
	$POD_{1^{st}}$	$POD_{2^{nd}}$
N, Re1k	0.8125	1.5620
N, Re2k	0.8065	1.6130
WS, Re1k	0.8056	0.9167
SS1, Re1k	0.8065	1.6130
SS1, Re2k	0.7955	0.7955
	1.5910	1.5910
	2.3865	2.3865
SS2, Re1k	0.7967	0.9066

Table 5.1: Frequencies, f captured by POD modes coefficients for all cases

The first and second mode spectra of the N, Re 1k case show clear peaks at the frequency 0.8125 Hz and 1.5620 Hz, which is shown in Fig. 5.13(c) and as for N, Re 2k (see Fig. 5.14(c)), the two peaks were detected at frequencies 0.8065 Hz, and 1.6130 Hz, respectively, from the first and second pair of POD mode.

For the strongly stable case 1 with Re = 1000, the temporal evolution of the time-varying coefficients shown in Fig. 5.15(b) & Fig. 5.15(ii) revealed a single frequency in both pair of POD modes at 0.8065 Hz and 1.6130 Hz as it can be seen in Fig. 5.15(c) whereas the POD modes of strongly stable case 1 with Re = 2000 captured the most energetic structures resulting in a mode that contained several frequencies as there are several peaks shown in Fig. 5.16(c) i.e. 0.7955 Hz, 1.5910 Hz, and 2.3865 Hz from the first and second pairs of POD modes.

Meanwhile, for both WS and SS2 at Re = 1000 (refer to Fig. 5.17(c) & Fig. 5.18(c)), the first pair of POD mode spectra show a clear peak at 0.8056 Hz and 0.7967 Hz, respectively while the second peak captured by the second pair of POD

modes at frequencies 0.9167 Hz and 0.9066 Hz.

The general patterns of the first and second pairs of the POD modes matched the corresponding wake flow structure and well-captured the same dominant frequencies identified by fluctuating streamwise velocity analysis of the physical space in previous Chapter 4.

5.4 POD Analysis of the Temperature Field

In this section, the first few temperature POD (PODT) modes computed from the temperature field, T, were studied and discussed. This chapter involves the four cases with the stratified atmospheric condition $\Delta T \neq 0$, which made the two neutral cases excluded. The equispaced temporal data comprising t number of snapshots (refer to Table 3.2) of the temperature fields is recorded and ensembled in a matrix form as Eq. 3.4.10. The four most energetic PODT modes of all cases representing almost 97.95% to 99.46% of the total contribution, as display in Fig. 5.19.

The illustration of all PODT modes in Fig. 5.20 – Fig. 5.23 demonstrate the first four modes capture the dominant features of the flow field. Every two PODT modes look alike due to their similarity in energy contribution. There are two helical structures in the first pair of PODT modes build from their positive and negative magnitudes. As the PODT mode index increases, the number of helical structures doubled. These observations, however, do not show any multi-pole like structure as it can be seen earlier form the POD modes. This is probably because of the fact that the temperature equation is completely decoupled from the Navier-Stokes equations, as described in Section3.1, since the viscosity does not depend on the temperature. Hence, the temperature is decoupled with the velocity as the solution to the Navier-Stokes equations just gives the velocity and pressure field for flows of fluids with constant viscosity and density.

As for the analysis of the PODT coefficients, every pair of PODT modes convincingly reflected as strong cycle-to-cycle variations, as portray by Fig. 5.24(a)&(i) – Fig. 5.27(a)&(i), and they change similarly to cosine and sine functions in a time-resolved study of the flow in Fig. 5.24(b)&(ii) – Fig. 5.27(b)&(ii). The PODT

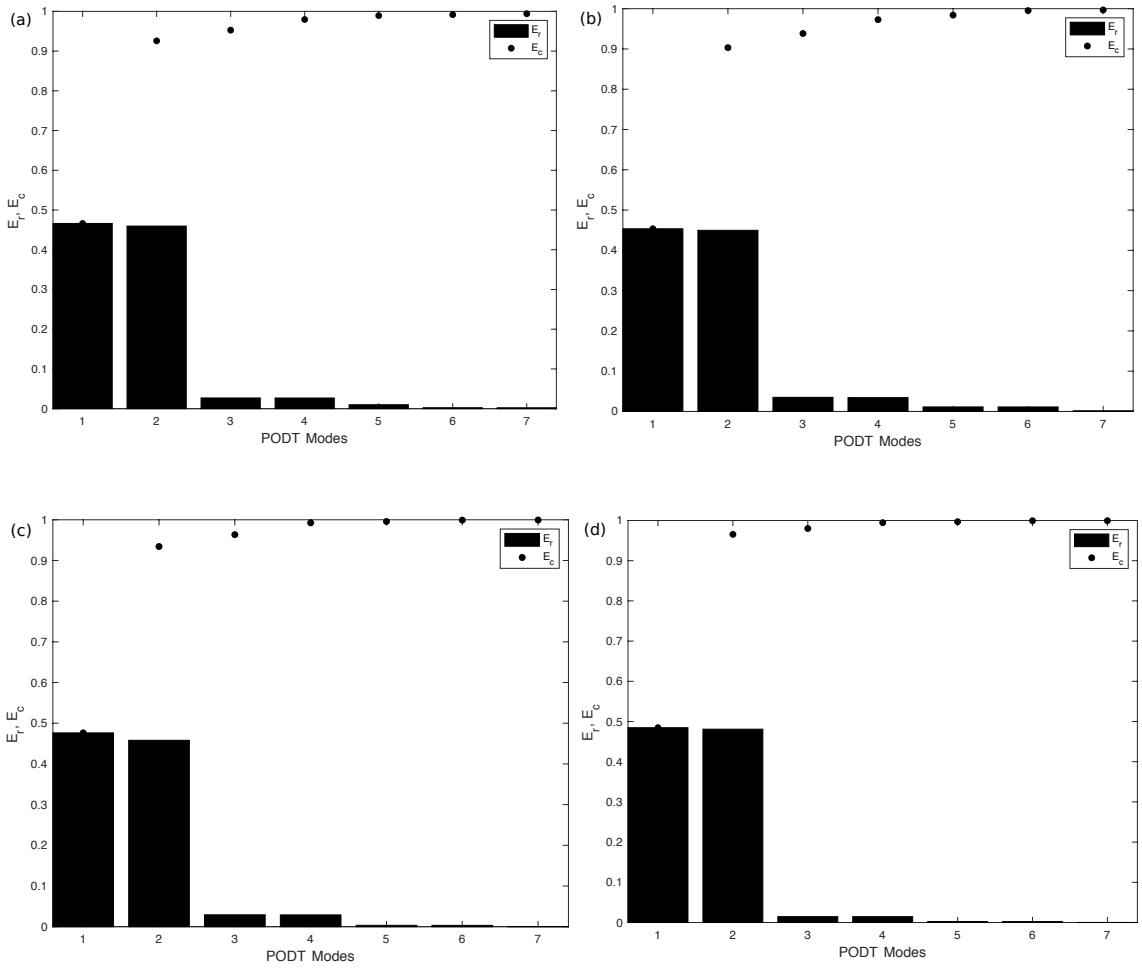

Figure 5.19: Energy Distribution of PODT Modes in Near Wake for: (a) SS1, Re1k, (b) SS1, Re2k, (c) WS, Re1k, and (d) SS2, Re1k.

coefficients successfully captured all the same frequencies, as listed in Table 5.1. All these agreements between POD and PODT modes conclude that the POD method gave a consistent result from both velocities and temperature fields.

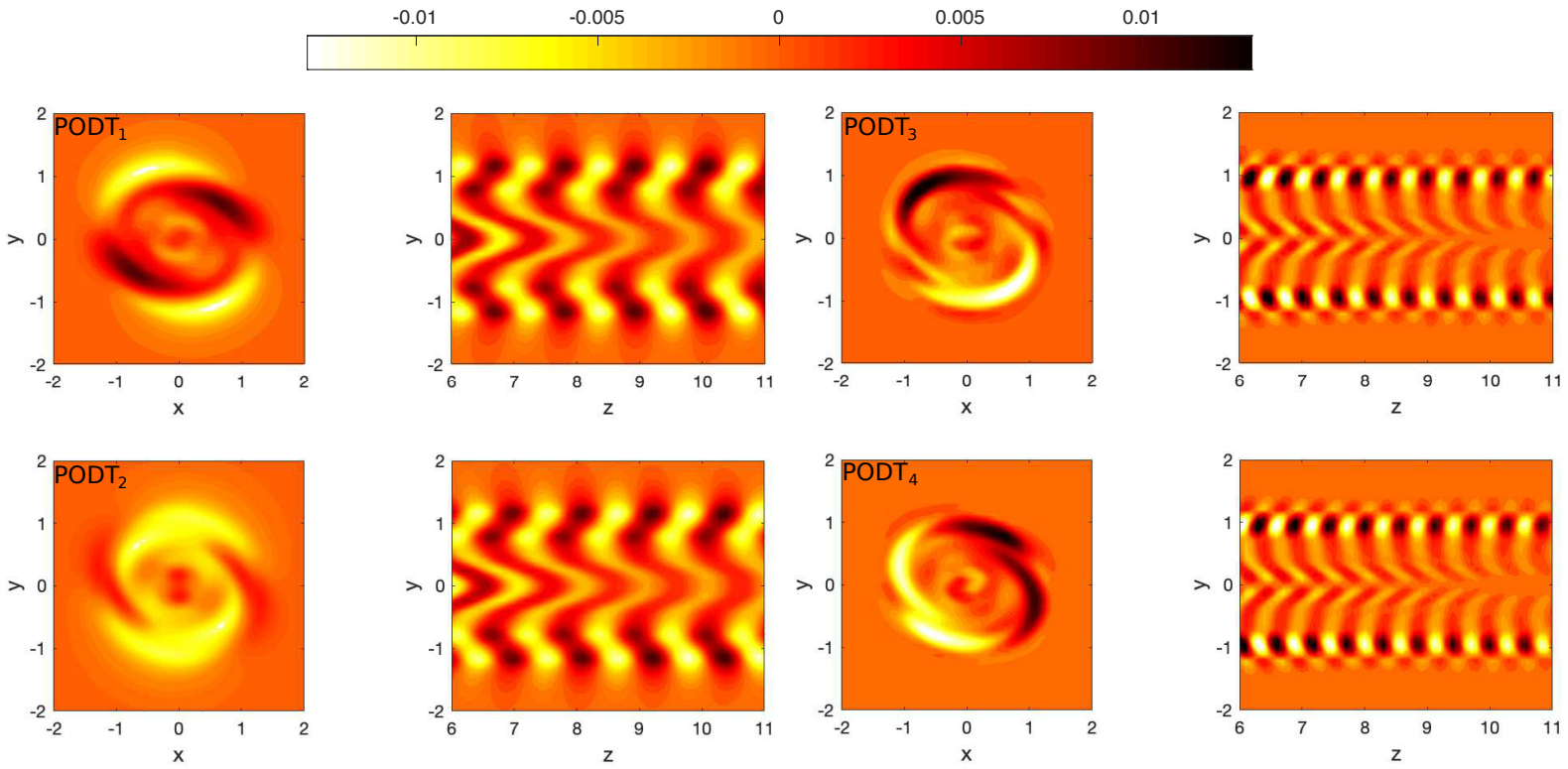

Figure 5.20: Temperature POD Modes illustrated using contours of $|\omega|$ for the corresponding first four dominant modes, i.e., PODT_1 (top left) followed by PODT_2, PODT_3, and PODT_4 respectively in xy-cut at $z = 8.5$ (left) and zy-cut at $x = 0$ (right) for SS1, Re1k.

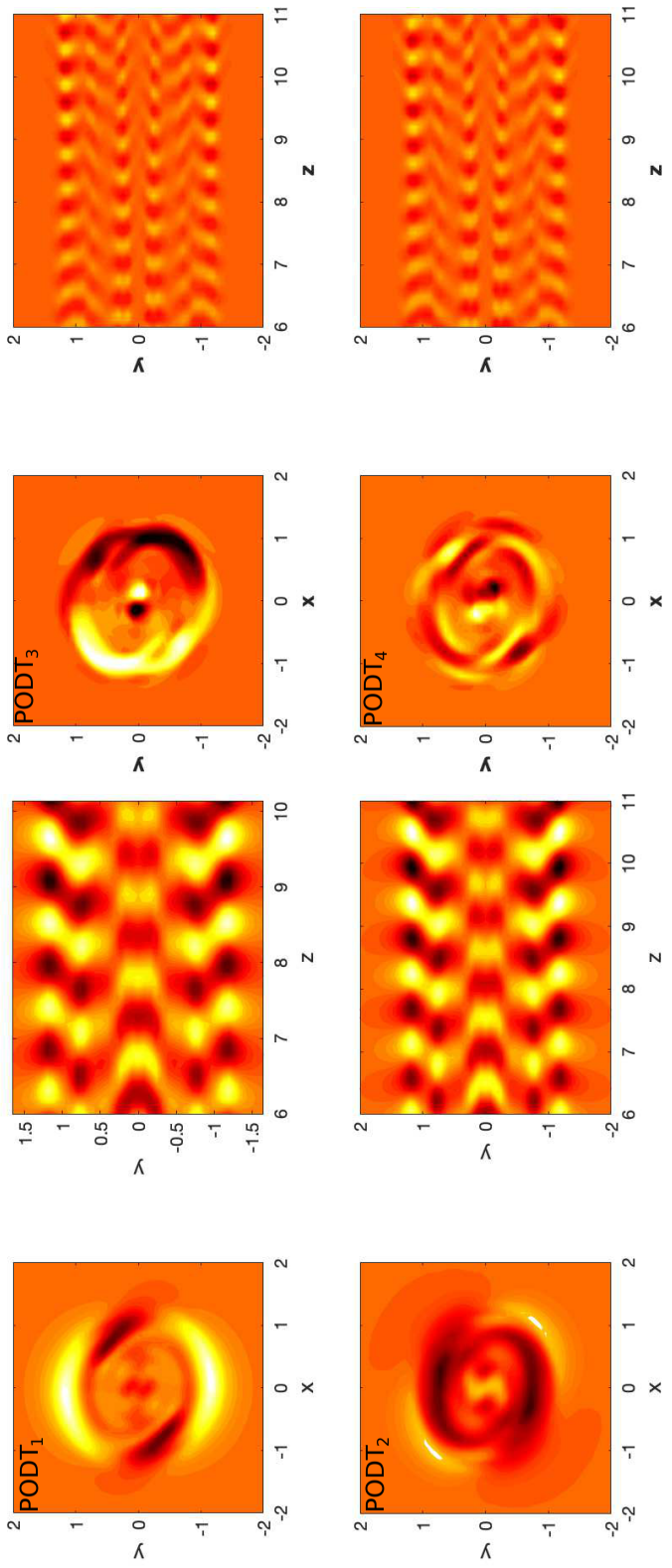

Figure 5.21: Caption and colormap as Fig. 5.20, but for SS1, Re2k.

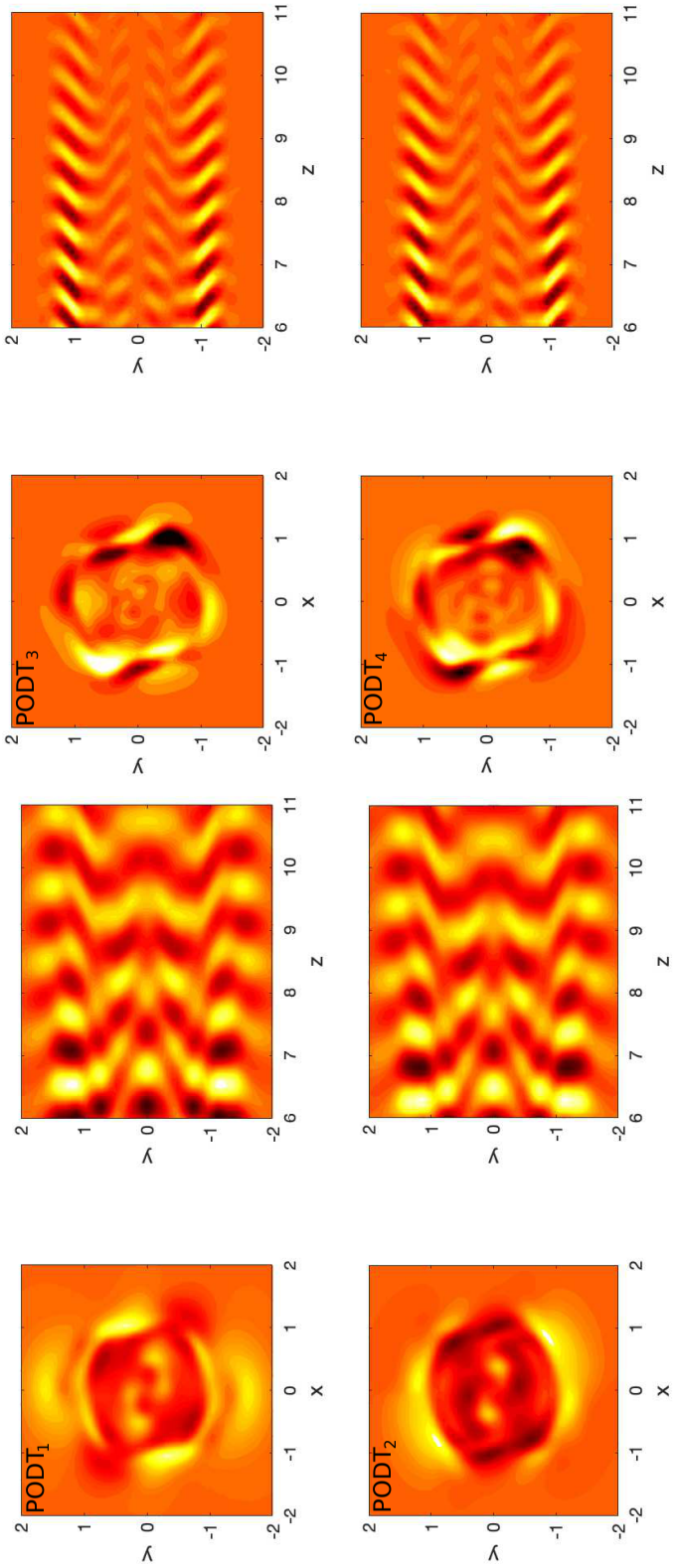

Figure 5.22: Caption and colormap as Fig. 5.20, but for WS, Re1k.

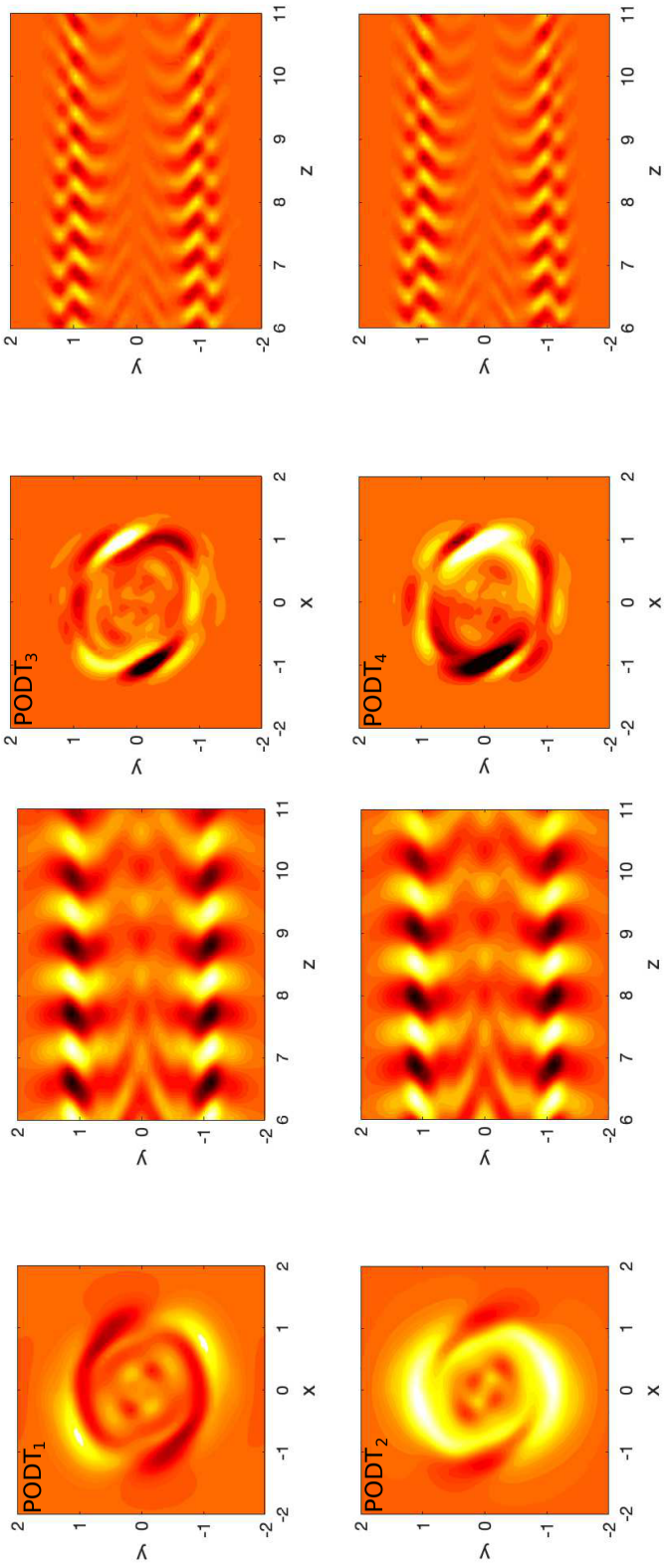

Figure 5.23: Caption and colormap as Fig. 5.20, but for SS2, Re1k.

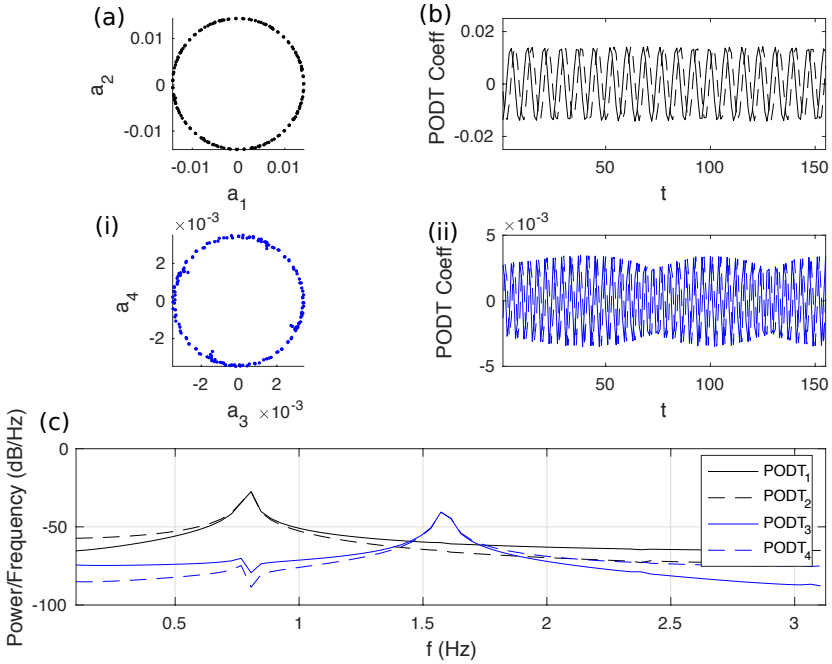

Figure 5.24: Distribution (a, i), and Time Variation (b, ii) of the first four PODT modes coefficients, a_1 & a_2 (a, b), and a_3 & a_4 (i, ii) for SS1, Re1k in the near wake region. (c) PSD of the first four PODT coefficients.

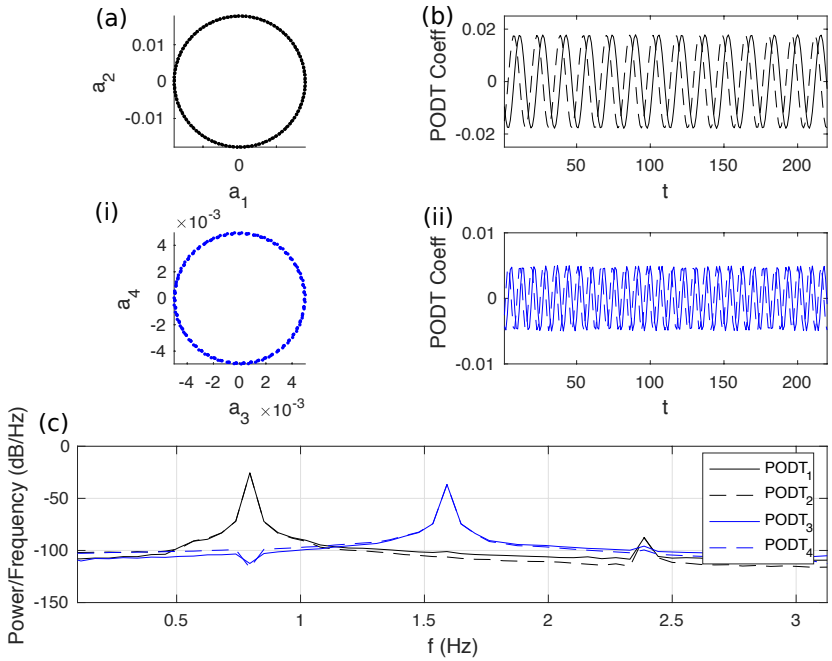

Figure 5.25: Caption as Fig. 5.24, but for SS1, Re2k.

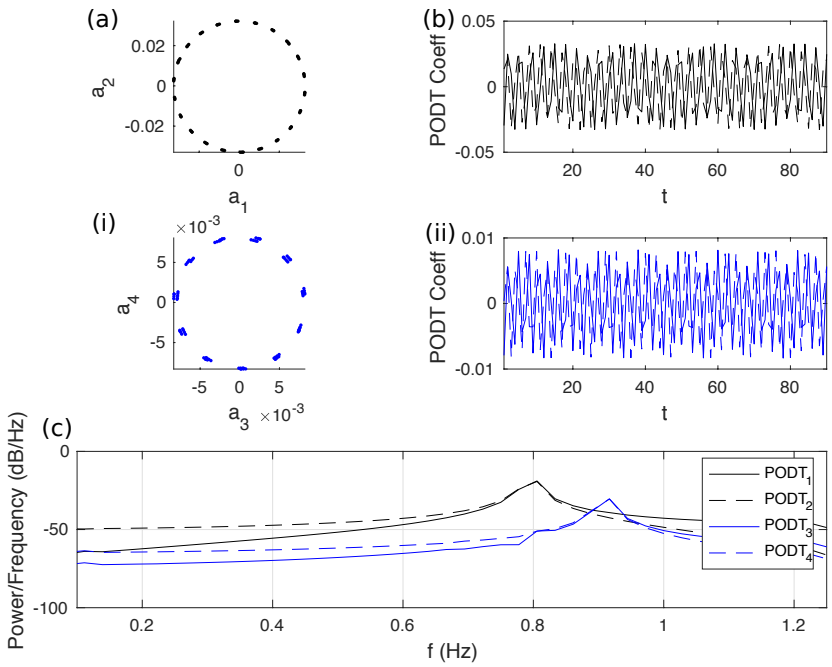

Figure 5.26: Caption as Fig. 5.24, but for WS, Re1k.

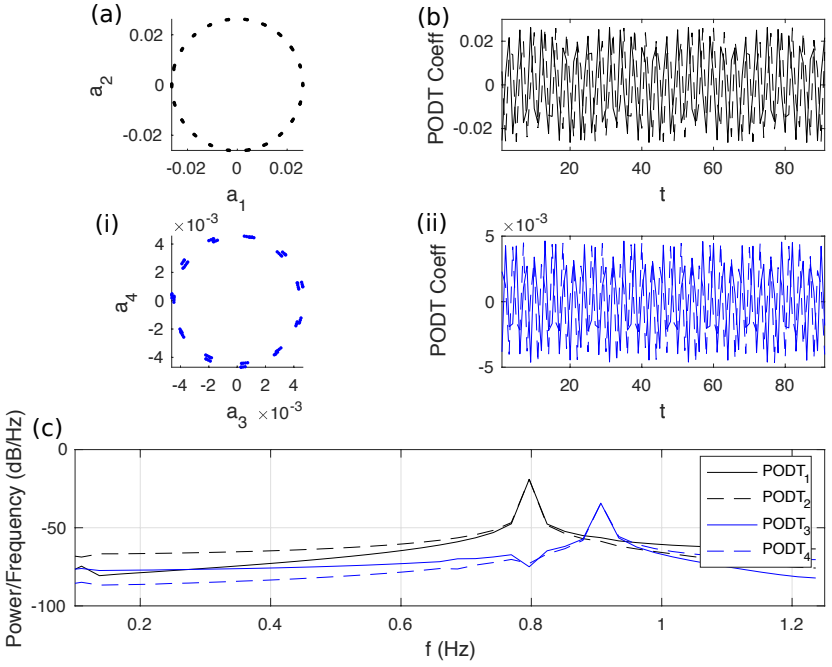

Figure 5.27: Caption as Fig. 5.24, but for SS2, Re1k.

5.5 POD Analysis of the Results in the Far-field Region

As mentioned earlier in Section 5.3, since the details of the blade from the far wake are less critical the velocity deficit in this region gradually decays downstream of the rotating blade, and the wake is fully developed. Therefore, in order to have a look at the difference of the wake between the near and far wake regions, an analysis was carried out just for the neutral case at Re = 1000.

Fig. 5.27 shows the time series (Fig. 5.27(a)) and PSD (Fig. 5.27(b)) of u' at three different core locations which are $(z, x, y) = (21, -1.04, -1.04), (23.5, -1.04, -1.04), (26, -1.04, -1.04)$ in Fig. 3.1. The mean velocity field then was illustrated using contours of $|\omega|$ in Fig. 5.27(c) and lastly, the isosurface plot of $|\omega|$ from the instantaneous velocity field was plotted in Fig. 5.27(d).

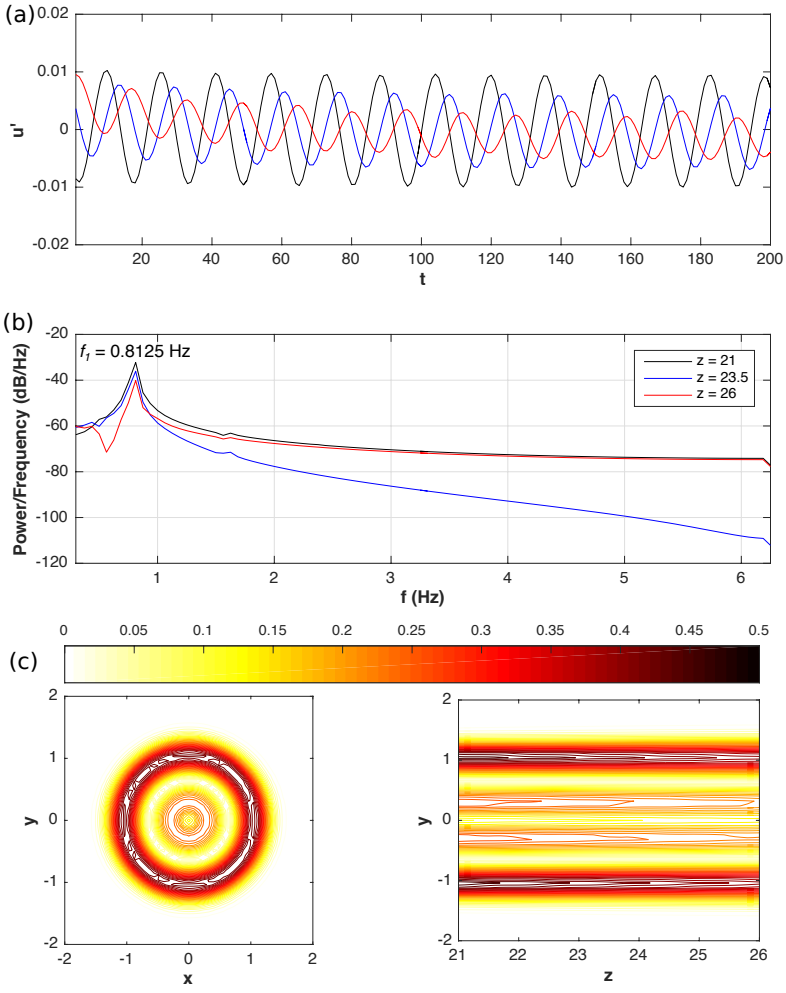

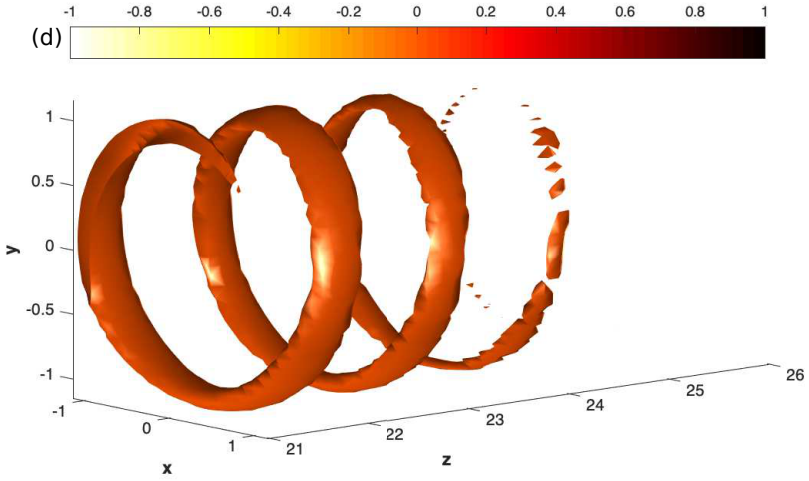

Figure 5.27: (a) Time Series, (b) Power Spectra Density, (c) Contour plot of $|\omega|$ from mean velocity field, and (d) Isosurface $|\omega| = 0.1$ from instantaneous velocity field for N, Re1k in the far wake region.

A steady time variation at $z = 21$ and 23.5 in Fig. 5.27(a) show that the flow is well sustained before it slowly reduced in magnitude at the end of the domain. From the pattern of this time series, one clear peak at frequency 0.8125 Hz can easily be detected in Fig. 5.27(b), and this is the same frequency captured by the PSD of u' as shown in Fig. 4.36(a). However, there is only one peak can be detected in the far-field region. The second peak at frequency 1.562 Hz was no longer observed. The disappearance of the peak suggests that the turbulence is dissipated in the far wake region. The turbulence energy was absorbed by breaking down the eddies into smaller and smaller eddies until viscous forces eventually converted it into heat.

POD was employed in the far wake region where the wake structure's coherence is weaker than in the near wake. Accordingly, the energy in this region is expected to be spread over a less number of modes than the near wake Fig. 5.4(a). This is indeed shown in Fig. 5.28. The energy distribution among the modes was found to differ significantly from that observed in the near wake. The first and second modes have more or less similar energy contribution, which is about 25 times the third mode. This implies that the first two POD modes are enough to capture approximately 98.5% of the turbulent kinetic energy of the flow field.

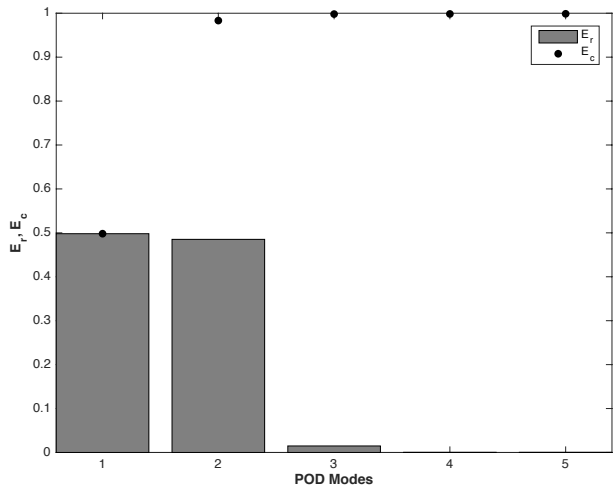

Figure 5.28: Relative and cumulative contribution of the POD modes for N, Re1k in the far wake region.

The most energetic POD mode, POD_1 was illustrated by the isosurface of its $|\omega|$ in Fig. 5.29 below:

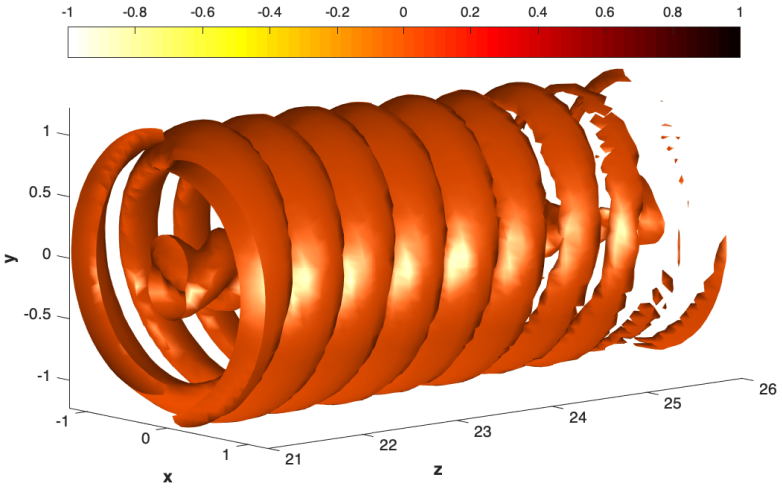

Figure 5.29: Isosurface plot of $|\omega| = 0.05$ corresponding to POD_1.

Next, the first four POD modes were plotted in Fig. 5.30. Notice there is a striking difference between the third and fourth modes, which reflects the difference in their energy contribution. On the other hand, the first two POD modes are quite similar as they contain the same energy. The POD_1 and POD_2, which are the most energetic modes in the far wake region, show a dipole structure, just like POD_1 and POD_2 in the near wake region (recall Fig. 5.5). Except that these two modes have a higher magnitude.

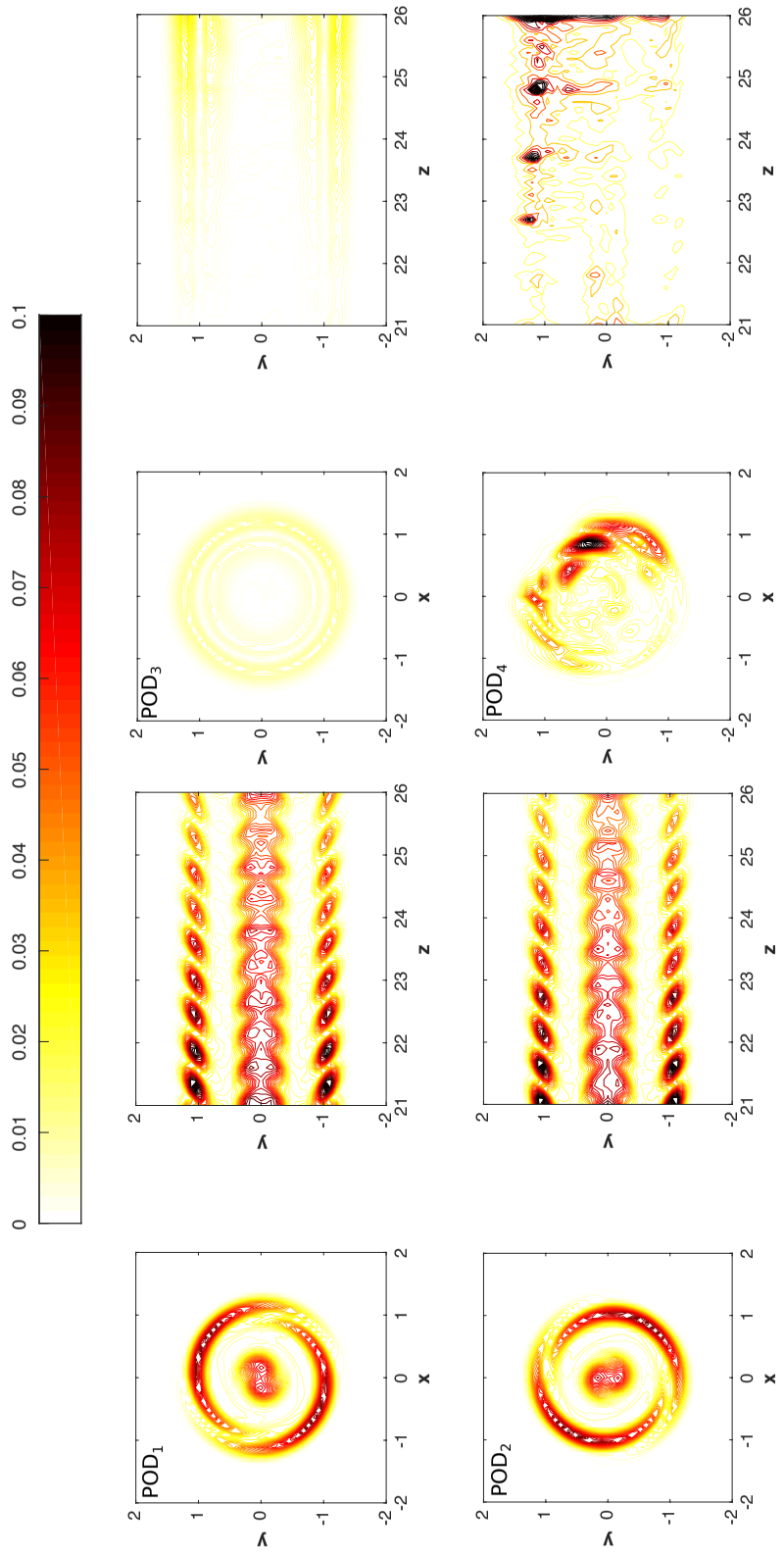

Figure 5.30: Contours of $|\omega|$ in Far Wake from N, Re1k.

As expected, the POD coefficients of the first two modes convincingly reflected as substantial cycle-to-cycle variations, as display in Fig. 5.31(a) and they change similarly to cosine and sine functions in a time-resolved study of the flow in Fig. 5.31(b). There is only one distinct amplitude peak at the frequency of 0.8125 Hz in Fig. 5.31(c) that readily picked up from both POD_1 & POD_2. Nevertheless, there is no correlation shown between POD_3 & POD_4, as in Fig. 5.31(i) since they are unpaired mode. On other hands, POD_3 acts as shift mode [17] in which it characterizes the base flow change between a steady and time-average periodic solution. This can be seen in Fig. 5.31(ii) as a solid line of POD_3 coefficient shows an increasing trend. The behaviour of the mode amplitudes corroborates this interpretation. POD_4, on the other hand, does not vary so regularly and caused the existence of several low-frequency peaks in the power spectra.

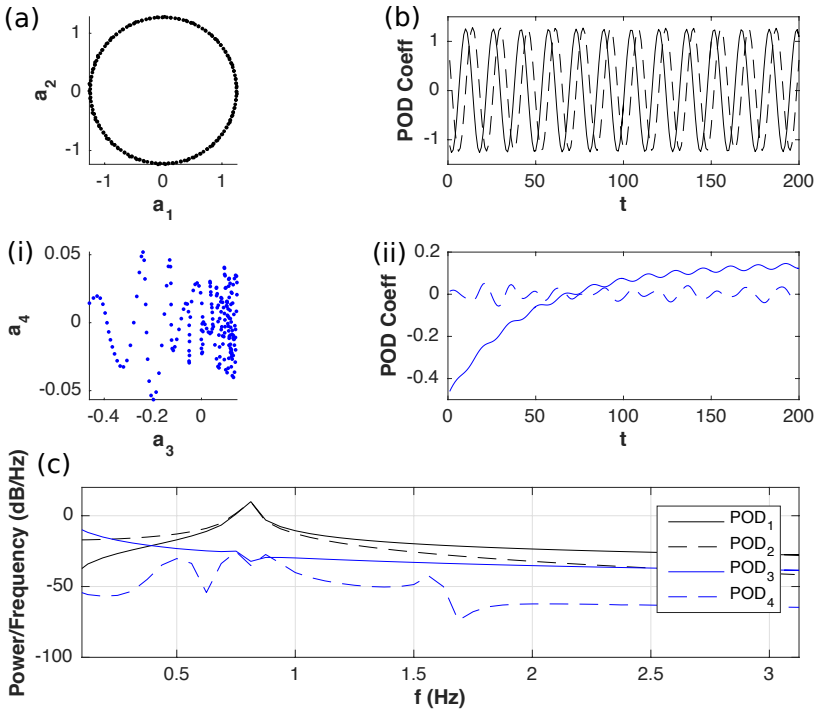

Figure 5.31: Caption as Figure 5.13, but for N, Re1k in the far wake region.

5.6 Chapter Summary

In the present chapter, a detail explanation on how the datasets were prepared before the modal analysis methods can be applied has been presented followed by a

comparison study on the separated and combined velocity-based POD as proposed by [86, 157] that both will give the same result in the near wake region but not in the far wake region. Even though the result from the present study agrees with the literature, it was decided to carry out the following POD and DMD analysis using the combined velocity. The POD analysis was done on the velocity field (the modes called POD modes) of the near and far wake region and on the temperature field (PODT modes), separately. Basically, the discussion on every section is about the energy distribution of POD/PODT modes, the spatial distributions of POD/PODT modes, and the coefficients of the first few energetic POD/PODT modes. Subsequently, DMD analysis will be presented and discussed in the upcoming chapter.

Chapter 6

Dynamic Mode Decomposition of the Helical Wake

In this chapter, the results from the DMD method will be presented, and the analysis of DMD in near wake, temperature field (DMDT), and far wake is to be discussed in Section 6.1, 6.2, and 6.3, respectively. Section 6.4 at the end of this chapter gives a conclusion of the chapter.

6.1 DMD Analysis of the Results in the near-field region

The temporal DMD analysis was performed, and the analysis was focused on parameters pertaining to the spatio-temporal behaviour of DMD modes such as modal energy, growth/decay rate, the eigenvalues & eigenvectors, and the mode coefficients. The result obtained for the wake flow in the range $6 < z < 11$ are shown with modes (most energetic modes corresponding to the one discovered in POD analysis) highlighted.

6.1.1 The Global Energy Norm

For the purpose of visualizing the DMD spectrum, the 'power' of each mode, $||\varphi||$ where φ obtained from Eq. 3.4.11 in Subsection 3.4.2.1 was plotted against its

frequency of oscillation, f. The norm of each mode indicated the energy in the corresponding mode. Fig. 6.1 plots the energy spectra of all DMD modes, in which each mode is accompanied by a vertical scaled with the magnitude of the mode at its corresponding frequency. Two modes with distinct amplitude peaks can be identified from the first case (N, Re1k), i.e., $f_1 = 0.7958$ Hz (after this will be called DMD_1) and $f_2 = 1.592$ Hz (DMD_2) in Fig. 6.1(a). Since the negative frequencies (refer to Eq. 3.4.5 in Subsection 3.4.2.1) correspond to the complex conjugate resulting from the decomposition process, only the positive frequency was shown in the figure. Here, the mode number sequences in terms of the magnitude of the global energy norm of each mode. Two to three modes have been selected, ranging from the highest to the lowest modal energy, as shown in Fig. 6.1.

The following Table 6.1 summarized the frequencies and energy spectra of Fig. 6.1.

Atmospheric Conditions	DMD Modes					
	DMD_1		DMD_2		DMD_3	
	f (Hz)	$\|\|\varphi\|\|$	f (Hz)	$\|\|\varphi\|\|$	f (Hz)	$\|\|\varphi\|\|$
N, Re1k	0.7958	24.4200	1.5920	0.8354	-	-
N, Re2k	0.8126	75.8300	1.6130	1.8890	2.19	2.445
WS, Re1k	0.7960	11.9300	0.9086	0.9083	1.0374	0.8739
SS1, Re1k	0.8025	14.9000	1.5800	2.3330	1.9565	1.4760
SS1, Re2k	0.7958	43.4900	1.5920	8.0220	2.3870	1.1260
SS2, Re1k	0.7958	15.96	0.9084	1.6670	-	-

Table 6.1: Power Spectra, $||\varphi||$ of temporal DMD modes with their respective frequency for all cases

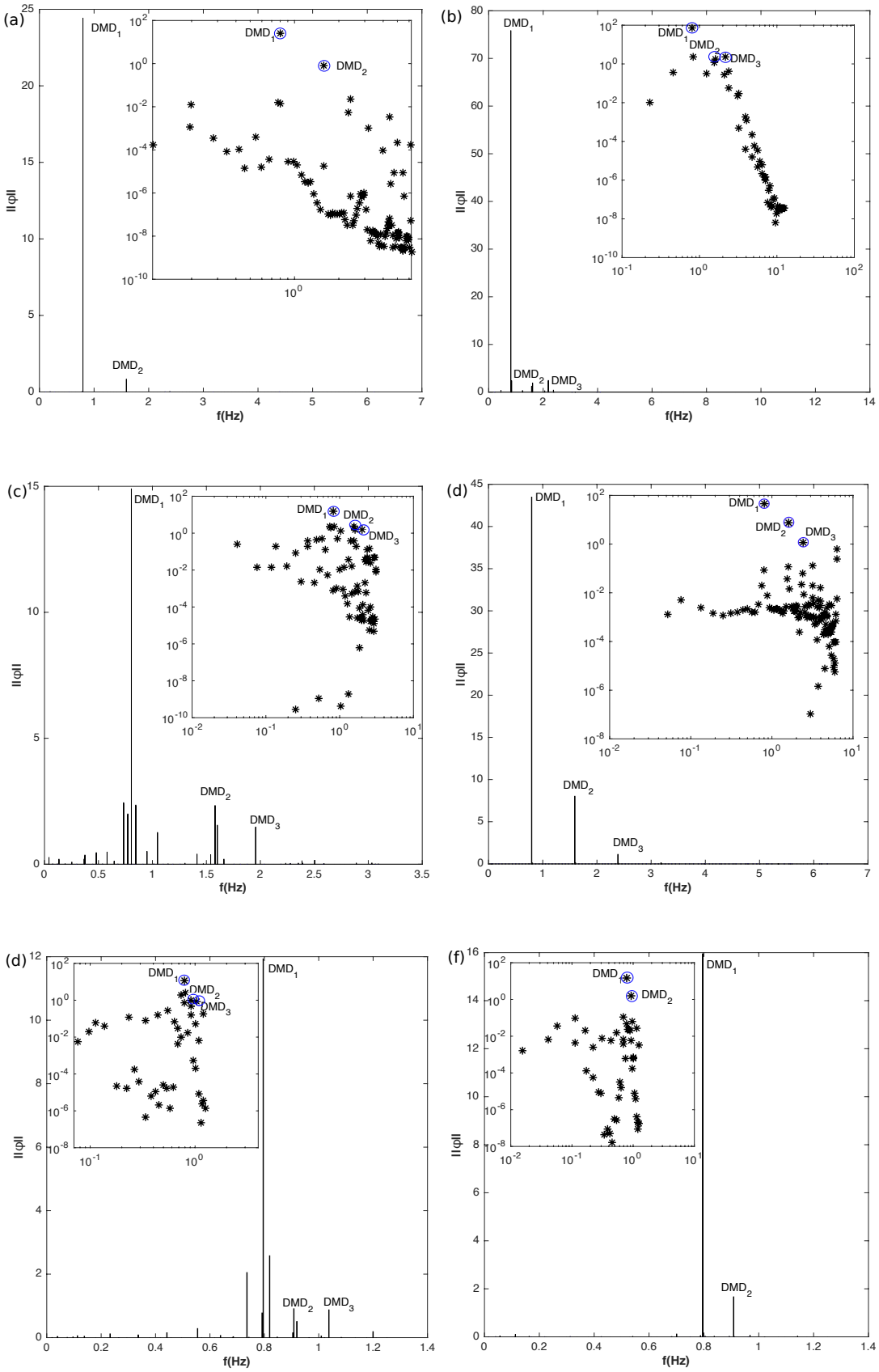

Figure 6.1: Energy Spectra of temporal DMD for (a) N, Re1k, (b) N, Re2k, (c) SS1, Re1k, (d) SS2, Re2k, (e) WS, Re1k, and (f) SS2, Re1k. Remark that the energy spectra were also plotted in log-log scale in the inside figure. The considered modes were circled by the blue marker and labelled accordingly.

In a brief glance, the energy contribution of the most dominant modes from both neutral cases is higher compared to all other stable cases. This proved that the coherent modes in atmospheric conditions without the temperature stratification are most durable. On the other hand, between both Reynolds numbers, the dominant modes of the case with Re = 2000 contained more energy than the case with Re = 1000. In contradict to the findings from the power spectrum of the instantaneous flow in Section 4.3 of Chapter 4, the most energetic DMD mode of N, Re2k contained the highest amount of energy, as shown in Fig. 6.1(b). This suggests that when the atmosphere is stratified, the turbulence level is low compared to the one without the stratification.

In analysing oscillatory dynamics, the Fourier transform, and power spectra are often used. By applying the FFT to the time series, one can determine approximate frequency values of the modes via the power spectrum before using a non-linear least-square solver to find growth rates of the modes. However, note that FFT analysis may be too inaccurate for exponentially growing or decaying oscillations. Recall Fig. 4.36 of Section 4.3, which shows the time series and the power spectrum provided by FFT and Fig. 6.1 was referred for DMD. While the DMD spectrum is sparse and is in excellent agreement with the time series, the FFT spectrum is seen to be fundamentally dense in the sense that the particular modes present in the time series are difficult to find. The DMD technique was applied to the wake flow measures in the global velocity field while the power spectrum method was applied to one time-step of the velocity field.

In Fig. 6.1(b), there are three amplitude peaks, which are DMD_1, DMD_2, and DMD_3, with the corresponding frequencies of 0.8126 Hz, 1.613 Hz, and 2.19 Hz, respectively are readily picked up from the extracted spectra based on the global energy norm of each mode. It is so much difference between the energy of the first mode compared to the second and third, which more or less have a similar energy contribution.

For strongly stable case 1, three energetic structures were extracted at frequencies 0.8025 Hz, 1.58 Hz, and 1.9565 Hz in the case with Re = 1000 as it can be seen in Fig. 6.1(c) and Fig. 6.1(d) clearly shows the three peaks with frequency 0.7958 Hz,

1.592 Hz, and 2.387 Hz from DMD_1, DMD_2, and DMD_3, respectively.

Lastly, the spectra obtained in Fig. 6.1(e) displays dominant peaks with three leading modes at frequencies 0.7960 Hz, 0.9086 Hz and 1.0374 Hz, respectively for the weakly stable atmospheric condition while for the second case of strongly stable, the two modes with the most substantial contributions to the total energy are the 0.7958 Hz, and 0.9084 Hz modes as can be found in Fig. 6.1(f).

In short, the magnitude of f_2 (from all cases except for WS, Re1k and SS2, Re1k) and f_3 (from SS1, Re2k) is just the integral multiple of the fundamental frequency, f_1 representing the higher-order harmonics in the flow field. It is not surprising to find that the f_1 is equal to the vortex shedding frequency since vortex shedding dominates the dynamics of wake flow. Altogether, the same dominant frequencies identified from the POD analysis in previous Chapter 5 were successfully extracted from the DMD method.

The drawback of the POD method is that it obtains the flow fields by statistical means, thus losing the phase information of the system. Because POD modes are still doped with vortex structures at a different frequencies, it is difficult to analyse the original flow field from the complex point. Coincidentally, the decomposition and extraction in DMD techniques are based on flow field dynamics, and the modes obtained are time irrelevant.

6.1.2 The Eigenvalues & Eigenvectors

The eigenvalues, λ (also known as the Ritz values), and DMD spectrum of all the DMD modes were subsequently calculated. Eventually, the spatial distributions of each dominant mode obtained from its eigenvectors as in Eq. 3.4.11 was illustrated using the contours of $|\omega|$. Note that for brevity, only the real part of each mode is being considered as a similar agreement is observed in the imaginary parts [58].

Observing the real and imaginary components of the eigenvalues determines the stability and energy of each mode. The unstable modes will grow in time, while the stable modes decay. In both spectra, the stable eigenvalues which are located inside the unit disk and in the left half-plane, respectively, were observed. The real and imaginary parts of the extracted Ritz values, λ (as listed in Table 6.2) shown in

Atmospheric Conditions	λ of DMD Modes		
	DMD_1	DMD_2	DMD_3
N, Re1k	$0.9211 + 0.3895i$ $(0.0005 + 5.0003i)$	$0.6967 + 0.7174i$ $(0 + 10.0001i)$	-
N, Re2k	$0.9802 + 0.2030i$ $(0.0246 + 5.1058i)$	$0.9130 + 0.3919i$ $(-0.1611 + 10.1376i)$	$0.6479 + 0.39751i$ $(-6.8571 + 13.7582i)$
WS, Re1k	$-0.4164 + 0.9088i$ $(-0.0008 + 5.0011i)$	$-0.6539 + 0.7567i$ $(0.0001 + 5.7086i)$	$-0.7066 + 0.4182i$ $(-0.4928 + 6.518i)$
SS1, Re1k	$0.6892 + 0.7233i$ $(-0.0058 + 5.0592i)$	$-0.0180 + 0.9940i$ $(-0.0369 + 9.9304i)$	$-0.3105 + 0.7423i$ $(-1.3588 + 12.2932i)$
SS1, Re2k	$0.9210 + 0.3894i$ $(-0.0005 + 5i)$	$0.6967 + 0.7173i$ $(-0.0003 + 10i)$	$0.3624 + 0.9320i$ $(-0.0002 + 15i)$
SS2,Re1k	$-0.4162 + 0.9093i$ $(0 + 5.0001i)$	$-0.6536 + 0.7568i$ $(0 + 5.7079i)$	-

Table 6.2: The eigenvalues, λ of temporal DMD modes for all cases with their logarithmic mapping in the form $(\sigma + oi)$.

Fig. 6.4(left) tend to be well distributed on the unit circle in the complex pane of $|\lambda| = 1$, with the exception of only several points locating inside the unit circle. This indicates that the states of the dynamic system evolve on an attractor, while those dynamic modes fallen inside the unit circle might have resulted from contamination of measurement noise. Also, the most dominant mode typically has Ritz values of $|\lambda| = 1$. The eigenvalues then were transformed via the logarithmic mapping and shown in Fig. 6.4(right). The real part of the eigenvalues, σ, gives the growth/decay rate of the mode while the imaginary part, o provides its frequency. Generally, the eigenvalues with real components ≈ 0 contain the highest energies with less damping and are worthy of analysis.

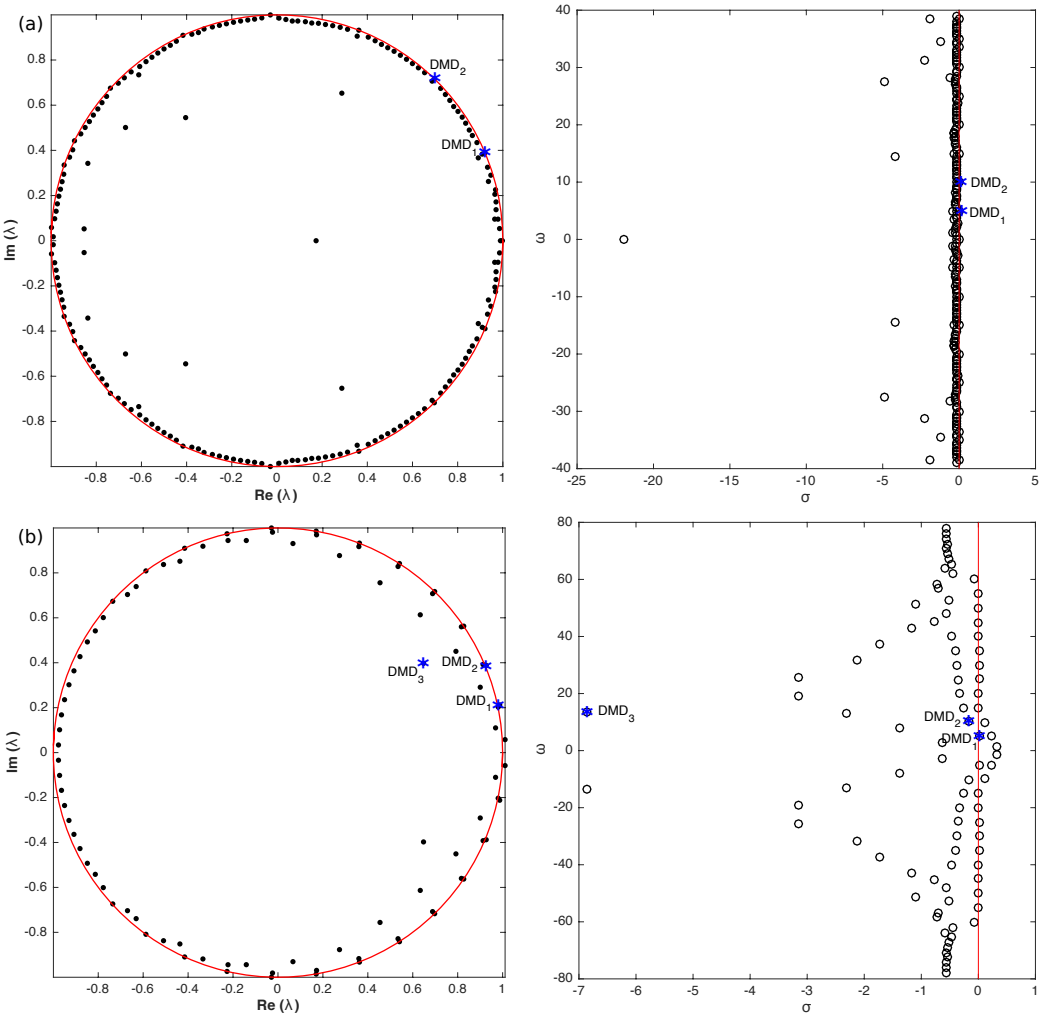
(a)
DMD2
DMD1
Im (λ)
Re (λ)
ω
σ
DMD2
DMD1
(b)
DMD3
DMD2
DMD1
Im (λ)
Re (λ)
ω
σ
DMD3
DMD2
DMD1

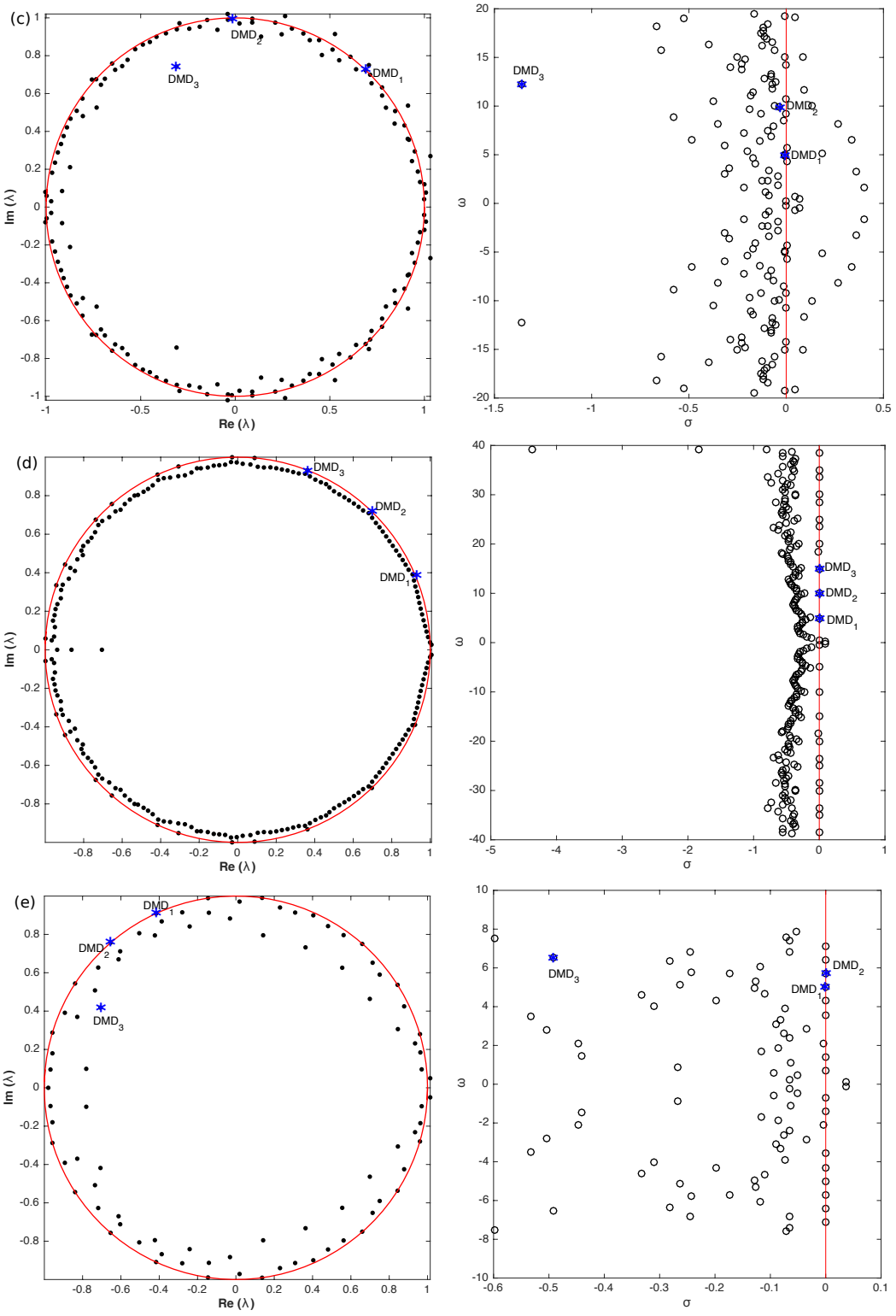
(c)
DMD1
DMD2
DMD3
Re (λ)
Im (λ)
σ
ω
(d)
DMD1
DMD2
DMD3
Re (λ)
Im (λ)
σ
ω
(e)
DMD1
DMD2
DMD3
Re (λ)
Im (λ)
σ
ω

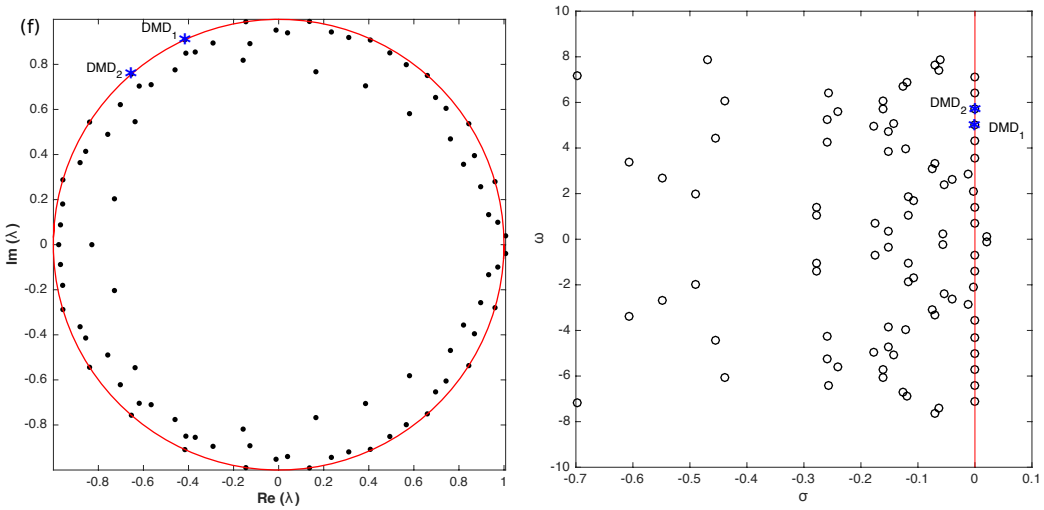

Figure 6.4: Dynamic eigenvalue characteristics of (a) N, Re1k, (b) N, Re2k, (c) SS1, Re1k, (d) SS1, Re2k, (e) WS, Re1k, and (f) SS2, Re1k. Ritz values (left) and DMD spectra (right) of temporal DMD modes. All considered modes marked by the blue star and labeled accordingly.

The eigenvalues of the first two dominant modes from every case, DMD_1 and DMD_2, were observed to lie exactly on the unit circle in the left figure of Fig. 6.4(a) – (f) and on the red line of the right figure. This explains the stability of the first two modes, which decayed over time and least damped. Taking DMD_1 with frequency $f_1 = \frac{o}{2\pi} = 0.7958$ Hz from N, Re1k as an example, the mode was observed to decay over time in the stable region since $\sigma_1 \approx 0$. This behaviour is expected once the mean flow was subtracted [80].

Different from the first two modes, DMD_3 from neutral at Re = 2000, strongly stable case 1 at Re = 1000, and weakly stable, which is a high-frequency mode with lower energy lies inside the unit circle as shown in the left figure of Fig. 6.4(b, c, e). The eigenvalues in the interior of the unit circle are strongly damped. Thus, they influence only early stages in the time evolution. While in the logarithmic mapping (refer to the right figures of Fig. 6.4(b, c, e)), that particular mode lies on the far left of the figure, and this shows how the mode severely decayed and become the most decayed mode.

Also, for some cases like SS1, Re1k, it was observed that there is several modes lay outside of the unit circle and located on the right half-plane of the logarithmic mapping figure, which proved the existing of unstable/grow modes. These high-frequency and low energy modes with severe temporal growth are not really interesting and hence will not be analysed further.

Last but not least, Fig. 6.5 – Fig. 6.10 are referred for the $|\omega|$ plots corresponding to each dominant mode. Since the frequency of the higher modes, DMD_3, and DMD_2 are larger than DMD_1, the spatial scale associated with this mode is correspondingly smaller, and this pattern can be noted in all figures from Fig. 6.5 to - Fig. 6.10. It is also known that each mode represents a flow structure that oscillates with one single frequency, and the superposition of several of these modes results in the quasi-periodic global system. For example, the spatial structures of modes with frequency 0.7716 Hz and 0.8462 Hz (see Fig. 6.1(c)) in SS1, Re1k are very similar to those of DMD_1, which elucidated in Fig. 6.7, as one expects since the frequencies are very close.

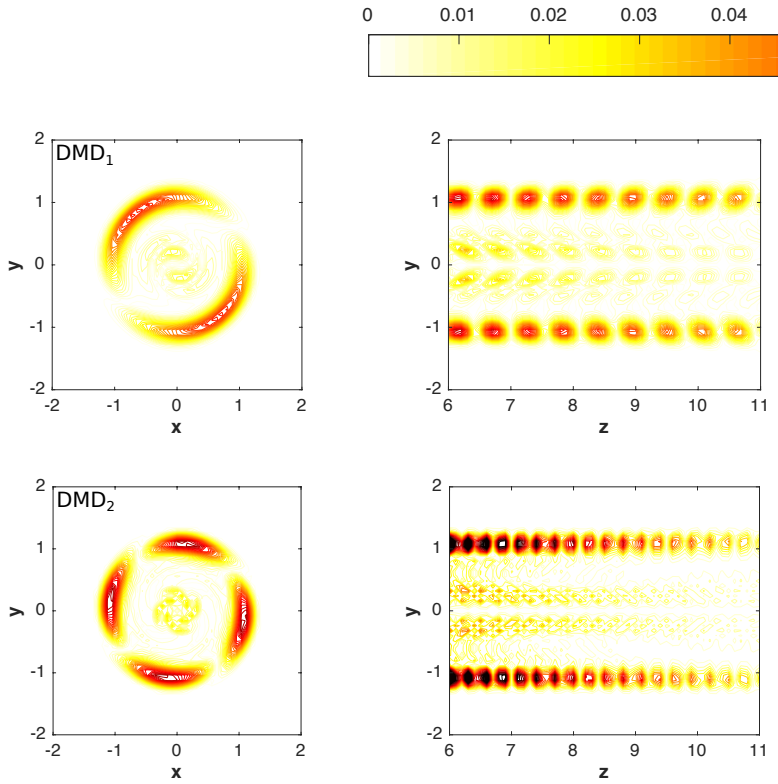

Figure 6.5: Contour plots of $|\omega|$ visualized by the real part of corresponding dominant modes, i.e DMD_1 (above) followed by DMD_2 and DMD_3 (if any) with λ values listed in Table 6.2, respectively in xy-cut at $z = 8.5$ (left) and zy-cut at $x = 0$ (right) for N, Re1k.

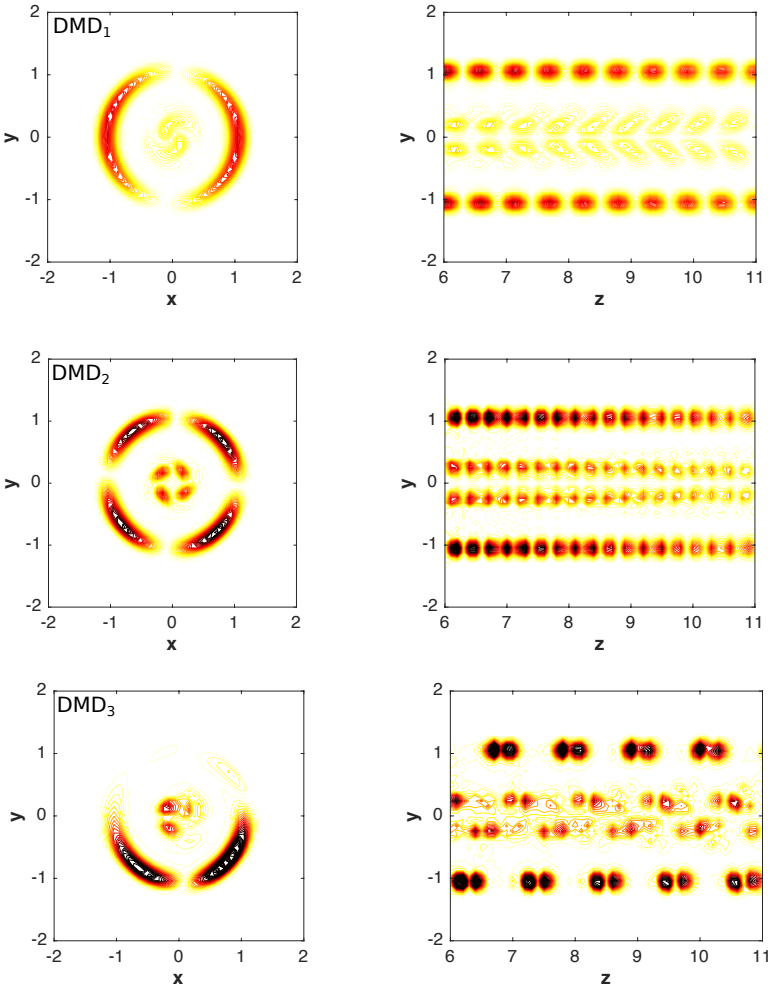

Figure 6.6: Caption and colormap as Fig. 6.5, but for N, Re2k.

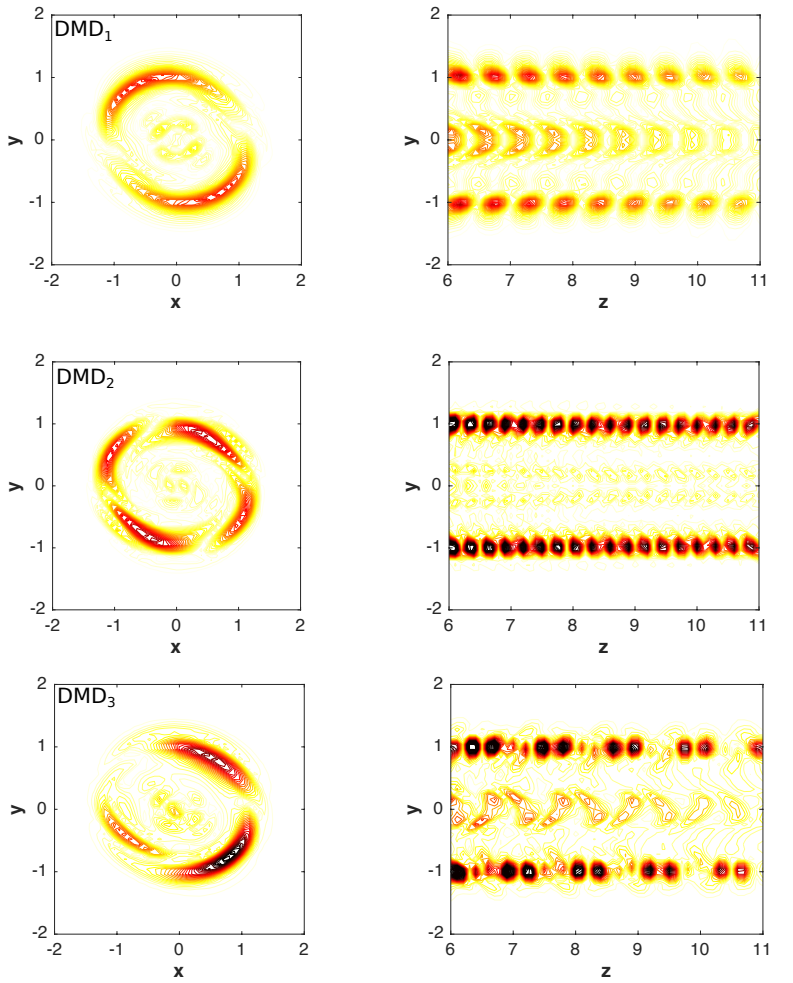

Figure 6.7: Caption and colormap as Fig. 6.5, but for SS1, Re1k.

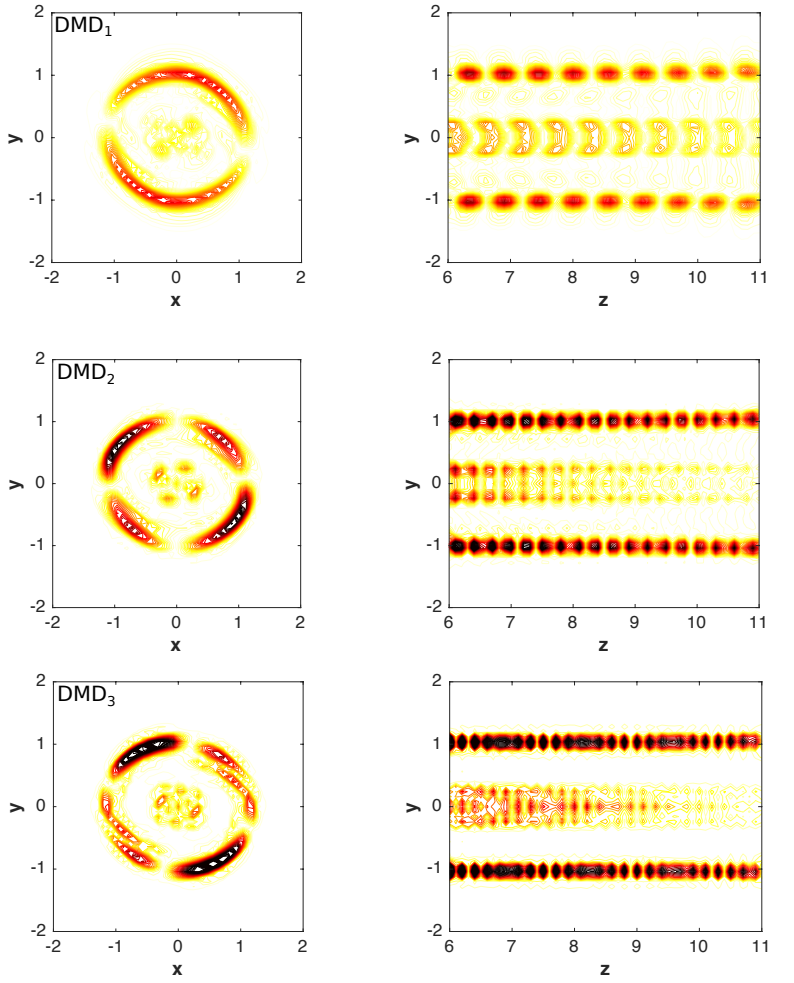

Figure 6.8: Caption and colormap as Fig. 6.5, but for SS1, Re2k.

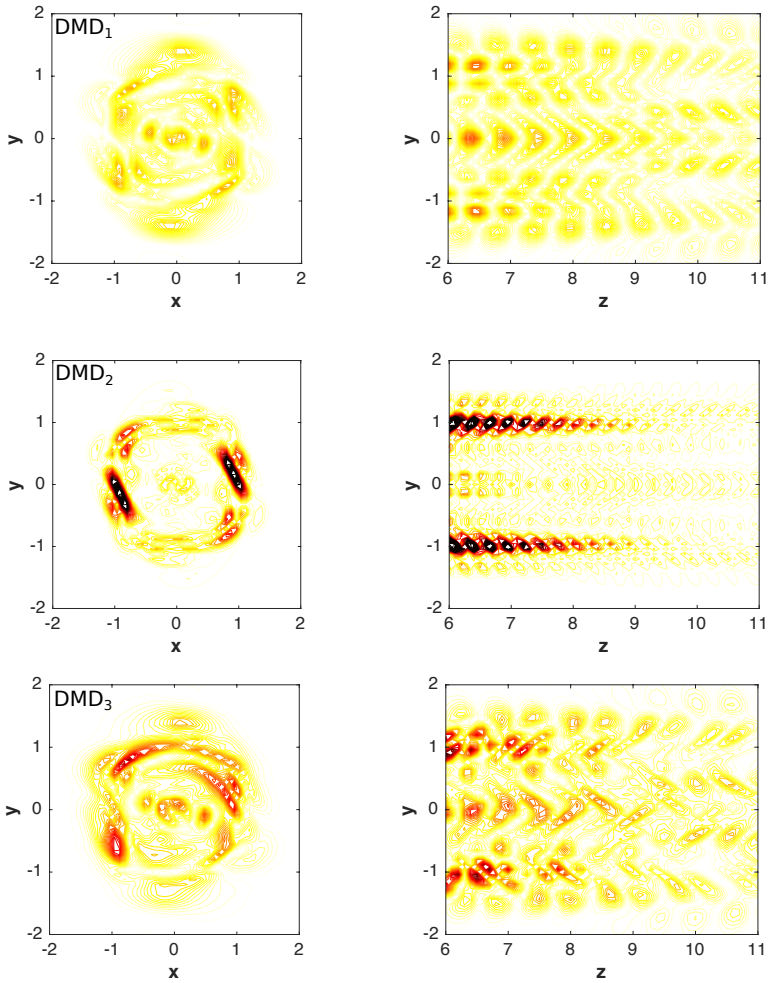

Figure 6.9: Caption and colormap as Fig. 6.5, but for WS, Re1k.

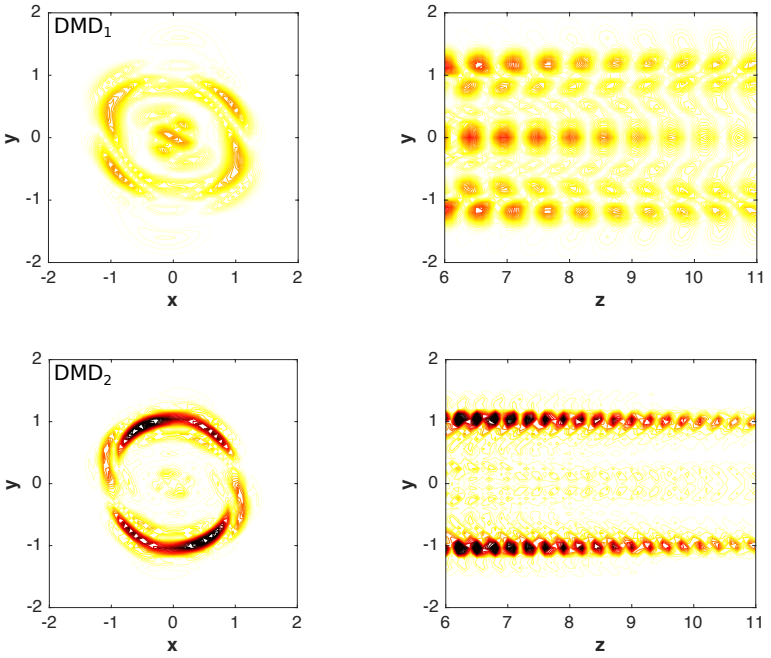

Figure 6.10: Caption and colormap as Fig. 6.5, but for SS2, Re1k.

Just like in POD modes, similar observation of vortex multi-pole formation was noted in the first two DMD modes of all cases (excluded the two cases from WS, Re1k and SS2, Re1k), and hence, the same arguments are applicable for this situation. From all these dipole and quadrupole structures, it is clear that the first two dynamic modes present periodically convect vortices in a hierarchy of descending scale, e.g., higher-order harmonics have finer-scale structures. These multi-pole observations indicate approximate statistical isotropy [39]. ABL clearly breaks the rotational symmetry. The extracted wake structure, therefore, behaves approximately isotropic in the non-isotropic ABL flow. [29]. Even there is no multipole-like structure observed in DMD modes from WS, Re1k and SS2, Re1k cases, the modes still show the same structure as the one from POD analysis in Chapter 5. Thus, the same arguments are valid for this result. A complex vortex flow was illustrated by DMD_3 of WS, Re1k, as the Fig. 6.9 showed a very messy, chaotic contour plot.

It is however, not necessarily the case for DMD_3 of N, Re2k, and SS1, Re1k. An expected hexapole-like structure could not be elucidated from DMD_3, instead, a vortex merging structure was observed. The spatial pattern of the mode depicts a highly damped (severe temporal decayed) asymmetric mode that spatially merged the two helical vortices. These co-rotating vortices travel (almost) the same distance side by side, as this can be seen in the zy-cut of Fig 6.5. On the other hand, DMD_3 of SS1, Re2k does show the hexapole-like structure, but two of the helical were moving closely together.

For better visualization of the most coherent mode, DMD_1, the isosurface of its $|\omega|$ in streamwise direction for all cases were plotted in Fig. 6.11 below:

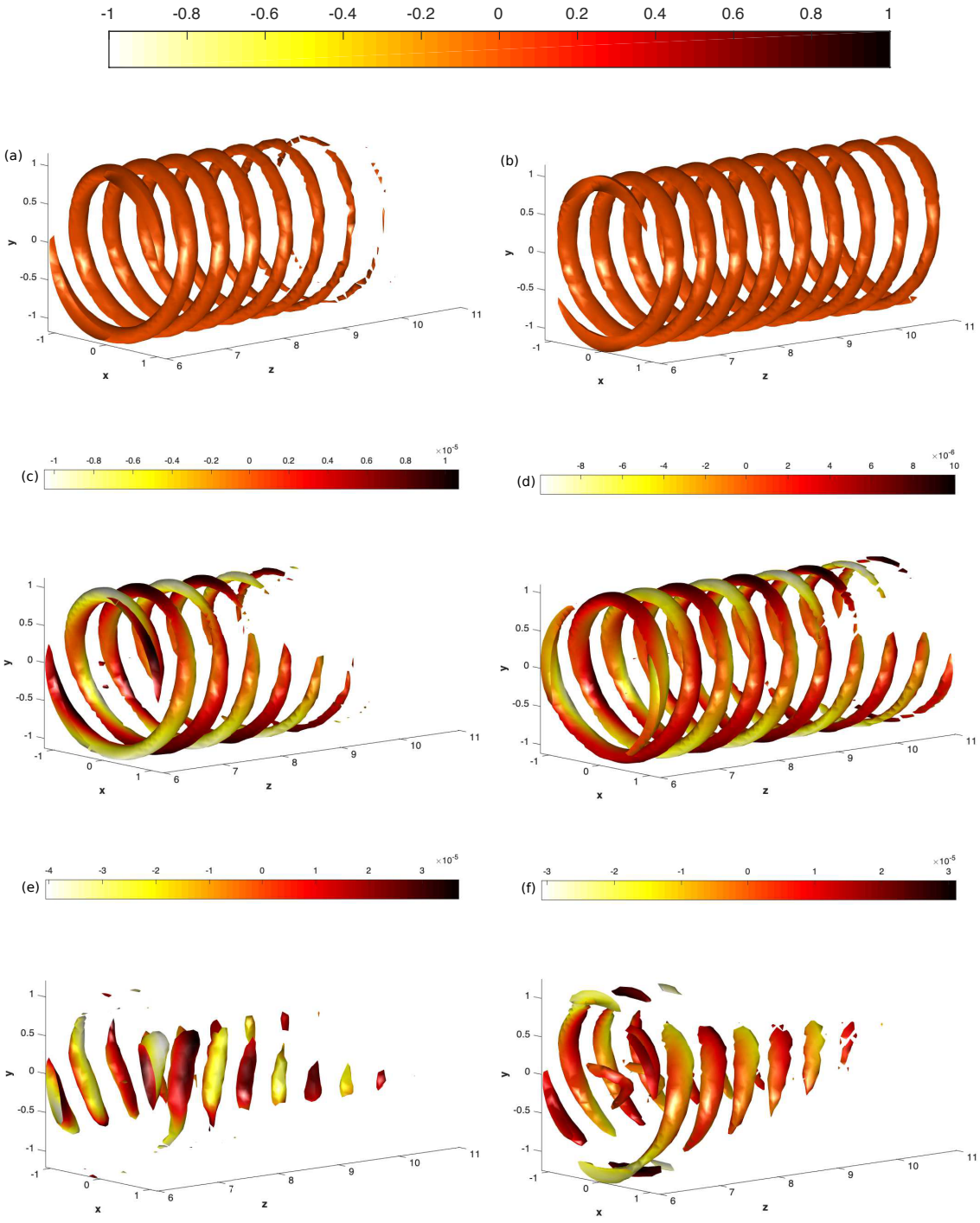

Figure 6.11: Isosurface of $|\omega| = 0.05$ DMD_1 for: (a) N, Re1k, (b) N, Re2k, (c) SS1, Re1k, (d) SS1, Re2k, (e) WS, Re1k, and (f) SS2, Re1k cases coloured by their respective DMD_1 of temperature field.

6.1.3 The DMD Mode Coefficients

The DMD mode coefficient, a_i which is the coefficient used when reconstructing the flow field with isolated dynamic modes was determined by

$$V_1^{N-1}(z,x,y) = \sum_{i=1}^{N-1} a_i(t)\varphi_i(z,x) \tag{6.1.1}$$

where a_i takes the form of $a_i(t) = e^{(\omega_r + i\omega_i)t}$; V_1^{N-1} is the input vector, and φ_i is the dynamic modes. The complex exponential of a_i is a complex-valued signal which simultaneously encapsulates a cosine wave as well as a sine wave by posting them on the real and imaginary components of the complex wave. In the exponential, the real part indicates the growth rate and the imaginary part indicates the oscillation frequency.

As stated by [182], the real and imaginary parts of a single DMD mode coefficient can be used to disclose the phase information of the respective vortical structure. For this reason, the correlation map of the considered DMD modes was plotted in Fig. 6.12(a, i , I) – Fig. 6.17(a, i , I). In this study, the phase shift is defined as any change that occurs in the phase difference between the real and imaginary part of the coefficient. In addition, the phase difference is the difference (expressed in degrees or radians) between the real and imaginary part of the DMD mode coefficient, which definitely having the same frequency and referenced to the same point in time. Now, the real and imaginary part of the DMD coefficient is said to be in phase if they oscillate together and cross the time, t at the same point in the same direction, otherwise, they are out of phase. The well-organized circular patterns of the first coherent mode, DMD_1 in all cases, as shown in Fig. 6.12(a) – Fig. 6.17(a) is convincingly reflected as strong cycle-to-cycle variations in the vortex-shedding processes. On the other hand, the distortion of the circular shape indicates variations in the phase differences, whereas the oscillation amplitudes changes caused dispersion of the circulation.

Next, in order to study the temporal variation in the above-mentioned DMD modes, the real and imaginary part of DMD mode coefficients were plotted together in Fig. 6.12(b, ii , II) – Fig. 6.17(b, ii , II). A global view of time-varying coefficients demonstrated their perfect periodic fashions. Recall the amplitude of the

DMD mode coefficients reflects the global trend of the corresponding event, which represents its growth or decay trend. Overall, the coefficients of DMD_1 from all cases do not represent appreciable variation in the peak magnitude, as depicted in Fig. 6.12(b) – Fig. 6.17(b). Besides, the amplitudes in higher mode (refer to DMD_2) were relatively small compared to in DMD_1 for all cases, as expected based on the eigenvalues. There is, however an exception for DMD_3 which will be discussed further in the following paragraph.

According to the Nyquist criterion, with a sampling interval of Δt, the highest frequency of $f = (2\Delta t)^{-1}$ was expected to be resolved. Note that the DMD technique is subject to the Nyquist frequency criterion for high frequencies, but it can determines modes with frequency even lower than the one given by the total time spanned by the snapshots [80]. Besides, the separation between samples must reflect the characteristic time-scale of the fluid phenomenon under investigation of a limited number snapshots. A too low (below the Nyquist frequency) or too high sampling frequency will yield unsatisfactory outcomes [126]. Following this, a PSD analysis was performed on the time-varying mode coefficients, and the spectrum curves are depicted in Fig. 6.12(c, iii, III) – Fig. 6.17(c, iii, III). As it has been mentioned earlier in the previous paragraph, DMD_1 mode with the real and imaginary part of its coefficients oscillate in a fixed amplitude resulting in the existence of a clear single dominant peak at $f_1 = 0.8125$ Hz, 0.8065 Hz, 0.8065 Hz, 0.7955 Hz, 0.8056Hz, and 0.7967 Hz, as elucidated in Fig. 6.12(c) – Fig. 6.17(c), respectively with no other peaks are detected. This is consistent with the afore-mentioned discussion in Section 6.1.1. Remark that this is an alternative analysis to extract the frequencies of the DMD modes besides the analysis discussed in Section 6.1.1 earlier.

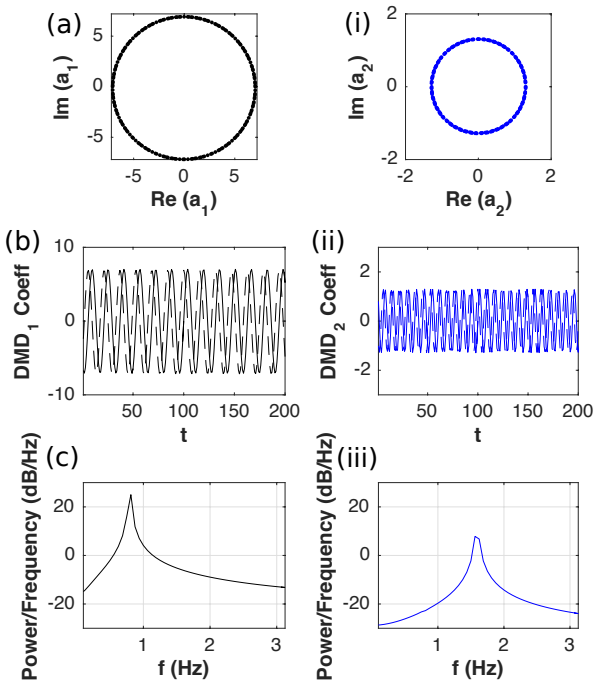

Figure 6.12: DMD Mode Coefficients characteristics of N, Re1k. (a, i, I) Correlation Maps, (b, ii, II) Time Variation, and (c, iii, III) Power Spectra Analysis, PSD. The black (a, b, c), blue (i, ii, iii) and red (I, II, III – if any) dots/lines are representative of DMD_1, DMD_2, and DMD_3, respectively. Note also the solid line in (b, ii, II) represents the real part of DMD Mode Coefficients while the dashed line refers to the imaginary part.

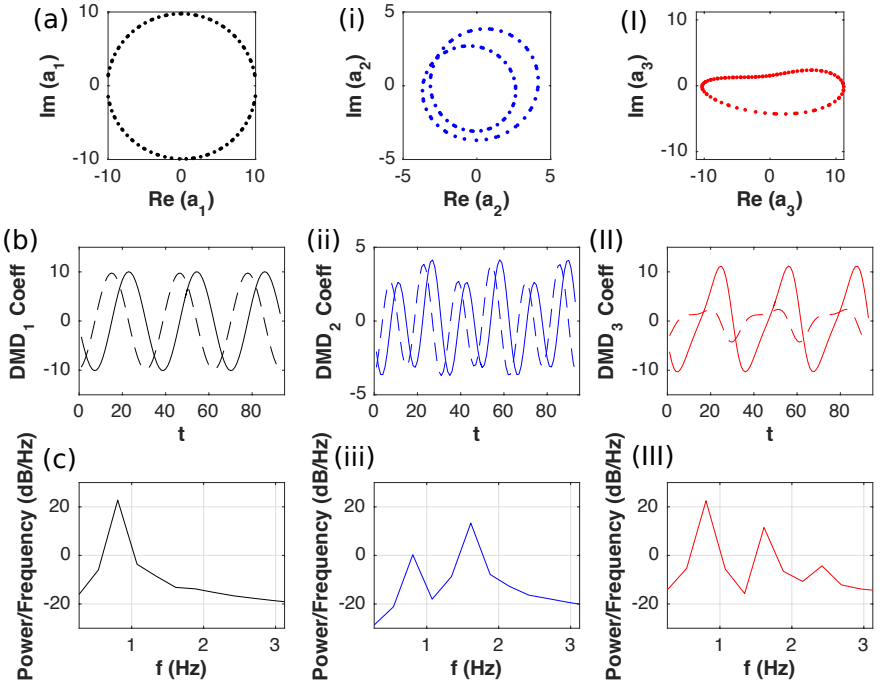

Figure 6.13: Caption as Fig. 6.12, but for N, Re2k.

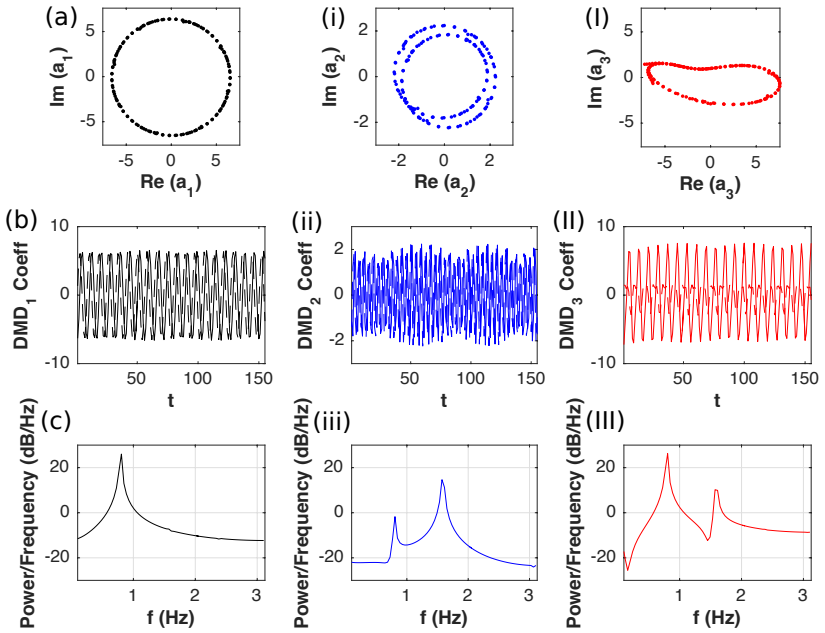

Figure 6.14: Caption as Fig. 6.12, but for SS1, Re1k.

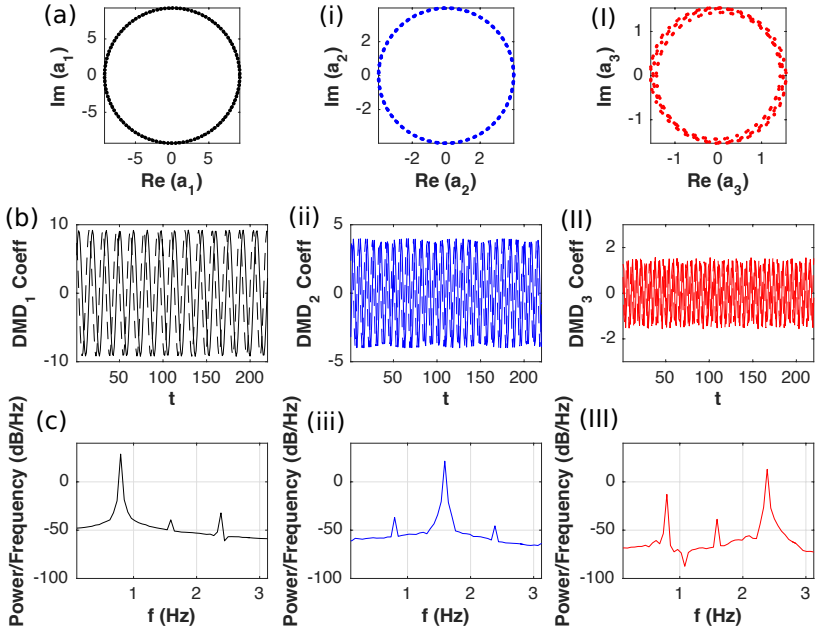

Figure 6.15: Caption as Fig. 6.12, but for SS1, Re2k.

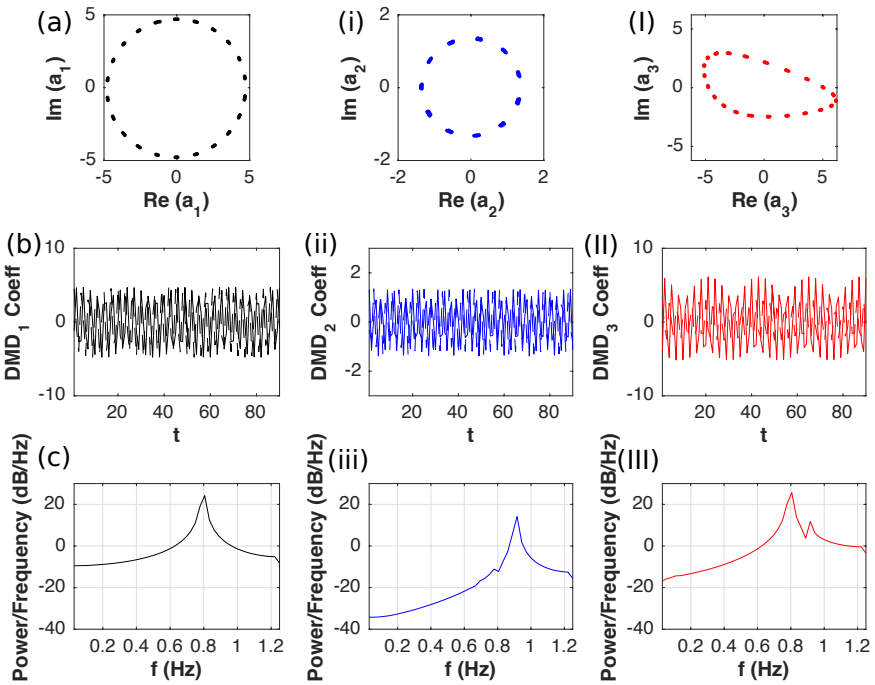

Figure 6.16: Caption as Fig. 6.12, but for WS, Re1k.

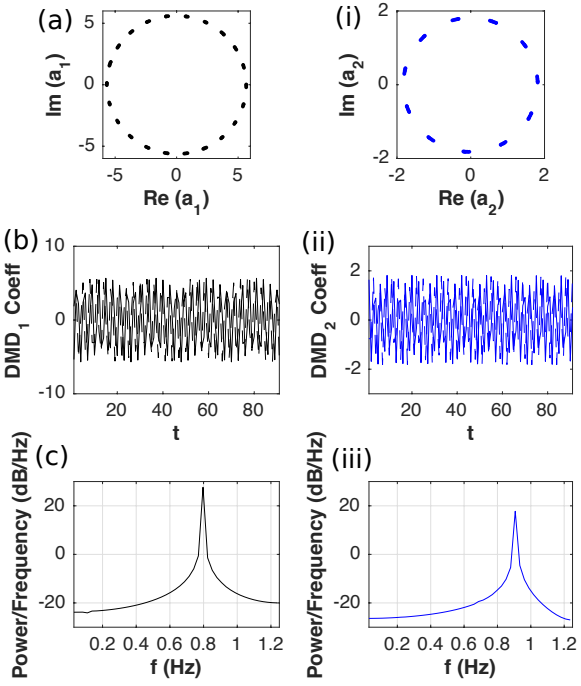

Figure 6.17: Caption as Fig. 6.12, but for SS2, Re1k.

Atmospheric Conditions	f (Hz)		
	DMD_1	DMD_2	DMD_3
N, Re1k	0.8125	1.5620	-
N, Re2k	0.8065	0.8065 1.6130	0.8065 1.6130 2.4190
WS, Re1k	0.8056	0.9167	0.8065 0.9167
SS1, Re1k	0.8065	0.8065 1.6130	0.8065 1.6130
SS2, Re2k	0.7955 1.5910 2.3860	0.7955 1.5910 2.3860	0.7955 1.5910 2.3860
SS2, Re1k	0.7967	0.9066	-

Table 6.3: Frequencies, f captured by DMD modes coefficients for all cases.

The correlation maps of DMD_2 mode coefficients of all cases except for neutral case at Re = 2000 and strongly stable case 1 at Re = 1000, display a circular pattern (refer to their figure (i)) and present periodical variation with amplitude almost fixed over periods (figure(ii)), providing further evidence that these dynamic modes are neutrally stable with time. Their spectrum curves in their figure(iii) determined a single dominant frequencies of $f_2 = 1.562$ Hz, 1.613 Hz, 0.9167 Hz, and 0.9066 Hz, respectively for the case N, Re1k; SS1, Re2k; WS, Re1k; and SS2, Re1k. This is again agreed with the result from Section 6.1.1.

Meanwhile, for the exceptional cases, the dispersion of the circular shape was obviously illustrated by DMD_2 mode coefficients, as can be identified in Fig. 6.13(i) & Fig. 6.14(i). This suggests that there are changes in the amplitudes of DMD_2, and Fig. 6.13(ii) & Fig. 6.14(ii) supported this suggestion. Because of this, there are two peaks extracted in spectra curves of DMD_2 at $f_2 = 0.8065$ Hz and 1.613 Hz (dominant peak), as shown in Fig. 6.13(iii) and $f_2 = 0.8065$ Hz and 1.573 Hz

(dominant peak) in Fig. 6.14(iii). These multiple peaks indicate the presence of mixed frequencies.

As for the last considered mode in this study, the distortion of the circular shape illustrated in Fig. 6.13(I), 6.14(I), and 6.16(I) proved that DMD_3 of these cases is an "out-of-phase" mode, and the mode amplitudes shown in Fig. 6.13(II), 6.14(II), and 6.16(II) supported this, as both of their real and imaginary parts of the coefficients vary irregularly and totally different from each other. This explains why there are multiple peaks at $f_3 = 0.8065$ Hz (dominant peak), 1.6130 Hz, and 2.419 Hz for N, Re2k; $f_3 = 0.8065$ Hz (dominant peak) and 1.573 Hz for SS1, Re1k; and $f_3 = 0.8056$ Hz (dominant peak), 0.9167 Hz for WS, Re1k in the PSD graph of this particular mode coefficient (see Fig. 6.13(III), 6.14(III), and 6.16(III), respectively). On top of this, none of the captured frequencies matched the one from Section 6.1.1. This comes to a conclusion where an "out-of-phase" mode can not be used to estimate the frequency of a flow system.

Furthermore, from all the previous discussions (recall its energy contribution, eigenvalue and eigenvector behaviours) on this third mode, it is finally concluded as just a random mode with no important role in the wake flow because of its low energy, high frequency, most decayed and lastly can't be used to estimate frequency.

On the other hand, there are exciting things about the three most energetic modes of the most strongly stable case at Re = 2000 (refer to Fig. 6.15). All the DMD mode coefficients were observed with a well-organized circular pattern in Fig. 6.15(a, i, I) and the variation of these three DMD mode coefficients, as shown in Fig. 6.15(b, ii, II) reveal that it contains by construction only a single frequency component. However, the fact that Fig. 6.15(c, iii, III) which shows the peak frequencies of $f_1 = 0.7955$ Hz (dominant peak), 1.591 Hz, and 2.386 Hz, $f_2 = 0.7955$ Hz, 1.591 Hz (dominant peak), and 2.386 Hz, and $f_3 = 0.7955$ Hz, 1.591 Hz, and 2.386 Hz (dominant peak) are distinctly discriminated in the spectrum of DMD_1, DMD_2, and DMD_3 mode coefficients, respectively gave a disagreement to this. Even so, those multiple peaks suggesting the existence of harmonic structure since the second and third frequency is approximately twice and thrice higher than the first one.

For overall comparison with POD analysis in previous Chapter 5, it came to the conclusion that the first two most coherent DMD modes were the same as the first two pairs of most energetic POD modes. Meanwhile, the DMD_3 for some instances is just another unstable modes with high energy. Similar to the energetic POD modes, these stable coherent DMD modes are identical to the corresponding wake flow structure and well-captured the same dominant frequencies identified in fluctuating streamwise velocity analysis in previous Chapter 4.

6.2 DMD Analysis of the Temperature Field

Moving to the temperature DMD (DMDT), the energy of the extracted modes are shown as a function of frequency in Fig. 6.18, where each DMDT mode is displayed with the vertical line scaled with its magnitude at its corresponding frequency. The most dominant DMDT mode from the first strongly stable case at $Re = 1000$ is the one with frequency $f_1 = 1.479$ Hz followed by $f_2 = 0.7967$ Hz and $f_3 = 0.3908$ Hz in Fig. 6.18(a). The other two DMDT modes with frequency 1.5926 Hz and 1.9607 Hz were highlighted and labelled with the pink font. These $DMDT_{2^*}$ and $DMDT_{3^*}$ modes are the modes with the same frequency as the second and third energetic modes identified from the DMD method on the velocity field. Meanwhile, $DMDT_2$ with frequency 0.7967 Hz shared the same frequency as DMD_1. However, the three amplitude peaks from SS1, Re2k, which are $DMDT_1$, $DMDT_2$, and $DMDT_3$ with the corresponding frequencies of 0.7958 Hz, 2.3908 Hz, and 1.5915 Hz as can be referred in Fig. 6.18(b) have exactly the same frequency as the three energetic DMD modes in the previous discussion.

The spectra obtained in Fig. 6.18(c) displays dominant peaks with three leading modes at frequencies 0.7959 Hz, 0.6422 Hz, and 0.9753 Hz for WS, Re1k. Just like SS1, Re1k, which their second and third modes frequency different to the previous DMD_2 and DMD_3, the two DMDT modes matched the frequency are $DMDT_{2^*}$ and $DMDT_{3^*}$ where $f_{2*} = 0.9086$ Hz and $f_{3*} = 1.0213$ Hz, respectively. For the second case of strongly stable, $DMDT_1$ and $DMDT_3$ of the first three dominant modes with frequency 0.7958 Hz, and 0.9084 Hz, respectively, shared the same frequency

as DMD_1 and DMD_2 while $DMDT_3$ in Fig. 6.18(d) with $f_3 = 0.9084$ Hz does not match any dominant mode in DMD of the velocity field.

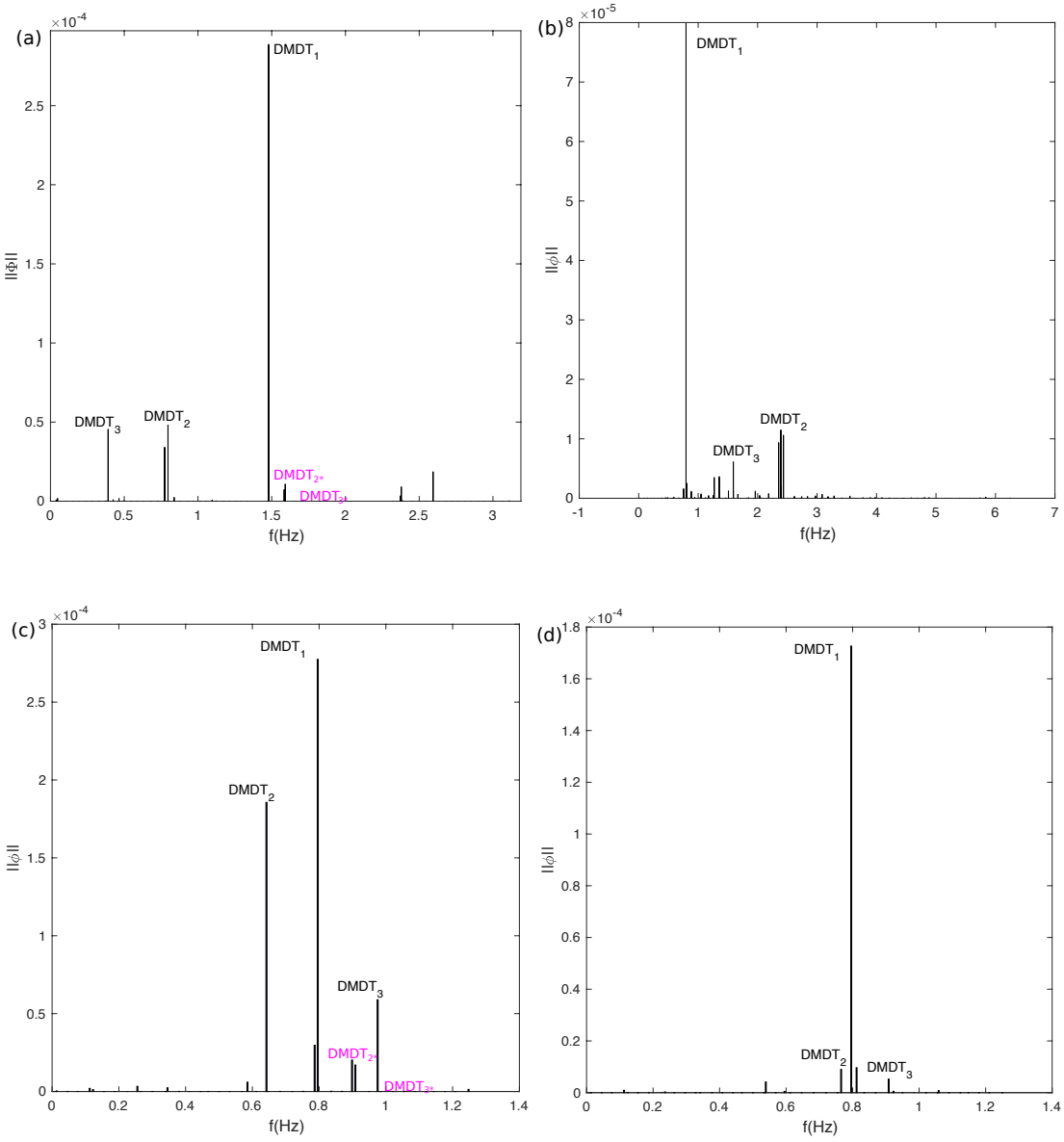

Figure 6.18: Energy Spectra of temporal DMDT Modes in Near Wake for: (a) SS1, Re1k, (b) SS1, Re2k, (c) WS, Re1k, and (d) SS2, Re1k. Remark that the three first DMDT modes with higher energy level were labelled by $DMDT_1$, $DMDT_2$, and $DMDT_3$ while the pink $DMDT_{2*}$, and $DMDT_{3*}$ are two DMDT modes with the same frequency as DMD_2 and DMD_3 from previous analysis of velocity field.

Atmospheric Conditions	λ of DMDT Modes				
	$DMDT_1$	$DMDT_2$	$DMDT_3$	$DMDT_{2^*}$	$DMDT_{3^*}$
WS, Re1k	$-0.4163 + 0.9090i$ $(-0.0005 + 5.0007i)$	$-0.0325 + 0.7517i$ $(-0.7110 + 4.0350i)$	$-0.6029i + 0.4979i$ $(-0.6152 + 6.1283i)$	$-0.6538 + 0.7565i$ $(-0.0003 + 5.7086i)$	$-0.8390 + 0.5434i$ $(-0.0008 + 6.4171i)$
SS1, Re1k	$0.0418 + 0.4972i$ $(-4.3448 + 9.2929i)$	$0.6962 + 0.7181i$ $(0.0011 + 5.0057i)$	$0.8439 + 0.3498i$ $(-0.5652 + 7.4556i)$	$-0.0302 + 0.9995i$ $(-0.0007 + 10.0064i)$	$-3.8313 + 0.9009i$ $(-0.1374 + 12.3198i)$
SS1, Re2k	$0.9211 + 0.3894i$ $(-0 + 5i)$	$0.3480 + 0.8998i$ $(-0.4485 + 15.0215i)$	$0.6967 + 0.7173i$ $(-0.0003 + 10i)$	-	-
SS2, Re1k	$-0.4162 + 0.9093i$ $(0 + 5.0001i)$	$-0.2896 + 0.7862i$ $(-0.4423 + 4.8093i)$	$-0.6536 + 0.7568i$ $(0 + 5.7079i)$	-	-

Table 6.4: The eigenvalues, λ of temporal DMDT modes for all cases with their logarithmic mapping in the form $(\sigma + oi)$.

The eigenvalues then were calculated and listed in Table 6.4 and subsequently displayed in Fig. 6.20, where the blue and pink stars indicate the highlighted DMDT modes. All the Ritz values are either almost on or within the unit circle $|\lambda| = 1$ in the left Fig. 6.20. It is a well-established fact that unstable modes are depicted when the eigenvalues lie outside the unit circle. They are stable when they lie inside the unit circle and are marginally stable when they lie on the unit circle itself. As for the DMDT spectrum, the eigenvalues were logarithmically mapped to the complex plane elucidated in Fig. 6.20(right).

It can be concluded that the eigenvalues of all DMDT modes which matched the frequency of DMD modes identified in the earlier study (including the pink DMDT modes except for $DMDT_{3*}$ of WS, Re1k) lie exactly on the unit circle in the left figure of Fig. 6.20 and on the red line of the right figure. These stable modes decayed over time and least damped. This, however, does not occur to $DMDT_1$, and $DMDT_3$ of SS1, Re1k, as well as $DMDT_2$ and $DMDT_3$ of WS, Re1k and $DMDT_2$ from SS2, Re1k. All these strongly damped modes lie inside the unit circle, as shown in the left figure. These particular modes are severely decayed, and $DMDT_1$ of SS1, Re1k, becomes the most decayed mode as elucidated in the logarithmic mapping figure, which lies on the far left.

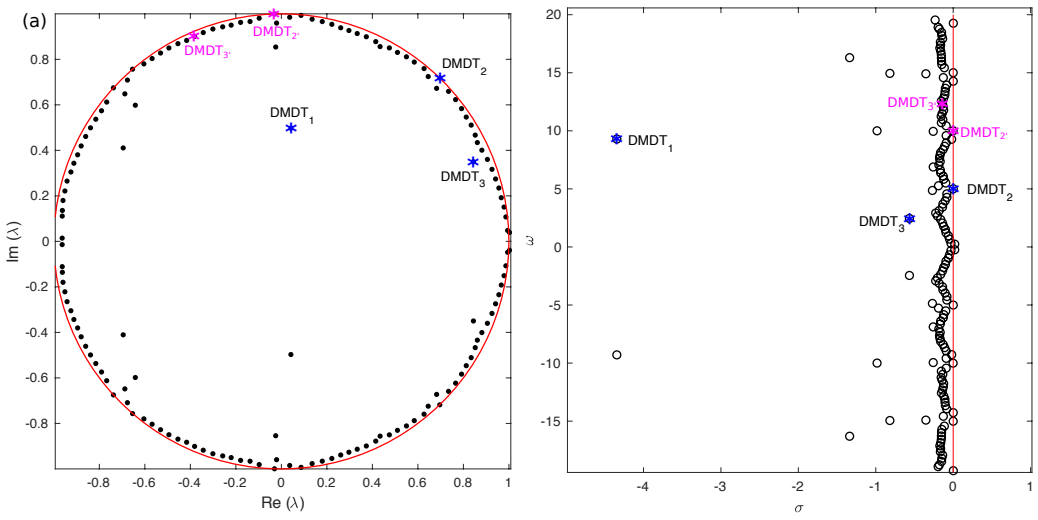

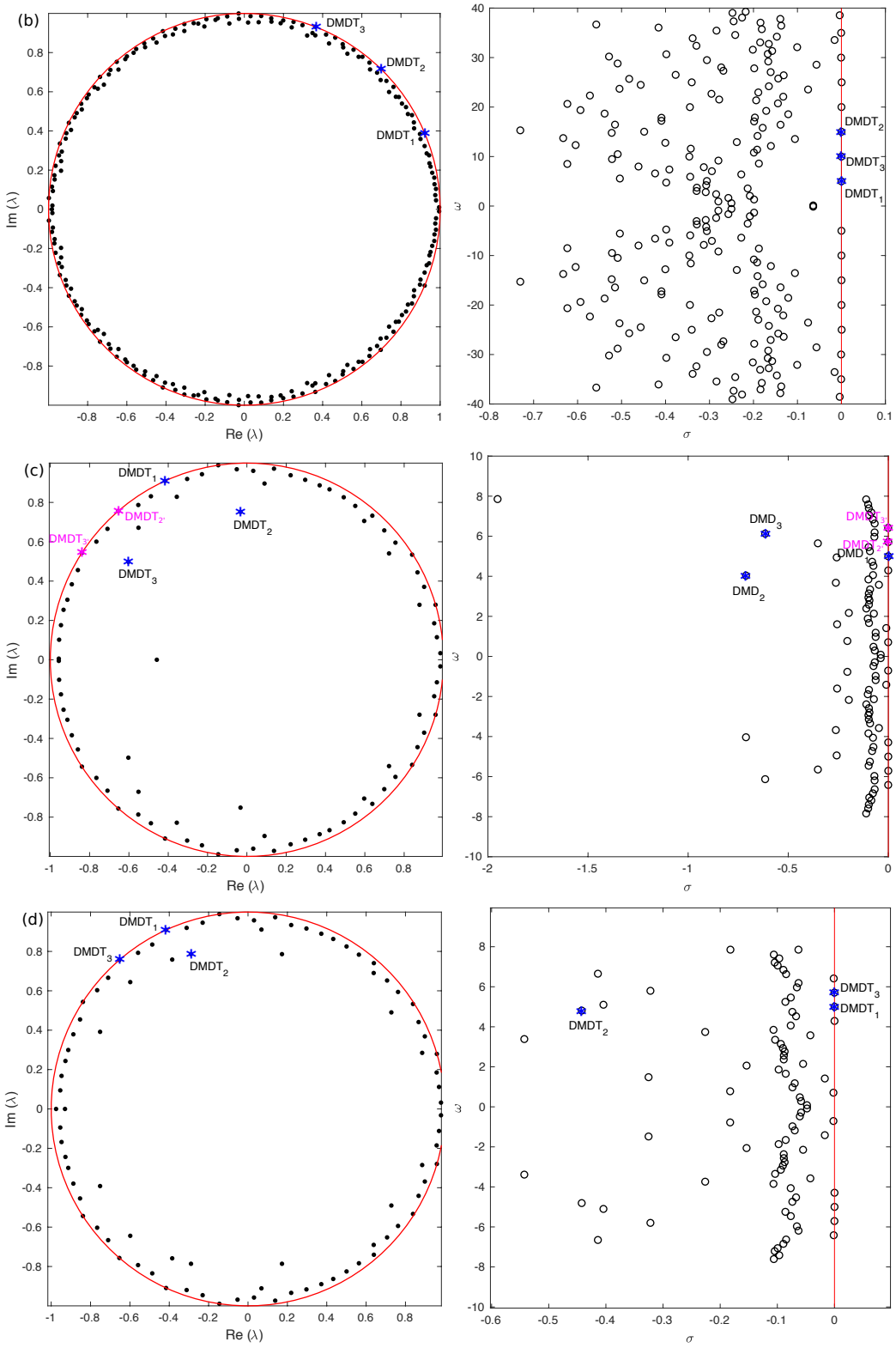

Figure 6.20: Dynamic eigenvalue characteristics of: (a) SS1, Re1k, (b) SS1, Re2k, (c) WS, Re1k, and (d) SS2, Re1k. Ritz values (left) and DMDT spectra (right) of temporal DMDT modes. All considered modes were marked by the blue star and labeled accordingly, including two extra considered DMDT modes marked by the pink marker.

The first three most dominant DMDT modes for SS1, Re1k; SS1, Re2k; WS, Re1k; and SS2, Re1k were illustrated using contours of $|\omega|$ and shown in Fig. 6.21, 6.23 ,6.25, and 6.26, respectively. Meanwhile, DMDT_{2^*} and DMDT_{3^*} of SS1, Re1k; and, WS, Re1k were depicted by Fig. 6.22 and 6.24.

If these to be associated with the PODT modes gained in the previous chapter, DMDT_2, and DMDT_{2^*} look exactly the same as the first and second pair of PODT modes (recall Fig. 5.20), respectively for SS1, Re1k. As for WS, Re1k, $\text{PODT}_1\&\text{PODT}_2$ closely resembles DMDT_1 and $\text{PODT}_3\&\text{PODT}_4$, as shown in Fig. 5.22 is just the same as DMDT_{2^*}. For the rest two cases, the exact match for the first and second pairs of PODT modes is the first and third DMDT modes. The same arguments as in Subsection 5.4 were applied for why there is no multi-pole like structure observed in the DMDT modes like the one detected in DMD modes.

On the other hand, the remaining modes like DMDT_1, DMDT_3 and DMDT_{3^*} from SS1, Re1k appeared as a vague contour plot of their $|\omega|$. The same remark was observed in DMDT_2, DMDT_3, and DMDT_{3^*} from WS, Re1k as well as in DMDT_2 of both SS1, Re2k, and SS2, Re1k. These contour plots were not as clear and sharp as the DMDT modes that matched the PODT modes. Looking back to the Ritz value of these DMDT modes, they were the ones located on the unstable side of Fig. 6.20. This explains the instability of the modes spatial distribution.

Last but not least, the phase information of each DMDT modes was revealed by the DMDT modes coefficient, as shown in the first row of Fig. 6.27 – Fig. 6.32. The circular correlation patterns for DMDT_2 and DMDT_{2^*} of SS1, Re1k; DMDT_1 and DMDT_{2^*} of WS, Re1k; DMDT_1 & DMDT_3 of SS1, Re2k and SS2, Re1k are reflected as strong cycle-to-cycle variation. The same argument was applied here since these DMDT modes here are the stable modes concluded from the prior analysis on their DMDT eigenvalues and eigenvectors. For the unstable modes, the distortion of the circular shape was plotted by these unstable DMDT mode coefficients.

This discrepancy of the DMDT modes coefficient can be connected to the changes in the amplitudes of the unstable modes, and the second row of Fig. 6.27 – Fig. 6.32 supported this. As a result, there are two or three peaks extracted in spectra curves, as portrayed in the last row of Fig. 6.27 – Fig. 6.32. Regarding the stable

modes, they change similarly to cosine and sine functions in a time-resolved study of the flow and hence extracted just a single dominant frequency. All the same frequencies listed in Table 6.3 from the foregoing investigation on DMD modes were successfully captured by these single peaks extracted by the stable DMDT mode coefficients. Full list of every peak frequency was compiled in the Table 6.5 below.

Atmospheric Conditions	f (Hz)				
	$DMDT_1$	$DMDT_2$	$DMDT_3$	$DMDT_{2^*}$	$DMDT_{3^*}$
WS, Re1k	0.8056	0.8065 0.9167	0.8065 0.9167	0.9167	0.8065 0.9167 1.0286
SS1, Re1k	0.8065 1.6130	0.8065	0.8065 1.6130	1.613	0.8065 1.6130
SS1, Re2k	0.7955 2.3860	0.7955 1.5910 2.3860	1.5910	-	-
SS2, Re1k	0.7967	0.7967 0.9066	0.9066	-	-

Table 6.5: Frequencies, f captured by DMDT modes coefficients.

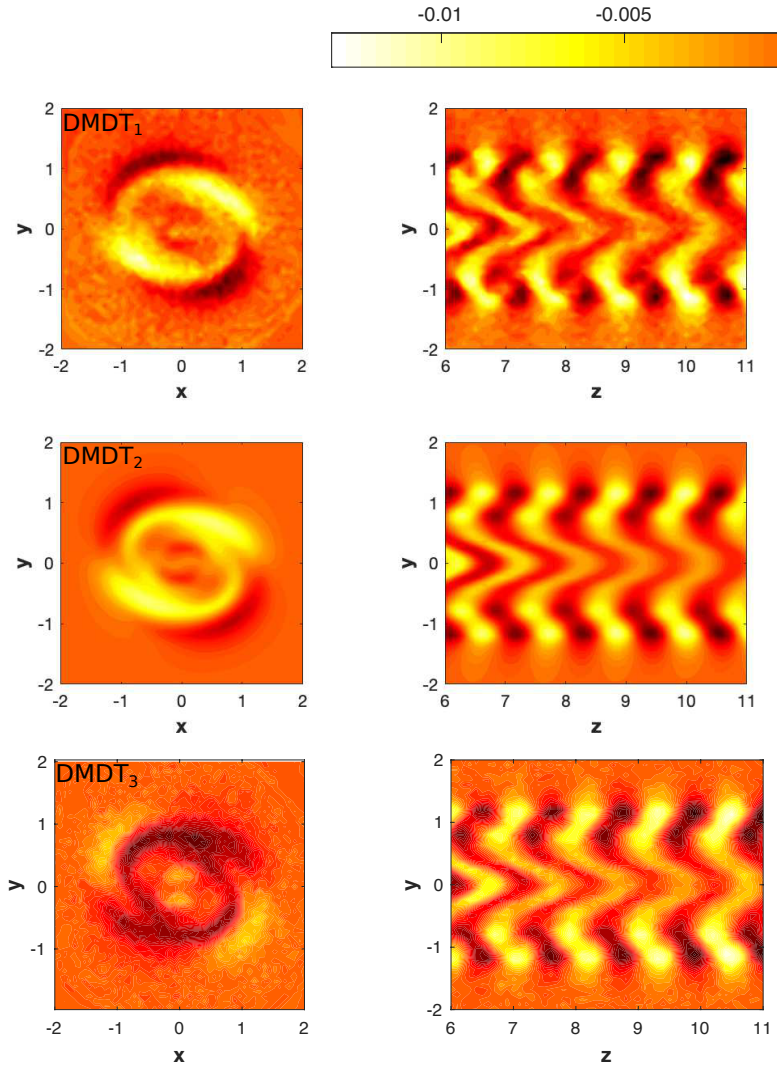

Figure 6.21: Contour plots of $|\omega|$ for DMDT_1, DMDT_2, and DMDT_3 respectively in xy-cut at $z = 8.5$ (left) and zy-cut at $x = 0$ (right) for SS1, Re1k.

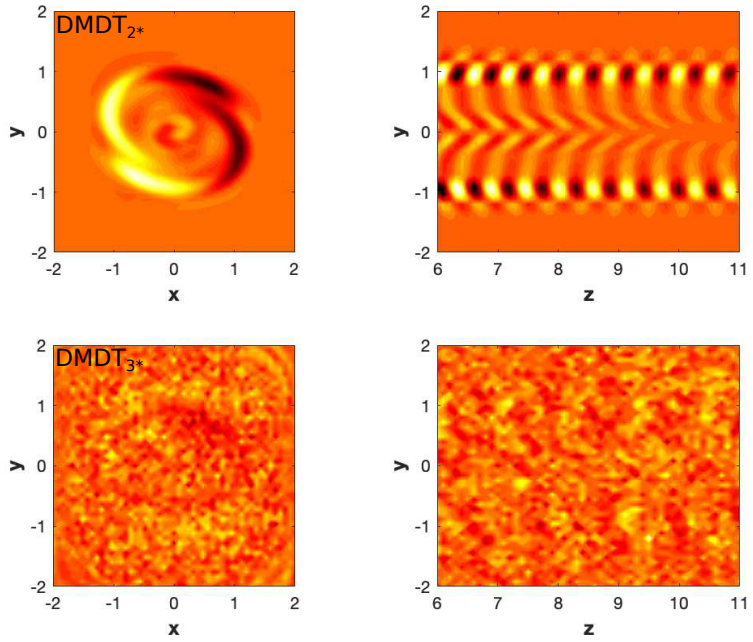

Figure 6.22: Caption and colormap as Fig. 6.21, but for DMDT_{2^*}, and DMDT_{3^*} of SS1, Re1k.

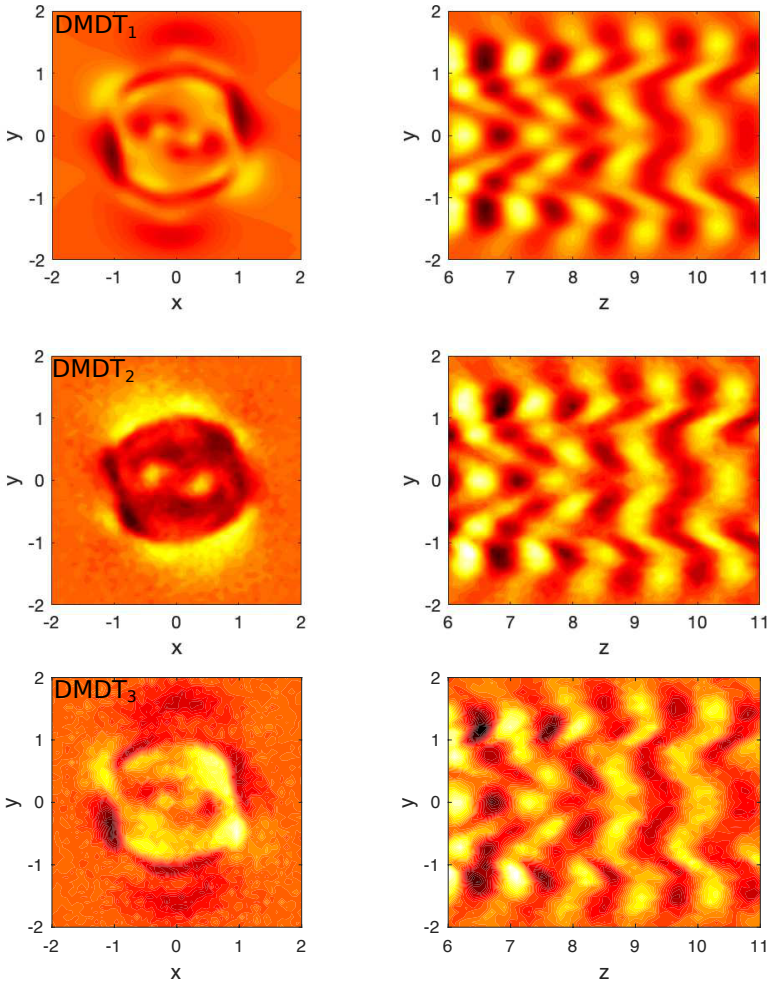

Figure 6.23: Caption and colormap as Fig. 6.21, but for WS, Re1k.

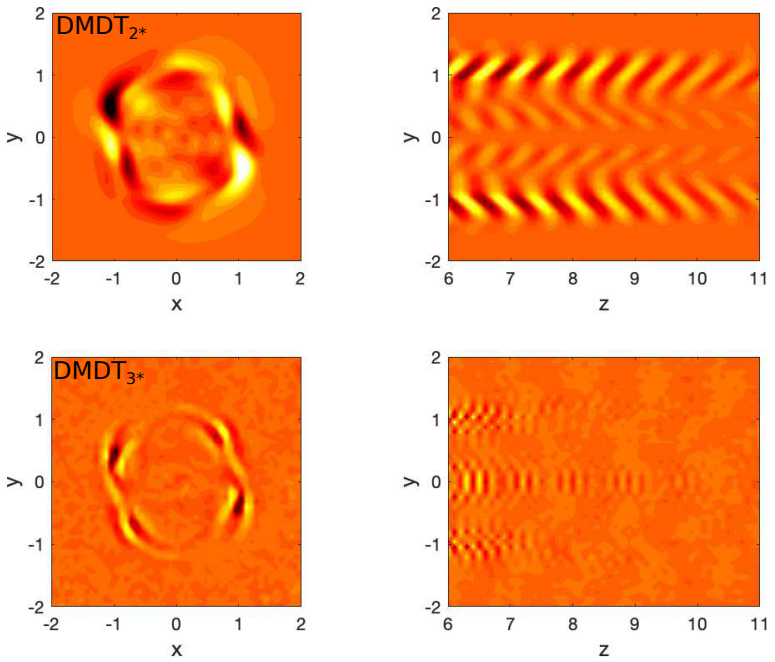

Figure 6.24: Caption and colormap as Fig. 6.21, but for $DMDT_{2^*}$, and $DMDT_{3^*}$ of WS, Re1k.

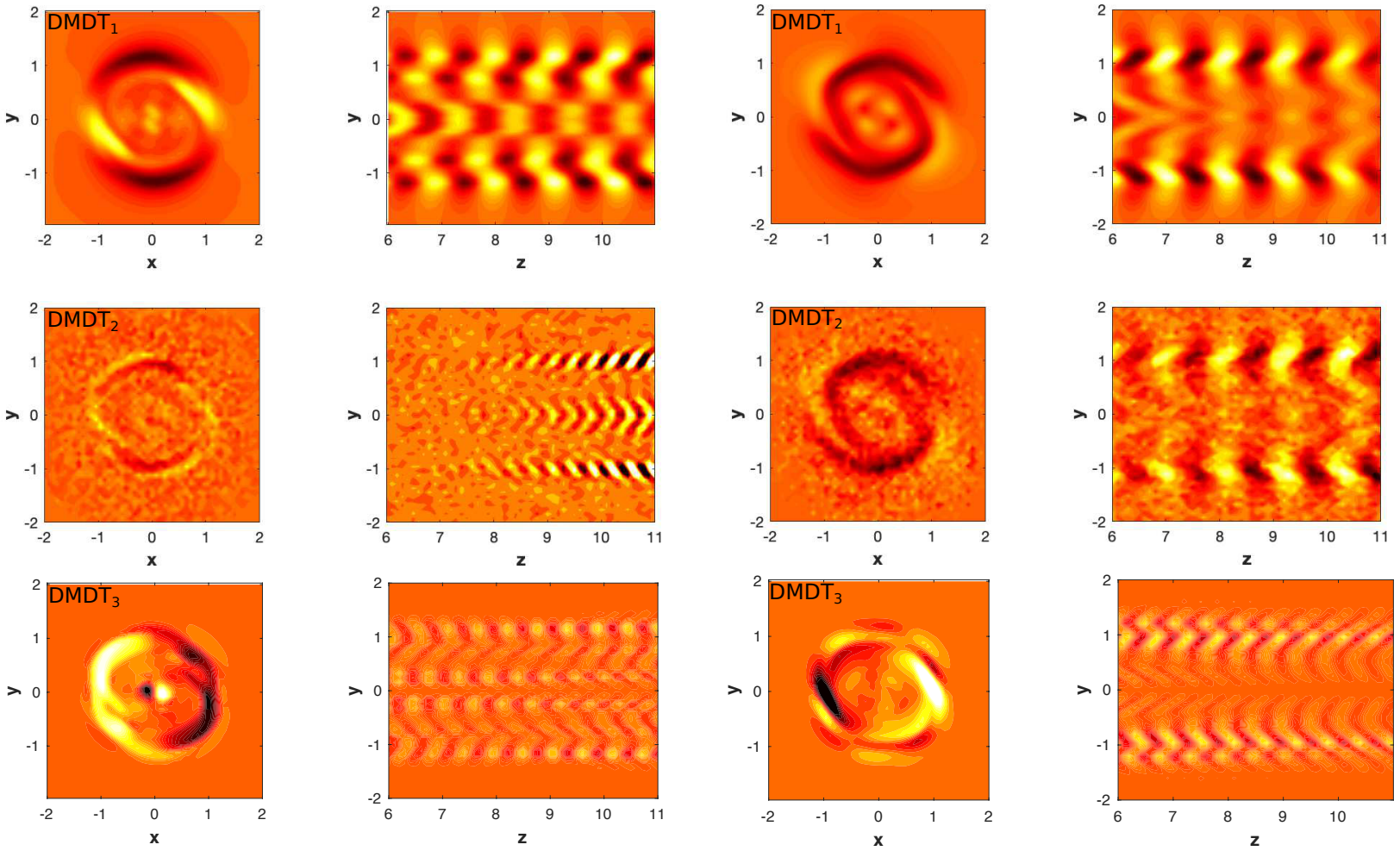

Figure 6.25: Caption and colormap as Fig. 6.21, but for SS1, Re2k.

Figure 6.26: Caption and colormap as Fig. 6.21, but for SS2, Re1k.

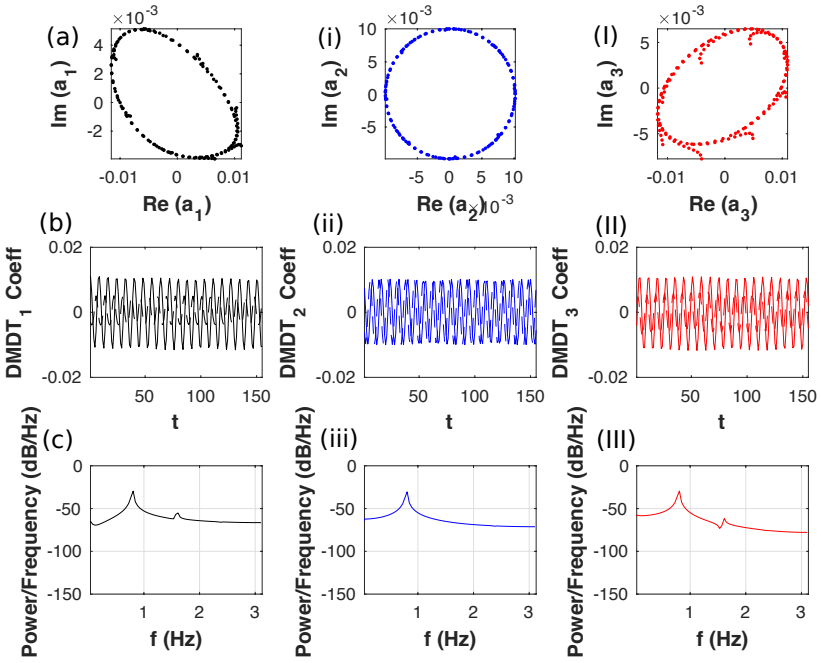

Figure 6.27: DMDT Mode Coefficients characteristics of SS1, Re1k. (a, i, I) Correlation Maps, (b, ii, II) Time Variation, and (c, iii, III) Power Spectra Analysis, PSD. The black (a, b, c), blue (i, ii, iii), and red (I, II, III – if any) dots/lines are representative of $DMDT_1$, $DMDT_2$, and $DMDT_3$, respectively. Note also the solid line in (b, ii, II) represents the real part of DMDT Mode Coefficients while the dashed line refers to the imaginary part.

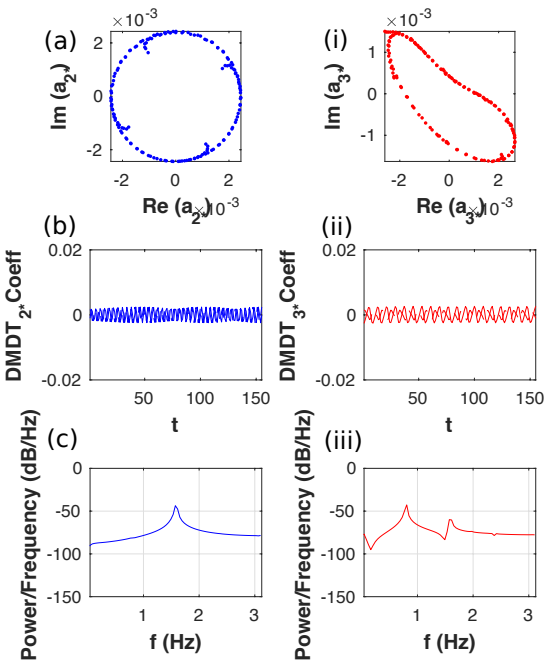

Figure 6.28: (a, i) Correlation Maps, (b, ii) Time Variation, and (c, iii) Power Spectra Analysis, PSD of SS1, Re1k DMDT Mode Coefficients. The blue (a, b, c) and red (i, ii, iii) dots/lines are representative of $DMDT_{2^*}$ and $DMDT_{3^*}$, respectively. Note also the solid line in (b, ii) represents the real part of DMDT Mode Coefficients while the dashed line refers to the imaginary part.

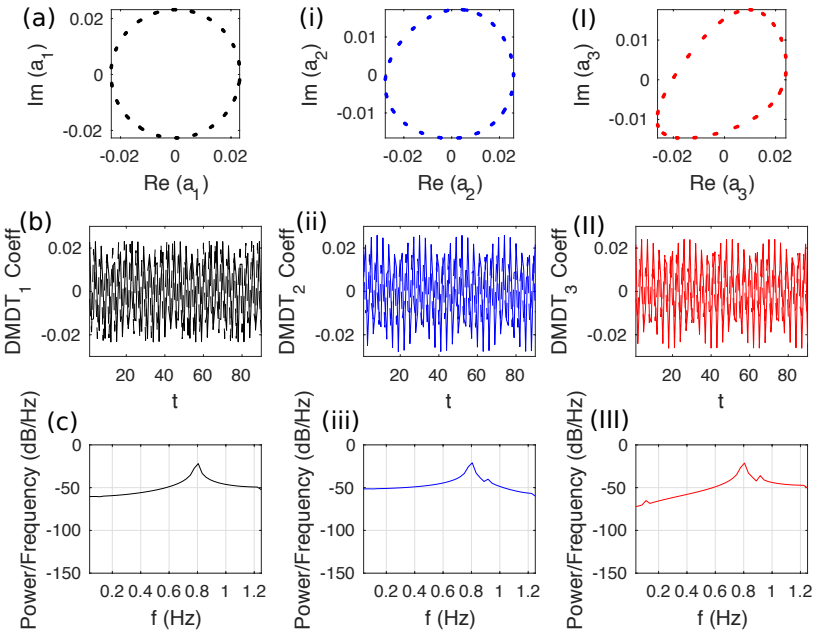

Figure 6.29: Caption as Fig. 6.27, but for WS, Re1k.

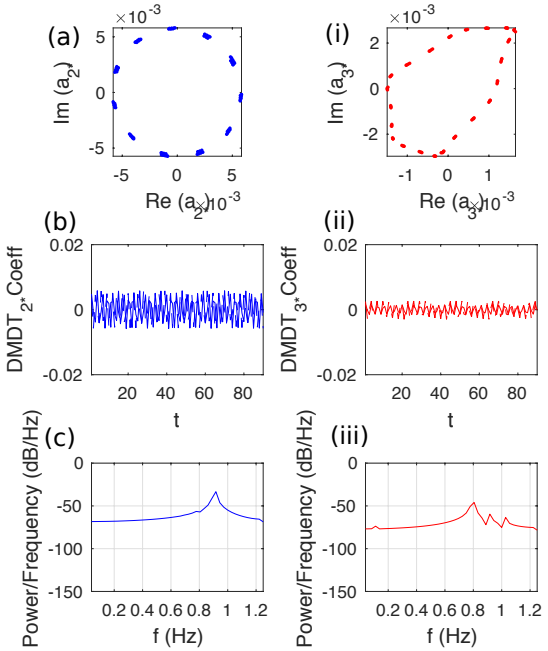

Figure 6.30: Caption as Fig. 6.28, but for WS, Re1k.

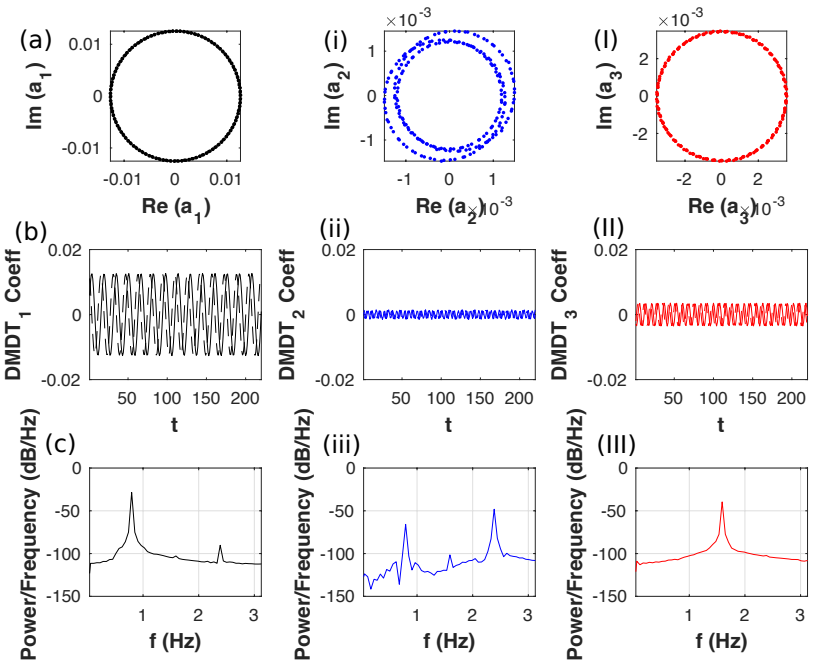

Figure 6.31: Caption as Fig. 6.27, but for SS1, Re2k.

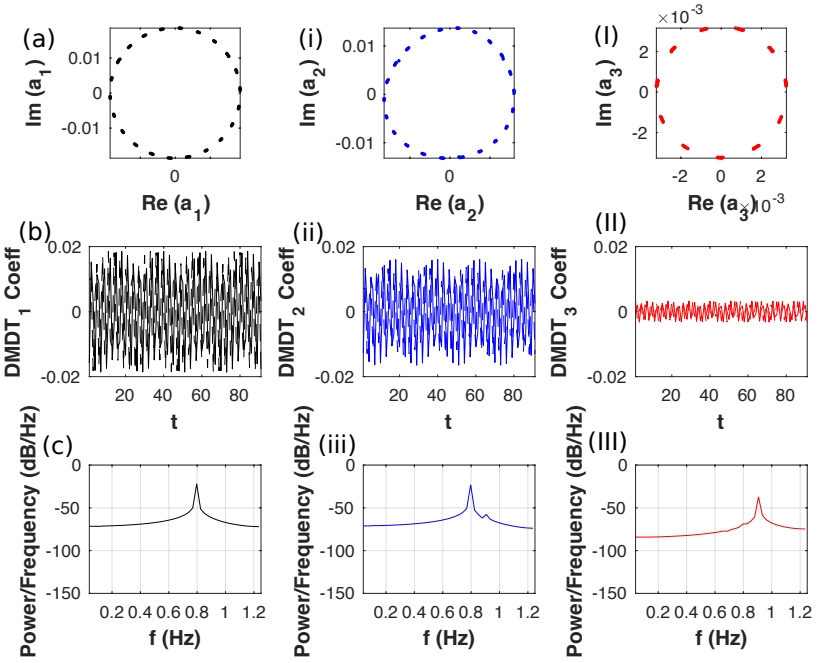

Figure 6.32: Caption as Fig. 6.27, but for SS2, Re1k.

6.3 DMD Analysis of Results in the far-field region

It now comes to the final analysis of this study where the decomposition of the far-field wake flow from N, Re 1k case was carried out, and the energy contributions of all modes were presented in the following Fig. 6.33. The only clear peak was identified at frequency $f = 0.7964$ Hz, and as it has been mentioned earlier, the other modes with the nearest frequencies as this coherent mode are considered to have similar characteristics.

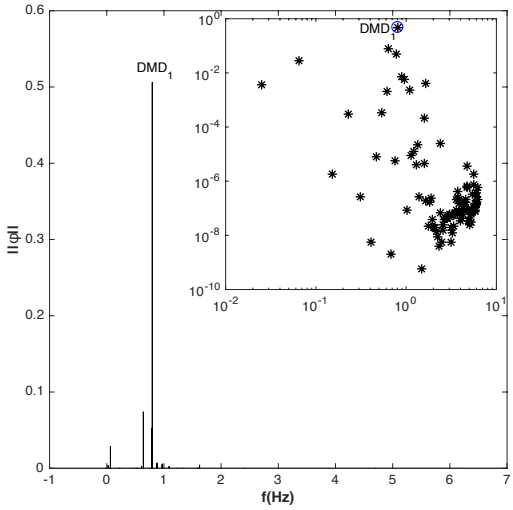

Figure 6.33: Energy Spectra of temporal DMD for N, Re1k in the far wake region. DMD_1 with $f = 0.7964$ Hz was labelled and circled by the blue marker.

Fig. 6.34 below was referred for the next discussion on the dominant mode. It seems to lie well on the unit circle in Fig. 6.34(a) and stable with σ = -0.0121 growth/decay rate in Fig. 6.34(b). Finally, its spatial distribution was illustrated by the contour and isosurface plot of DMD_1 in Fig. 6.34(c). That particular mode shows a spatial decay in $|\omega|$ after $z \approx 24D$ and resembles the first pair POD modes that can be found in Subsection 5.5. The frequency of the most dynamic mode in the far wake region is more or less similar to the frequency of DMD_1 in the near wake region. However, the energy of the first mode in this case ($||\varphi|| \approx 0.5$) is much less compared to the prior region where the energy is approximately fifty times higher.

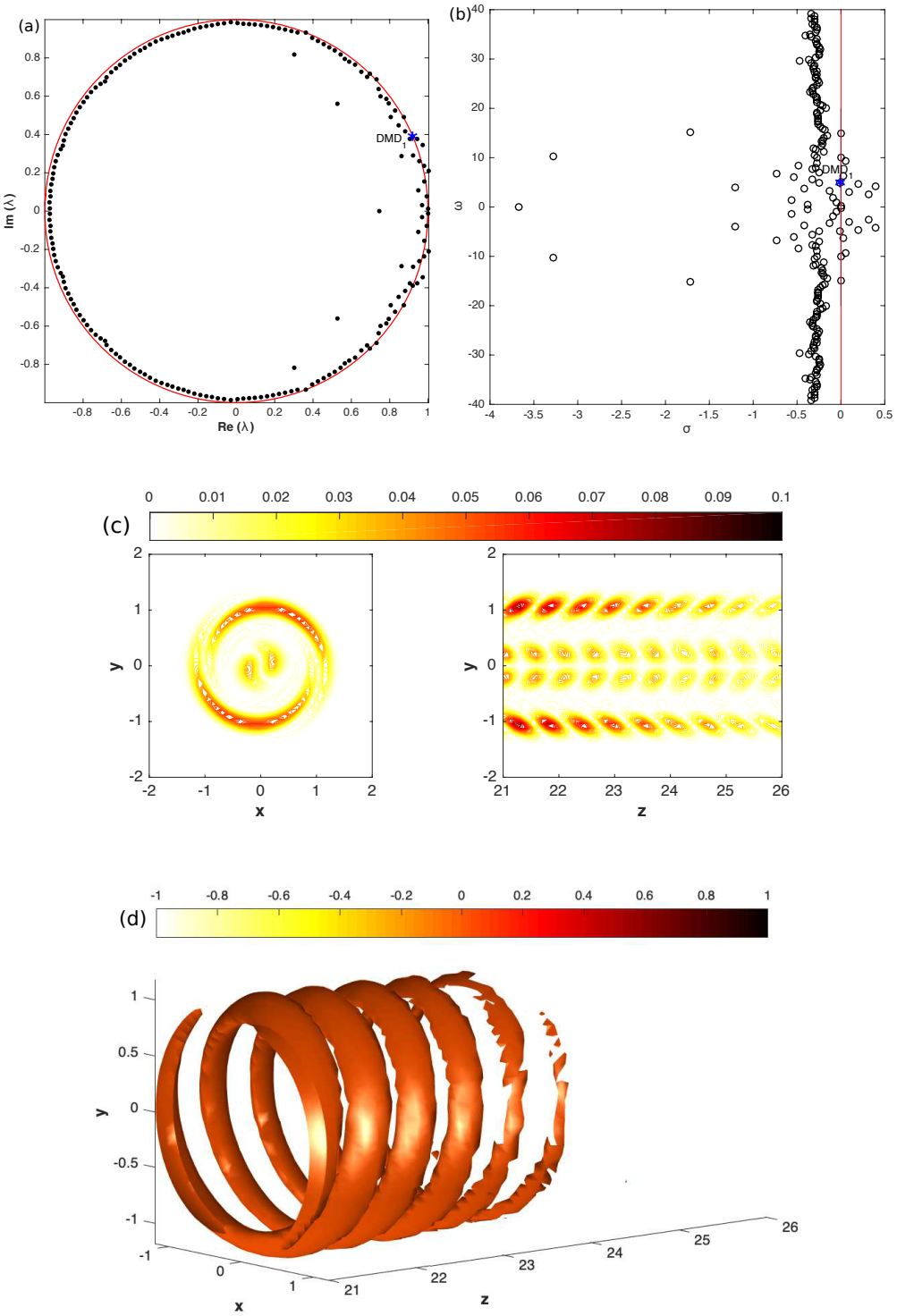

Figure 6.34: Dynamic eigenvalue characteristics of N, Re1k. (a) Ritz values and (b) DMD spectra of temporal DMD_1. (c) $|\omega|$ contour plot in xy-cut at $z = 23.5$ (left) and zy-cut at $x = 0$ (right). (d) Isosurface plot of $|\omega| = 0.05$ corresponding to DMD_1 ($\lambda = 0.9201 + 0.3893i$).

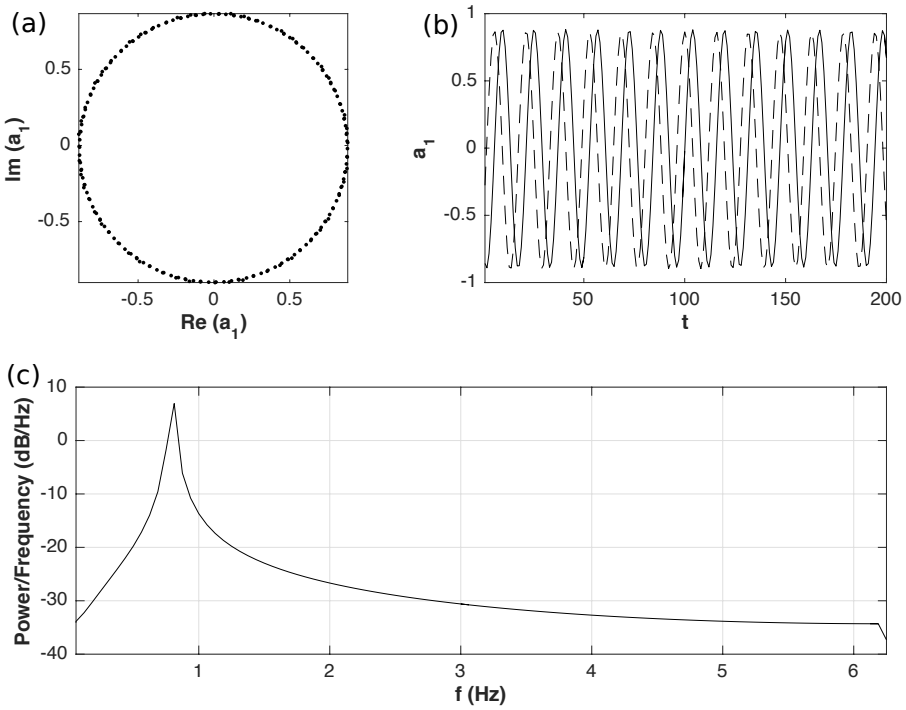

Figure 6.35: DMD Mode Coefficients characteristics. (a) Correlation Maps, (b) Time Variation, and (c) PSD of N, Re1k in the far-field region.

The circular distribution of real and imaginary parts of the mode coefficient, a_1 (see Fig. 6.35(a)), suggests a cyclic variation of the dominant mode and Fig. 6.35(b) presents periodical variation with a fixed amplitude over periods, providing further evidence that this dynamic mode is neutrally stable with time. Moreover, the power spectrum of the mode coefficient (Fig. 6.35(c)) captured a similar frequency, as in Fig. 6.33, which is $f = 0.8125$ Hz, at once demonstrating the ability to orthogonalize the temporal dynamics from DMD.

All these examples and analysis clarify how the DMD method decomposes the flow structure and reveals the essential dynamic information.

6.4 Chapter Summary

The present chapter performed an analysis on temporal DMD where the DMD method were employed to the velocity field (the modes called DMD modes) of the near and far wake region and on the temperature field (DMDT modes), separately. In each section, the spatio-temporal behaviour of DMD/DMDT modes such as modal

energy, growth/decay rate, the eigenvalues & eigenvectors, and the mode coefficients were presented and compared to the POD/PODT modes gained from the previous chapter. The final chapter will be about the overall discussion on the findings before the conclusion will be made based on the crossed analysis of all six cases. On top of that, a couple of descriptions and suggestions for the future direction of this research will be granted at the end of this thesis.

Chapter 7

Conclusion and Future Directions

This thesis details a number of analyses on the vortex characteristic of three-dimensional unsteady fluid flow behind a rotating blade in thermally stratified atmosphere besides the use of proper orthogonal decomposition (POD) and dynamic mode decomposition (DMD) to extract the coherent and energetic modes of the flow. Some of these are direct contributions to the understanding of POD and DMD, whereas others make use of POD and DMD as a means to other ends. In this chapter, a general discussion and conclusion of the main findings will be presented, and the description of future directions in which this work can be extended is given at the end of the thesis.

7.1 Conclusion

Altogether, in the near wake region, the helical wake flow behind a rotating blade in the thermally stratified atmosphere did affect in terms of their characteristics, dynamics and stability compared to the one without stratification. It is, however, difficult to apply the same analysis on the far wake region for the stratified case because the flow is not fully developed for sufficiently long time in the simulation. After applying the two modal decomposition techniques, the effect of atmospheric stratification towards the helical wake flow becomes more apparent and convincing.

Table 7.1 summarised all the results gained from this study. The first three columns introduce the different flow conditions considered in this study by giving the

respective atmospheric conditions, Re and their contour plot of vorticity magnitude, $|\omega|$ from the last cycle. The RMS column refers to the RMS values of tip vortices from the last cycle, while the vorticity tilting column shows the contour plot of vorticity tilting along their dominant direction, respectively. The following column lists the streamwise location of the flow in which the breaking mechanism started to occur. The last two columns represent the size and the circulation of the last core as the flow moves downstream, respectively.

It was observed that the circular helical wake behind a rotating blade in the physical space, of four cases with atmospheric stratification conditions, were distorted. The weakly stable stratified atmosphere distorted much stronger compared to the others (refer to the highlighted row in the third column of Table 7.1). This non-circularity of the helical flows was quantified by the RMS values of tip vortices, and WS appeared to have the highest value, followed by SS2 and SS1.

The deformation phenomena were supported by the result obtained from the vorticity tilting of streamwise vorticity, ω_z along the radial, r- and tangential, τ- direction in the rotating Cartesian frame as the flow goes downstream. The region with the highest vorticity tilting value was observed to be the reason for the distortion of the helical structure. Table 7.1 is referred to for the observation. The contribution of the tilting along the radial direction for all thermally stratified atmosphere is significant compared to the tangential direction, and is totally contradicting the neutral case as it dominates in the tangential direction.

In the weakly stable stratified atmosphere, the breaking of the helical flow happens earlier compare to the others. As has been highlighted in Table 7.1, the helical flow of WS breaks as early as at $z = 5.6$, based on the chosen threshold, followed by SS2 and SS1. In other words, another threshold will give a different z value. The analysis of the Gaussian peak of the core verified these findings since the helical flow of WS is the earliest to decay, for it has the lowest Gaussian peak's value. This can be seen in Fig. 4.31.

The size of the core in both z- and y- directions increases, whereas the circulation declines as the flow moves downstream. This happens to all cases, including the one without atmospheric stratification. Simply put, the energy of the core reduces as

the core keep growing. As highlighted in the last two columns, the energy of core calculated from the circulation of WS and SS2 flows are quite low for their size. In contrast to other cases, the size of the core is still reasonable for the energy contained in the flow. In the same order as the prior conclusion, the fastest to decay with the lowest Γ value is the helical flow from WS, followed by SS2 and SS1.

Fig. 4.36 deduced that the power spectra of the instantaneous wake flow in the thermally stratified atmosphere has a higher turbulence level compare to the neutral one. Accordingly, two well-known modal analysis techniques, which are POD and DMD, were employed to the DNS dataset to see if they are capable of producing the same findings from their global analysis and indirectly supports the result from the analyses done to the instantaneous wake flow.

The POD/PODT analysis focused on the most energetic mode while the DMD/ DMDT analysis discussed the dynamics of the corresponding modes found earlier in the POD study. The snapshot technique of POD, PODT, DMD, and DMDT have been applied successfully on DNS datasets for four different atmospheric stratification conditions. All four most energetic modes from POD and PODT show the similarity in terms of energy distribution and their POD/PODT modes coefficients. Meanwhile, few distinct findings were obtained in DMD and DMDT. The Ritz values of both studies extracted energetic modes at different frequency. These different dominant modes have dissociated stability, growth/decay rate, spatial distribution, and gave a totally unrelated mode coefficients outcomes.

In POD and DMD analyses, the results from the spatial distribution show that the modes have a multipole-like structure; even so, this does not happen in both PODT and DMDT modes. As for the spatial distribution of all energetic modes, whether form POD, PODT, DMD, or DMDT, where observed carefully, it is clearly disclosed how messy and chaotic the modes from the weakly stable case are. On the contrary, the modes from the neutral case seem very clear and well-organized. Similar to the significant effect seen in the analysis of instantaneous wake flow, the dominant modes extracted from both modal decomposition techniques were remarkably affected by the variation of the thermal stratification.

All in all, the helical wake flow in the weakly stable stratified atmosphere is the one with the lowest physical stability. The foregoing analysis and conclusion proved this, be it the raw data analysis (Chapter 4), the analysis conducted to study the distortion of circular helical flow (Subsection 4.2.2); the vorticity tilting (Subsection 4.2.3); the decay (Subsection 4.2.5) and breaking flow (Subsection 4.2.4); the core analysis covering the circulation and core size (Subsection 4.2.5), be it modal decomposition analyses (Chapter 5 & Chapter 6) which show the chaotic and complex structure of their most dominant (energetic) modes. This vigorously concludes that varying the thermal stratification did influence the helical wake behind a rotating blade.

Atmospheric Conditions	Re	Vorticity Magnitude, $\|\omega\|$	Analyses				
			RMS	Vorticity Tilting	Breaking	Core Size in z & y direction	Circulation, Γ
N	1000	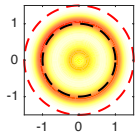	0	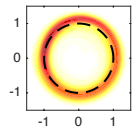	$z = 8.7$	0.639 0.438	0.654
	2000	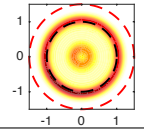	0	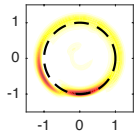	$z = 8.7$	0.453 0.342	0.821
WS	1000	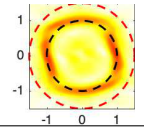	0.071	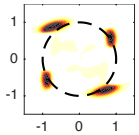	$z = 5.6$	0.394 0.276	0.212
SS case 1, SS1	1000	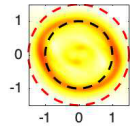	0.066	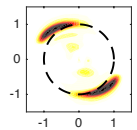	$z = 7.0$	0.429 0.374	0.489
	2000	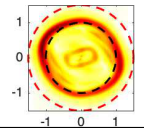	0.050	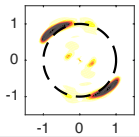	$z = 7.8$	0.343 0.283	0.511
SS case 2, SS2	1000	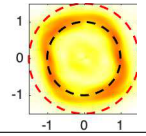	0.065	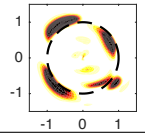	$z = 5.8$	0.3847 0.356	0.290

Table 7.1: Summary of overall findings.

7.2 Suggestion for Future Works

While the work presented in this thesis has answered a number of questions about the physics, POD, and DMD of the wake flow behind a rotating blade in the stratified atmosphere, it has also led to some of new ones. As an example, while the vorticity magnitude, ω was being discussed in Chapter 4 to represent the flow, it still allows to consider other quantity to represent the flow such as helicity or other velocity/vorticity components, and discuss their characteristics, instead. Besides, there are several questions related to the inherent characteristics of the flow with a different type of dataset that merits further study. These include the following:

- The simulation data using LES with higher Re – As DNS is well-known for its high-priced computational cost and restricted the Reynold number to a low value, one can run a numerical computation using LES enlarging the Re values, instead, so that a free-stream turbulence dataset can be simulated affordably. Haywood & Sescu, for example, worked on the study of wakes in stratified atmospheric boundary layer flows simulated using LES with considering a Reynolds number on the order of 10^7 [74].

- The unstable stratified atmosphere – Due to time limitation, this study can only be carried out for the stable stratification wake flow and the one without any stratification (neutral). This study will be more interesting if the wake flow in an unstable stratification can be included, studied, analysed, and discussed further together with the neutral and stable cases. Thus, future works are recommended for the exploration of wake flow in unstable stratified atmosphere (convective). As it has been described briefly in Section 3.2, the unstable stratification atmospheric condition occurs during the daytime, when the surface is warmer than the air.

- The experimental data to validate the result – Usually, validation experiments and validation analyses are conducted to confirm the data and result in precision. Again, as a consequence of the time restriction, the validation study can not be provided. Therefore, it is suggested to compare the findings obtained

from this present simulation study with the experimental analysis and hence, validate it with verified precision.

A number of future directions also arise from the decomposition techniques of POD, and DMD discussed in Chapter 5 & 6, respectively, such as:

- Modify or improvise POD or DMD method with new definition and algorithm in order to either strengthen or enhance the robustness and applicability of the existing approach – While this present study focused on applying the method of POD and DMD, the development of its underlying theory was always welcomed to be explored by the future researcher. For instance, Optimized DMD is a modification of the original DMD algorithm intended to compensate for two constraints of that approach [80] whereas Exact DMD algorithm generalizes the original DMD algorithm in two ways [58]; First, it accepts a data set of snapshot pairs, and second, its algorithm removes the pre-processing step (the step where the data set was projecting onto a set of POD modes), and can produce DMD modes that can not be written as the superposition of POD modes. In addition, Extended DMD is a modification of Exact DMD that strengthens the connection between DMD and the Koopman operator. In 2014, Tu et al. [58] proposed a new definition in which DMD was interpreted as an approximate eigendecomposition of the best-fit (in a least-squares/minimum-norm sense) operator relating two data matrices. As a result, it can generalize the DMD algorithm to arbitrary datasets, not just sequential time-series (as are typically considered).

- Use other modal decomposition techniques so that wide information on the various type of systems can be explored – There are few other modal analysis techniques as reviewed by Taira et al. in [83] such as Balanced Proper Orthogonal Decomposition (BPOD), Spectral Proper Orthogonal Decomposition (SPOD), Higher-Order Dynamic Mode Decomposition (HODMD), empirical mode decomposition, Koopman analysis, global linear stability analysis, resolvent analysis, and more, that have their own strengths and weaknesses. Future researchers can consider these decomposition methods for their dataset and

discuss on the information these methods can provide. For instance, BPOD is capable of capturing the dynamics of the non-normal systems with large transient growth, while Koopman analysis offers an alternative operator-theoretic perspective to dynamical systems and allows the representation and analysis of non-linear systems using linear techniques. Global linear stability analysis determines a spectrum of (discrete and continuous) eigenmodes, especially with the matrix-based approach. Resolvent analysis can use the mean flow as the base state (instead of the exact solution to the Navier–Stokes equations), even in the case of turbulent flows, and it identifies the form of the most amplified inputs, the corresponding output, and the gain.

Bibliography

[1] A. Crespo, J. Hernandez, and S. Frandsen (1999). Survey of Modelling Methods for Wind Turbine Wakes and Wind Farms. *Wind Energy*, **2**, pp 1-24.

[2] A. Greenbaum (1997). *Iterative Methods for Solving Linear Systems*. SIAM Publishing, Philadelphia.

[3] A. Hyvärinen, G. Lacagnina, and A. Segalini (2018). A Wind-tunnel Study of the Wake Development behind Wind Turbines over Sinusoidal Hills. *Wind Energy*, **21**(8), pp 605–617.

[4] A. Jiménez, A. Crespo, and E. Migoya (2009). Application of a LES Technique to Characterize the Wake Deflection of a Wind Turbine in Yaw. *Wind Energy*, **13**(6), pp 559?572.

[5] A. K. M. F. Hussain (1983). Coherent Structures–Reality and Myth. *Physics of Fluids*, **26**(10), pp 2816–2850.

[6] A. K. M. F. Hussain, and M. Hayakawa (1987). Eduction of Large-scale Organized Structure in a Turbulent Plane Wake. *Journal of Fluid Mechanics*, **180**, 193.

[7] A. Nemes (2015). Helical Vortices in Rotor Wakes. *Ph.D. thesis Monash University.*

[8] A. Nemes, M. Sherry, D. Lo Jacono, H. M. Blackburn, and J. Sheridan (2014) Evolution and Breakdown of Helical Vortex Wakes Behind a Wind Turbine. *Journal of Physics: Conference Series*, **555**, 012077.

[9] A. Ruhe (1984). Rational Krylov Sequence Methods for Eigenvalue Computation *Linear Algebra and Its Applications*, **58**, pp 279–316.

[10] A. Seena, and H. J. Sung (2011). Dynamic Mode Decomposition of Turbulent Cavity Flows for Self-sustained Oscillations. *International Journal of Heat and Fluid Flow*, **32**(6), pp 1098–1110.

[11] A. Towne, O. T. Schmidt, and T. Colonius (2018). Spectral Proper Orthogonal Decomposition and its Relationship to Dynamic Mode Decomposition and Resolvent Analysis. *Journal of Fluid Mechanics*, **847**, pp 821–867.

[12] B. Cheng, S. Sane, G. Barbera, D. Troolin, T. Strand, and X. Deng (2013). Three-dimensional Flow Visualization and Vorticity Dynamics in Revolving Wings. *Experiments in Fluids*, **54**(1), 1423.

[13] B. E. Launder, and D. B. Spalding (1972). *Mathematical Models of Turbulence.* Academic Press.

[14] B. E. Launder, G. J. Reece, and W. Rodi (1975). Progress in the Development of a Reynolds Stress Turbulence Closure. *Journal of Fluid Mechanics*, **68**, pp 537–566.

[15] B. G. Green, E. A. Gillies, and R. E. Brown (2011). The Flow Field around a Rotor in Axial Descent. *Journal of Fluid Mechanics*, **534**, pp 237–261.

[16] B. P. Gupta and R.G. Loewy (1974). Theoretical Analysis of the Aerodynamic Stability of Multiple, Interdigitated Helical Vortices. *AIAA Journal*, **12**(10), 1381–1387.

[17] B. R. Noack, K. Afanasiev, M. Morzynski, G. Tadmor, and F. Thiele (2003). A Hierarchy of Low-dimensional Models for the Transient and Post-transient Cylinder Wake. *Journal of Fluid Mechanics*, **497**, pp 335–363.

[18] B. R. Noack, W. Stankiewicz, M. Morzynski, and P. J. Schmid (2016). Recursive Dynamic Mode Decomposition of a Transient and Post-transient Wake Flows. *Journal of Fluid Mechanics*, **809**, pp 843–872.

[19] B. Sanderse (2009). Aerodynamics of Wind Turbine Wakes – Literature Review. *Technical Report*, ECN-E-09-016.

[20] B. Witha, G. Steinfeld, M. Dörenkämper, and D. Heinemann (2014). Large-eddy Simulation of Multiple Wakes in Offshore Wind Farms. *Journal of Physics: Conference Series*, **555**(1), 012108.

[21] C. M. St. Martin, J. K. Lundquist, A. Clifton, G. S. Poulos, and S. J. Schreck (2016). Wind Turbine Power Production and Annual Energy Production depend on Atmospheric Stability and Turbulence. *Wind Energy Science*, **1** pp 221–236.

[22] C. Pan, D. Yu, and J. J. Wang (2011). Dynamical Mode Decomposition of Gurney Flap Wake Flow. *Theoretical and Applied Mechanics Letters*, **1**, pp 012002.

[23] C. Rosales and C. Meneveau (2005). Linear Forcing in Numerical Simulations of Isotropic Turbulence: Physical Space Implementations and Convergence Properties. *Physics of Fluids*, **17**, 095106.

[24] C. VerHulst, and C. Meneveau (2014). Large Eddy Simulation Study of the Kinetic Energy Entrainment by Energetic Turbulent Flow Structures in Large Wind Farms. *Physics of Fluids*, **26**, 025113.

[25] C. W. Rowley, I. Mezić, S. Bagheri, P. Schlatter, and D. S. Henningson (2009). Spectral Analysis of Nonlinear Flows. *Journal of Fluid Mechanics*, **641**, pp 115–127.

[26] C. W. Rowley, and S. T. M. Dawson (2017). Model Reduction for Flow Analysis and Control. *Annual Review of Fluid Mechanics*, **49**(1), pp 387–417.

[27] CH (2011, September 11). Circular Wing Tip Trails. Retrieved July 24$^{\text{th}}$, 2019, from https://atoptics.wordpress.com/tag/helicopter/

[28] D. Bastine, B. Witha, M. Wächter, and J. Peinke (2014). POD Analysis of a Wind Turbine Wake in a Turbulent Atmospheric Boundary Layer. *Journal of Physics: Conference Series*, **524**(1), 012153.

[29] D. Bastine, B. Witha, M. Wächter, and J. Peinke (2015). Towards a Simplified Synamic Wake Model using POD Analysis. *Energies*, **8**(895).

[30] D. Duke, J. Soria, and D. Honnery (2012). An Error Analysis of the Dynamic Mode Decomposition. *Experiments in Fluids*, **52**(2), pp 529–542.

[31] D. K. Bisset, R. A. Antonia, and L. W. B. Browne (1990). Spatial Organization of Large Structures in the Turbulent Far Wake of a Cylinder. *Journal of Fluid Mechanics*, **218**, 439.

[32] D. Maniaci (2014). Wakes and Rotors: The National Rotor Testbed. *Sandia National Laboratories.*

[33] D. Rempfer, H. Fasel (1994). Evolution of Three Dimensional Coherent Structures in a Flat Plate Boundary Layer. *Journal of Fluid Mechanics*, **260**, pp 351–375.

[34] E. T. G. Bot (2015). FarmFlow Validation against Full Scale Wind Farms. *Tech. Rep.* ECN-E–15-045, Energy research Centre of the Netherlands.

[35] F. Bingöl, G. C. Larsen, and J. Mann (2007). Wake Meandering–An Analysis of Instantaneous 2D Laser Measurements. *Journal of Physics: Conference Series* , **75**, 012059.

[36] F. Massouh, and I. Dobrev (2007). Exploration of the Vortex Wake behind of Wind Turbine Rotor. *Journal of Physics: Conference Series* , **75**, 012036.

[37] F. X. Caradonna (1999). Performance Measurement and Wake Characteristics of a Model Rotor in Axial Flight. *Journal of the American Helicopter Society*, **44**(2), pp 101–108.

[38] FYFD (2014, July 7). Retrieved July 24th, 2019, from https://fyfluiddynamics.com/post/91050225974/smoke-released-from-the-end-of-a-test-blade-shows

[39] G. Berkooz, P. Holmes, and J. L. Lumley (1993). The Proper Orthogonal Decomposition in the Analysis of Turbulent Flows. *Annual Review of Fluid Mechanics* , **25**(1), pp 539–575.

[40] G. C. Larsen, H. A. Madsen, F. Bingöl, J. Mann, S. Ott, J. N. Sørensen, V. Okulov, N. Troldborg, M. Nielsen, K.Thomsen, T. J. Larsen, and R. Mikkelsen (2007). Dynamic Wake Meandering Modeling. *Risø National Laboratory*, **Risø-R-1607**, pp 84.

[41] G. C. Larsen, H. A. Madsen, K.Thomsen, and T. J. Larsen (2008). Wake Meandering: A Pragmatic Approach. *Wind Energy*, **11**(4), pp 377–395.

[42] G. Cortina, R. B. Cal, and M. Calaf (2016). Distribution of Mean Kinetic Energy around an Isolated Wind Turbine and a Characteristic Wind Turbine of a Very Large Wind Farm. *Physical Review Fluids*, **1**, 074402, pp 1–18.

[43] G. España, S. Aubrun, S. Loyer, and P. Devinant (2011). Spatial Study of the Wake Meandering using Modelled Wind Turbines in a Wind Tunnel. *Wind Energy*, **14**, pp 923–937.

[44] G. Gilka, D. M. Luchtenburg, F. Thiele, and M. Morzynski (2010). Dynamic Characterization of an Actuated Bluff Body Wake. *V European Conference on Computational Fluid Dynamics ECCOMAS CFD 2010*, J. C. F. Pereira and A. Sequeira (Eds), pp 14–17.

[45] G. Haller (2001). Distinguished Material Surfaces and Coherent Structures in 3D Fluid Flows. *Physica D: Nonlinear Phenomena*, **149**(4), pp 248–277.

[46] G. K. Batchelor (1967). *An Introduction to Fluid Dynamics*. Cambridge University Press, Cambridge.

[47] H. Bolnot, S. Le Dize's, and T. Leweke (2014). Spatio-temporal Development of the Pairing Instability in an Infinite Array of Vortex Rings. *Fluid Dynamics Research*, **46**(6), pp 134–137.

[48] H. Hu, Z. Yang, and P. Sarkar (2012). Dynamic Wind Loads and Wake Characteristics of a Wind Turbine Model in an Atmospheric Boundary Layer Wind. *Experiments in Fluids*. **52**, pp 1277–1294.

[49] H. U. Quaranta, H. Bolnot, and T. Leweke (2015). Long-wave Instability of a Helical Vortex. *Journal of Fluid Mechanics*, **780**, pp 687–716.

[50] H. Snel (1998). Review of the Present Status of Rotor Aerodynamics. *Wind Energy*, **1**(s 1), pp 46–69.

[51] H. Snel, J. G. Schepers, and B. Montgomerie (2007). The MEXICO Project (Model Experiments in Controlled Conditions): The Database and First Results of Data Processing and Interpretation. *Journal of Physics: Conference Series* **75**(1), 012014.

[52] I. Mezić (2005). Spectral Properties of Dynamical Systems, Model Reduction and Decompositions. *Nonlinear Dynamics*, **41**(1-3), pp 309–325.

[53] J. C. R. Hunt, A. A. Wray, and P. Moin (1988). Eddies, Streams, and Convergence Zones in Turbulent Flows. In *Center for Turbulence Research Proceedings of the Summer Program*, **CTR-S88**, pp 193–208.

[54] J. Deardorff (1970). A Numerical Study of Three-dimensional Tturbulent Channel Flow at Large Reynolds Numbers. *Journal of Fluid Mechanics*, **41**(2), pp 453-480.

[55] J. Delville, L. Ukeiley, L. Cordier, J. P. Bonnet, and M. Glauser (1999). Examination of Large-scale Structures in a Turbulent Plane Mixing Layer. Part 1. Proper Orthogonal Decomposition. *Journal of Fluid Mechanics*, **391**, pp 91–122.

[56] J. F. Ainslie (1988). Calculating the Flow Field in the Wake of Wind Turbines. *Journal of Wind Engineering and Industrial Aerodynamics*, **27**(1-3), pp 213–224.

[57] J. G. M. Eggels, F. Unger, M. H. Weiss, J. Westerweel, R. J. Adrian, R. Friedrich, and F. T. M. Nieuwstadt (1994). Fully Developed Turbulent Pipe

Flow: A Comparison Between Direct Numerical Simulation and Experiment. *Journal of Fluid Mechanics*, **268**, pp 175–209.

[58] J. H. Tu, C. W. Rowley, D. M. Luchtenburg, S. L. Brunton SL, and J. N. Kutz (2014). On Dynamic Mode Decomposition: Theory and Applications. *Journal of Computational Dynamics*, **1**(2), pp 391–421.

[59] J. H. Tu, C. W. Rowley, J. N. Kutz, and J. K. Shang (2014). Spectral Analysis of Fluid Flows Using Sub-Nyquist-rate PIV Data. *Experiments in Fluids*, **55**(9), pp 1–13.

[60] J. Higham (2017). The Application of Modal Decomposition Techniques for the Analysis of Environmental Flows. *Ph.D. thesis University of Sheffield.*

[61] J. Jeong, and F. Hussain (1995). On the Identification of a Vortex. *Journal of Fluid Mechanics*, **285**, pp 69–94.

[62] J. J. Trujillo, F. Bingöl, G. C. Larsen, J. Mann, and M. Kuehn (2011). Light Detection and Ranging Measurement of Wake Dynamics. Part II. Two-Dimensional Scanning. *Wind Energy*, **14**(1), pp 61–75.

[63] J. K. Thorne (2009, August 23). Circular Wing Tip Trails. Retrieved July 24$^{\text{th}}$, 2019, from http://www.vansairforce.com/community/showthread.php?t=47071

[64] J. L. Lumley (1967). The Structure of Inhomogeneous Turbulent Flow. *Atmospheric Turbulence and Radio Wave Propagation*, pp 66–178.

[65] J. L. Proctor, S. L. Brunton, J. N. Kutz (1967). Dynamic Mode Decomposition With Control. *SIAM Journal on Applied Dynamical Systems*, **15**(1), pp 142–161.

[66] J. M. Pedersen, and K. E. Meyer (2002). POD Analysis of Flow Stuctures in a Scale Model of a Ventilated Room. *Experiments in Fluids*, **33**(6), pp 940–949.

[67] J. N. Kutz (2013). *Data-driven Modeling & Scientific Computation: Methods for Complex Systems & Big Data.* Oxford University Press.

[68] J. N. Kutz, S. L. Bruton, B. W. Bruton, and J. L. Proctor (2016). *Dynamic Mode Decomposition: Data-driven Modeling of Complex Systems*. SIAM Publishing, Philadelphia.

[69] J. N. Kutz, X. Fu, and S. L. Bruton (2016). Multi-Resolution Dynamic Mode Decomposition. *SIAM Journal on Applied Dynamical Systems*, **15**(2), pp 713–735.

[70] J. N. Sørensen (2011). Aerodynamic Aspects of Wind Energy Conversion. *Annual Review of Fluid Mechanics*, **43**, pp 427–448.

[71] J. N. Sørensen, and A. Myken (1992). Unsteady Actuator Disc Model for Horizontal Axis Wind Turbines. *Journal of Wind Engineering and Industrial Aerodynamics*, **39**(1), pp 139–149.

[72] J. N. Sørensen, and W. Z. Shen (2002). Numerical Modeling of Wind Turbine Wakes. *Trans. ASME: Journal Fluids Engineering*, **124**(2), pp 393–399.

[73] J. R. Garrat (1994). Review: the Atmospheric Boundary Layer. *Earth-Science Reviews*, **37**(1–2), pp 89–134.

[74] J. S. Haywood, and A. Sescu (2019). Wakes in Stratified Atmospheric Boundary Layer Flows: an LES Investigation. In *ArXiv e-prints*. arXiv: 1901.06420 [physics.flu-dyn].

[75] J. Smagorinsky (1963). General Circulation Experiments with the Primitive Equation. *Monthly Weather Review*, **91**(3), pp 99-164.

[76] J. Zhou, R. Adrian, S. Balachandar, and T. Kendall (1999). Mechanisms for Generating Coherent Packets of Hairpin Vortices in Channel Flow. *Journal of Fluid Mechanics*, **387**, pp 353–396.

[77] K. E. Meyer, J. M. Pedersen, and O. Ozcan (2007). A Turbulent Jet in Crossflow Analysed with Proper Orthogonal Decomposition. *Journal of Fluid Mechanics*, **583**, pp 199–227.

[78] K. E. Meyer, D. Cavar, and J. M. Pedersen (2007). POD as tool for comparison of PIV and LES data. in *7th International Symposium on Particle Image Velocimetry*, Rome: Faculty of Engineering, University "La Sapienza".

[79] K. Fukunaga (1990). *Introduction to Statistical Pattern Recognition*. Academic Press.

[80] K. K. Chen, J. H. Tu, and C. W. Rowley (2012). Variants of Dynamic Mode Decomposition: Boundary Condition, Koopman, and Fourier Analyses. *Journal of Nonlinear Science*, **22**(6), pp 887–915.

[81] K. Nilsson, S. Ivanell, K. S. Hansen, R. Mikkelsen, J. N. Sørensen, S. P. Breton, and D. Henningson (2015). Large-eddy Simulations of the Lillgrund Wind Farm. *Wind Energy*, **18**(3), pp 449–467.

[82] K. S. Hansen, R. J. Barthelmie, L. E. Jensen, and A. Sommer (2012). The Impact of Turbulence Intensity and Atmospheric Stability on Power Deficits due to Wind Turbine Wakes at Horns Rev Wind Farm. *Wind Energy*, **15**(1), pp 183–196.

[83] K. Taira, S. L. Brunton, S. T. M. Dawson, C. W. Rowley, T. Colonius, B. J. McKeon, O. T. Schmidt, S. Gordeyev, V. Theofilis, and L. S. Ukeiley (2017). Modal Analysis of Fluid Flows: An Overview. *AIAA Journal*, **55**(12), pp 1–46.

[84] K. Vyas (2018). World's Largest Offshore Wind Farm Begins Operations off England's Coast. Retrieved July 24$^{\text{th}}$, 2019, from https://interestingengineering.com/worlds-largest-offshore-wind-farm-begins-operations-off-englands-coast

[85] L. A. Martínez, S. Leonardi, M. J. Churchfield, and P. J. Moriarty (2012). A Comparison of Actuator Disk and Actuator Line Wind Turbine Models and Best Practices for Their Use. *50th AIAA Aerospace Sciences Meeting. Nashville, TN*, 09 - 12 January 2012.

[86] L. Feng, J. Wang, C. Pan (2011). Proper Orthogonal Decomposition Analysis of Vortex Dynamics of a Circular Cylinder under Synthetic Jet Control. *Physics of Fluids*, **23**(1), 014106.

[87] L. HaoFeng, J. J. Wang, and C. Pan (2010). Effect of Novel Synthetic Jet on Wake Vortex Shedding Modes of a Circular Cylinder. *Journal of Fluids and Structures*, **26**(6), pp 900–917.

[88] L. Mahrt (1999). Stratified Atmospheric Boundary Layers. *Boundary-Layer Meteorology*, **90**(3), pp 375–396.

[89] L. Massa, R. Kumar, and P. Ravindran (2012). Dynamic Mode Decomposition Analysis of Detonation Waves. *Physics of Fluids*, **24**(6).

[90] L. N. Trefethen, and D. Bau (1997). *Numerical Linear Algebra*. SIAM Publishing, Philadelphia.

[91] L. Sirovich (1987). Turbulence and the Dynamics of Coherent Structures. Part I. Coherent Structures. *Quarterly of Applied Mathematics*, **45**(3), pp 561–571.

[92] L. Vermeer, J. N. Sørensen, and A. Crespo (2003). Wind Turbine Wake Aerodynamics. *Progress in Aerospace Sciences*, **39**, pp 467-510.

[93] M. Abkar, and F. Porté-Agel (2015). Influence of Atmospheric Stability on Wind-turbine Wakes: A Large-eddy Simulation Study. *Physics of Fluids*, **27**, 035104.

[94] M. Abkar, A. Sharifi, and F. Porté-Agel (2016). Wake Flow in a Wind Farm during a Diurnal Cycle. *Journal of Turbulence*, **17**(4), pp 420–441.

[95] M. A Green, C. W. Rowley, and G. Haller (2007). Detection of Lagrangian Coherent Structures in three-dimensional Turbulence. *Journal of Fluid Mechanics* **572**, pp 111–120.

[96] M. Bastankhah, and F. Porté-Agel (2017). Wind Tunnel Study of the Wind Turbine Interaction with a Boundary-layer Flow: Upwind Region, Turbine Performance, and Wake Region. *Physics of Fluids*, **29**(9), 065105.

[97] M. Bergmann, L. Cordier, and J. P. Brancher (2005). Optimal Rotary Control of the Cylinder Wake Using Proper Orthogonal Decomposition Reduced-order Model. *Physics of Fluids*, **17**(9), pp 1–21.

[98] M. Beychok (2013). Atmospheric Lapse Rate. Retrieved March 23rd, 2020, from http://editors.eol.org/eoearth/wiki/Atmospheric_lapse _rate

[99] M. Calaf, C. Meneveau, and J. Meyers (2010). Large Eddy Simulation Study of Fully Developed Wind- Turbine Array Boundary Layers. *Physics of Fluids*, **22**(1), 015110.

[100] M. Cervarich. The Effect of Wind Farms on Near-surface Meteorology. Retrieved July 24th, 2019, from https://www.atmos.illinois.edu/ cervari2/bl.html

[101] M. Felli, R. Camussi, F. di Felice (2011). Mechanisms of Evolution of the Propeller Wake in the Transition and Far Fields. *Journal of Fluid Mechanics*, **682**, pp 5–53.

[102] M. J. Bhagwat, and J. G. Leishman (2000). Stability Analysis of Helicopter Rotor Wakes in Axial Flight. *Journal of the American Helicopter Society*, **45**, pp 165–178.

[103] M. Kaushik (2019). *Theoretical and Experimental Aerodynamics*. Springer.

[104] M. Matin (2017). Predicting Interference Patterns between Offshore Wind Farms through Wake Analysis. *Master's Thesis Carleton University Ottawa, Ontario.*

[105] M. O. L. Hansen, J. N. Sørensen, S. Voutsinas, N. Sørensen, H. A. Madsen (2006). State of the Art in Wind Turbine Aerodynamics and Aeroelasticity. *Progress in Aerospace Sciences*, **42**, pp 285-330.

[106] M. S. Chong, A. E. Perry, and B. J. Cantwell (1990). A General Classification of Three-Dimensional Flow Fields. *Physics of Fluids*, **2**(5), pp 765–777.

[107] M. S Hemati, C. W. Rowley, E. A. Deem, L. N. Cattafesta (2017). De-Biasing the Dynamic Mode Decomposition for Applied Koopman Spectral Analysis. *Theoretical and Computational Fluid Dynamics*, **31**(4), pp 349–368.

[108] M. Sherry, A. Nemes, D. Lo Jacono, H. M. Blackburn, and J. Sheridan (2013). The Interaction of Helical Tip and Root Vortices in a Wind Turbine Wake. *Physics of Fluids*, **25**, 117102.

[109] M. V. Melander, and F. Hussain (1993). Polarized Vorticity Dynamics on a Vortex Column. *Physics of Fluids*, **5**:1992

[110] N. Ali, G. Cortina, N. Hamilton, M. Calaf, and R. B. Cal (2017). Turbulence Characteristics of a Thermally Stratified Wind Turbine Array Boundary Layer via Proper Orthogonal Decomposition. *Journal of Fluid Mechanics*, **828**, pp 175–195.

[111] N. Ali, N. Hamilton, M. Calaf, and R. B. Cal (2019). Turbulence Kinetic Energy Budget and Conditional Sampling of Momentum, Scalar, and Intermittency Fluxes in Thermally Stratified Wind Farms. *Journal of Turbulence*, **20**(1), pp 32–63.

[112] N. Coudou, S. Buckingham, and J. van Beeck (2017). Experimental Study on the Wind-turbine Wake Meandering inside a Scale Model Wind Farm Placed in an Atmospheric-boundary-layer Wind Tunnel. *Journal of Physics: Conference Series*, **854**, 012008.

[113] N. E. Joukowski (1912). Vortex Theory of Screw Propeller. *Trudy Otdeleniya Fizicheskikh Nauk Obshchestva Lubitelei Estestvoznaniya*, **16**(1), pp 1–31.

[114] N. Hamilton, M. Tutkun, and R. B. Cal (2015). Wind Turbine Boundary Layer Arrays for Cartesian and Staggered Configurations: Part II, Low-dimensional Representations via the Proper Orthogonal Decomposition. *Wind Energy*, **18**(2), pp 297–315.

[115] N. Hamilton, M. Tutkun, and R. B. Cal (2015). Low-order Representations of the Canonical Wind Turbine Array Boundary Layer via Double Proper Orthogonal Decomposition. *Physics of Fluids*, **28**(2), 025103.

[116] N. Murray, E. Sällström, and L. Ukeiley (2009). Properties of Subsonic Open Cavity Flow Fields. *Physics of Fluids*, **21**(9), pp 1–16.

[117] N. O. Jensen (1983). A Note on Wind Generator Interaction. *Risø National Laboratory*, **Risø-M-2411**, pp 84.

[118] N. Troldborg (2009). Actuator Line Modelling of Wind Turbine Wakes. *Ph.D. thesis Technical University of Denmark*,

[119] P. Bachant, and M. Wosnik (2015). Characterising the Near-wake of a Cross-flow Turbine. *Journal of Turbulence 2015*, **16**, pp 392–410.

[120] P. Burattini, S. Leonardi, P. Orlandi, R. A. Antonia (2008). Comparison Between XEperiments and Direct Numerical Simulations in a Channel Flow with Roughness on One Wall. *Journal of Fluid Mechanics*, **600**, pp 403–426.

[121] P. Chakraborty, S. Balachandar, R. J. Adrian (2005). On the Relationships Between Local Vortex Identification Schemes *Journal of Fluid Mechanics*, **535**, pp 189–214.

[122] P. Hémon, and F. Santi (2007). Simulation of a Spatially Correlated Turbulent Velocity Field Using Biorthogonal Decomposition. *Journal of Wind Engineering and Industrial Aerodynamics*, **95**(1), pp 21–29.

[123] P. Holmes, J. L. Lumley, G. Berkooz, and C. W. Rowley (1996). *Turbulence, Coherent Structures, Dynamical Systems and Symmetry*. Cambridge University Press.

[124] P. J. Diamessis, R. Gurka, A. Liberzon (2010). Spatial Characterization of Vortical Structures and Internal Waves in a Stratified Turbulent Wake using Proper Orthogonal Decomposition. *Physics of Fluids*, 22, 086601.

[125] P. J. Schmid (2010). Dynamic Mode Decomposition of Numerical and Experimental Data. *Journal of Fluid Mechanics*, **656**, pp 5–28.

[126] P. J. Schmid (2011). Application of the Dynamic Mode Decomposition to Experimental Data. *Experiments in Fluids*, **50**(4), pp 1123–1130.

[127] P. J. Schmid, and D. S. Henningson (2001). *Stability and Transition in Shear Flows*. Springer.

[128] P. J. Schmid, and J. L. Sesterhenn (2008). Dynamic Mode Decomposition of Numerical and Experimental Data. *Bulletin of the American Physical Society, 61^{st} APS meeting*. pp 208. San Antonio.

[129] P. J. Schmid, K. E. Meyer, and O. Pust (2009). Dynamic Mode Decomposition and Proper Orthogonal Decomposition of Flow in a Lid-driven Cylindrical Cavity. in *8_{th} international symposium on Particle Image Velocimetry-PIV09*, **3**, pp 1–4.

[130] P. J. Schmid, L. Li, M. P. Juniper, and O. Pust (2011). Applications of the Dynamic Mode Decomposition. *Theoretical and Computational Fluid Dynamics*, **25**(1-4), pp 249–259.

[131] P. J. Schmid, D. Violato, O. Pust, and F. Scarano (2012). Decomposition of Time-Resolved Tomographic PIV. *Experiments in Fluids*, **52**(6), pp 1567–1579.

[132] P. Kundu, and I. Cohen (2004). *Fluids Mechanics, 4th Edition*. Amsterdam, The Netherlands: Elsevier Academic Press

[133] P. M. Munday, and K. Taira (2014). Wall-normal Vorticity Injection in Separation Control of NACA 0012 Airfoil. *AIAA Paper*, pp 2014–2685.

[134] P. Stoica, and R. Moses (2005). *Spectral Analysis of Signals*. Prentice Hall, Upper Saddle River, New Jersey.

[135] Q. Zhang, Y. Liu, and S. Wang (2014). The Identification of Coherent Structures Using Proper Orthogonal Decomposition and Dynamic Mode Decomposition. *Journal of Fluids and Structures*, **49**, pp 53–72.

[136] R. B. Cal, J. Lebrø'n, L. Castillo, H. S. Kang, C. Meneveau (2010). Experimental Study of the Horizontally Averaged Flow Structure in a Model Windturbine Array Boundary Layer. *Journal of Renewable and Sustainable Energy 2*, **2**, 013106.

[137] R. B. Fisher, and D. K. Naidu (1996). A Comparison of Algorithms for Subpixel Peak Detection. In *Advances in Image Processing, Multimedia and Machine Vision* J. Sanz, Ed. Berlin: Springer-Verlag, pp 385–404.

[138] R. B. Lehoucq (2001). Implicitly Restarted Arnoldi Methods and Subspace Iteration. *SIAM Journal on Matrix Analysis and Applications*, **23**(2), pp 551–562.

[139] R. B. Stull (1988). An Introduction to Boundary Layer Meteorology. Springer.

[140] R. F. Mikkelsen (2003). Actuator Disc Methods Applied to Wind Turbines. *Ph.D. thesis Technical University of Denmark*, MEK-FM-PHD **2003-02**.

[141] R. Gurka, A. Liberzon, G. Hetsroni (2006). POD of Vorticity Fields: A method for Spatial Characterization of Coherent Structures. *International Journal of Heat and Fluid Flow*, **27**(3), pp 416–423.

[142] R. J. Adrian (2007). Hairpin Vortex Organization in Wall Turbulence. *Physics of Fluids*, **19**(4), 041301.

[143] R. J. Adrian, I. Marusic (2012). Coherent Structures in Flow over Hydraulic Engineering Surfaces. *Journal of Hydraulic Research*, **50**(5), pp 451–464.

[144] R. W. Metcalfe, F. Hussain, S. Menon, and M. Hakayawa (1985). Coherent Structures in a Turbent Mixing Layer: A Comparison between Numerical Simulations and Experiments. In *Turbulent Shear Flows 5 ed.*, (F. Durst, B. E. Launder, J. L. Lumley, F. W. Schmidt & J. H. Whitelaw) Springer. pp 110.

[145] S. A. Orszag, and G. S. Patterson (1972). Numerical Simulation of Turbulence: Statistical Models and Turbulence. *Lecture Notes in Physics*, **12**, pp 127–147. Springer-Verlag, Berlin.

[146] S. Bagheri(2014). Effects of Weak Noise on Oscillating Flows: Linking Quality Factor, Floquet Modes, and Koopman Spectrum. *Physics of Fluids*, **26**(9), 094104.

[147] S. Bagheri, P. Schlatter, P. J. Schmid, and D. S. Henningson (2009). Global Stability of a Jet in Crossflow. *Journal of Fluid Mechanics*, **624**, pp 33–44.

[148] S. Bernero, and H. E.Fiedler (2000). Application of Particle Image Velocimetry and Proper Orthogonal Decomposition to the Study of a Jet in a Counterflow. *Experiments in Fluids*, **29**, pp S274–S281.

[149] S. C. Selçuk (2016). Numerical Study of Helical Vortices and Their Instabilities. *Ph.D. thesis Université Pierre et Marie Curie,*.

[150] S. Chandrasekhar (1961). *Hydrodynamic and Hydromagnetic Stability*. Clarendon Press, Oxford.

[151] S. E. Widnall (1972). The Stability of a Helical Vortex Filament. *Journal of Fluid Mechanics*, **54**(4), pp 641–663.

[152] S. Frandsen, R. Barthelmie, S. Pryor , O. Rathmann, S. Larsen, J. Højstrup, and M. Thøgersen (2006). Analytical Modelling of Wind Speed Deficit in Large Offshore Wind Farms. *Wind Energy*, **9**(1-2), pp 39–53.

[153] S. Ivanell, J. N. Sørensen, R. Mikkelsen, and D. S. Henningson(2009). Analysis of Numerically Generated Wake Structures. *Wind Energy*, **12**(1), pp 63–80.

[154] S. Ivanell, R. Mikkelsen, J. N. Sørensen, and D. S. Henningson(2010). Stability Analysis of the Tip Vortices of a Wind Turbine. *Wind Energy*, **13**(8), pp 705–715.

[155] S. J. Andersen, J. N. Sørensen, and R. Mikkelsen (2013). Simulation of the Inherent Turbulence and Wake Interaction inside an Infinitely Long Row of Wind Turbines. *Journal of Turbulence*, **14**(4), pp 1–24.

[156] S. L. Brunton, B. W. Brunton, J. L. Proctor, E. Kaiser, and J. N. Kutz (2017). Chaos as an Intermittently Forced Linear System. *Nature Communications*, **8**(1).

[157] S. L. Tang, L. Djenidi, R.A. Antonia, and Y. Zhou (2015). Comparison Between Velocity- and Vorticity-based POD Methods in a Turbulent Wake. *Experiments in Fluids*, **56**(8).

[158] S. S. Varghese, S. H. Frankel, and P. F. Fischer (2007). Direct Numerical Simulation of Stenotic Flows Part 1: Steady Flow. *Journal of Fluid Mechanics*, **582**, pp 253–280.

[159] S. Sarmast, R. Dadfar Reza, R. F. Mikkelsen, P. Schlatter, S. Ivanell, J. N. Sørensen, and D. S. Henningson (2014). Mutual Inductance Instability of the Tip Vortices behind a Wind Turbine. *Journal of Fluid Mechanics*, **755**, pp 705–731.

[160] S. Schreck (2002). The NREL Full-scale Wind Tunnel Experiment: Introduction to the Special Issue. *Wind Energy*, **5**(2-3), pp 77–84.

[161] S. Shah, and E. Bou-Zeid (2014). Very-large-scale Motions in the Atmospheric Boundary Layer Educed by Snapshot Proper Orthogonal Decomposition. *Boundary-Layer Meteorology*, **53**(3), pp 355–387.

[162] S. Stegmaier, U. Rist, and T. Ertl (2005) . Opening the Can of Worms: An Exploration Tool for Vortical Flows. *Proceedings of IEEE Visualization '05*, Minneapolis, MN, pp 463–47.

[163] S. Tirunagari, V. Vuorinen, O. Kaario, and M. Larmi (2012). Analysis of Proper Orthogonal Decomposition and Dynamic Mode Decomposition on LES of Subsonic Jets. *CSI Journal of Computing*, **1**, pp 20–26.

[164] S. T. M. Dawson, M. S Hemati, M. O. Williams, and C. W. Rowley (2016). Characterizing and Correcting for the Effect of Sensor Noise in the Dynamic Mode Decomposition. *Experiments in Fluids*, **57**(3), pp 1–19.

[165] S. V. Gordeyev, and F. O. Thomas (2000). Coherent Structure in the Turbulent Planar Jet. Part 1. Extraction of Proper Orthogonal Decomposition Eigenmodes and their Self-similarity. *Journal of Fluid Mechanics*, **414**, pp 145–194.

[166] S. V. Gordeyev, and F. O. Thomas (2002). Coherent Structure in the Turbulent Planar Jet. Part 2. Structural Topology via POD Eigenmode Projection. *Journal of Fluid Mechanics*, **460**, pp 349–380.

[167] S. Wharton, and J. K. Lundquist (2012). Atmospheric Stability Affects Wind Turbine Power Collection. *Environmental Research Letter*, **7**(1), 014005.

[168] T. Sayadi, P. J. Schmid, J. W. Nichols, and P. Moin (2013). Dynamic Mode Decomposition of Controlled H- and K- type Transitions. in *Annual Research Briefs 2013*, Center for Turbulence Research, Stanford University pp 189–200.

[169] T. W. Muld, G. Efraimsson, and D. S. Henningson (2012). Flow Structures around a High-speed Train Extracted Using Proper Orthogonal Decomposition and Dynamic Mode Decomposition. *Computers and Fluids*, **57**(4), pp 87–97.

[170] V. Kolář (2007). Vortex Identification: New Requirements and Limitations. *International Journal of Heat and Fluid Flow* **28**, pp 638–652.

[171] V. L. Okulov (2004). On the Stability of Multiple Helical Vortices. *Journal of Fluid Mechanics*, **521**, pp 319–342.

[172] V. L. Okulov, and J. N. Sørensen (2007). Stability of Helical Tip Vortices in a Rotor Far Wake. *Journal of Fluid Mechanics*, **576**, pp 1–25.

[173] V. Theofilis (2003). Advances in Global Linear Instability Analysis of Nonparallel and Three-dimensional Flows. *Progress in Aerospace Sciences*, **39**(4), pp 249–315.

[174] V. Theofilis (2011). Global Linear Instability. *Annual Review of Fluid Mechanics*, **43**(1), pp 319–352.

[175] W. S. Edwards, L. S. Tuckerman, R. A. Friesner, and D. C.Sorensen (1994). Krylov Methods for the Incompressible Navier-Stokes Equations. *Journal of Computational Physics*, **110**(1), pp 82–102.

[176] Wingtip Vortices. Retrieved July 24$^{\text{th}}$, 2019, from https://www.wikiwand.com/en/Wingtip_vortices

[177] X. Mao, and F. Hussain (2017). Dynamics of Helical Vortices Behind a Wind Turbine in a Stratified Atmosphere. *70th Annual Meeting of the APS Division of Fluid Dynamics*, **62**(14).

[178] X. Mao, and J. N. Sørensen (2018). Far-wake Meandering Induced by Atmospheric Eddies in Flow Past a Wind Turbine. *Journal of Fluid Mechanics*, **846**, pp 190–209.

[179] X. J. Xiang, K. K. Chen, and G. R. Spedding (2017). Dynamic Mode Decomposition for Estimating Vortices and Lee Waves in a Stratified Wake. *Experiments in Fluids*, **58**(5).

[180] Y. Feng, J. Goree, and B. Liu (2007). Accurate Particle Position Measurement from Images. *Review of Scientific Instruments*, **78**(5), pp 53–59.

[181] Y. Jin, H. Liu, R. Aggarwal, A. Singh and L. P. Chamorro (2016). Effects of Freestream Turbulence in a Model Wind Turbine Wake *Energies*, **9**(10), pp 830.

[182] Y. Liu, and Q. Zhang (2015). Dynamic Mode Decomposition of Separated Flow over a Finite Blunt plate: Time-resolve Particle Image Velocity Measurements. *Experiments in Fluids*, **56**(148), pp 1–17.